Università degli Studi di Napoli "Federico II"

Facoltà di Scienze Matematiche, Fisiche e Naturali

Ph. D. Course in Fundamental and Applied Physics

XXVII Cycle

2016

Doctor of Philosophy Thesis

Beyond the Standard Model Higgs search at High Mass in the $H \to ZZ \to \ell^{\pm}\ell^{\mp}q\bar{q}$ channel with the ATLAS detector at LHC

Tutors:
Prof. Leonardo Merola

Dott. Francesco Conventi

Candidate: Giovanni Zurzolo

Contents

Introduction **vi**

1 Standard Model and Beyond **1**

1.1 Quantum Field Theory and Elementary Particles 1

1.1.1 Fermions: Matter Particles 3

1.1.2 Bosons: Force Carriers 4

1.2 The Standard Model 4

1.2.1 Quantum Electrodynamics (QED) 5

1.2.2 Quantum Chromodynamics (QCD) 8

1.2.3 Electroweak Theory 10

1.2.4 The Higgs-Brout-Englert Model 11

1.3 The Standard Model Higgs Boson 17

1.3.1 Theoretical Constraints 18

1.3.2 Experimental constraints 22

1.3.3 The Higgs boson discovery 27

1.4 Beyond the Standard Model (BSM) 29

1.4.1 Two-Higgs-Doublet Models ($2HDM$) 30

2 The ATLAS experiment at the LHC **36**

2.1 The Large Hadron Collider 36

2.1.1 The acceleration chain 38
2.1.2 The grid structure 40
2.1.3 Beam luminosity 41
2.2 The ATLAS experiment 44
2.2.1 ATLAS reference system 46
2.2.2 The magnetic system 48
2.2.3 Inner Detector 50
2.2.4 Calorimetric system 55
2.2.5 The muon spectrometer 60
2.2.6 The ATLAS Trigger 68

3 Physics objects reconstruction 76
3.1 Electrons 76
3.1.1 Electron reconstruction 76
3.1.2 Electron identification 80
3.1.3 Reconstruction and Identification efficiencies 82
3.2 Muons 85
3.2.1 Muon reconstruction and identification 85
3.2.2 Reconstruction and identification efficiencies 87
3.3 Jets 89
3.3.1 Jet reconstruction 90
3.3.2 Jet Energy Calibration 92
3.3.3 Jet Energy Resolution 97
3.4 *b*-tagging 97
3.4.1 Lifetime-based tagging algorithms 99
3.5 Missing Transverse Energy 104

4 The SM Higgs boson at ATLAS 106

4.1 Higgs boson phenomenology . . . 106

4.2 Mass measurement . . . 111

4.2.1 $H \to \gamma\gamma$ decay channel . . . 111

4.2.2 $H \to ZZ^* \to 4\ell$ decay channel . . . 113

4.2.3 Combined mass measurement . . . 114

4.3 Signal strength measurement . . . 117

4.3.1 $H \to \gamma\gamma$ . . . 117

4.3.2 $H \to ZZ^* \to 4\ell$ . . . 118

4.3.3 $H \to WW^*$ . . . 118

4.3.4 $H \to \tau\tau$ . . . 120

4.3.5 VH with $H \to b\bar{b}$ . . . 120

4.3.6 $H \to Z\gamma$ . . . 121

4.3.7 $H \to \mu\mu$ . . . 122

4.3.8 ttH production . . . 122

4.3.9 Global signal strength . . . 123

4.3.10 Individual production processes . . . 125

4.4 Indirect limits on BSMs . . . 128

4.4.1 *2HDM*s indirect limits . . . 129

5 The $H \to ZZ \to \ell^{\pm}\ell^{\mp}q\bar{q}$ channel 133

5.1 Data and Monte Carlo samples . . . 134

5.1.1 Data sample . . . 134

5.1.2 Signal samples . . . 134

5.1.3 Background samples . . . 137

5.2 Physics objects selection . . . 141

5.2.1 Muons . . . 141

5.2.2 Electrons . . . 143

5.2.3 Jets . . . 146
5.2.4 Missing transverse energy . . . 152
5.2.5 Overlap removal . . . 153
5.3 Event selection . . . 153
5.3.1 Trigger and preselection . . . 154
5.3.2 $Z \to \ell\ell$ selection . . . 155
5.3.3 $H \to ZZ \to \ell\ell qq$ selection . . . 156
5.4 Backgrounds . . . 169
5.4.1 Z+jets background . . . 170
5.4.2 Top quark background . . . 187
5.4.3 Multi-jet background . . . 189
5.4.4 Diboson background . . . 191
5.4.5 W+jets background . . . 191
5.4.6 SM $Zh, h \to bb$ production . . . 191
5.5 Systematic uncertainties . . . 191
5.5.1 Experimental systematic uncertainties . . . 192
5.5.2 Signal and background modelling systematics . . . 200
5.6 Resolution and binning of the $m_{\ell\ell jj}$ distributions . . . 209
5.6.1 Resolution . . . 209
5.6.2 Binning . . . 209
5.7 Results . . . 211
5.7.1 Resolved ggF category . . . 211
5.7.2 Merged ggF category . . . 214
5.7.3 VBF category . . . 214
5.8 Statistical interpretation . . . 214
5.8.1 Likelihood definition . . . 216
5.8.2 Fit inputs and variables . . . 217

5.8.3 Nuisance parameters: normalization and systematic uncertanties . . . 218
5.8.4 Nuisance parameters: statistical uncertainties . . . 220
5.8.5 Pruning of the systematic uncertainties . . . 220
5.8.6 Understanding the fit configuration . . . 222
5.8.7 Nuisance parameter ranking . . . 223
5.8.8 Post-fit plots . . . 223
5.9 Exclusion limits . . . 226
5.9.1 Exclusion limits on narrow-width Higgs . . . 226
5.9.2 Exclusion limits on *2HDM* . . . 226
5.10 Combination of $H \to ZZ$ searches . . . 240

6 Conclusions **246**

Bibliography **272**

Introduction

The Standard Model of particle physics is the theoretical framework that include the actual knowledge of elementary particles and their fundamental interactions. It has been developed during the 20th century and it has a very high predictive power at very high precision level: throughout the past decades its predictions has been confirmed in many experiments, last but not least the existence of the Higgs boson.

The discovery of the Higgs boson announced by the ATLAS and CMS Collaborations at CERN on 4^{th} July 2012 is a milestone of particle and high energy physics, since it confirmed that the Higgs model well describes the scalar sector of the Standard Model. However, the existence of a single Higgs boson relies on the simplest assumption about the scalar sector structure and there is still room for many other important analyses which test a wide variety of beyond the Standard Model scenarios.

The Large Hadron Collider at CERN permits to perform pp collisions at the highest center-of-mass energy ever achieved and equal to 8 TeV during the 2012 operational run. The ATLAS detector is one of the four LHC main experiments: a multi-purpose detector which collects the collision data and allows to full reconstruct the collision events and perform a very wide variety of physics analyses.

At the LHC energies, the Higgs boson can be probed in a wide range of mass values and in several decay channels, one of which is the decay into two Z bosons

$H \to ZZ$. The final signature of such events depends on the specific decay channel of the two Z bosons and a sensible reduction of the hadronic background is achievable by requiring the leptonic decay of one of them $Z \to \ell\ell$. However, the branching ratio of hadronic decays $\mathrm{BR}(Z \to qq)$ is higher and the requirement that the second Z boson decays into quarks $Z \to qq$ permits to enhance the overall cross section of the searched process.

This thesis work presents the search for a high-mass Higgs boson in the $H \to ZZ \to \ell^{\pm}\ell^{\mp}q\bar{q}$ in the $200 - 1000$ GeV mass range using 20.3 fb^{-1} of integrated luminosity of pp collisions data collected by the ATLAS detector during the 2012 LHC run at a center-of-mass energy of 8 TeV. The major challenge of this search is constituted by the hadronic signature components. Beneath they permit to obtain a higher cross section with respect to a full leptonic decay, jets are more difficult to study and a careful and tight selection must be performed to properly reduce the hadronic backgrounds while keeping a high signal selection efficiency. Furthermore, for values of Higgs boson mass above 700 GeV, jets coming from the Z boson decay are highly boosted along the flight direction and could not be resolved as single jets. A dedicated selection is then needed to recover the efficiency loss due to this experimental issue.

In the Chapter 1 of this thesis, a brief review of the Standard Model is presented with a closer look at the spontaneous symmetry breaking mechanism. Along with the Brout-Englert-Higgs model and its experimental confirmation, the theoretical and experimental constraints on the Higgs boson mass before the 4th July 2012 discovery are presented. Finally, a brief description of the two-Higgs-doublet model is given, providing a beyond the Standard Model interpretation to the existence of an addition heavy Higgs boson.

In Chapter 2, the Large Hadron Collider and the ATLAS detector are presented by describing in all its subparts the experimental apparatus that permitted the

present search.

In Chapter 3, the reconstruction and identification procedures of the final physics objects used in this search, *i.e.* electrons, muons, jets and missing transverse energy, are presented with a description of the dedicated algorithms.

The Chapter 4 offers a brief review of the actual status of experimental measurements on the Higgs boson, along with the indirect limits on the two-Higgs-doublet model obtained from these measurements.

In Chapter 5, a detailed description of the $H \to ZZ \to \ell^{\pm}\ell^{\mp}q\bar{q}$ analysis is given encompassing: the data and Monte Carlo samples used in this search, the physics objects and event selection performed, all backgrounds that contributed to the analyzed channel and the systematic uncertainties that affected the measurements. The final results, the exclusion limits on a heavy Higgs boson and the constraints on the Type I and Type II two-Higgs-doublet models are also given, along with their statistical interpretation.

Chapter 1

Standard Model and Beyond

The Standard Model (SM) is a non-abelian gauge theory that describes strong and electroweak interactions. It was first proposed in the 60's and it received several experimental confirmations. Actually, it is the model used to study high energy and particles physics.

1.1 Quantum Field Theory and Elementary Particles

The Quantum Field Theory is the theoretical framework that merges Quantum Mechanics and the Relativity Principle into a single theory. The dynamical variables are represented by quantized fields, which are linear operators on Hilbert space of states, dependent from space-time point and with well-defined transformation properties for changes of the reference system.
Under specific conditions, fields can be expanded into quantized plane waves and the corresponding creation operators, applied to the vacuum state, originate states of a relativistic particles with mass and spin given by transformation properties of the field.

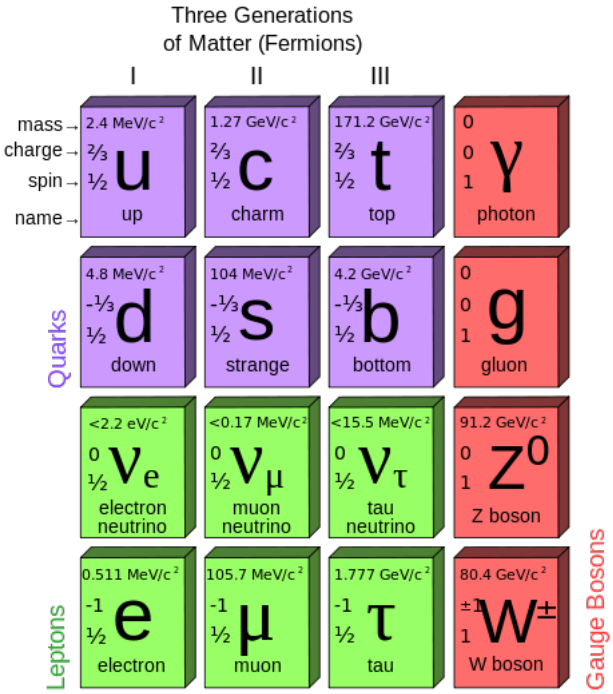

Figure 1.1: List of elementary particles in the Standard Model

In the Standard Model, fields are divided into two categories depending on the spin value:

- matter fields correspond to particles with a half-integer valued spin; they obey to Fermi-Dirac statistics and, for this reason, they are called fermions;
- force fields correspond to particles with an integer valued spin; they obey to Bose-Einstein statistics and, for this reason, they are called bosons.

These two categories group all known particles and three of their known interactions (electromagnetic, weak and strong forces). In fact, interactions can be described as an exchange of bosons that are defined, for this reason, as force carriers.

1.1.1 Fermions: Matter Particles

Fermions are classified into two categories: quarks and leptons. Quarks possess a baryonic number $B = \frac{1}{3}$ and they are the fundamental constituents of hadrons. Furthermore, quarks interact via both electroweak and strong forces. Leptons, instead, possess a leptonic number $L = 1$ and, unlike quarks, they do not interact via strong force.

Both quarks and leptons are classified into three groups called families or generations, each consisting in a couple of distinct particles (doublet).

The first generation of quarks consists of two quarks called *up* (u) and *down* (d) with, respectively, an electric charge (in units of electron charge, e) of $+\frac{2}{3}$ and $-\frac{1}{3}$. The other two generations similarly consist of two quarks, a u-type and a d-type quarks, with same quantum numbers but with mass values that gradually increase with generations, namely the *charme* - *strange* (c - b) and the *top* - *bottom* (t - b) doublets. Since quarks interact also via strong force, they possess a color charge and can exist in three different color states (namely *red*, *green* and *blue*).

Similarly to quarks families, each lepton generation consists of a doublet of particles: an electrically charged lepton, namely *electron* (e), *muon* (μ) and *tau* (τ), and the corresponding *neutrino* (ν_e, ν_μ and ν_τ) with a null electric charge. Also lepton families are ordered in terms of increasing mass values, although the mass of neutrinos needs a different and more complex explanations and it is here considered as null.

Finally, for both quarks and leptons, a corresponding antiparticle exists with quantum numbers of opposite sign and same mass value.

1.1.2 Bosons: Force Carriers

In nature there exist four fundamental forces: electromagnetic, weak, strong and gravitational interactions. The first three of these are described by the Standard Model as emissions and absorptions of specific force carriers, integer spin particle called bosons. The latter, instead, is negligible at the energy scale of particle physics and it is not considered within the Standard Model.
Electromagnetic force is responsible of interactions between electrically charged particles and the *photon* (γ), a massless boson, is its mediator. It mainly acts, at the atomic scale, to bind electrons to nuclei as well as to rule both molecules formations and interactions.
Strong force is, instead, responsible of interactions between coloured particles and eight massless bosons called *gluons* (g) are its mediators. It mainly acts, at the atomic scale, to bind nucleons (*protons* and *neutrons*) within nuclei.
Finally, weak force is responsible of particles and atomic decays and three massive bosons, called Z and $W^{\pm}$, are its mediators.

1.2 The Standard Model

The Standard Model is the theoretical framework that describes, through Quantum Field Theory, electroweak and strong interactions of elementary particles.
Unification of special relativity and quantum mechanics started in the late 1920s with the work of Dirac [1], Heisenberg and Pauli [2, 3] by developing a general formalism which can in principle be applied to all fundamental forces. Their works leaded, in the late 1940s, to the development of the field theory of quantum electrodynamics (QED), thanks to the independent works of Feynman [4–6], Schwinger [7,8], Dyson [9,10] and Sin-Itiro Tomonaga [11]. This theory permitted

calculations consistent with experimental results to a very high degree of accuracy. In the 1930s, furthermore, Fermi proposed a theory of weak interactions [12, 13] that provided the basis of the present theoretical model, although not capable to explain weak interactions overall. An advancement towards the current Standard Model was made by Glashow [14], Weinberg [15] and Salam [16] which, in the 1960s, proposed a unification of weak and electromagnetic interactions into the electroweak theory. Nowadays, it is known that also strong interactions can be described by a gauge field theory, called quantum chromodynamics (QCD), in which colour charge plays the same role of electric charge into the QED theory. All these theories as a whole and, in particular, the unification of electroweak theory and QCD compose the theoretical framework currently known with the name of Standard Model.

1.2.1 Quantum Electrodynamics (QED)

Quantum electrodynamics (QED) is an abelian gauge theory that describes the interaction of charged fermions with photons, the quanta of the electromagnetic field.

According to the Feynman representation of QED processes, it is possible to describe the interaction with the electromagnetic field of charged fermions, which are moving between two points of the space-time, as either the absorption or the emission of a photon (γ) in a given interaction point called *vertex*. In Figure 1.2 two Feynman diagrams for two basic QED processes are shown, namely electron-electron scattering $e^-e^- \to e^-e^-$ and electron-positron annihilation with muon-antimuon production $e^-e^+ \to \mu^-\mu^+$. In the Feynman diagrams fermions are represented by a straight line whereas photon by a wavy line, with time flowing either in the horizontal or in the vertical direction according to conservation laws.

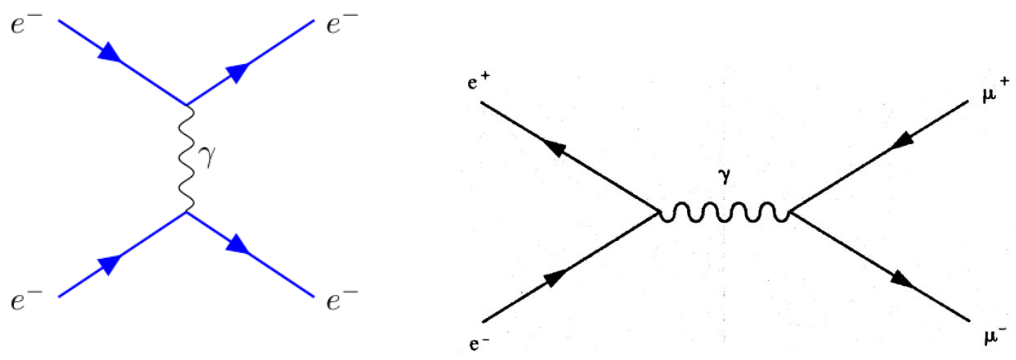

(a) $e^-e^- \to e^-e^-$ scattering (b) $e^+e^- \to \mu^+\mu^-$ annihilation

Figure 1.2: Feynman diagrams for two QED processes

Fermions absorb or emit a photon in the interaction *vertex* and the intensity of interaction is determined by the coupling constant between the fermion and the quantum field. Since electromagnetic field couples to electric charge (e), electromagnetic coupling constant, called *fine-structure constant* (α), is defined in terms of unit charge e as $\frac{e^2}{4\pi} \simeq \frac{1}{137}$ (in natural units). A single Feynman diagram is composed at least of two interaction vertices. A complete QED process, instead, is described by adding in quadrature the probability amplitudes of all possible Feynman diagrams with the same initial states leading to the same final states of the considered process. Usually, the simplest processes with the smallest number of interaction vertices are called *tree-level* or *leading-order* diagrams whereas more complex processes are called *high-order* diagrams. Anyway, the contribution of *high-order* processes to the *tree-level* one is progressively smaller as the number of vertices increase, since each vertex contributes to the overall probability amplitude by reducing it of a factor proportional to the coupling constant α.

In a QFT, dynamics of quantum fields is described by a Lagrangian density $\mathcal{L}(x)$ that is a local function of fields and their derivatives. From application of Minimal Action Principle to the Lagrangian density is possible to derive equations

of motion through Euler-Lagrange equations. In general, a minimal Lagrangian is composed of two distinct terms: a free term, which is determined by the properties of the field itself (e.g. mass and spin), and an interaction term, which depends on symmetry properties of interactions and is treatable with perturbation theory, under specific conditions.

In *QED*, considering a lepton ℓ coupled to electromagnetic field, the Lagrangian density $\mathcal{L}_{QED}$ can be written as:

$$\mathcal{L}_{QED} = -\frac{1}{4}F^{\mu\nu}F_{\mu\nu} - \bar{\psi}_\ell\gamma^\mu\left[\partial_\mu + ieA_\mu\right]\psi_\ell - m_\ell\bar{\psi}_\ell\psi_\ell \tag{1.1}$$

The first term in *QED* Lagrangian density (Eq. 1.1) describes the free electromagnetic field through the electromagnetic tensor $F_{\mu\nu} = \partial_\mu A_\nu - \partial_\nu A_\mu$, where $A_\mu \equiv (\phi, \overrightarrow{A})$ is the electromagnetic four-potential. The last term describes the free lepton of mass m_l at rest, where ψ_l is a four-component Dirac spinor. The part written in terms of the 4-derivative inside the middle term represents the kinetic energy of the free lepton and it composes, together with the mass term, the Lagrangian density of a free lepton. The corresponding Euler-Lagrangian equations give the Dirac equation. Finally, the second part of the middle term describes the interaction of electromagnetic field with the lepton current $J^\mu_\ell = ie\bar{\psi}_\ell\gamma^\mu\psi_\ell$.

Since *QED* is a *QFT*, if two different observers are studying the same system of events into two different Inertial Reference Systems, then the Relativity Principle imposes that the two Inertial Systems have to be equivalent. Thus, the field dynamics will be described by each observer with a Lagrangian density characterized by the same field functional dependence. Therefore, the Relativity Principle implies that *QED* Lagrangian density must be invariant (or symmetric) under Lorentz transformations group. The relevance of studying symmetries arises from Noether theorem, which states that to each infinitesimal generator of a continuous symmetry corresponds a conserved current and an associated time-independent observable. So, the analysis of Lagrangian density symmetries plays a crucial role

in the study of conservation laws of field dynamics.

A fundamental aspect of the SM is represented by gauge invariance, i.e. invariance of Lagrangian under a continuous group transformations. In the case of *QED*, for example, the Lagrangian density of a free lepton is invariant under global gauge (or phase) transformations, which belong to the unitary group $\mathbb{U}(1)$. According to Noether theorem, this leads to the conserved current $J^{\mu}_{\ell} = ie\bar{\psi}_{\ell}\gamma^{\mu}\psi_{\ell}$ that implies the conservation of the electric charge e, as experimentally verified. For this reason, the natural gauge group of *QED* is the $\mathbb{U}(1)_{em}$ group and it represents the only exact internal symmetry actually observed in Nature. By using different symmetry groups, it is possible to extend this framework to both strong and weak interactions.

1.2.2 Quantum Chromodynamics (*QCD*)

Quantum chromodynamics (*QCD*) is a non-abelian gauge theory that describes the interaction of coloured quarks (q) with gluons (g), the quanta of the strong field. Since strong force couples to color charge and only quarks are coloured, leptons are not involved into strong interactions.

As in the *QED* context, strong interactions can be described by Feynman diagrams. Figure 1.3 shows a quark-antiquark annihilation process ($q\bar{q} \rightarrow g \rightarrow q'\bar{q}'$), where gluons ($g$) are depicted by a curly line. Whereas quarks carry a color charge and antiquarks carry an anticolour charge, gluons carries both colour and anti-colour charges. Since quarks can exist in three different colour states, *QCD* is invariant under transformations of $\mathbb{SU}(3)_C$ group, i.e. the group of 3×3 matrices with unitary determinant. In order to maintain invariance of *QCD* Lagrangian density under $\mathbb{SU}(3)_C$ transformations, eight massless bosons must exist, corresponding to the eight coloured gluons.

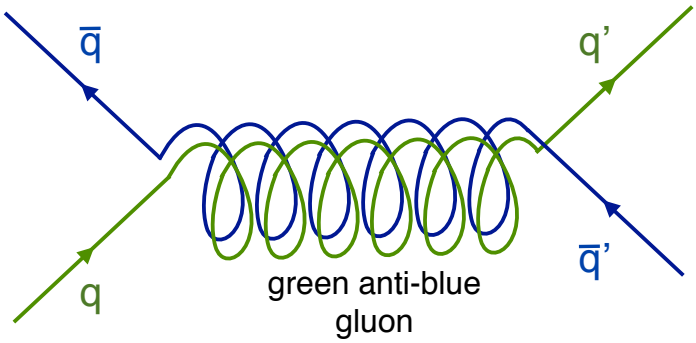

Figure 1.3: Feynman diagram for a simple $q\bar{q} \to q'\bar{q}'$ *QCD* process.

A major difference with the *QED* is that the gauge group $\mathbb{SU}(3)_C$ of strong interactions is a non-abelian group, *i.e.* its generators do not commute. This implies that, unlike photons, gluons carry colour charge leading to self-interaction terms in the *QCD* Lagrangian density. An important consequence is that the colour field lines of force between quark and antiquark are compelled to form a sort of tube as if there were attractive forces between the field lines. Thus, as the distance r between quark and antiquark increases the potential energy of the system increases proportionally to r, making quarks and gluons unable to exist as free particles and leading to their complete *confinement* inside hadrons. Anyway, beyond a certain distance r ($r \simeq 1$ fm) called *confinement barrier*, it is energetically more favorable to break the flux tube by creating a new quark-antiquark couple.

1.2.3 Electroweak Theory

The theory of electroweak unification, developed by Glashow [14], Weinberg [15] and Salam [16], is a Yang-Mills theory [17] based on the local gauge invariance of the electroweak Lagrangian density under transformations of the $\mathbb{SU}(2)_L \otimes \mathbb{U}(1)_Y$ group.

In this model, fermions are identified by three generations of distinct chiral field $f_{L,R} = \frac{1}{2}(1 \mp \gamma_5)f$. *Left-handed* fermions f_L are represented by weak isospin doublets ($I_3 = \pm\frac{1}{2}$), whereas *right-handed* fermions are represented by weak isospin singlet ($I_3 = 0$). Neutrinos, which interact only through weak force, exist only in the *left-handed* chiral state. Besides the weak isospin connected to the gauge invariance under transformations of the $\mathbb{SU}(2)_L$ group, a *hypercharge* for each fermionic field is defined as $Y = 2(Q - I_3)$ which is connected to gauge invariance under transformations of $\mathbb{U}(1)_Y$ group.

In a Yang-Mills theory, the request of a local gauge invariance imposes the existence of field connectors between distinct points of space-time, i.e. gauge field mediators of the interaction, equal in number to the generators of the considered symmetry group. Thus, in the electroweak sector, four fields are defined: the field B_μ, which corresponds to the generator Y of the $\mathbb{U}(1)_Y$ group, and the triplet of fields W^i_μ (with $i = 1, 2, 3$), which correspond to the generator T^i of $\mathbb{SU}(2)_L$ group, equal to the Pauli matrices divided by two and with the same commutation rules. The minimal coupling between fermions and gauge fields can be written by means of covariant derivative defined as:

$$D_\mu\psi = (\partial_\mu - igT_iW^i_\mu - ig'\frac{Y}{2}B_\mu)\psi \tag{1.2}$$

which leads to coupling between fermions and gauge field described by $-g_i\bar{\psi}V_\mu\gamma^\mu\psi$ terms. So, the Standard Model Lagrangian density $\mathcal{L}_{\mathrm{SM}}$, with no mass terms, can

be written as:

$$\begin{aligned}\mathcal{L}_{\mathrm{SM}} = &-\frac{1}{4}W^a_{\mu\nu}W^{\mu\nu}_a - \frac{1}{4}B_{\mu\nu}B^{\mu\nu} + \bar{L}_i i D_\mu \gamma^\mu L_i + \bar{e}_{R,i} i D_\mu \gamma^\mu e_{R,i} \\ &+ \bar{Q}_i i D_\mu \gamma^\mu Q_i + \bar{u}_{R,i} i D_\mu \gamma^\mu u_{R,i} + \bar{d}_{R,i} i D_\mu \gamma^\mu d_{R,i}\end{aligned} \tag{1.3}$$

At this point of the theory, both gauge bosons and fermions are considered massless because the addition of mass terms, as $\frac{1}{2}M_W^2 W_\mu W^\mu$ for W bosons or $-m_e \bar{e}e$ for electron, would violate the gauge invariance of Lagrangian under $\mathbb{SU}(2)_L \otimes \mathbb{U}(1)_Y$ transformations. To avoid the problem of massless gauge bosons, Glashow introduced into the SM Lagrangian density an *ad hoc* mass term, producing a model able to unify both electromagnetic and weak interaction into a single force. In fact, this model showed how was possible to give mass to each neutral generator of the $\mathbb{SU}(2)_L \otimes \mathbb{U}(1)_Y$ symmetry group, namely W^3 and B, keeping unchanged the *QED* gauge local invariance by introducing two physical bosons: the already known massless photons (A_μ) and a new massive Z boson (Z_μ), which are a linear combination of generators W^3 and B. The Glashow model created the conditions for the insertion of the *spontaneous symmetry breaking mechanism* within the unified electroweak theory, as made by Weinberg and Salam, leading to the so called Glashow-Weinberg-Salam model. Indeed, the theoretical solution to the problem of how gauge bosons can acquire mass in a Yang-Mills theory had been solved some years before by Higgs, Brout and Englert.

1.2.4 The Higgs-Brout-Englert Model

In the 1960s, a major problem of particles physics was to integrate within the gauge theory of elementary particles the possibilities to generate gauge bosons and fermions masses without violating the $\mathbb{SU}(2)_L \otimes \mathbb{U}(1)_Y$ gauge invariance. The solution to this problem was made by three independent groups in the 1964: by

Peter Higgs [18–20]; by Robert Brout and François Englert [21]; and by Gerald Guralnik, Carl Richard Hagen and Tom Kibble [22,23]. They introduced the *spontaneous symmetry breaking mechanism* into the non-abelian gauge theory leading to current Standard Model framework.

The starting point of the *spontaneous symmetry breaking mechanism* is the Goldstone model that explains how a global continuous symmetry can spontaneously be broken. Let us consider the Lagrangian density of a complex scalar field with a quartic interaction term:

$$\mathcal{L} = \partial_\mu \phi \partial^\mu \phi^\dagger - V(\phi) = \partial_\mu \phi \partial^\mu \phi^\dagger - \mu^2 \phi \phi^\dagger - \lambda (\phi \phi^\dagger)^2 \tag{1.4}$$

where the potential $V(\phi)$ is composed by the last two terms and the correspondent energy density can be written as $\theta^{00} = \partial_0 \phi \partial_0 \phi^\dagger + (\nabla \phi)(\nabla \phi^\dagger) + V$. Since the first two terms are positive-definite, the stability of the theory requests that the potential $V(\phi)$ must be bounded from below. In the case of a free theory with $\lambda = 0$, this implies that $\mu^2 > 0$. If $\lambda \neq 0$, instead, the condition that the Hamiltonian density must have a finite lower bound implies that $\lambda > 0$, since the quartic terms is dominant. Thus, considering the second case, two distinct theories exist depending on the sign of μ^2. Anyway, the field configuration that minimizes the Hamiltonian must be a space-time invariant corresponding to the absolute minimum of the $V(\phi)$ potential. The corresponding quantum states of the minimum energy configuration that is invariant for space-time transformations is the *vacuum state*, which contains no particles. Let us now consider the two cases $\mu^2 > 0$ and $\mu^2 < 0$ separately.

$\mu^2 > 0$ case If the sign of μ^2 is positive, then the potential $V(\phi)$ is described by a concave function of fields, as shown in the left side of the Figure 1.4. The

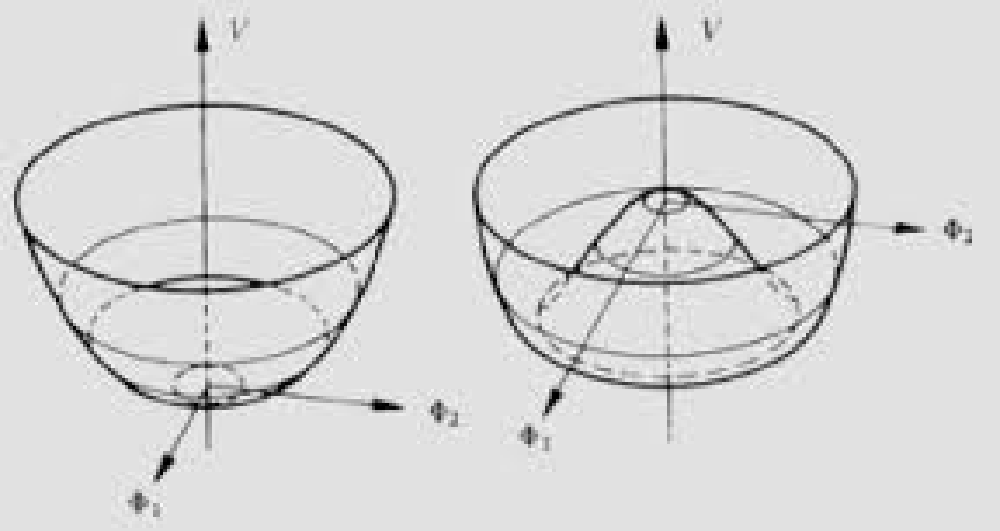

Figure 1.4: Representation of the potential term $V(\phi)$ for the $\mu^2 > 0$ (left) and $\mu^2 < 0$ (right) cases as a function of the two field components ϕ_1 and ϕ_2.

absolute minimum is located at the origin corresponding to $V(\phi) = 0$ for $\Re e(\phi) = \Im m(\phi) = 0$. In the limit for $\lambda \to 0$, the Lagrangian in Equation 1.4 reduces to the case of a Klein-Gordon complex field in which ϕ is a combination of annihilation and creation operators for a particle with mass μ^2. In the case of small values of λ, the model can be solved by applying the perturbation theory which describes charged scalar particles with interactions symmetric for global gauge transformations. So, the $\mu^2 > 0$ case corresponds to a theory with an *exact symmetry*.

$\mu^2 < 0$ **case** If the sign of μ^2 is negative, instead, then the potential $V(\phi)$ is described by a function similar to that shown in the right side of the Figure 1.4. The configuration with $\Re e(\phi) = \Im m(\phi) = 0$ is now a local maximum and it does not minimize the potential. The minimum, in this case, is localized on the points which lay on the dashed circle centered at the origin and the *vacuum expectation*

value becomes:

$$\langle 0|\, \phi(0)\, |0\rangle = \eta = \sqrt{\frac{-\mu^2}{2\lambda}} \neq 0 \tag{1.5}$$

Since the configuration of minimum energy is no longer symmetric, the symmetry is *spontaneously broken* by the fundamental state. By expanding the complex field around its vacuum value, it is possible to show that the two degrees of freedom associated to the ϕ field are now represented by two particles of mass $4\lambda\eta^2$ and 0, respectively. Thus, besides the massive particle corresponding to the ϕ field, a new massless particle appears, the so called *Goldstone boson*. This is the crucial aspect of the *Goldstone theorem* [24, 25]: for every spontaneously broken continuous symmetry, the theory contains a number of massless scalar (spin-0) particles equal to the number of broken generators.

The Higgs-Brout-Englert model, or Higgs model for short, analogously describes the *spontaneous symmetry breaking* but in the case of a local gauge symmetry. Unlike the previous case, the Lagrangian density needs a vectorial field A^μ, similar to the electromagnetic field, in addition to the scalar field ϕ, assuming the form:

$$\mathcal{L} = (D_\mu \phi)^\dagger D^\mu \phi - V(\phi) - \frac{1}{4} F_{\mu\nu} F^{\mu\nu} \tag{1.6}$$

Also in this case, the λ parameter must be positive to ensure the stability of the theory, whereas the sign of μ^2 can be either positive or negative. If $\mu^2 > 0$, then the configuration of minimum energy corresponds to $\phi = 0$ and $A^\mu = 0$. The quantization of these fields results in a theory with a charged particle (and its antiparticle) with mass μ and a spin-1 massless particle with two polarization states, quite similar to the photon. If $\mu^2 < 0$, instead, then the configuration of minimum energy corresponds to $A^\mu = 0$ but, for the scalar part, the model is similar to the Goldstone model: the vacuum expectation value is non-null and equal to $\langle 0|\, \phi(0)\, |0\rangle = \eta \neq 0$. If the scalar field is expanded around the minimum

by choosing the unitary gauge and leaving its real component only, it is possible to describe the scalar field ϕ as $\phi = \eta + \frac{\sigma(x)}{\sqrt{2}} = \rho(x)$ and the Lagrangian density become:

$$\mathcal{L} = \frac{1}{2}\partial_\mu\sigma\partial^\mu\sigma + e^2\rho(x)^2 A_\mu A^\mu - V(\rho) - \frac{1}{4}F_{\mu\nu}F^{\mu\nu} \tag{1.7}$$

This Lagrangian describes a neutral scalar particle with mass $M_H = 4\lambda\eta^2$ associated to the scalar field σ and a spin-1 particle with mass $M_A = 2e^2\eta^2$ associated to the vector field A^μ. This is the crucial aspect of the Higgs model: in the case of a local gauge symmetry, a spontaneous symmetry breaking implies that the corresponding gauge fields acquire mass.

The Higgs model can be applied to the electroweak sector in which the symmetry group is identified by the non-abelian $\mathbb{SU}(2)_L \otimes \mathbb{U}(1)_Y$ group and the corresponding Lagrangian density is shown in Equation 1.3. In this case, the scalar field must trigger the spontaneous symmetry breaking mechanism but keeping unchanged the gauge symmetry of electromagnetism, by following the scheme $\mathbb{SU}(2)_L \otimes \mathbb{U}(1)_Y \rightarrow \mathbb{U}(1)_{em}$. The choice of Weinberg and Salam permits to generate mass not only for vector bosons but also for leptons and quarks and it consists in a $\mathbb{SU}(2)_L$ Higgs doublet with hypercharge $Y = +1$:

$$\Phi = \begin{pmatrix} \phi^+ \\ \phi^0 \end{pmatrix}_{Y=+1} \text{ and } D_\mu = \left[\partial_\mu + ig\overrightarrow{W}_\mu \cdot \frac{\overrightarrow{\tau}}{2} + ig'(+\frac{1}{2}B_\mu)\right]\Phi \tag{1.8}$$

with a Lagrangian density $\mathcal{L} = (D_\mu\Phi)^\dagger (D^\mu\Phi) - \mu^2\Phi^\dagger\Phi - \lambda\left(\Phi^\dagger\Phi\right)^2$. Since the scalar field Φ must broke the $\mathbb{SU}(2)_L \otimes \mathbb{U}(1)_Y$ symmetry, it must have a non-null vacuum expectation value:

$$\bar{\Phi} = \langle 0|\,\Phi\,|0\rangle = \begin{pmatrix} 0 \\ \eta \end{pmatrix} \tag{1.9}$$

which is invariant under transformation of the $\mathbb{U}(1)_Q$ group, realizing in this way the scheme $\mathbb{SU}(2)_L \otimes \mathbb{U}(1)_Y \rightarrow \mathbb{U}(1)_{em}$. By means of the unitary gauge choice,

the Higgs doublet can be written in a real form with only the lower component different from zero:

$$\Phi(x) = \begin{pmatrix} 0 \\ \eta + \frac{\sigma(x)}{\sqrt{2}} \end{pmatrix} \tag{1.10}$$

that contains only one physical field $\sigma(x)$ corresponding to a neutral scalar particle, the *Higgs boson*. By substituting this result into both the electroweak and Higgs field Lagrangian densities and by taking the quadratic terms throgh the covariant derivatives, the mass matrix for both $\mathbb{SU}(2)_L$ and $\mathbb{U}(1)_Y$ gauge fields can be extracted:

$$\mathcal{M} = \begin{pmatrix} M^2 & M_{03}^2 \\ M_{03}^2 & M_0^2 \end{pmatrix} = \frac{1}{2}\eta^2 \begin{pmatrix} g^2 & -gg' \\ -gg' & (g')^2 \end{pmatrix} \tag{1.11}$$

where M is the mass of the charged vector boson $W^{\pm}$, whereas M_0 and M_{03} are not still connected to physical bosons beneath the null value of the mass matrix determinant gives an hint on the null mass of one of the two physical bosons, namely the photon. In fact, by diagonalizing the mass matrix $\mathcal{M}$, the corresponding eigenvector can be found, which correspond to the massive Z^μ and the electromagnetic A^μ fields:

$$\begin{aligned} Z_\mu &= \cos\theta_W W_\mu^3 - \sin\theta_W B_\mu \\ A_\mu &= \sin\theta_W W_\mu^3 + \cos\theta_W B_\mu \end{aligned} \tag{1.12}$$

Since the electromagnetic field A^μ is required to be massless, the relations between the coupling constants g and g', the electroweak mixing angle θ_W and the electrical charge e are constrained to be:

$$\tan\theta_W = \frac{g'}{g} \text{ and } g\sin\theta_W = g'\cos\theta_W = e \tag{1.13}$$

whereas the mass M_Z of the massive Z^μ boson can be found through the trace $Tr\,(\mathcal{M})$ of the mass matrix, resulting in the relation $M_Z^2 = \frac{M^2}{\cos^2\theta_W}$. All of these very important theoretical results are in very good agreement with experimental data. Until the first decade of the 21th century only one free parameter remained unknown: the Higgs boson mass.

1.3 The Standard Model Higgs Boson

The introduction of the Higgs model within the electroweak theory permits to describe the spontaneous symmetry breaking mechanism through which elementary particles acquire mass. The interaction vertices of the Higgs boson with the gauge bosons are defined by the following Lagrangian density:

$$\mathcal{L}_{\phi W} = g^2 \frac{1}{4}\eta^2 \boldsymbol{W}_\mu \boldsymbol{W}^\mu + (g')^2 \frac{1}{4}\eta^2 B_\mu B^\mu - \frac{1}{2}\eta^2 W^3_\mu B^\mu \tag{1.14}$$

whereas interactions with fermions are described by the Yukawa Lagrangian density:

$$\mathcal{L}_F = -\lambda_e \bar{L}\Phi e_R - \lambda_u \bar{Q}\Phi u_R - \lambda_d \bar{Q}\Phi d_R + h.c. \tag{1.15}$$

By following the Feynman normalization rules, the corresponding coupling constants can be derived leading to:

$$g_{Hff} = i\frac{m_f}{\eta} \ , \ g_{HVV} = -2i\frac{M_V^2}{\eta} \ , \ g_{HHVV} = -2i\frac{M_V^2}{\eta^2} \tag{1.16}$$

Furthermore, from the free Lagrangian of the Higgs boson, which is composed by the kinetic part plus the potential, that corresponds to:

$$\mathcal{L}_H = \frac{1}{2}\left(\partial_\mu H\right)\left(\partial^\mu H\right) - \lambda\eta^2 H^2 - \lambda\eta H^3 - \frac{1}{4}H^4 \tag{1.17}$$

the cubic and quartic self-interactions coupling of the Higgs boson can be derived as well as the Higgs boson mass term:

$$g_{HHH} = 3i\frac{M_H^2}{\eta} \text{ and } g_{HHHH} = 3i\frac{M_H^2}{\eta^2} \text{ with } M_H^2 = 2\lambda\eta^2 = -2\mu^2 \tag{1.18}$$

Since the vacuum expectation value η is defined, within the electroweak theory, through the Fermi constant G_F as $\eta = \left(2\sqrt{2}G_F\right)^{-1/2} \simeq 188$ GeV, the coupling constants in Equation 1.16 are directly estimable. Higgs boson self-interaction terms, instead, depend on the value of the λ constant that is not known and the Higgs boson mass M_H remains a free parameter of the theory. However, some important theoretical constraints restrict the range of possible M_H values.

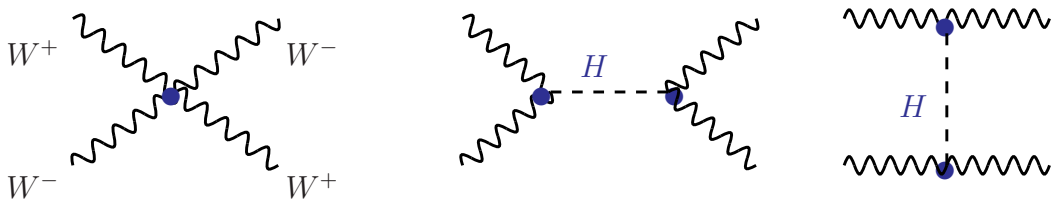

Figure 1.5: Some Feynman diagrams for the scattering of W bosons at high energy.

1.3.1 Theoretical Constraints

Some important theoretical constraints on the permitted Higgs boson mass values arise from assumptions on the energy range in which the Standard Model is valid before perturbation theory breaks down and new phenomena should emerge, namely: unitarity in scattering amplitudes, perturbativity of the Higgs self-coupling, stability of the electroweak vacuum and fine-tuning.

Unitarity One of the major arguments to abandon the Fermi theory of weak interactions was that it violates unitarity at energy close to the Fermi scale. In fact, in this model, the cross section of the process $\nu_\mu e \to \nu_e \mu$ at high energy $\sqrt{s}$ becomes $\sigma \simeq G_F^{-1/2} s$ and at energy greater than $\sqrt{s} \simeq G_F^{-1/2} \simeq 300$ GeV it would violate unitarity. The introduction of the intermediate massive W boson solved this problem but an identical one arose in the $\nu\bar{\nu} \to W^+W^-$, which was solved in turn with the introduction of the massive neutral Z boson. However a similar problem still remained open in processes involving the longitudinal components of vector bosons, such as the $W^+W^- \to W^+W^-$ scattering process. The scattering amplitudes of a given process can be always expressed as a linear combination of plane waves and, by following the optical theorem, the corresponding cross section

can be written as:

$$\sigma = \frac{1}{s}\Im m\left[A\left(\theta = 0\right)\right] = \frac{16\pi}{s}\sum_{l=0}^{\infty}\left(2l+1\right)\left|a_l\right|^2 \tag{1.19}$$

that leads to the unitary condition:

$$\left|\Re e\left(a_l\right)\right| < \frac{1}{2} \tag{1.20}$$

The $J = 0$ partial wave for the amplitude of the W^+W^- scattering process can be written as:

$$a_0 = -\frac{M_H^2}{16\pi\eta^2}\left[2 + \frac{M_H^2}{s - M_H^2} - \frac{M_H^2}{s}\log\left(1 + \frac{s}{M_H^2}\right)\right] \tag{1.21}$$

By assuming the Higgs boson mass much smaller than the invariant mass $\sqrt{s}$, the application of the unitarity condition leads to the upper bound:

$$a_0 \xrightarrow{M_H^2 \ll s} -\frac{M_H^2}{8\pi\eta^2} \Longrightarrow M_H \lesssim 870 \text{ GeV} \tag{1.22}$$

Actually, the scattering channel W^+W^- should be considered together with three more neutral channel (ZZ, HH and ZH) and two charged one (W^+H and W^+Z), leading to a more stringent upper bound:

$$M_H \lesssim 710 \text{ GeV} \tag{1.23}$$

Therefore, the unitarity condition imposes to the Higgs boson to have a mass lower than $\mathcal{O}(700$ GeV), otherwise greater values would violate unitary unless new phenomena emerge to restore it.

Triviality and Stability The coupling constants, as well as particles masses, depend on the energy scale (Q^2) because of quantum corrections and, for this reason, they are defined as *running* constants. The running constant of quartic Higgs coupling $\lambda(Q^2)$ is a monotonically increasing function of Q^2 and the condition

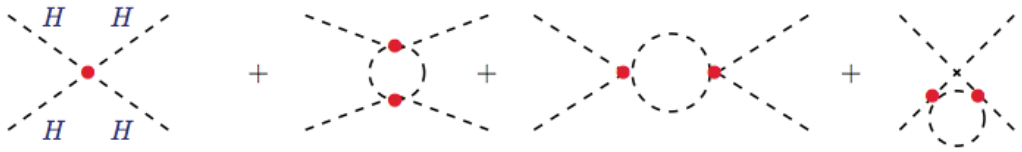

Figure 1.6: Typical Feynman diagrams for the tree-level and one-loop Higgs self-coupling.

to be not trivial imposes some constraint on the value of the Higgs boson mass. By taking into account the contribution of the Higgs boson only to the one-loop corrections, shown in Figure 1.6, the running constant λ can be written as:

$$\lambda\left(Q^2\right) = \lambda\left(\eta^2\right)\left[1 - \frac{3}{4\pi^2}\lambda\left(\eta^2\right)\log\left(\frac{Q^2}{\eta^2}\right)\right]^{-1} \tag{1.24}$$

with the choice of the energy of the electroweak spontaneous symmetry breaking η^2 as energy reference. From the Equation 1.24, if $Q^2 \ll \eta^2$ then the running constant becomes very small going to zero $\lambda\left(Q^2\right) \simeq \frac{\lambda\left(\eta^2\right)}{\log(0)} \to 0_+$ and the quartic coupling vanishes leading to a trivial theory. On the contrary, if $Q^2 \gg \eta^2$ then the running constant becomes very large going to infinity $\lambda\left(Q^2\right) \simeq \frac{\lambda\left(\eta^2\right)}{1-1} \gg 1$. The value for which this happens is called *Landau pole* defined as:

$$\Lambda_C = \eta \exp\left(\frac{4\pi^2}{3\lambda}\right) = \eta \exp\left(\frac{4\pi^2\eta^2}{M_H^2}\right) \tag{1.25}$$

that represents the cut-off value below which the coupling constant is finite and permits to determine the energy range of validity for the Standard Model. Actually, also gauge bosons and fermions contribute to the running constant but only massive vector bosons and the top quark give a relevant contribution. In this case, the running constant can be written as:

$$\lambda\left(Q^2\right) = \lambda\left(\eta^2\right) + \frac{1}{16\pi^2}\left\{-12\frac{m_t^4}{\eta^4} + \frac{3}{16}\left[2g^4 + \left(g^2 + \left(g'\right)^2\right)^2\right]\right\}\log\frac{Q^2}{\eta^2} \tag{1.26}$$

from which follows that, if the running constant is very small, then the top quark contribution is dominant and leads to negative value potential $\lambda\left(Q^2\right) < 0$, making the vacuum unstable. The stability condition, instead, imposes that the potential

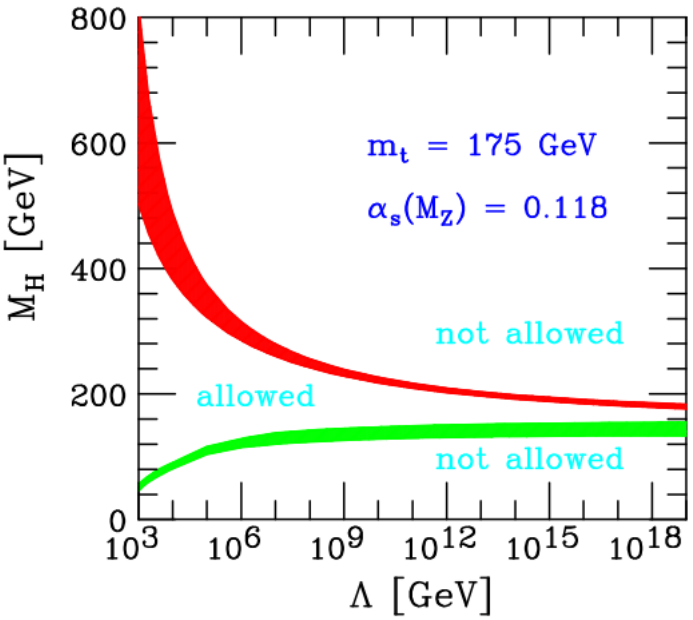

Figure 1.7: The triviality (upper) bound and the vacuum stability (lower) bound on the Higgs boson mass as a function of the new physics or cut-off scale Λ for a top quark mass $m_t = 175 \pm 6$ GeV and $\alpha_s(M_Z) = 0.118 \pm 0.002$; the allowed region lies between the bands and the colored/shaded bands illustrate the impact of various uncertainties.

and, consequently, the running constant must have a lower bound $\lambda(Q^2) > 0$, leading to a lower bound on the Higgs boson mass value:

$$M_H^2 > \frac{\eta^2}{8\pi^2}\left\{-12\frac{m_t^4}{\eta^4} + \frac{3}{16}\left[2g^4 + \left(g^2 + (g')^2\right)^2\right]\right\}\log\frac{Q^2}{\eta^2} \tag{1.27}$$

depending on the cut-off value Λ_C. The combination of both the conditions of triviality and stability, as a function of the Landau pole, is shown in Figure 1.7, where the major uncertainties are on the values of the strong coupling constant $\alpha_S = 0.118 \pm 0.002$ and of the top quark mass $m_t = 175 \pm 6$ GeV [26]. From Figure 1.7 follows that if the cut-off scale is $\mathcal{O}$ (TeV) then the permitted values for the Higgs boson mass are:

$$\Lambda_C \simeq 1 \text{ TeV} \Rightarrow 50 \text{ GeV} \lesssim M_H \lesssim 800 \text{ GeV} \tag{1.28}$$

whereas if the cut-off scale is around the scale of Grand Unification $\Lambda_C \simeq 10^16$ GeV then Higgs boson mass should lie in the range:

$$\Lambda_C \simeq 10^{16} \text{ GeV} \Rightarrow 130 \text{ GeV} \lesssim M_H \lesssim 180 \text{ GeV} \tag{1.29}$$

1.3.2 Experimental constraints

Experimental constraints on the Higgs boson mass value can be divided in two distinct categories, depending on the specific research method: indirect searches, which consist in measurement of Higgs boson contributions to radiative corrections to the electroweak theory, and direct searches, which consist in the measurement of the Higgs boson decay products and the corresponding production mechanisms in high energy colliders.

1.3.2.1 Indirect searches

Since Higgs boson contributes to radiative corrections to electroweak theory, then precision measurements in this sector permit to extract tight limits on the range of possible values of the Higgs boson mass. The major measurements performed in the last decades can be summarized in:

- the observables of the Z resonance lineshape at LEP, namely: the total decay width Γ_Z, the hadronic cross section at the Z peak σ^0_{had}, the partial decay width of Z boson decay into leptons and heavy quarks (c,b) normalized to the hadronic one $R_{l,c,b}$ and the forward-backward asymmetry for both leptons and heavy quarks production $A^{b,c}_{FB}$;
- the longitudinal polarization asymmetries A^f_{LR} and the left-right forward-backward asymmetries for heavy quarks production $A^{b,c}_{LR,FB}$ as measured at SLC;

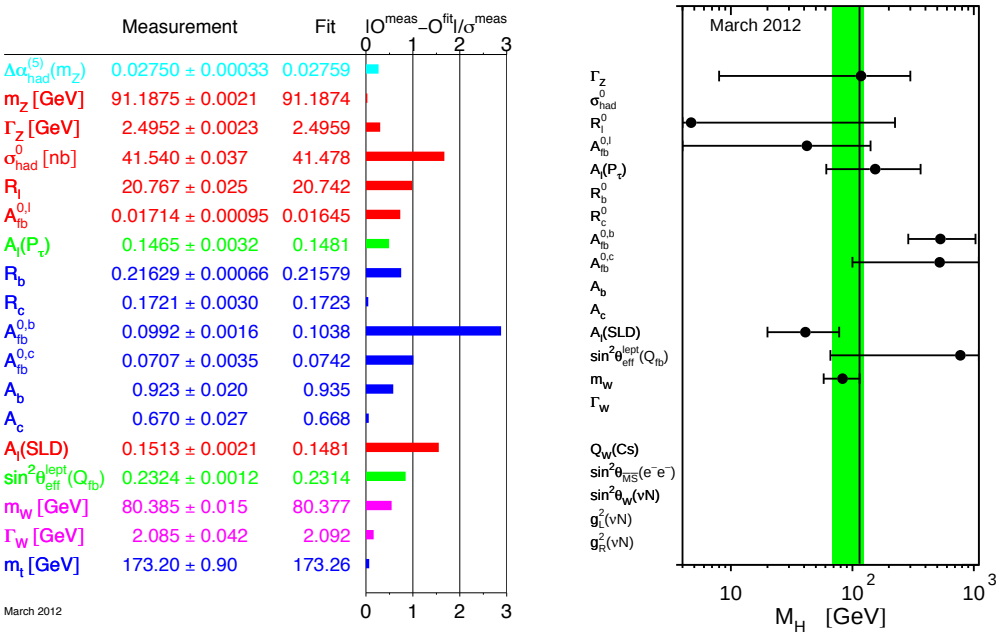

(a) (b)

Figure 1.8: (a) Summary of electroweak precision measurements at LEP1, LEP2, SLC and Tevatron. The SM fits results, which have been derived including all radiative corrections, and the standard deviations are also shown. (b) Electroweak precision measurements as a function of the Higgs boson mass; the vertical green band denotes the overall constraint on the Higgs mass derived from the fit to all data, while the vertical black line denotes the limit on the Higgs mass obtained from the direct search at LEP2.

- the mass value m_W and the total decay width Γ_W of W vector boson as measured at LEP2 and Tevatron;
- the measurements of left and right coupling constants of fermions to Z boson as measured from deep inelastic scattering of ν_μ and $\bar{\nu}_\mu$ on nucleons;
- the top quark mass value m_t as measured at Tevatron;
- the measurement of strong interactions coupling constant α_s and the corresponding correction $\Delta\alpha^{(5)}_{had}$.

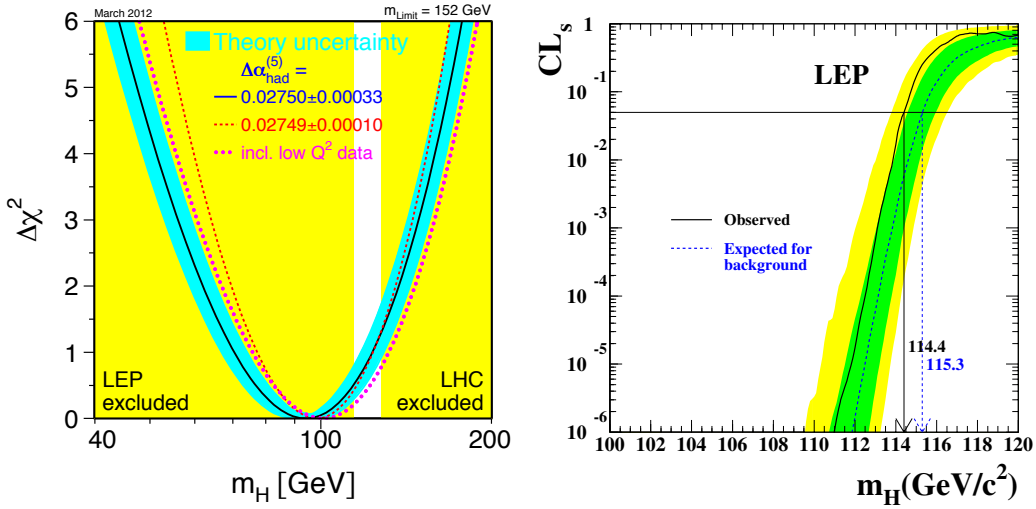

(a) (b)

Figure 1.9: (a) The $\Delta\chi^2$ of the fit to the electroweak precision data as a function of Higgs boson mass m_H. The solid line results when all data are included and the blue shaded band is the estimated theoretical error from unknown higher-order corrections. The effect of including the low Q^2 data and the use of a different value for $\Delta\alpha_{(\mathrm{had})}$ are also shown. The excluded (yellow) region corresponds to the July 2011 Tevatron combination (156-177 GeV) and the December 2011 LHC exclusion (127-600 GeV, CMS). (b) Confidence level CL_S for the signal plus background hypothesis in Higgs production at LEP2. The solid/red line is for the observation, the dashed line is the median background expectation, the green and yellow shaded bands around the median expected line correspond to the 68% and 95% simulated probability bands. The intersection of the horizontal line at $\mathrm{CL}_S = 0.05$ with the observed curve defines the 95% CL lower bound for m_H.

The results listed above and summarized in Figure 1.8(a) can be used to indirectly estimate the Higgs boson mass as shown in Figure 1.8(b) in which the green vertical band denotes the overall constraint on the Higgs mass derived from the fit to all data. Furthermore, the $\Delta\chi^2$ of the combined fit on all measured Standard Model parameters at high-Q^2 depicted in Figure 1.9(a) shows the preference for a low mass Higgs boson with a best value of 92^{+34}_{-26} GeV and an upper bound at the 95% of confidence level equal to 161 GeV.

1.3.2.2 Direct searches

Direct searches of the Higgs boson has been performed at both LEP and Tevatron. The Standard Model predicts production cross section of the Higgs boson as well as the decay partial with together with the corresponding branching ratios. The analysis of specific final states of events produced in high energy colliders then permits to either observe or exclude a given process at a desired confidence level. At the Large Electron-Positron (LEP) collider, the Higgs boson has been searched at energy of about the Z boson mass ($\sqrt{s} \simeq M_Z$, LEP1) as well as at higher energy values ($\sqrt{s} = 209$ GeV). The direct searches has been mostly conducted in the so called *Higgsstrahlung* production channel in which the Higgs boson is radiated from the Z boson. Anyway, no evidence of such process has been found leading to set a lower bound on the permitted mass range. Figure 1.9(b) shows the confidence level for the signal plus background hypothesis (CL_s) as a function of the Higgs boson mass m_H from which a Higgs boson mass value lower than 114.4 GeV can be excluded at the 95% of the confidence level.

Similarly, several direct searches of the Higgs boson has been performed at Tevatron by analyzing all decay channels and production mechanisms accessible at the proton-antiproton $p\bar{p}$ collider. Neither these studies conducted to any evidence

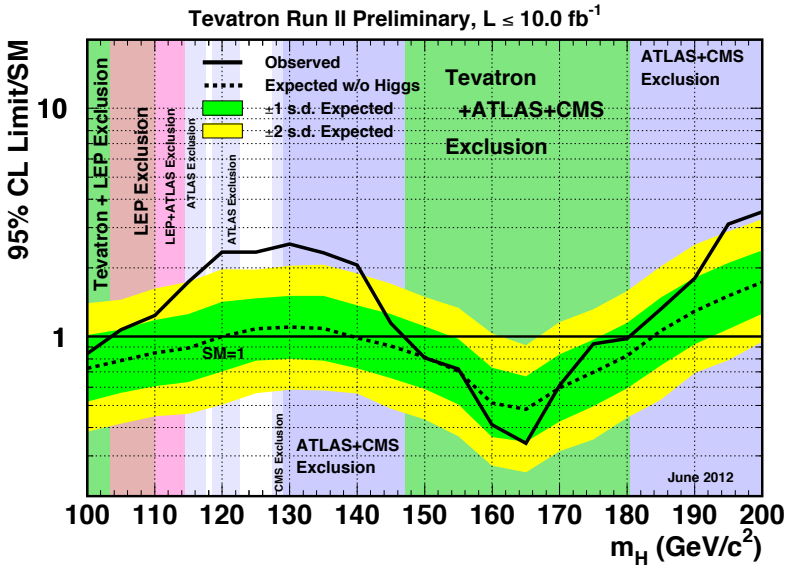

Figure 1.10: Observed and expected (median, for the background-only hypothesis) 95% CL upper limits on the ratios to the SM cross section, as functions of the Higgs boson mass for the combined CDF and D0 analyses. The limits are expressed as a multiple of the SM prediction for test masses (every 5 GeV/c^2) for which both experiments have performed dedicatedsearches in different channels. The points are joined by stra ight lines for better readability. The bands indicate the 68% and 95% probability regions where the limits can fluctuate, in the absence of signal. The limits displayed in this figure are obtained with the Bayesian calculation.

of the Higgs boson existence but they permitted to further restrict the allowed mass range. Figure 1.10 shows the observed and expected 95% CL upper limits on the ratios to Standard Model for the background-only hypothesis, as a function of the Higgs boson mass for the combined analyses of the CDF and D0 experiments. Thus, the combination of the analyzed decay channels at Tevatron permitted to exclude a Higgs boson with a mass m_H between 147 and 180 GeV.

Excluding the early analyses performed at the Large Hadron Collider, the combination of LEP and Tevatron studies left two allowed regions in the Higgs boson mass range:

$$114.4 \text{ GeV} \leq m_H \leq 147 \text{ GeV and } 180 \text{ GeV} \leq m_H \tag{1.30}$$

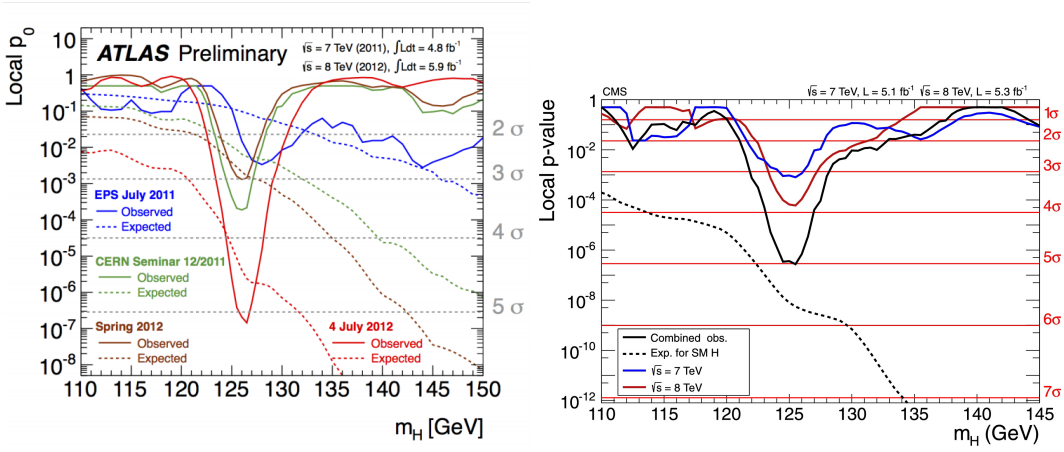

(a) (b)

Figure 1.11: (a) Evolution through years of the ATLAS observed (solid) local p_0 as a function of m_H in the low mass range. The dashed curve shows the expected local p_0 under the hypothesis of a SM Higgs boson signal at that mass. The horizontal dashed lines indicate the p-values corresponding to significances of 1 to 6 σ. (b) The observed CMS local p-value for 7 TeV and 8 TeV data, and their combination as a function of the SM Higgs boson mass. The dashed line shows the expected local p-values for a SM Higgs boson with a mass m_H.

until July 4$^{\text{th}}$ 2012 when the ATLAS and CMS collaborations announced at CERN the discovery of a Higgs-like particle exactly in the first mass range of Equation 1.30.

1.3.3 The Higgs boson discovery

After two years of work dedicated to collect and analyze the data recorded in proton-proton pp collisions at the Large Hadron Collider, on July 4$^{\text{th}}$ 2012 the ATLAS and CMS collaborations announced to the public the discovery of a Higgs-like particle with a mass of about 125 GeV. Collision data were collected at an invariant mass $\sqrt{s}$ equal to 7 TeV and 8 TeV in the 2011 and 2012, respectively, corresponding to about 4.8 fb^{-1} and 5.9 fb^{-1} of integrated luminosity.

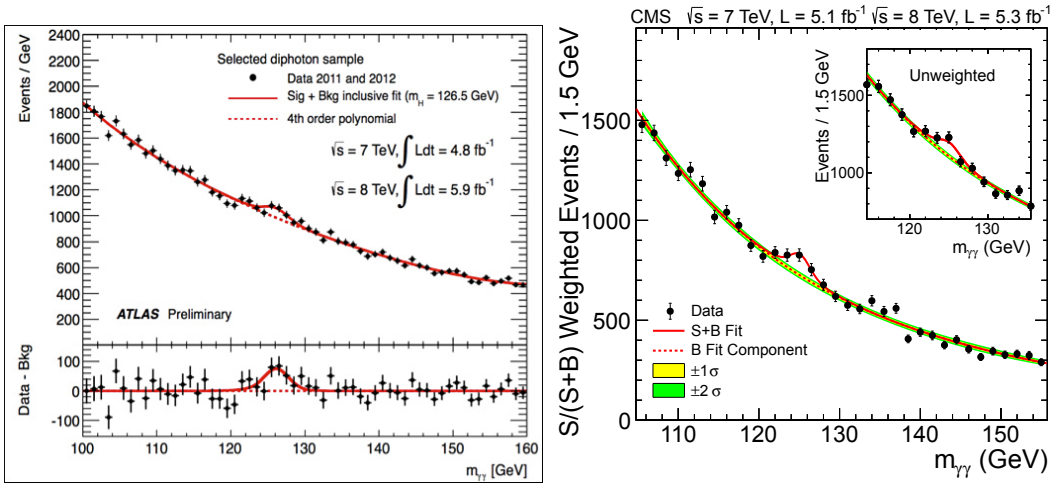

(a) (b)

Figure 1.12: Invariant mass distribution of ATLAS (a) and CMS (b) diphoton candidates for the combined $\sqrt{s} = 7$ TeV and 8 TeV data samples. The result of a fit to the data of the sum of a signal and background component is superimposed. The bottom inset in (a) displays the residuals of the data with respect to the fitted background component.

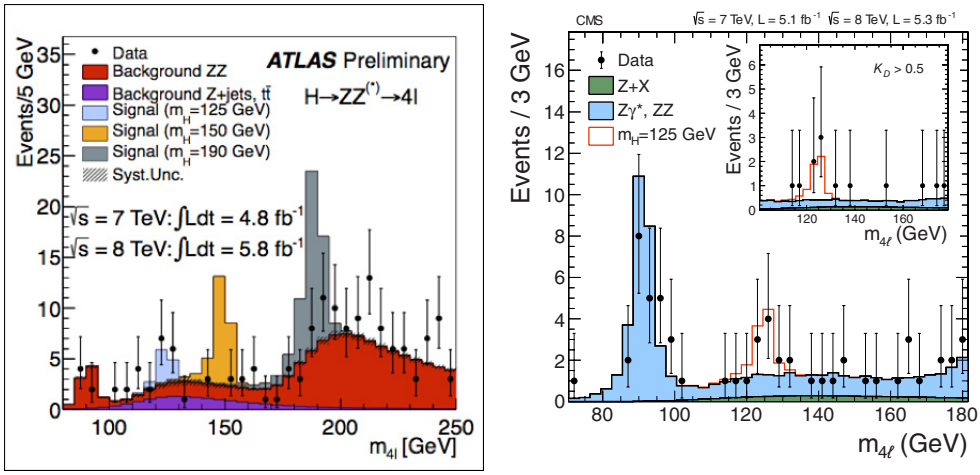

(a) (b)

Figure 1.13: The distribution of the four-lepton invariant mass $m_{4\ell}$ for the selected candidates compared to the background expectation for the low mass range for the $\sqrt{s} =$ 7 TeV and 8 TeV combined datasets. Both ATLAS (a) and CMS (b) plots are shown.

Figure 1.11(a) shows the evolution through years of the p-value for the background-only hypothesis for the combined Higgs searches performed by ATLAS collaboration as a function of the Higgs boson mass value. The horizontal dotted lines in the figure indicates the significance level of plotted results showing that on the 4^{th} of July 2012 the local significance for the exclusion of the background-only hypothesis reached the 5σ level. Figure 1.11(b) analogously shows the p-value for the combined Higgs searches performed by CMS collaboration for both 7 TeV and 8 TeV analysis.

The main decay channels used to achieve the results described above are the decay of Higgs boson into two photons ($H \to \gamma\gamma$) and into four leptons ($H \to ZZ \to 4\ell$). Figure 1.12 and Figure 1.13 show the event distributions as a function of the invariant mass of the final states for both ATLAS and CMS collaborations and for either of the analyzed channels from which is clear visible the invariant mass peak corresponding to a Higgs-like boson with a mass of about 125 GeV.

Thanks to the discovery of the Higgs boson announced during a press conference at CERN in the 2012, which confirmed the theoretical model proposed 50 years before, P. Higgs and F. Englert awarded in the 2013 the Nobel Prize in Physics.

1.4 Beyond the Standard Model (*BSM*)

The gauge boson and fermion sectors of Standard Model received many experimental confirmations so far. Furthermore, the discovery at the Large Hadron Collider of a Higgs-like boson in 2012 also confirmed the Brout-Englert-Higgs model as the correct theory to describe the spontaneous electroweak symmetry breaking mechanism. In the Standard Model the simplest choice for the scalar sector is assumed, *i.e.* a $\mathbb{SU}(2)$ doublet, whereas the fermion sector is described by a more complex

structure consisting in three distinct mixing families.

A critical aspect for the scalar sector of Standard Model is the ρ paramater that in a $\mathbb{SU}(2)_L \otimes \mathbb{U}(1)_Y$ gauge theory can be written, at tree-level, as:

$$\rho = \frac{\sum_{i=1}^{n} \left[I_i \left(I_i + 1 \right) - \frac{1}{4} Y_i^2 \right] v_i}{\sum_{i=1}^{n} \frac{1}{2} Y_i^2 v_i} \tag{1.31}$$

where n is the number of existing scalar multiplets ϕ_i and I_i, Y_i and v_i are, respectively, the corresponding weak isospin, hypercharge and vacuum expectation values. The experimental measurement of the ρ parameter is very close to one, resulting in a very stringent constraint on the possible choices for the scalar multiplets ϕ_i. According to Equation 1.31, both $\mathbb{SU}(2)$ singlets with $Y = 0$ and $\mathbb{SU}(2)$ doublets with $Y = \pm 1$ are consistent with experimental results. Thus, the introduction of such scalar fields is the simplest way to extend the current scalar sector of Standard Model.

1.4.1 Two-Higgs-Doublet Models (*2HDM*)

One of the simplest extension of the Standard Model is the two-Higgs-doublet model (*2HDM*) in which the Higgs sector is extend by adding a new scalar doublet. There are many motivations for *2HDM*s and the most known is supersymmetry. In the supersymmetric theory, scalars are represented by chiral multiplets and the corresponding complex conjugate are multiplets with opposite chirality; since multiplets of different chirality cannot couple together in the Lagrangian, then a single Higgs doublet is not able to give mass to both u-type and d-type quarks. Thus, two Higgs boson doublets are assumed in the Minimal Supersymmetric Model (*MSSM*). Another interesting motivation for *2HDM*s lays in the baryon asymmetry of the Universe that the Standard Model is unable to describe.

In fact, the two-Higgs-doublet models produce flexible scalar mass spectra and introduce additional sources of either explicit or spontaneous CP violation which are able to explain the actual baryogenesis process.

In general, the vacuum structure of *2HDM*s is described by scalar potential containing 14 parameters and CP-conserving, CP-violating and charge-violating minima. However, several simplifying assumptions can be made and it is usually assumed that CP is conserved in the Higgs sector, that CP is not spontaneously broken and discrete symmetries eliminate from the potential all quartic terms odd in either of the doublets. Under those assumptions, the most general scalar potential for two doublet Φ_1 and Φ_2 with $Y = +1$ can be written as:

$$\begin{aligned} V(\Phi_1, \Phi_2) = {} & m_{11}^2 \Phi_1^\dagger \Phi_1 + m_{22}^2 \Phi_2^\dagger \Phi_2 - m_{12}^2 \left(\Phi_1^\dagger \Phi_2 + \Phi_2^\dagger \Phi_1 \right) + \frac{\lambda_1}{2} \left(\Phi_1^\dagger \Phi_1 \right)^2 \\ & + \frac{\lambda_2}{2} \left(\Phi_2^\dagger \Phi_2 \right)^2 + \lambda_3 \Phi_1^\dagger \Phi_1 \Phi_2^\dagger \Phi_2 + \lambda_4 \Phi_1^\dagger \Phi_2 \Phi_2^\dagger \Phi_1 \\ & + \frac{\lambda_5}{2} \left[\left(\Phi_1^\dagger \Phi_2 \right)^2 + \left(\Phi_2^\dagger \Phi_1 \right)^2 \right] \end{aligned} \tag{1.32}$$

where all parameters are real and the minimization of this potential gives the vacuum expectation values for the two doublets

$$\langle 0 | \Phi_1 | 0 \rangle = \begin{pmatrix} 0 \\ \frac{v_1}{\sqrt{2}} \end{pmatrix} \text{ and } \langle 0 | \Phi_2 | 0 \rangle = \begin{pmatrix} 0 \\ \frac{v_2}{\sqrt{2}} \end{pmatrix} \tag{1.33}$$

The two complex scalar $\mathbb{SU}(2)$ doublets can be expanded about the minima giving eight fields:

$$\Phi_a = \begin{pmatrix} \phi_a^+ \\ \frac{v_a + \rho_a + i\eta_a}{\sqrt{2}} \end{pmatrix} \text{ with } a = 1, 2 \tag{1.34}$$

Three of these eight fields are "eaten" to give mass to $W^\pm$ and Z^0 gauge bosons whereas the remaining five fields are physical Higgs-like fields: two charged scalars, two neutral scalars and a pseudoscalar A. Expansion about minima leads to the

mass terms that, for charged and pseudoscalar Higgs bosons, are given by:

$$\begin{aligned}\mathcal{L}_{\phi^{\pm},mass} &= -\left[m_{12}^2 - (\lambda_4+\lambda_5)\frac{v_1 v_2}{2}\right](\phi_1^-,\phi_2^-)\begin{pmatrix}\frac{v_2}{v_1} & -1\\ -1 & \frac{v_1}{v_2}\end{pmatrix}\begin{pmatrix}\phi_1^+\\ \phi_2^+\end{pmatrix}\\ \mathcal{L}_{\eta,mass} &= -\frac{1}{2}\frac{m_A^2}{v_1^2+v_2^2}(\eta_1,\eta_2)\begin{pmatrix}v_2^2 & -v_1 v_2\\ -v_1 v_2 & v_1^2\end{pmatrix}\begin{pmatrix}\eta_1\\ \eta_2\end{pmatrix}\end{aligned} \tag{1.35}$$

The mass matrices can be simultaneously diagonalized by an orthogonal rotation matrix in which the rotation angle β has a crucial role in the model. The β parameter can be defined in terms of vacuum expectation values as:

$$\tan\beta = \frac{v_1}{v_2} \tag{1.36}$$

and, in order to preserve W and Z bosons mass values as in the Standard Model, the vacuum expectation values must hold to the $v^2 = v_1^2 + v_2^2 = \left(\sqrt{2}G_F\right)^{-1/2} \simeq (246\text{ GeV})^2$ relation. The null determinant of the mass matrices in Equation 1.35 means that two Goldstone bosons exist for both charged $G^{\pm}$ and neutral G^0 modes which are in turn absorbed by $W^{\pm}$ and Z bosons to become massive. The mass values of the remaining charged and pseudoscalar physical bosons, instead, can be written in terms of the model parameters as:

$$\begin{aligned}m_{H^{\pm}}^2 &= \left(\frac{m_{12}^2}{v_1 v_2} - \frac{\lambda_4+\lambda_5}{2}\right)\left(v_1^2+v_2^2\right) = M^2 - \frac{1}{2}(\lambda_4+\lambda_5)v^2\\ m_A^2 &= \left(\frac{m_{12}^2}{v_1 v_2} - \lambda_5\right)\left(v_1^2+v_2^2\right) = M^2 - \lambda_5 v^2\end{aligned} \tag{1.37}$$

where $M^2 = \frac{m_{12}^2}{\sin\beta\cos\beta}$. The CP-even scalar sector is slightly more complicated than previous cases and the corresponding mass term can be written as:

$$\mathcal{L}_{\rho,mass} = -\frac{1}{2}(\rho_1,\rho_2)\begin{pmatrix}m_{12}^2\frac{v_2}{v_1} + \lambda_1 v_1^2 & -m_{12}^2 + \lambda_{345}v_1 v_2\\ -m_{12}^2 + \lambda_{345}v_1 v_2 & m_{12}^2\frac{v_1}{v_2} + \lambda_2 v_2^2\end{pmatrix}\begin{pmatrix}\rho_1\\ \rho_2\end{pmatrix} \tag{1.38}$$

where $\lambda_{345} = \lambda_3 + \lambda_4 + \lambda_5$. The mass matrix above can be diagonalized by an orthogonal rotation matrix in which the rotation angle α can be written as:

$$\tan 2\alpha = \frac{(M^2 - \lambda_{345}v^2)\sin 2\beta}{(M^2-\lambda_1 v^2)\cos^2\beta - (M^2-\lambda_2 v^2)\sin^2\beta} \tag{1.39}$$

The eigenstates of the CP-even mass matrix in Eq.(1.39) can be written in terms of the rotation angle α as:

$$\begin{aligned} H &= \rho_1 \cos\alpha + \rho_2 \sin\alpha \\ h &= -\rho_1 \sin\alpha + \rho_2 \cos\alpha \end{aligned} \tag{1.40}$$

where, by convention, h and H represent the lighter and the heavier CP-even states respectively. The corresponding mass values can be written as:

$$m^2_{h,H} = \frac{1}{2}\left[\mathcal{M}_{11} + \mathcal{M}_{22} \pm \sqrt{(\mathcal{M}_{11} - \mathcal{M}_{22})^2 + 4\mathcal{M}^2_{12}}\right] \tag{1.41}$$

where $\mathcal{M}_{ij}$ corresponds to the element of the i-th row and j-th column of the mass matrix in Equation 1.39. The Standard Model Higgs boson H^{SM} can be expressed in terms of the h and H states in Equation 1.40 as:

$$H^{\mathrm{SM}} = \rho_1 \cos\beta + \rho_2 \sin\beta = H\cos(\alpha - \beta) - h\sin(\alpha - \beta) \tag{1.42}$$

meaning that the SM Higgs boson would correspond either to the lighter state h for $\cos\alpha = \sin\beta$ and $\sin\alpha = -\cos\beta$ or to the heavier one H for $\cos\alpha = \cos\beta$ and $\sin\alpha = \sin\beta$. Since the two α and β parameters determine the interactions between the various Higgs fields with both vector bosons and fermions, they play a central role in discussing *2HDM*s phenomenology.

1.4.1.1 *2HDM*s with natural flavor conservation

A potential problem facing all *2HDM*s is the possibility of tree level flavor-changing neutral currents (*FNCN*s). In the Standard Model, for example, the diagonalization of the mass matrix for quarks automatically diagonalizes the Yukawa interactions ruling out the existence of tree-level *FCNC*s whereas the same does not hold for *2HDM*. Anyway, it is possible to assume that tree level *FCNC*s are completely absent by imposing a discrete or continuous symmetry. In fact, by following the

	Type I	Type II	Lepton-specific	Flipped
ξ_h^u	$\cos\alpha/\sin\beta$	$\cos\alpha/\sin\beta$	$\cos\alpha/\sin\beta$	$\cos\alpha/\sin\beta$
ξ_h^d	$\cos\alpha/\sin\beta$	$-\sin\alpha/\cos\beta$	$\cos\alpha/\sin\beta$	$-\sin\alpha/\cos\beta$
ξ_h^ℓ	$\cos\alpha/\sin\beta$	$-\sin\alpha/\cos\beta$	$-\sin\alpha/\cos\beta$	$\cos\alpha/\sin\beta$
ξ_H^u	$\sin\alpha/\sin\beta$	$\sin\alpha/\sin\beta$	$\sin\alpha/\sin\beta$	$\sin\alpha/\sin\beta$
ξ_H^d	$\sin\alpha/\sin\beta$	$\cos\alpha/\cos\beta$	$\sin\alpha/\sin\beta$	$\cos\alpha/\cos\beta$
ξ_H^ℓ	$\sin\alpha/\sin\beta$	$\cos\alpha/\cos\beta$	$\cos\alpha/\cos\beta$	$\sin\alpha/\sin\beta$
ξ_A^u	$\cot\beta$	$\cot\beta$	$\cot\beta$	$\cot\beta$
ξ_A^d	$-\cot\beta$	$\tan\beta$	$-\cot\beta$	$\tan\beta$
ξ_A^ℓ	$-\cot\beta$	$\tan\beta$	$\tan\beta$	$-\cot\beta$

Table 1.1: Yukawa couplings of u-type quarks, d-type quarks and leptons ℓ to the neutral Higgs bosons h, H, A in the four different models.

Paschos-Glashow-Weinberg theorem, if all fermions with the same quantum numbers couple to the same Higgs multiplet, then tree level *FCNC*s do not exist. In *2HDM*, this can only be ensured by introducing new discrete or continuous symmetries, which lead to different types of *2HDM* depending on the chosen symmetry.

Looking at the quark sector of the *2HDM*, two different choices can be made to avoid the tree level *FCNC*s problem:

- type I *2HDM*: all quarks couple to just one of the Higgs doublets (conventionally chosen to be Φ_2), which can be enforced with a $\Phi_1 \to -\Phi_1$ discrete symmetry;

- type II *2HDM*: the right-handed u-type quarks ($Q = +\frac{2}{3}$) couple to one Higgs doublet (conventionally chosen to be Φ_2) whereas the right-handed d-type quarks ($Q = -\frac{1}{3}$) couple to the other (Φ_1), which can be enforced with a $\Phi_1 \to -\Phi_1$, $d_R^i \to -d_R^i$ discrete symmetry.

Supersymmetric models, for example, use the same Yukawa couplings as in the type II *2HDM* but with continuous symmetries. In type I and type II *2HDM*s, furthermore, it is conventionally assumed that right-handed leptons satisfy the same symmetry as the d-type quarks d_R^i and thus leptons couple to the same Higgs boson as the $Q = -\frac{1}{3}$ quarks. However, the Paschos-Glashow-Weinberg theorem does not require this assumption, thus permitting two more possibilities:

- lepton-specific model: all right-handed quarks couple to Φ_2 whereas right-handed leptons couple to Φ_1;
- flipped model: the right-handed u-type quarks couple to Φ_2 and the right-handed d-type quarks couple to Φ_1, as in the type II *2HDM*, whereas the right-handed leptons now couple to Φ_2.

With these assumptions, for each *2HDM* type, the corresponding Yukawa couplings, as a function of α and β parameters, can be determined. In fact, in the Standard Model the coupling of fermions f to the Higgs boson is $\frac{m_f}{v}$ whereas in *2HDM*s this value is modified by a factor $\xi(\alpha, \beta)$. The ξ factors for each *2HDM* type and for each coupling of fermions to scalar bosons are listed in Table 1.1.
The coupling of scalar bosons to W and Z vector bosons, instead, are the same in all *2HDM*s. The coupling of the lighter Higgs h and the heavier Higgs H bosons to WW and ZZ are the same as in the Standard Model times, respectively, a factor $\sin(\alpha - \beta)$ for h and $\cos(\alpha - \beta)$ for H. The coupling of the pseudoscalar A boson to vector bosons vanishes.

Chapter 2

The ATLAS experiment at the LHC

The *Large Hadron Collider* (LHC) is a particle accelerator in which two beams of protons collide at high energies. The particles produced in these collisions are detected by four major experiments, ALICE, ATLAS, CMS and LHCb.

2.1 The Large Hadron Collider

The Large Hadron Collider is a proton-proton (pp) collider at CERN in Geneva within the same tunnel that had previously hosted the LEP accelerator (*Large Electron-Positron Collider*) (see Figure 2.1). The maximum energy reached from each beam of protons in head-on collisions has been of 3.5 TeV (4 TeV) in 2011 (2012), resulting in a center of mass energy of 7 TeV (8 TeV) and making LHC the largest and most energetic particle collider ever built. Collisions between ion beams (Pb nuclei) are also provided with an energy of 2.76 TeV/nucleon, equivalent to a total center of mass energy of 1.15 PeV and studied by a dedicated experiment (ALICE), located at the interaction point 2 (IP 2) (see Figure 2.3).

The Large Hadron Collider consists of two superconducting rings that act as

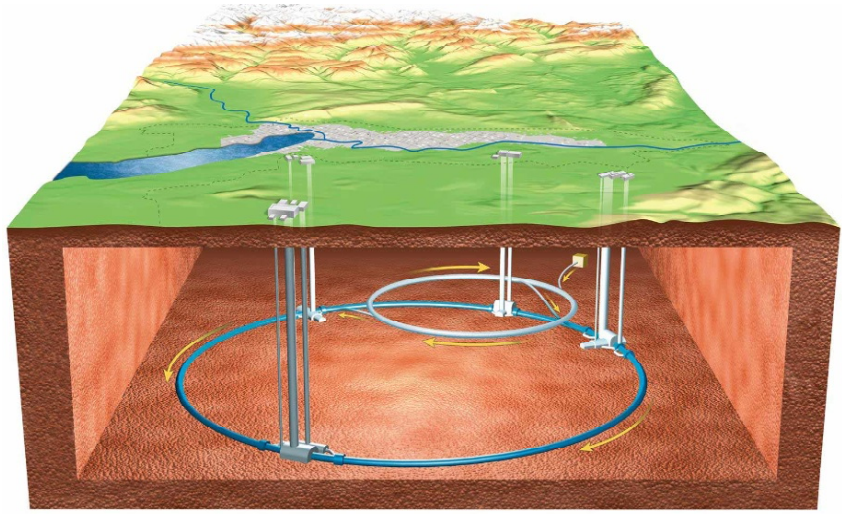

Figure 2.1: Schematic view of the underground area where LHC is located.

both hadron accelerators and colliders. Its length is of 26.7 km and it is placed in a tunnel built underneath the Franco-Swiss border near Geneva, where CERN headquarters are located. The accelerator complex at CERN serves as injectors and the connection to LHC is realized through two transfer lines 2.5 km long. The tunnel consists of 8 straight sections and 8 curved sections and lies between 45 m and 170 m of depth. To contain the costs of this work, most of the existing infrastructures have been reused, modifying them according to the characteristics required by the LHC. Previously existing sites has been adapted even for surface structures, in fact the ALICE and LHCb experiments (points 2 and 8 in Figure 2.3) are located in areas where LEP experiments also were located. Instead, for ATLAS and CMS (Points 1 and 5 in Figure 2.3) new caverns has been built.

2.1.1 The acceleration chain

The process of beam acceleration takes place in several steps in which the beam passes through different devices. The injectors chain has been inherited from LEP and, from the source of protons until the last stage, consists of:

- LINAC2
- Proton SynchrotronBooster (PSB)
- Proton Synchrotron (PS)
- Super Proton Synchrotron (SPS)
- LHC

as shown in Figure (2.2). Both PS and SPS, which date back to the '70s, have required significant upgrades to meet the stringent demands of the LHC operation: many and very intense proton bunches, with a reduced transverse emittance and with a well defined longitudinal emittance.

The acceleration starts from a proton source, *i.e.* a *Duoplasmatron*, from which the proton beam is extracted with an energy of 92 keV and a beam current of 300 mA. From this source, the protons are collected and injected in the LINAC2, which increases the beam energy up to 50 MeV. Carried out the first acceleration stage, the particles pass to the PSB, which increases the beam energy up to 1.4 GeV, then to the PS where the beam reaches the energy of 25 GeV and, finally, the SPS attains the energy of 450 GeV, before LHC injection. At this stage the bunches are injected through two transfer tunnels in the Large Hadron Collider, where they will be brought up to the energy of 3.5 (4) TeV.

At LHC the two beams (one per ring) circulate within two vacuum chambers horizontally spaced of 194 mm. Only $\approx$ 100 m before the impact points (IP), the

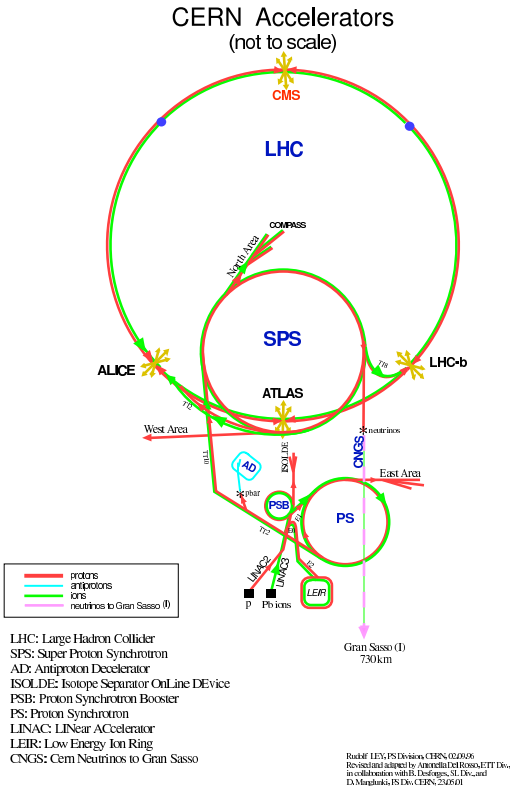

Figure 2.2: Diagram of the pre-acceleration and acceleration devices at the LHC.

chambers are intersected. The acceleration within the collider is provided by 8 resonant cavities. The electric field within the radiofrequency (RF) cavities oscillates at 400.8 MHz in order to give a boost in energy of 0.5 MeV/cycle. At the maximum energy, the field intensity reaches about 5.5 MV/m. Beams are confined by 1232 superconducting magnetic dipoles which generate a magnetic field of $B = 8.33$ T. This very intense magnetic field allows to bend the accelerated protons of ≈ 0.6 mm per meter. The magnetic dipoles are immersed in a superfluid helium at a pressure of about 0.13 MPa (1.3 bar) and at a temperature of 1.9 K, to maintain the condition of superconductivity and to contain about 600 MJ of energy.

Space limitations and the need to contain costs, led to the adoption of a "two in

one" configuration for most of LHC magnets.

This structure allowed to include the two beam channels within a single, common cryogenic mass, with magnetic fluxes circulating in opposite directions inside the two channels. This makes the magnets structure very complicated, especially for dipoles, in which the separation between the two channels is small enough to make them both magnetically and mechanically coupled.

2.1.2 The grid structure

The two symmetrical rings of the LHC are divided into eight octants consisting of arches and straight sections of about 528 meters (Figure 2.3). The two zones of maximum luminosity, where ATLAS and CMS experiments are located, are placed in two diametrically opposite straight sections: Point 1 and Point 5.

The other two major experiments, ALICE and LHCb, are located at the Point 2 and Point 8 respectively, where the machine reaches the minimum luminosity. In the remaining four straight sections there are no more beam intersections. The injection points are located in the 2 and 8 octants for the clockwise and counter-clockwise bunches injection, respectively. The 3 and 7 octants, instead, contain the beam cleaning and collimation apparatuses. The radio frequency (RF) cavities are placed in the fourth octant and constitute two independent systems (one in each direction).

The straight section at Point 6 contains the devices for the beam extraction: this operation is carried out using a combination of fast pulsed magnets able to produce deflections either in the vertical or horizontal direction.

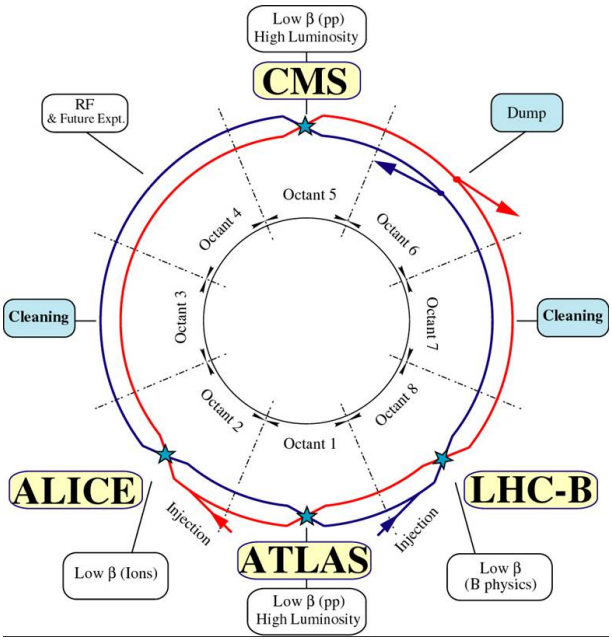

Figure 2.3: LHC grid structure

2.1.3 Beam luminosity

In a particle accelerator, the rate of events produced by collisions is given by:

$$R = \sigma \times \mathcal{L} \tag{2.1}$$

where σ is the cross section of the considered process and $\mathcal{L}$ is the instantaneous luminosity. The latter factor depends only on beam parameters and, for a Gaussian beam, it can be written as:

$$\mathcal{L} = \frac{N_{\mathrm{p}}^2 n_{\mathrm{b}} f_{\mathrm{rev}} \gamma_r}{4\pi \epsilon_n \beta^*} F \tag{2.2}$$

where N_{p} is the number of particles per bunch, n_{b} the number of bunches per beam, f_{rev} the revolution frequency, γ_r the relativistic factor, ϵ_n the normalized transverse emittance, β^* the beta function at the collision point and F the luminosity reduction factor due to the geometric crossing angle at the interaction point (IP).

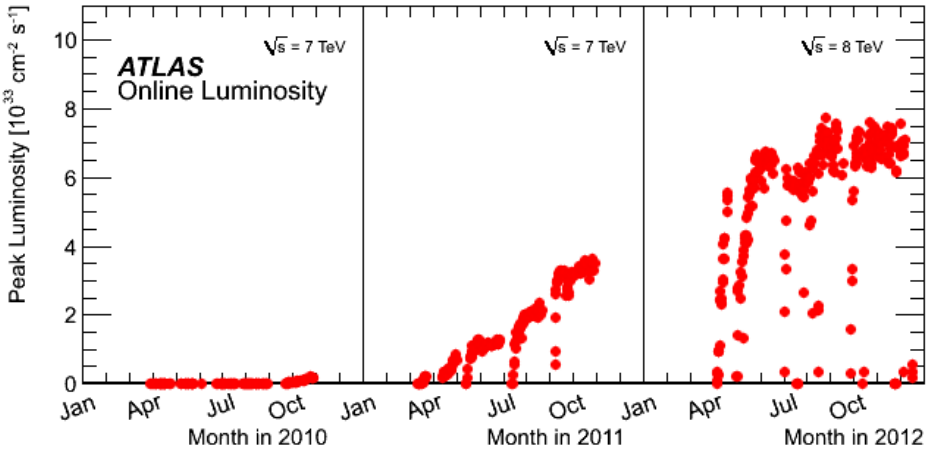

Figure 2.4: The peak instantaneous luminosity $\mathcal{L}$ delivered to ATLAS per day versus time during the *pp* runs of 2010, 2011 and 2012.

Figure 2.4 shows the instantaneous luminosity $\mathcal{L}$ delivered to the ATLAS experiment during the 2010, 2011 and 2012 *pp* runs. The instantaneous luminosity increased with time, reaching a maximum of about 8×10^{33} cm^{-2}s^{-1} during the 2012 8 TeV *pp* collision data taking. This high luminosity has been achieved with beam train of about 1400 bunches per beam (see Figure 2.5), each containing 10^{11} protons, and spaced of 50 ns in time, giving a collision rate of 80 MHz.

Figure 2.6 shows the total integrated luminosity $\int \mathcal{L}dt$ delivered to and recorded by the ATLAS experiment during the 2010-2012 runs. The *pp* collisions data collected during the 2012 8 TeV run corresponds 21.3 fb^{-1} of integrated luminosity with a loss of 1.5 fb^{-1} of data due to the data acquisition (DAQ) chain inefficiency. The high number of colliding bunches, shown in Figure 2.5, and the high instantaneous luminosity give rise to a very important phenomenon, called *pile-up*, that must be taken into account: with a very intense beam, the probabilities to have more than one hard scattering interactions per bunch crossing is very high. Figure 2.7 shows that, during the 2012 8 TeV run, the average number of collisions per bunch crossing was of $< \mu >= 20.7$, which may affect the data taking in several

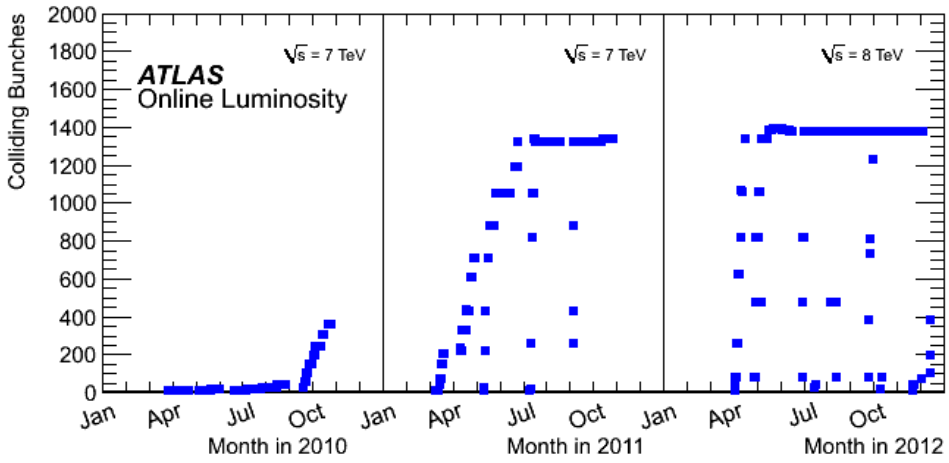

Figure 2.5: The number of colliding bunches in ATLAS versus time during the *pp* runs of 2010, 2011 and 2012.

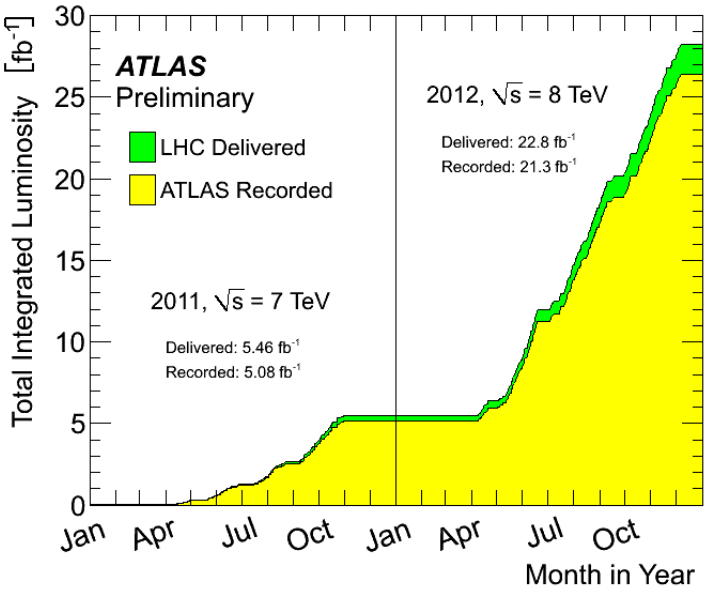

Figure 2.6: Cumulative luminosity versus time delivered to (green) and recorded by ATLAS (yellow) during stable beams and for *pp* collisions at 7 and 8 TeV centre-of-mass energy in 2011 and 2012.

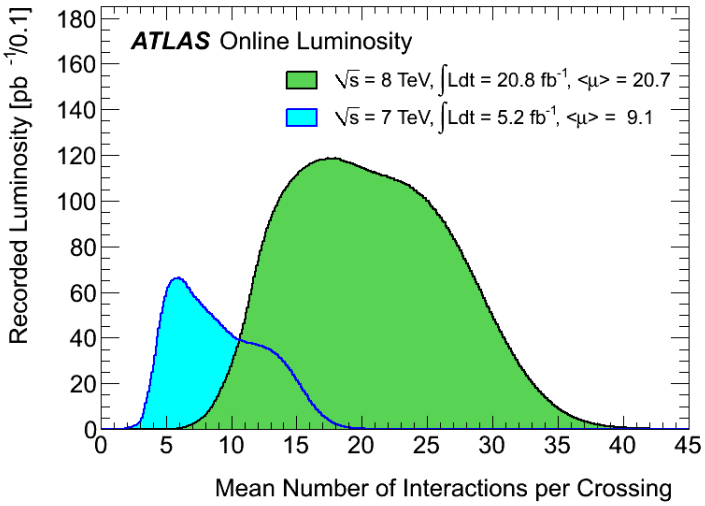

Figure 2.7: Luminosity-weighted distribution of the mean number of interactions per crossing for the 2011 and 2012 data. This shows the full 2011 and 2012 *pp* runs.

ways. Thus, dedicated selections and corrections must be performed in order to reduce the impact of *pile-up* on the current analysis.

2.2 The ATLAS experiment

The ATLAS (*A Toroidal Lhc ApparatuS*) detector is one of four experiments designed to fulfill the LHC research programme by exploiting the full collider potential.

The ATLAS structure (Figure 2.8) is typical of a multi-purpose experiment at particle colliders: it consists of a cylindrical geometry section around the beam axis, called *barrel*, 42 m long with a radius of about 11 m, which is closed at the ends by two regions, called *end-cap*, designed to optimize the detection in the forward region. The system covers almost the entire solid angle around the interaction point by means of several detectors of different types:

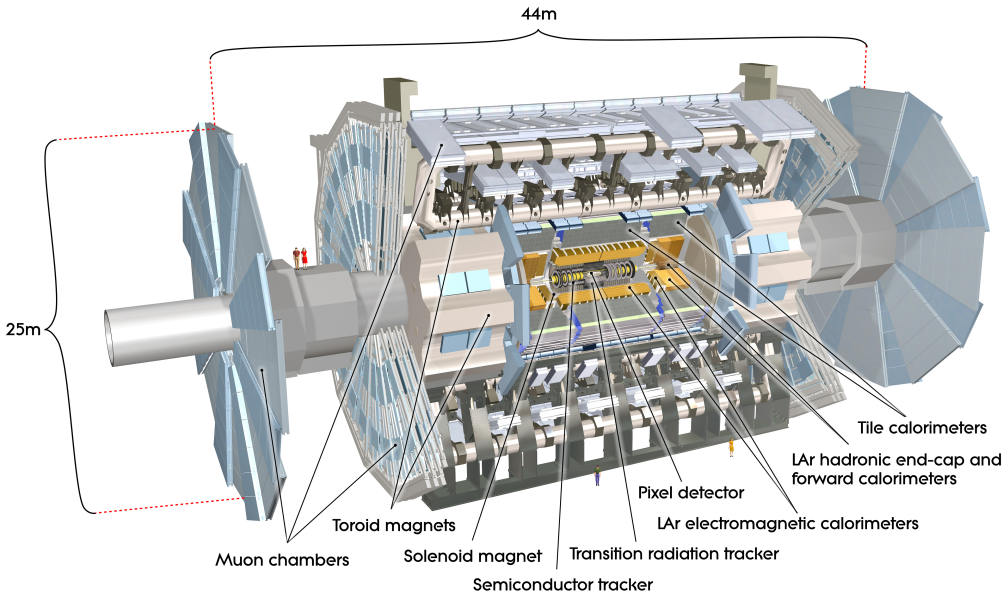

Figure 2.8: Diagram of the ATLAS experimental apparatus.

- a inner tracking system, for the measurement of charged particle momenta and the position of interaction vertices;
- a solenoidal superconducting magnet to provide a uniform magnetic field along the beam axis;
- an electromagnetic calorimeter (ECAL), for the detection and measurement of electromagnetic cascades induced by photons and electrons;
- a hadron calorimeter (HCAL), for the detection and measurement of hadron showers and the study of jet structure;
- a muon spectrometer, which allows the tracking and measurement of penetrating muons with a very high precision;
- an air-cored superconducting toroidal magnets to provide the magnetic field to the muon spectrometer.

2.2.1 ATLAS reference system

The reference system used in ATLAS (see Figure 2.9) is a right-handed system in which the x axis points to the center of the LHC ring, the z axis lies on the beam direction and the y axis is directed upwards. The representation in spherical coordinates of the reference system can be introduced by defining an azimuthal angle $\phi \in [-\pi, \pi]$, equal to zero along the x axis which increases clockwise while looking in the positive z direction, and a polar angle θ measured with respect to the z axis positive direction. The interaction point defines two regions, a "forward" ($z > 0$) and a "downward" region ($z < 0$).

Given a particle with energy E and longitudinal momentum component (parallel to the z axis) p_{L}, the particle rapidity can be defined as:

$$y = \frac{1}{2} \ln \left[\frac{E + p_{\mathrm{L}}}{E - p_{\mathrm{L}}} \right] \tag{2.3}$$

The rapidity difference is a relativistic invariant for longitudinal boost transformations, *i.e.* for Lorentz transformation along the z axis.

In the ultra-relativistic limit $E \approx p_{\mathrm{L}}$ the rapidity of a particle can be approximated by the *pseudorapidity*, defined as:

$$\eta = -\ln \left[\tan \left(\frac{\theta}{2} \right) \right] \tag{2.4}$$

which is equal to zero for $\theta = 90°$ and asymptotically increases as $\theta \to 0°$, as shown in Figure 2.10. An important derived variable, useful in physics analysis and trigger efficiency studies, is the angular separation in the η-ϕ plane, defined as:

$$\Delta R = \sqrt{(\Delta\eta)^2 + (\Delta\phi)^2}. \tag{2.5}$$

Since LHC is a hadronic collider, in which non-elementary particles composed of partons (quarks and gluons) are colliding, the effective interaction energy in the center of mass system is not exactly known, since it depends on the momentum

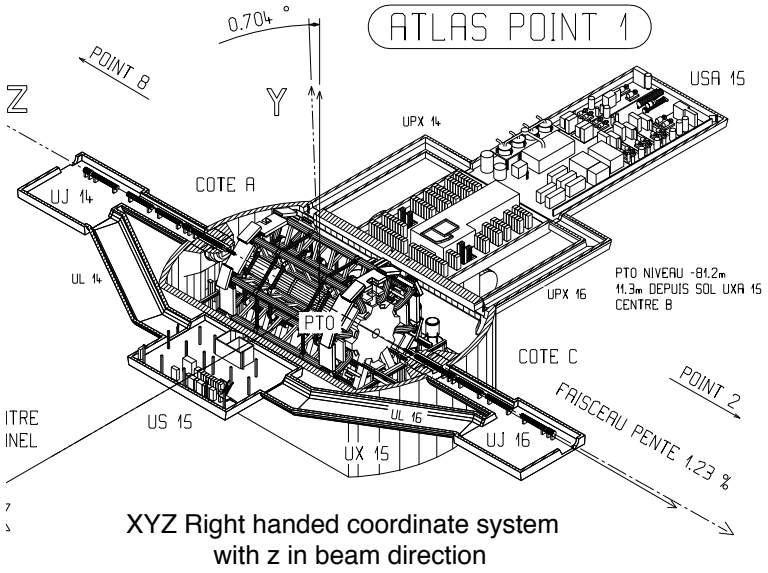

Figure 2.9: Global coordinate reference system used in ATLAS.

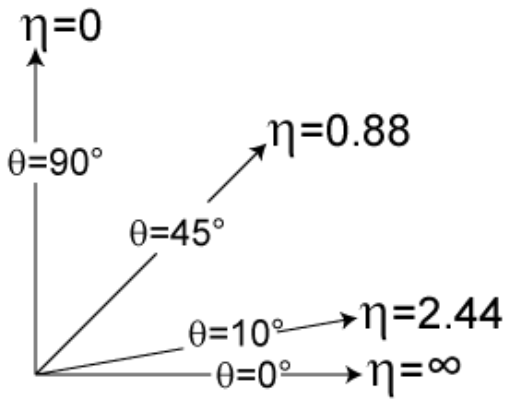

Figure 2.10: Pseudorapidity η for some given polar angle values θ.

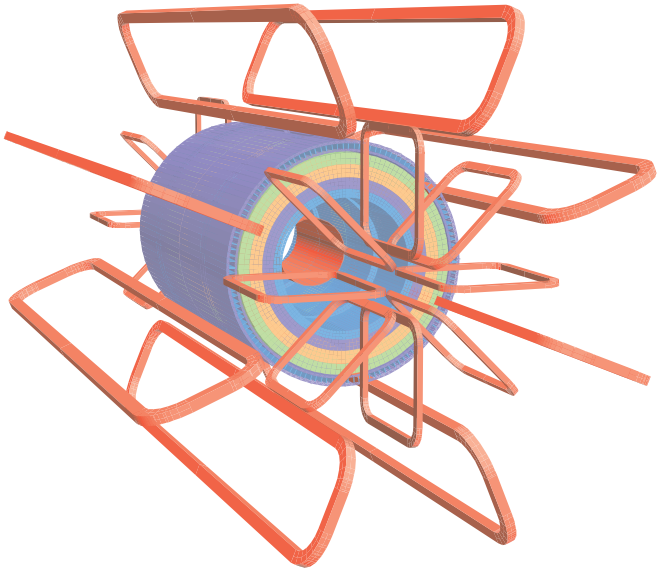

Figure 2.11: Geometry of the coils and magnetic structures. Eight coils which generate the toroidal magnetic field are visible in the *barrel* and *end-cap* regions. The structure that generates the solenoid magnetic field is located within the calorimetric system schematically depicted by four layers with different magnetic properties. The last layer is the return yoke.

fraction carried by the partons that actually participate to the hard scattering process. It is therefore natural to study the kinematics of interactions in the xy transverse plane (the average transverse momentum of parton is negligible and is invariant for Lorentz transformation along the z axis) where the energy conservation requirement is still valid.

2.2.2 The magnetic system

Figure 2.11 shows the ATLAS superconducting magnetic system consisting of a central solenoid (CS), which provides the magnetic field inside the inner detector. The CS is surrounded by a system of three superconducting toroids (one central and two at the opposite ends) designed to generate a large magnetic volume (cov-

ering the region $|\eta| < 3$) with an air-cored structure to minimize the contribution of multiple scattering to the momentum resolution. The toroidal magnetic system provides the magnetic field to the muon spectrometer.

The magnetic system is 26 m long and has a diameter of 20 m. The two *end-cap* toroids (ECT) are located at the ends cylindrical *barrel* toroids (BT) and are aligned with the CS. They are 5 m long, with an outer diameter of 10.7 m and an internal diameter of 1.65 m.

The CS, which is 5.3 m long with a internal diameter of 2.4 m, is able to provide to the inner detector a central field equal to 2 T with a peak of 2.6 T upon the superconductor surface. The magnetic field peaks on the BT and ECT superconductor magnet are equal to 3.9 T and 4.1 T, respectively. The yield in terms of bending power (see Figure 2.12) is defined through the $\int B_\phi dl$ integral, where B_ϕ is the azimuthal component of the field and the integral is calculated along the straight line from the inner to outer radius of the toroids.

The BT provides a bending power between 2 and 6 T×m whereas the ECTs contribute with a bending power between 4 and 8 T×m in the $0 < |\eta| < 1.3$ and $1.6 < |\eta| < 2.7$ regions, respectively. The bending power is less intense in the transition regions in which the two magnets overlap ($1.3 < |\eta| < 1.6$). The CS coil is designed to be as thin as possible in order to ensure high operational safety and reliability.

Each toroid consists of eight rectangular coils radially and symmetrically assembled around the beam axis. The ECT coil system is rotated by 22.5° with respect to the BT system in order to generate a radial superimposition and optimize the bending power in the interface regions between the two systems. The coils consist of 20.5 kA windings of NbTi superconductor compound stabilized with aluminum. Finally, the magnets are indirectly cooled down by a forced flux of helium with a temperature of 4.5 °K through tubes welded on the windings coat.

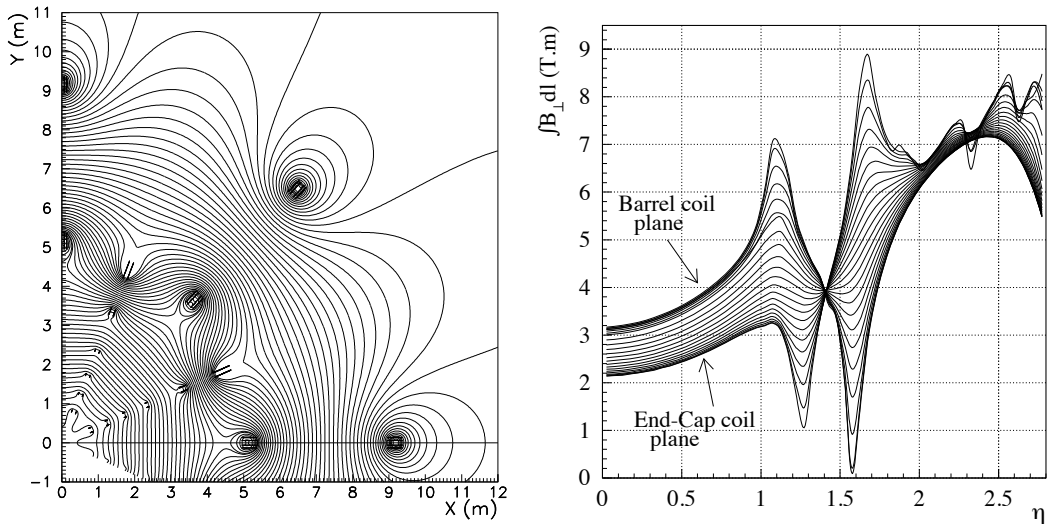

(a) (b)

Figure 2.12: (a) Magnetic field lines in the x-y plane. (b) Bending power as a function of η.

2.2.3 Inner Detector

The ATLAS physical analyses demand high precision measurements and require detectors with high granularity because of the enormous track density expected at LHC.

The Inner Detector (ID) structure [27, 28] is shown in Figure 2.13. It combines high-resolution detectors in the innermost layer with continuous tracking elements in the outermost layer, all of these within the central solenoid (CS), which produces a nominal magnetic field of 2 T.

The semiconductor tracker detectors, with pixel technologies and silicon microstrips (SCT), have the best features, but the total number of precision layers must be limited because of the large amount of the material of which they are composed

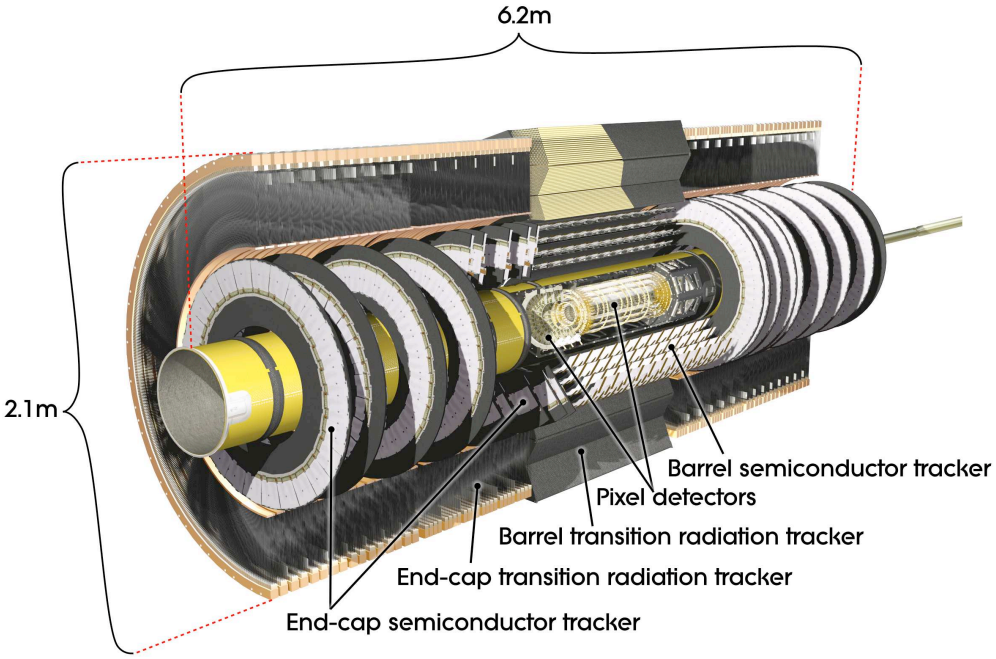

Figure 2.13: ATLAS Inner Detector structure.

(which causes multiple scattering scattering and degrades the resolution on the transverse impact parameter). Also the high cost of this technology limits its use. Each track typically passes through three pixel layers and eight silicon stripes, while in the outermost region a transition radiation tracker (TRT) provides a very high number of track points, about 36 per track, with a low quantity of material and a very low cost with respect to the SCT.

These two techniques allow to easily reconstruct the charged particle trajectories with very high precision in both ϕ and z coordinates.

The outermost radius of the cavity within the ID is 115 cm long and covers a total length of 7 m. Mechanically, the detector is divided into three units: a cylindrical component, extended up to ± 80 cm from the interaction point, and two identical parts in the *endcap* regions occupying the remaining cylindrical cavity.

In the cylindrical region, the high precision detector layers are arranged in concen-

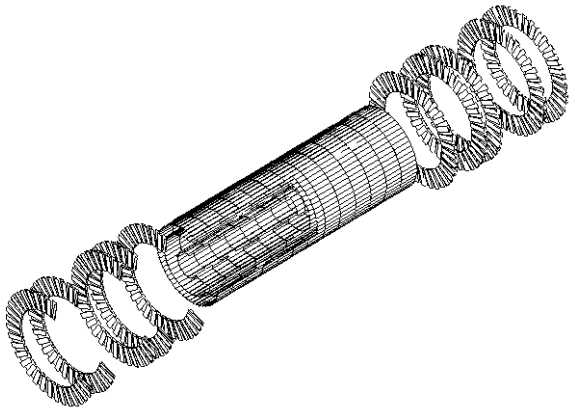

Figure 2.14: 3D view of the pixel detector.

tric cylinders around the beam axis and contained in a 56 cm long radius, while the detectors in the *endcap* regions are mounted on disk perpendicular to the beam axis.

This type of detector is the most subject to damage caused by radiation, for which it needs a relatively frequent substitution in order to maintain high performances.

2.2.3.1 The pixel detectors

The pixel detectors [29] is designed to provide a set of three high-precision measurements in innermost region near to interaction point. This system significantly contribute to the resolution of the impact parameter measurement and to the ability to reconstruct particles with a short average lifetime, as B hadrons and τ leptons.

The two-dimensional sensor segmentation (in both the r-ϕ plane and along the z axis) provides point measurements with no ambiguity but it requires the use of advanced electronic techniques. The readout chips have large areas, with individual circuits for each pixel element including buffers to store data while waiting for the first level trigger decision.

The system contains about 140 million of detector elements, in steps of 50μm along the *R*-ϕ direction and 300μm along the z axis, and consists of three cylindrical bodies with an average radius of about 4, 11 and 14 cm respectively, and five discs for each side with a radius between 11 and 20 cm, which complete the angular coverage (see Figure 2.14).

The detector is designed to be highly modular and contains about 1500 modules in the cylinders and 700 the disks modules. The dimensions of the modules are identical for both types: 64.2 mm in length times 22.4 mm in width. The thickness of each layer is equal to about 1.7% of a radiation length with a normal incidence. Space resolutions, averaged over the pseudorapidity range, are: $\sigma(r\text{-}\phi) \simeq 12$ μm for all pixels, $\sigma(z) \simeq 66$ μm for the *barrel* region and $\sigma(r) \simeq 77$ μm for discs.

2.2.3.2 Semiconductor Tracker

The SemiConductor Tracker (SCT) is designed to provide eight precision measurements per track in the intermediate radial region, thus contributing to the measurement of track momenta, impact parameters and vertex locations, as well as to the recognition of trajectories through its high granularity.

Eight layers of silicon microstrips are located in the cylindrical region, which provide the measurement of r-ϕ and z coordinates. The size of each element is of 6.36×6.40 cm^2 with 768 readout strips in steps of 80 μm.

The readout is first amplified, discriminated and then only signals above a given threshold are stored in a buffer up waiting for the first trigger level decision. Overall, the SCT system contains 61 m^2 of silicon detectors, for a total of 6.2 million of readout channels.

The spatial resolution is of 16 μm in r-ϕ and 580 μm in z coordinates.

The modules in the cylindrical region are mounted on four carbon fiber cylinder,

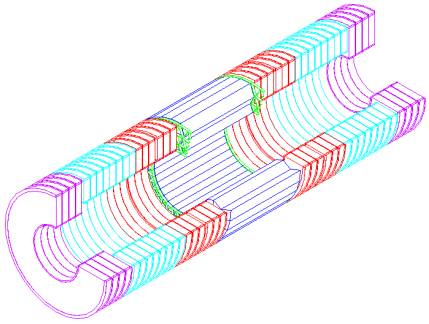

Figure 2.15: 3D view of the TRT detector. The *barrel* TRT is located in the center with the *endcap* discs placed at each end.

which contain the cooling system, with radii of 30.0, 37.3, 44.7 and 52.0 cm. The *endcap* modules are mounted on nine discs, up to a maximum of three rings each, which cover the pseudorapidity range $|\eta| \leq 2.5$. Both the pixel detectors and the SCT system have been constructed with materials with a low thermic expansion coefficient and integrated with a robust cooling system to guarantee a very high stability.

2.2.3.3 Transition Radiation Tracker

The Transition Radiation Tracker (TRT), shown in Figure 2.15, is based on the use of straw detector with a small diameter and able to operate in the condition of a high particles flux as expected at the LHC thanks to the detecting wires isolated within single gas volumes.

The electron identification is achieved by using an uninflammable gas mixture composed of 70% Xe, 20% CO_2 and 10% CF_4. The drift tubes are surrounded by a propylene foam with a porous structure characterized by tiny air bubbles within the material. At the passage of a ultra-relativistic charged particle, the electric field on the contact surfaces varies abruptly thus generating the so-called

transition radiation, which is due to the different dielectric constants of air and propylene (radiator).

The energy thresholds for the photons emission, are the following: $E = 500$ MeV for electrons and $E \approx 100$ GeV for the heaviest hadrons. Photons, which are emitted with an angle $\theta \simeq 1/\gamma$, are absorbed for photoelectric effect from the gas contained in the tubes with a cross section $\sigma_{\text{f.e.}} \propto Z^5$ (from which the choice of a heavy noble gas as the Xe_{54}).

The cylindrical section covers the radial range from 56 up to 107 cm, with individual modules containing a number of axial tubes between 329 and 793. The *end-cap* regions are each composed of 18 disks. The first 14 discs near to the interaction point cover a radial range between 64 and 103 cm, whereas the last 4 discs extend down to a radius of 48 cm.

The large number of tubes per track ensures an overall resolution of at least 50 μm, averaged over all tubes and including a systematic error of about 30 μm due to alignment.

2.2.4 Calorimetric system

The ATLAS calorimetric system, shown in Figure 2.16, is designed to fully reconstruct the energy of electrons, photons, hadrons and jets, as well as to allow the measurement of missing transverse energy and the particle identification. It is composed of different section:

- an electromagnetic calorimeter (EM), which covers the pseudorapidity range $|\eta| < 3.2$;
- a cylindrical hadron calorimeter (HCAL), which covers the pseudorapidity range $|\eta| < 1.7$;

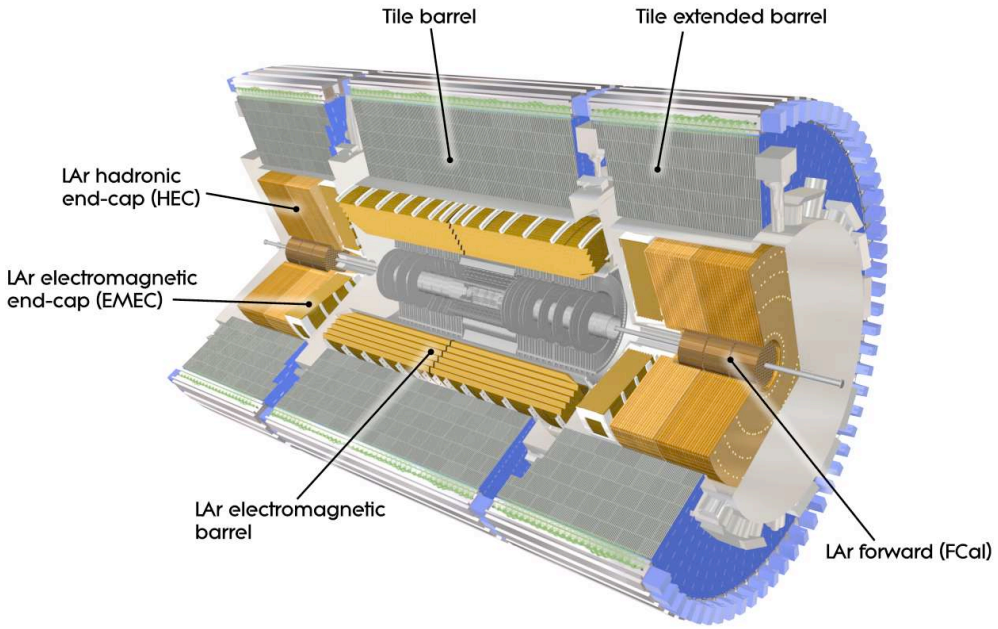

Figure 2.16: Calorimetric system.

- two hadron calorimeters in the *endcap* regions (HEC), which cover the pseudorapidity range $1.5 < |\eta| < 3.2$;
- two forward calorimeters (FCAL), which cover the pseudorapidity range $3.1 < |\eta| < 4.9$.

The electromagnetic calorimeter [30] is a lead (Pb) and liquid argon (LAr) detector with an accordion geometry contained in a cylindrical cryostat, which surrounds the inner detector cavity. In the pseudorapidity range $|\eta| < 1.8$, it is preceded by a pre-sampler with the purpose of correcting the measures for the energy lost in the upstream calorimeter material (inner detector, cryostats, coils).

The cylindrical hadron calorimeter [31] is divided into three sections, a central cylinder and two identical extended cylinders, and is based on a sampling technique by means of plastic scintillator plates immersed in an iron absorber. The same technique is used in the central gap where the intermediate plates calorimeter

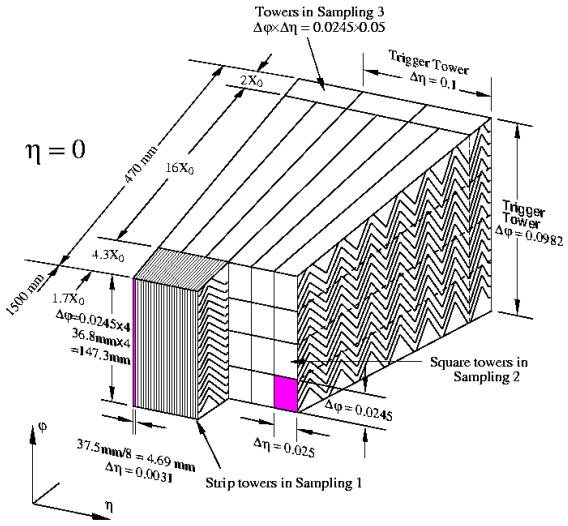

Figure 2.17: Structure of the electromagnetic calorimeter.

is located.

For the *endcap* calorimeters copper (Cu) and liquid argon are used, whereas for the forward calorimeters is liquid argon and bar-shaped electrodes in a tungsten matrix are used. Also in the *endcap* regions, two cryostats are located to hold both electromagnetic and hadronic calorimeters and the forward one.

2.2.4.1 Electromagnetic Calorimeter

The electromagnetic calorimeter consists of a cylindrical ($|\eta| < 1.475$) and two *endcap* ($1.375 < |\eta| < 3.2$) components. The cylindrical component consists of two identical half-cylinders separated by a thin slit (6 mm) in the $z = 0$ plane. The *endcap* calorimeters are divided into an inner disk ($2.5 < |\eta| < 3.2$) and an external coaxial one ($1.375 < |\eta| < 2.5$).

Calorimetric cells are segmented ($\Delta\eta \times \Delta\phi = 0.025 \times 0.025$), in correspondence of readout electrodes. The longitudinal sampling of the showers is obtained by

repeating 4 times the cell structure along the radial direction. Moreover, the accordion geometry allows to obtain a complete symmetry in the ϕ coordinate with no cracks in the azimuthal direction.

The total thickness amounts to about 25 X_0 (where X_0 is the radiation length) in the *barrel* region and to more than $26X_0$ in the *endcap*. Overall, the electromagnetic calorimeter provides about 190000 readout channels.

The energy resolution for an electromagnetic calorimeter is given by:

$$\frac{\sigma_E}{E} = \frac{a}{\sqrt{E}} \oplus \frac{b}{E} \oplus c \tag{2.6}$$

where a is the sampling term (which also includes the statistical fluctuations), b is the term that takes into account the noise due to electronics and overlapping signals and c is a constant that takes into account mechanical effects, calibration and non-uniform sources which involve systematic errors. These parameters determine the energy resolution, which is equal to $\frac{\sigma_E}{E} = \frac{10\%}{\sqrt{E[\mathrm{GeV}]}} \oplus 10\%$ in the energy range between 2 GeV and 5 TeV.

The angular resolution amounts to about 40 mrad$/\sqrt{E[\mathrm{GeV}]}$ which allows a good measurement in η of the showers direction.

2.2.4.2 Minimum Bias Trigger Scintillators

In each region of the *endcap* electromagnetic calorimeter, 2×16 scintillator plates connected to photomultiplier tubes (PMT) are mounted. This scintillator system, called *Minimum Bias Trigger Scintillators* (MBTS), is located at $|z| = 3.56$ m and is segmented in η (two segments) and ϕ (eight segments) coordinates, covering the pseudorapidity range $2.09 < |\eta| < 3.84$.

The MBTS system has been used in the first months of low luminosity data taking, for the study of the minimum bias event trigger, *i.e.* interactions with low

multiplicity and low transverse momentum particles production. The signature for this kind of events consists of charged particles signal coincidence in one or both *endcap* stations.

2.2.4.3 Hadronic calorimeters

The hadronic calorimeters cover the pseudorapidity range $|\eta| < 4.9$, which use different techniques depending on the region in which they operate. The thickness has been chosen to provide a good containment for hadronic showers and to minimize the number of particles able to pass to the spectrometer; for $\eta = 0$, the thickness amounts to 8 interaction lengths λ which can provide a good resolution for high energy jets and a good measurement of missing transverse energy $E_{\mathrm{T}}^{\mathrm{miss}}$.
The system consists of a central plus two other cylinders, which radially extend from an internal radius of 2.28 m up to an external radius of 4.25 m. They are longitudinally segmented into three layers and azimuthally divided into 64 modules, for a total amount of about 10000 readout channels.
In the cylindrical components, a sampling technique with an iron absorber and sparkling plates as active material is used. The structure is periodic along z with sparkling plates 3 mm thick and iron plates of total thickness equal to 14 mm in a single period.
In the *endcap* regions, each section of the hadron calorimeter consists of two independent discs with an external radius equal to 2.03 m. The upstream disk is composed of copper plates 25 mm thick, while the other, more far from the interaction point, is composed of plates 50 mm thick. The active component consists of liquid argon. The segmentation of readout calorimetric cells is equal to $\Delta\eta \times \Delta\phi \simeq 0.1 \times 0.1$ in both the *barrel* and *endcap* regions.
The forward calorimeter (FCAL) has a particularly complex structure due to the

high level of radiation in the region where it is located, about 4.7 m away from the interaction point of interaction. It provides an excellent calorimetric coverage and ensures a reduced level of background radiation in the muon spectrometer, but it is more subject to deterioration than the other detectors. It consists of three sections, the first made of copper, the other two of tungsten, and in each of them a metal matrix with channels regularly spaced lengthwise and filled with bars and concentric tubes is present. Also in this case, the active component consists of liquid argon, which fills the gaps between the bars and the tubes. The total number of readout channels is equal to 3.584.

The energy resolution for a hadronic calorimeter can be written as:

$$\frac{\sigma_E}{E} = \sqrt{\frac{c_{\text{int}}^2 + c_{\text{samp}}^2}{E}} \oplus a \tag{2.7}$$

where a accounts for non-Gaussian fluctuations in the electromagnetic component of the shower, c_{int} accounts for the intrinsic fluctuations in the fraction of the initial energy that is transformed into sensible energy and c_{samp} accounts for statistical and sampling fluctuations. The energy resolution is equal to $\frac{50\%}{\sqrt{E[\text{GeV}]}} \oplus 3\%$ in the pseudorapidity range $|\eta| < 3.0$ and to $\frac{100\%}{\sqrt{E[\text{GeV}]}} \oplus 10\%$ in the pseudorapidity range $3.0 < |\eta| < 4.9$.

2.2.5 The muon spectrometer

The high resolution muon spectrometer is a very important detector since high momentum muon pairs are among the most clear and simple experimental signatures in many physics searches. It is equipped with an independent trigger system independently able to perform standalone measurements in a wide range of transverse momentum, pseudorapidity and azimuth angle.

The spectrometer has been designed to be independent from the other detectors

and to satisfy the following requests:

- a transverse momentum resolution of 1% for the reconstruction of final states with 2 and 4 muons and for the identification of the muons electrical charge;
- a good pseudorapidity coverage in the range $|\eta| < 3$, which guarantees a good efficiency for the reconstruction of "high-mass objects" decaying into muons;
- the measurement of the second spatial coordinate ϕ with a spatial resolution of 5-10 mm for the offline track reconstruction;
- a good trigger discrimination power;
- a good time resolution in order to ensure the correct identification of the colliding bunches that generate the event selected by the trigger, *i.e.* the bunch-crossing identification.

The spectrometer is present in both the *barrel* ($|\eta| < 1.05$) and the *endcap* ($|\eta| > 1.4$) regions, as well as in the intermediate transition region.
In the r-ϕ plane (see Figure 2.18) the muon system is divided into 16 segments according to the octant symmetry of to the toroidal magnet and, because of the different coverage in ϕ, it consists of both small and large sectors.

The operating principle of the spectrometer is based on the deflection of the muon track while crossing the toroidal magnetic field generated by the three large magnets (one in the *barrel* and two in the *endcap* regions) described in Section 2.2.2.
The position of the detecting devices within the spectrometer is designed to efficiently exploit the magnets bending power, to covers a wide pseudorapidity ($|\eta| \leq 3$) and the entire azimuthal angle ($0 \leq \phi \leq 2\pi$) ranges, by using a projective towers geometry towards the interaction point.

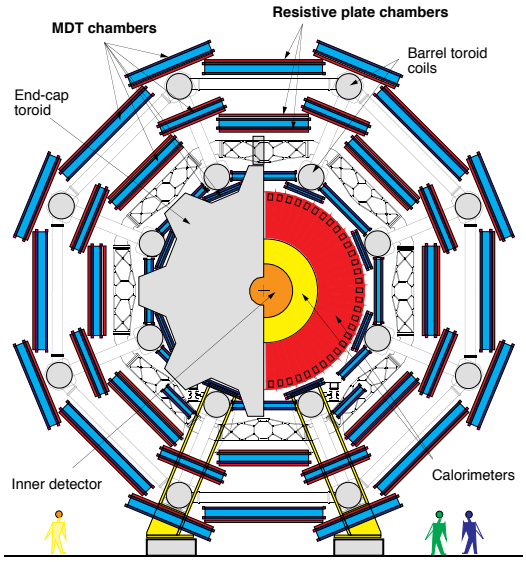

Figure 2.18: Muon spectrometer section in the x-y plane.

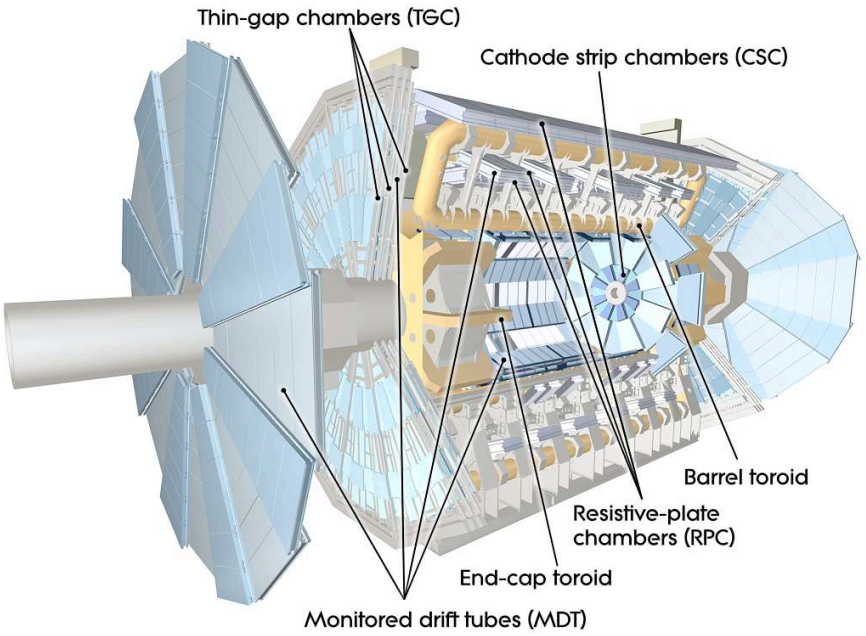

Figure 2.19: Layout of the muon spectrometer and the arrangement of the different chambers within the spectrometer.

Within the magnetic volume, the precision chambers are arranged in several layers, to achieve a high spatial resolution for the muon transverse momentum measurement, in combination with layers of trigger chambers, for a fast time response (see Figure 2.19).

The precision chambers are divided into three stations. In the *barrel* they are arranged in three cylinders concentric to the beam axis with radius of about 5, 7.5 and 10 m for the inner, middle and outer stations, respectively, covering a pseudorapidity range $|\eta| < 1$. The *endcap* chambers, with a trapezoidal shape, covers the pseudorapidity range $1 < |\eta| < 2.7$, and are arranged in four disks concentric to the beam axis with a distance of 7, 10, 14 and 21 m, respectively, from the interaction point.

Precision measurements of the muon track are performed in the r (in the transition and *endcap* regions) and the z (in the *barrel* region) projections.

The *Monitored Drift Tubes* (MDT) chambers [32] covers a wide pseudorapidity range, providing high precision measurements. At large values of pseudorapidity and in the innermost region close to the interaction vertex ($2 < |\eta| < 2.7$), *Cathode Strip Chambers* (CSC) [32] are used, since they offer a finer granularity able to sustain the high particle rate and the difficult background conditions; the arrangement of these two tracking systems is shown in Figure 2.19.

The trigger system covers the pseudorapidity range $|\eta| < 2.4$. In the *barrel*, *Resistive Plate Chambers* (RPC) are arranged in three layers, two of which are located on both sides of the MDT chambers in the middle station and one above (below) the MDT in the large (small) sector of the outer station. Along the z axial coordinate, chambers are segmented into 6 or 7 unit of 2.6 m, following the MDT chambers segmentation, and are located in the same mechanical structure to guarantee a good mechanical tolerance and a good alignment with respect to the absolute ATLAS reference system.

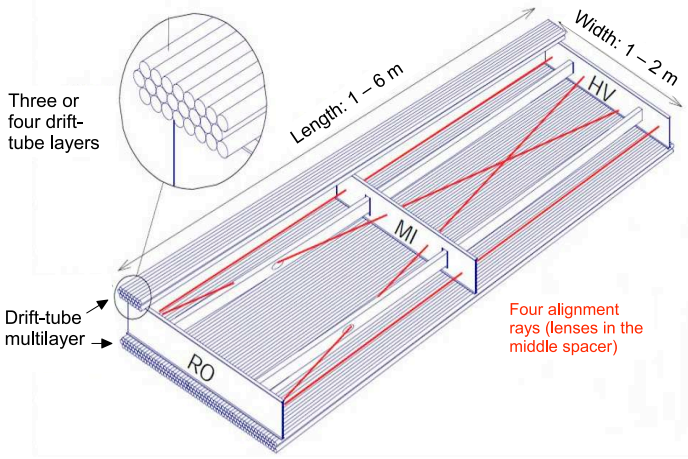

Figure 2.20: MDT chambers

In the *endcap* region, trapezoidal *Thin Gap Chambers* (TGC) are used in a vertical arrangement. They are segmented into unit with a 3 m maximum width, depending on their position and according to the octant geometry of the toroids. The trigger chambers have the purpose to identify the bunch-crossing with a time resolution of 25 ns. They also provide a measurement of the second spatial coordinate ϕ, orthogonal to the precision chambers measurement, with a typical resolution of 5-10 mm.

2.2.5.1 The precision and trigger chambers

MDT The MDT chambers consists of two multilayer aluminum drift tubes, mounted on both sides of a rigid spacer frame. Each multilayer consists of three layers of drift tubes for the middle and outer stations and four layers for the inner station. Each tube has an external diameter equal to 3 cm and contains a anodic central wire of 50 μm and a non-flammable gas mixture of 93% Ar and CO_2 at a pressure of 3-5 bar, which ensure the linearity of the drift time, a small Lorentz angle and a good device lifetime. The tubes are supported by a structure that

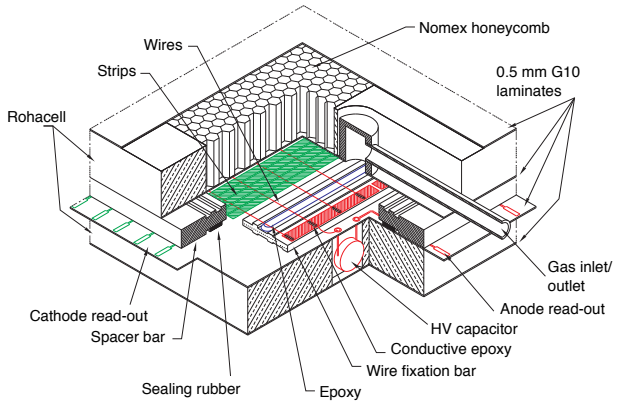

Figure 2.21: Diagram of a CSC detector.

avoids the deformation used by gravity or temperature and operates under a proportional regime with a maximum drift time of ≈ 700 ns. They are oriented along the plane orthogonal to the beam axis, allowing the measurement of the r-η coordinate with a single wire resolution of ≈ 80 μm. The 1194 MDT chambers cover an overall area equal to 5500 m^2 for a total number of about 3.7×10^4 readout channels.

CSC CSCs are multiwire proportional chambers with a symmetrical cell in which the anode-cathode distance equals the spacing between the anodes (see Figure 2.21). The gas used is a 30% Ar, 50% CO_2 and 20% CF_4 mixture. Precision position measurements along the anodic wire exploit the technique of the center of gravity of the charge induced by the cascade on one of the two cathodes appropriately segmented into strips with a 5 mm pitch. The transverse coordinate can be determined by segmenting the second cathode in strips parallel to the anodic wires or, in alternative, by directly reading the signal of the anodic wires. The maximum drift time is less than 25 ns, while the resolution on position measurements along the anodic wires is of the order of 50 μm.

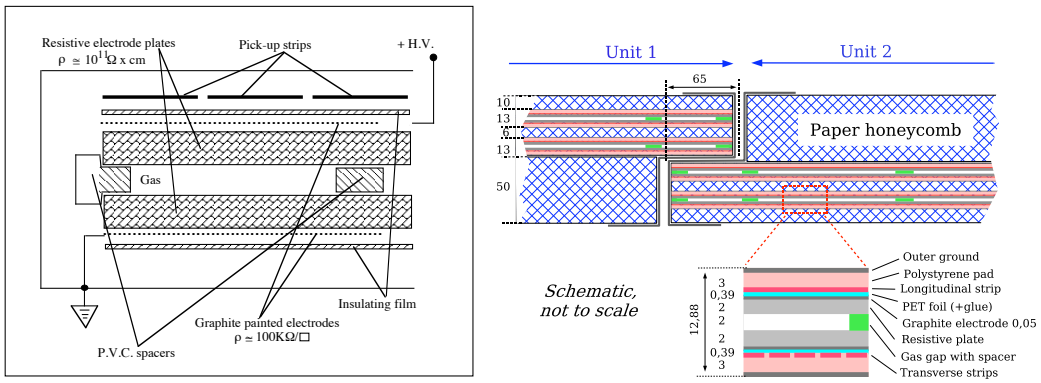

(a) (b)

Figure 2.22: (a) Diagram of a RPC with single gap. (b) Position of the RPCs along z the direction.

RPC The RPCs are gas detectors constituted by a pair of parallel bakelite plates, a material with resistivity $\rho \simeq 10^{10} \div 10^{11}$ Ωcm (see Figure 2.22), and separated by a gap of $\approx$ 2 mm by means of insulating polycarbonate spacers equally distributed. The volume between the planes is filled with a gas mixture composed of 96.7% tetrafluoroethane ($C_2H_2F_4$), 3.0% isobutane ($(CH_3)_3\,CH$) and 0.3% sulfur hexafluoride (SF_6). The external surfaces of the two bakelite planes are covered by a thin layer of graphite paint, with one layer connected to the high voltage system, the other to ground. The graphite is in turn covered with an insulating film of polyethylene (PET) with a thickness of 200 μm. The ions produced by the primary ionization, caused by the interaction of the particles within the gas volume, are accelerated by a strong electric field (5 kV/mm) applied to planes generating new ionizations. The produced signal is capacitively induced on two planes of copper strips orthogonal to each other, which provide the measurements of η and ϕ coordinates. A strip behaves as a transmission line of and allows the signal to be propagate in two opposite directions with minimal amplitude and timing

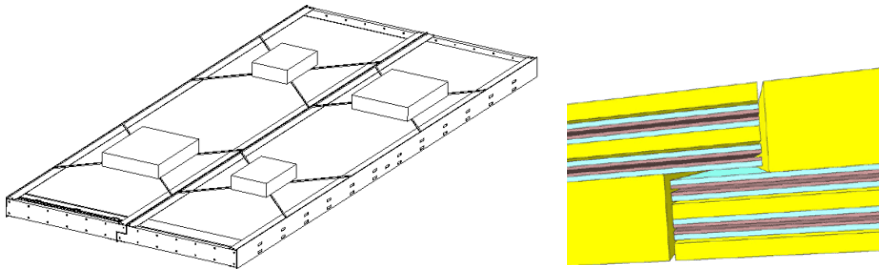

(a) (b)

Figure 2.23: (a) Trigger chamber composed by assembling two RPC unit. (b) Detail of the overlapping region of two RPC unit

information losses. The charge induced on strips is divided into two equal parts: one to front-end electronics while the other is absorbed by a resistor located at one end of the readout strip. The pitch of η-strips varies between $26.5 \div 35.3$ mm, that of ϕ-strips between $26.6 \div 30.5$ mm. Finally, each RPC unity consists of two or four independent subunit distributed on two layers. A trigger chamber consists of one or two RPC unit assembled together (see Figure 2.23). In the latter case the two units are overlapped to avoid death regions. The total number of RPC units in the muon spectrometer is 1088, for a total surface coverage of 3500 m^2. The typical spatial resolution is of the order of ≈ 1 cm, while the time resolution is of ≈ 1 ns. Furthermore, to face the very high flow of particles produced at the LHC, the RPCs are able to operate in an avalanche regime with low gain in which, unlike the standard streamer regime, they can tolerate flows up to ≈ 1 kHz/cm^2.

TGC The TGC detectors are similar to the multiwire chambers, except for an anode-to-anode distance greater than the anode-cathode distance. These chambers operate in a saturation regime and use wires with a diameter equal to 50μm, with a 2 mm pitch, enclosed by two graphite cathodes with a distance of 1.4 mm from the anode plane. On the outer surfaces of the graphite layers strips parallel to the

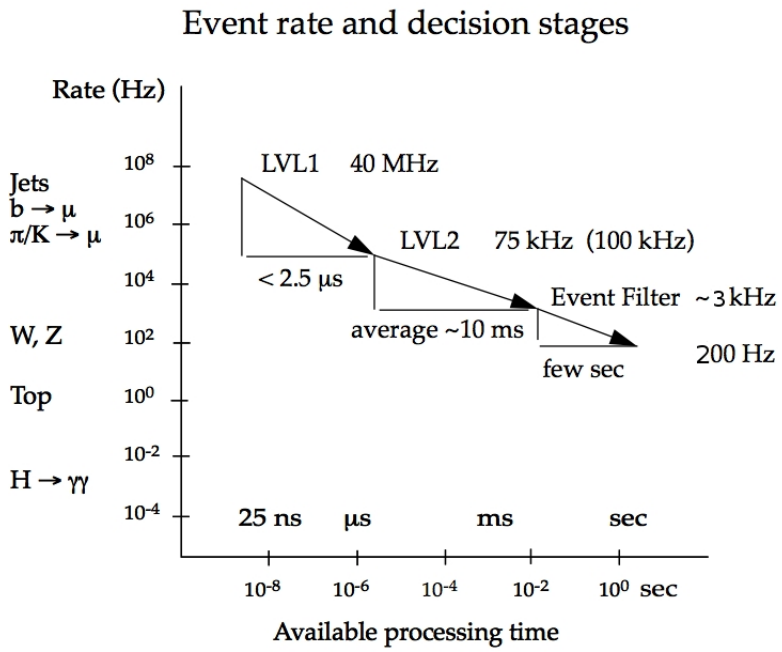

Figure 2.24: The event rate at which interesting physics occur (referred to LHC design parameters) and the processing time of each trigger level

anodic MDT wires are installed, which provide the trigger signal, plus another set strips orthogonal to the first, which provide the second coordinate measurement.

2.2.6 The ATLAS Trigger

The LHC is designed to provide collisions at a frequency of 40 MHz and, since the average dimension of an ATLAS event is ≈ 1.5 MB, a recording rate of ≈ 60 TB per second would be needed, while the current technology allows to record data at about 300 MB/s. This is not a huge problem, since the interesting physics at LHC does not occurs at that rate but at lower ones, as shown in Figure 2.24, so the events to be recorded can be selected without loosing the relevant informations. This selection is performed online by the ATLAS trigger and data acquisition system [33]. The ATLAS trigger is designed to rapidly inspect the events detected by

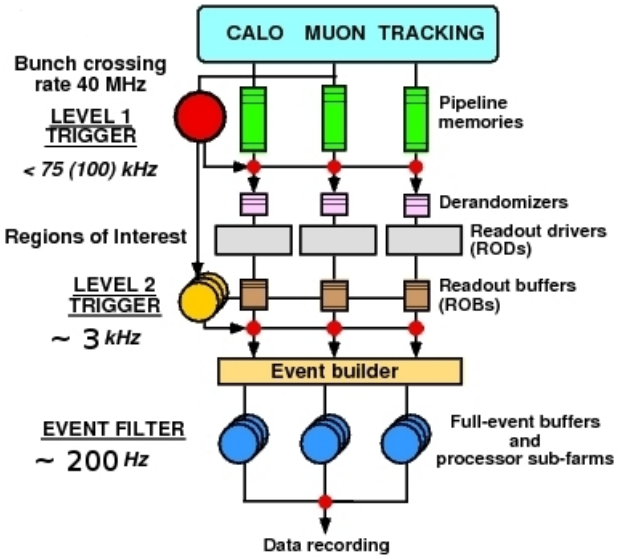

Figure 2.25: Main structure of the ATLAS trigger system: it is made of three levels, each improving the measurement of the previous levels also combining informations from different subdetectors

the ATLAS detector and choose whether record or discard the event after having compared its main features with a set of predefined thresholds contained in the trigger menu.

The ATLAS trigger system has a three level structure: each level refines the measurements of the previous level introducing also new selection criteria and combining the information from different subdetectors, as shown in Figure 2.25.

The first level of the ATLAS trigger (L1 or LVL1) is completely hardware-based and it makes use of only the data collected by the calorimetric system and the muon spectrometer: the L1 trigger only looks for high-p_{T} muons candidates or calorimetric objects (electrons/photons, jets) by means of fast and rough measurements performed by ad-hoc detectors in the Muon Spectrometer (RPC, TGC) and simplified object identification in the calorimeter. The L1 is designed to take a decision on the event in 2.5μs and its output is a list of so-called *Regions of Interest* (RoI), which are $\eta - \phi$ regions of the detector in which interesting activity

has been detected, and the output rate is about 100 kHz.

The second level of the ATLAS trigger (L2 or LVL2) is completely software-based. It takes as input the RoIs provided by the L1, and refines the measurement into these regions: data of the precision chambers are used in the Muon Spectrometer (MDT, CSC) as well as the data from the ID, while the measurement of the calorimetric objects is refined using higher level algorithms. Moreover the data of the different subdetectors are combined together in order to obtained better object reconstruction/identification (e.g. the ID and the MS tracks are combined for the muons, ID and calorimetric informations are combined to discriminate between electrons and photons). The L2 takes its decision in $\mathcal{O}$(10ms) and its output rate is about 3 kHz. The third level of the ATLAS trigger (Event Filter, EF) is completely software-based and forms, together with the L2, the High Level Trigger (HLT). At this stage a full reconstruction of the detector is performed (the measurement is not restricted to the RoIs), and the algorithms run at the EF are mostly the offline reconstruction algorithms adapted to the online environment. The decision of the EF is taken in $\mathcal{O}$(1s) and the output rate is about 400 Hz.

Figure 2.26 shows the total trigger rate for all the three levels as a function of the instantaneous luminosity: how can be seen the trigger rates are kept stable. This happens thanks to changes in the prescales and in the trigger menu, where higher thresholds or quality criteria on the trigger objects are required as the luminosity increases.

2.2.6.1 Electron Trigger

The electron trigger follows the three level ATLAS trigger structure, in which the measurements and the selections are refined at each stage.

At the first level the electron trigger makes use only of the calorimeters, and hence

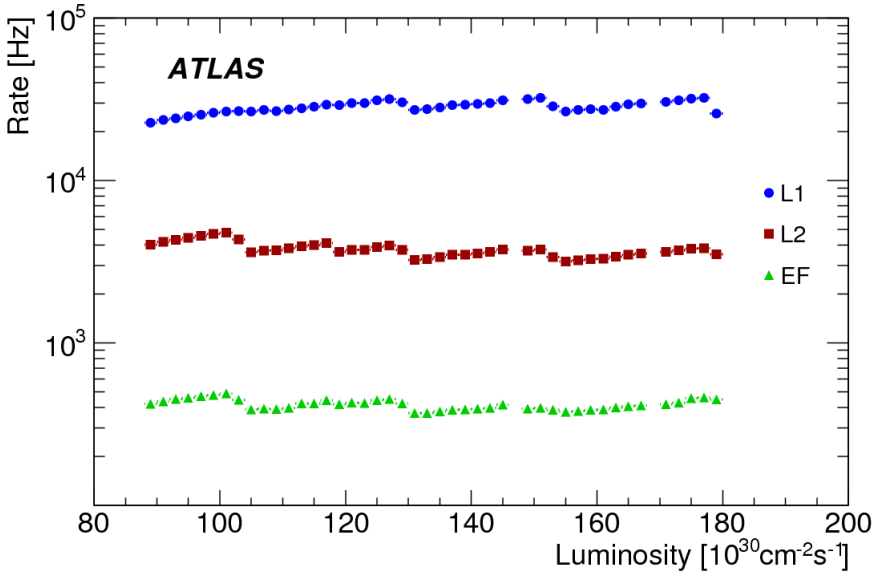

Figure 2.26: Total trigger rates at each level of the ATLAS trigger

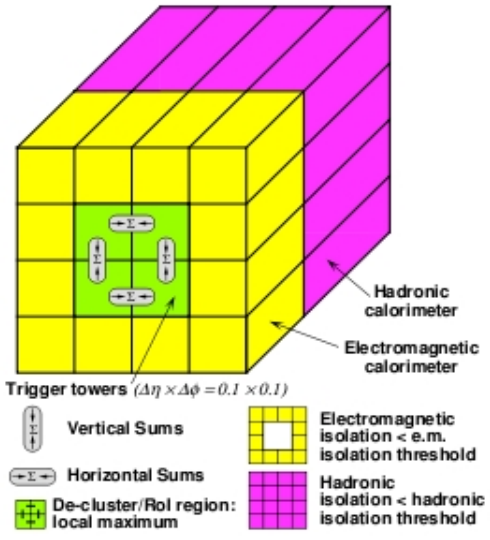

Figure 2.27: The L1 trigger for calorimetric objects in the Electromagnetic calorimeter: the green area represents the RoI cluster, the yellow area is the region used for the isolation requirements, and the pink area is the region used for the hadronic isolation.

no distinction between electrons and photons is possible since they are both identified as "calorimetric objects". In particular the L1 trigger measurement is a real calorimetric measurement even if it is done with reduced granularity (see Figure 2.27): once a relevant amount of energy is detected, the total energy in a little 2×2 cluster is measured (green area), and the isolation with respect to electromagnetic (yellow area) and hadronic activity (pink area, *e.g.* due to electrons coming from heavy quark decay) is computed. If the these three parameters (E_{T}, electromagnetic and hadronic isolation) fullfill the requirements, then the electromagnetic calorimeter is accepted as a good calorimetric object and its RoI is propagated to the L2.

The L2 trigger basically refines the calorimetric measurement, accessing the full granularity of the calorimeters and studying the shape of the energy deposit (e.g. π^0/γ separation), and includes the data of the inner tracking system. At this level a "calorimetric object" may become an electron if an ID track consistent with it is found. Since the measurements are more precise at this level, tighter conditions on the quality and the kinematic features of the electron candidates can be required.

At the end of the chain the EF further refines the measurements performed at the L2 on the electron candidates, running algorithms very similar to the offline ones and having access to the data of all the subdetectors with full granularity.

Figure 2.28 shows the distribution of the difference between the offline and the value measured at different trigger levels of the E/p variables for electrons. This shows how the EF measurement (blue line) is better than the L2 measurement (red line), since the former is allowed to use reconstruction algorithms very similar to the offline ones thanks to the large processing time available (see Figure 2.24), while the latter has to rely on simplified algorithms.

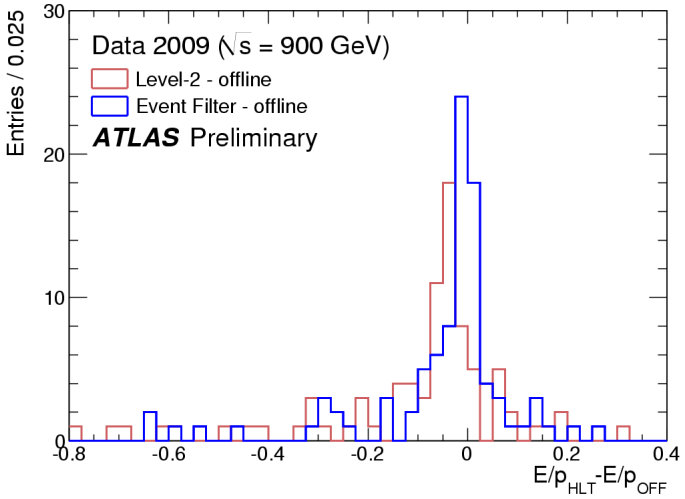

Figure 2.28: E/p distribution found by the HLT and the offline for the electron trigger. The distributions are shown for L2 and EF separately

2.2.6.2 Muon Trigger

The L1 muon trigger relies on the temporal and geometric correlation of the hits left by a muon on the different layers of RPC detectors installed in the muon spectrometer, as shown in Figure 2.29. When a muon coming from the interaction point crosses the RPC detectors, it leaves hits on each of them: starting from the hit on the central station (also known as *pivot* plane, RPC2 in Figure 2.29) a "correlation window" (several windows are opened for several p_{T} thresholds) is opened on the RPC1 layer. If a good hit (i.e. hits in both η and ϕ and in time with the hit on the pivot plane) is found on the RPC1 layer then a low-p_{T} muon candidate is found. The same algorithm is applied using the RPC3 plane to look for high-p_{T} muon candidates. Once a muon candidate is found, the RoI is propagated to the L2.

At the L2 the muon track is reconstructed for the first time: there are algorithms which reconstruct the muon tracks in the ID and in the MS separately and then combine them in order to determine of p_{T}, η and ϕ. At this level the p_{T} measure-

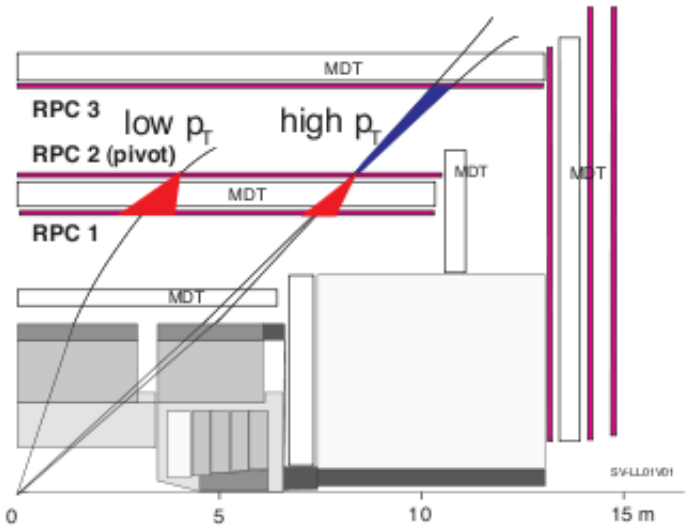

Figure 2.29: L1 muon trigger algorithm: a muon coming from the interaction point leaves hits on the three layers of RPC detectors installed in the muon spectrometer. The position of the different hits is correlated as a function of the muon p_{T}

ment is not done by a fit, but *look-up tables* are used: the p_{T} estimation is done starting from the relation

$$\frac{1}{s} = A_0 \cdot p_{\mathrm{T}} + A_1 \tag{2.8}$$

where s is the sagitta of the muon track and A_0 and A_1 are two constant values needed to take into account the magnetic field and the energy loss in the calorimeters respectively. A look-up table is basically a table whose columns and rows represent the $\eta - \phi$ segmentation of the ATLAS detector, and in each cell a (A_0, A_1) pair is contained. For each muon candidate, given η, ϕ and s, a fast estimation of the p_{T} is possible. This method is used since at the L2 there is not enough time to perform a real fit to precisely measure the track p_{T}. Once the full track is reconstructed (from the ID to the MS), the calorimetric activity around it is measured, in order to apply the isolation requirements.

At the EF the muon reconstruction algorithms perform again the operations performed by the L2 algorithms, but now the full detector with its full granular-

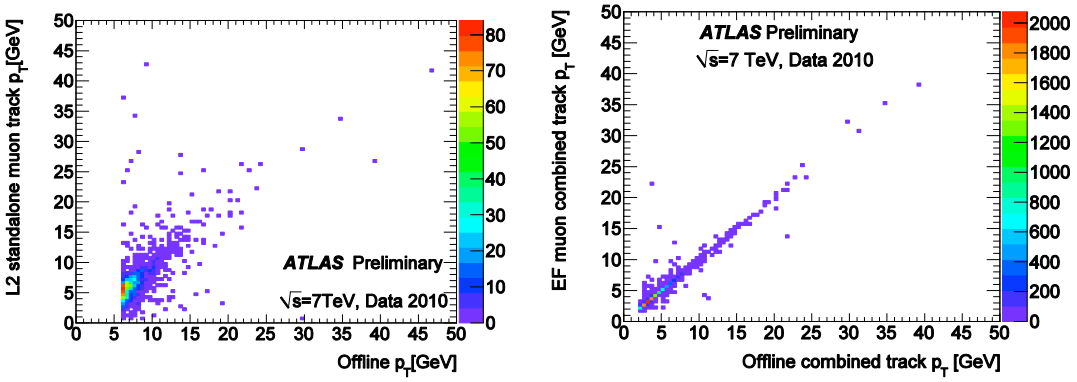

(a) (b)

Figure 2.30: Correlation between the muon p_{T} reconstructed at several trigger levels (level 2 in (a) and event filter in (b)) and the offline reconstruction.

ity can be accessed, and a real fit of the muon track is performed. Figure 2.30 shows the correlation between the muon p_{T} reconstructed at different trigger levels and the offline reconstruction: in Figure 2.30(a) the correlation between the L2 stand alone p_{T} is shown, while in Figure 2.30(b) the correlation between the EF combined p_{T} measurement and the offline one is shown. As can be seen the EF measurement is much more accurate and precise compared to the one performed at L2. The corresponding plot for L1 is not shown since at L1 the muon p_{T} is not really measured, but, as explained above, only a threshold is available.

Chapter 3

Physics objects reconstruction

Reconstruction of pp collisions with the ATLAS detector at the LHC relies on the offline analysis of the recorded events. Through several dedicated algorithms, all particles produced in each collision event can be reconstructed, with the obvious exception of neutrinos which are transparent to the detector. The offline analysis actually permits to fully reconstruct and identify all physical objects produced in the collisions by measuring all observable physical quantities in the laboratory frame, *e.g.* the particles four-momenta.

3.1 Electrons

3.1.1 Electron reconstruction

Electrons are reconstructed in the central region of the ATLAS detector ($|\eta| < 2.47$) as energy deposits (clusters) in the EM calorimeter matched to reconstructed tracks in the inner detector.

3.1.1.1 Electron seed-cluster reconstruction

The first step of the reconstruction procedure is based on the division of the $\eta - \phi$ space of the EM calorimeter into a grid of $N_\eta \times N_\phi = 200 \times 256$ towers of size $\Delta\eta^{tower} \times \Delta\phi^{tower} = 0.025 \times 0.025$, according to the granularity of the EM accordion calorimeter middle layer. Then, the energy of the cells in all longitudinal layers is summed to obtain the energy of the calorimeter tower. A *sliding-window* algorithm [34], with a window size of 3×5 in the $\eta - \phi$ space, is then applied to search for seed clusters with a total cluster transverse energy $E_{\mathrm{T}}^{cluster} > 2.5$ GeV. Finally, a dedicated algorithm is applied to remove cluster duplicates.
Clusters reconstruction in MC simulations shows a very high efficiency for true electrons: about 95% for electrons with a transverse energy E_{T} of 7 GeV and it reaches 99% at $E_{\mathrm{T}} = 15$ GeV and 99.9% at $E_{\mathrm{T}} = 45$ GeV.

3.1.1.2 Electron-track candidate reconstruction

Around the seed cluster barycenter, a region-of-interest (ROI) is defined with a cone-size of $\Delta R = 0.3$ if the cluster passes the loose shower requirements $R_\eta > 0.65$ and $R_{had} < 0.1$, where R_η is the ratio of the energy in the 3×7 cells over the energy in the 7×7 cells around the electron cluster position and R_{had} is the ratio of E_{T} in the hadronic calorimeter to E_{T} of the EM cluster.
Track reconstruction then proceeds in two steps: pattern recognition and track fit. The pattern recognition [35] starts from a seed-track consisting of three hits in different layers of the silicon detector with a transverse momentum $p_{\mathrm{T}} > 1$ GeV. If the seed-track can not be successfully extended to a full track of at least seven hits by using the pion hypothesis for energy loss at material surface but it falls within a EM cluster ROI, then the track is re-analyzed to take into account the hypothesis of a possible energy loss of the electron due to bremsstrahlung.

The track candidate is then fitted either with the pion or the electron hypothesis according to the hypothesis used in the pattern recognition. The final matching of tracks to an EM cluster is realized by requiring either of following two conditions:

- tracks with at least four silicon hits are extrapolated to the middle layer of the EM accordion calorimeter from the point of the closest approach with respect to the primary vertex. The tracks must further satisfy the conditions to be either within 0.2 in ϕ of the EM cluster on the side the track is bending towards or within 0.05 on the opposite side and to be within 0.05 in η of the EM cluster. Tracks with less than four silicon hits (TRT-only) are, instead, extrapolated from the last measurement point and the condition on the η difference between cluster and track is not required, since at this stage their η coordinate is not precisely measured;

- after rescaling the tracks momentum to the measured cluster energy, tracks must satisfy the same requirements as before but the difference in ϕ between cluster and track is lowered to 0.1 value on the side the track is bending towards. This criterion is applied to recover tracks of low momentum that potentially suffered significant energy losses before reaching the calorimeter.

The application of the above procedure defines all electron-track candidates. The track parameters, with the exception of TRT-only tracks, are then re-estimated using an optimized electron track fitter [36]. These tracks are finally used to perform the track-cluster matching to build the electron candidates and to provide information for particle identification.

3.1.1.3 Electron-candidate reconstruction

An electron is reconstructed if at least one track is matched to the seed cluster. The track-cluster matching proceeds as previously described for the electron-track candidate reconstruction but using the re-fitted tracks. Additionally, TRT-only tracks must satisfy a looser condition on track-cluster difference in η and a tighter one in ϕ: $|\Delta\eta| < 0.35$ (0.2) in the barrel (endcap) TRT and $|\Delta\phi| < 0.03$ (0.02) on the (opposite) side the track is bending towards.

The best matched track is chosen as the primary track to determine the kinematics and the charge of the electron and to check the electron identification criteria. To avoid random matches between nearby tracks in case of cascade due to bremsstrahlung, tracks with at least one hit in the pixel detector are preferred. The choice of the best matching track relies on two angular variables in the $\eta - \phi$ plane: the distance ΔR between the cluster barycenter and the extrapolated track in the middle layer of the EM accordion calorimeter and the same distance calculated when the track momentum is rescaled to the measured cluster energy before the extrapolation to the middle layer $\Delta R^{\text{rescaled}}$. Comparing two i and j tracks, if $|\Delta R_i^{\text{rescaled}} - \Delta R_j^{\text{rescaled}}| > 0.01$ then the track with the smaller $\Delta R^{\text{rescaled}}$ is chosen. If $|\Delta R_i^{\text{rescaled}} - \Delta R_j^{\text{rescaled}}| \leq 0.01$ and $|\Delta R_i - \Delta R_j| > 0.01$ then the track with the smaller ΔR is chosen. For all other cases in which both ΔR and $\Delta R^{\text{rescaled}}$ are similar, the track with more pixel hits is chosen as primary track and a hit in the first layer of the pixel detector counts twice to prefer tracks with early hits. All seed clusters matched to a track at least are treated as electron candidates. Each electron cluster is rebuilt in all four layers starting from the middle one by using 3×7 (5×5) cells in $\eta \times \phi$ in the barrel (endcaps) region of the EM accordion calorimeter. The cluster position is adjusted to take into account the deposited energy distribution.

The cluster energy is then determined from the energy in the three layers of the

EM accordion calorimeter by applying a correction factor determined by a linear regression using a multivariate algorithm. The input variables used for both electrons and photons are: the total energy measured in the accordion calorimeter, the ratio of the presampler energy to the accordion one, the shower depth, the pseudo-rapidity of the cluster barycenter in the ATLAS coordinate system and the $\eta - \phi$ positions of the cluster barycenter in the calorimeter coordinate system. Finally, large samples of collected $Z \to ee$ events permit an in-situ energy calibration for data events whereas an energy smearing is applied to simulated events.
In conclusion, the four-momentum of central electrons ($|\eta| < 2.47$) is built by taking the energy from the cluster and the $\eta - \phi$ directions from the corresponding track parameters, with the exception of TRT-only tracks for which $\eta - \phi$ directions are taken from the clusters.

3.1.2 Electron identification

The physics objects built by the electron-candidate reconstruction procedure are not always signal electron, since many background sources can significantly contribute: hadronic jets erroneously reconstructed as electron (*i.e.* fake electrons) as well as real electrons coming from photon conversions, Dalitz decays and semi-leptonic decays of heavy flavor hadrons. Thus, electron identification procedures aim to maximize the electron background rejection while keeping a high selection efficiency for signal electrons. The electron identification in ATLAS is based, in the $|\eta| < 2.47$ central region, on discriminating variables which are used in both sequential cuts and multivariate analysis (MVA) methods: the longitudinal and transverse shapes of the electromagnetic showers in the calorimeters, the track properties in the inner detector and the matching quality between tracks and energy clusters.

3.1.2.1 Cut-based identification

The cut-based identification procedures are defined by a set of cuts on discriminating variables. Going from *loose* to *medium* and to *tight* identification qualities, the number of the discriminating variables used increases and the cuts are tightened with respect to the looser selections. Furthermore, in 2012 a new operating point, called *multilepton*, has been added to optimize the selection of low energy electrons in the $H \to ZZ^* \to 4\ell$ analysis, with a similar efficiency to the *loose* identification quality but with a better background rejection.

3.1.2.2 Likelihood identification

Multivariate analysis (MVA) methods combine the evaluation of several properties to make a selection decision. In ATLAS, the MVA identification procedure is based on the electron likelihood (LH) because of its simple construction and interpretation. The LH is constructed using the signal and background probability density functions (PDFs) of the discriminating variables on which an overall probability for the object to be signal or background is evaluated. Then, signal and background probabilities for a given electron candidate are combined into a discriminant on which a cut is applied. The PDFs for signal and background used in the electron LH identification are obtained from data and the LOOSE, MEDIUM and VERY TIGHT LH selections are designed to roughly match the electron efficiencies of *multilepton*, *medium* and *tight* cut-based selections. The LH discriminant for the different LH identification qualities are constructed using different sets of variables. For example, the LOOSE LH uses variables mostly useful to reject light-flavor jets, whereas MEDIUM and VERY TIGHT operating points use ad-

ditional variables to further reject heavy-flavor jets and electrons from conversions.

3.1.2.3 Electron isolation

In order to enhance the rejection of hadronic jets mis-identified as electrons, in addition to the identification procedure described above, an isolation requirement is imposed in many analyses and can be calorimeter or track based:

- calorimetric isolation is imposed with a cut on the sum of the transverse energy deposited in the calorimeter cells in a cone of ΔR around the electron $E_{\mathrm{T}}^{\mathrm{cone}}$, excluding the contribution within $\Delta\eta \times \Delta\phi = 0.125 \times 0.175$ around the electron cluster barycenter. Furthermore, the E_T^{cone} variable is corrected for energy leakage from the electron to the isolation cone and for effect of pile-up events;

- track isolation is imposed with a cut on the sum of the transverse momentum of the tracks with $p_{\mathrm{T}} > 0.4$ GeV in a cone of ΔR around the electron $p_{\mathrm{T}}^{\mathrm{cone}}$, excluding the contribution of the electron track itself. Furthermore, the $p_{\mathrm{T}}^{\mathrm{cone}}$ variable is constructed using the tracks that come from the primary vertex associated to the electron track and they must have at least nine silicon hits, one of which in the innermost pixel layer.

3.1.3 Reconstruction and Identification efficiencies

The reconstruction and identification efficiencies of central region electrons in the ATLAS detector are determined with a tag-and-probe method. Reconstruction efficiencies are measured for electrons from $Z \to ee$ decays whereas identification efficiencies are estimated by combining measurements from $J/\psi \to ee$ and $Z \to ee$ decays using data-to-MC efficiency ratios. Figure 3.1 shows the combined effi-

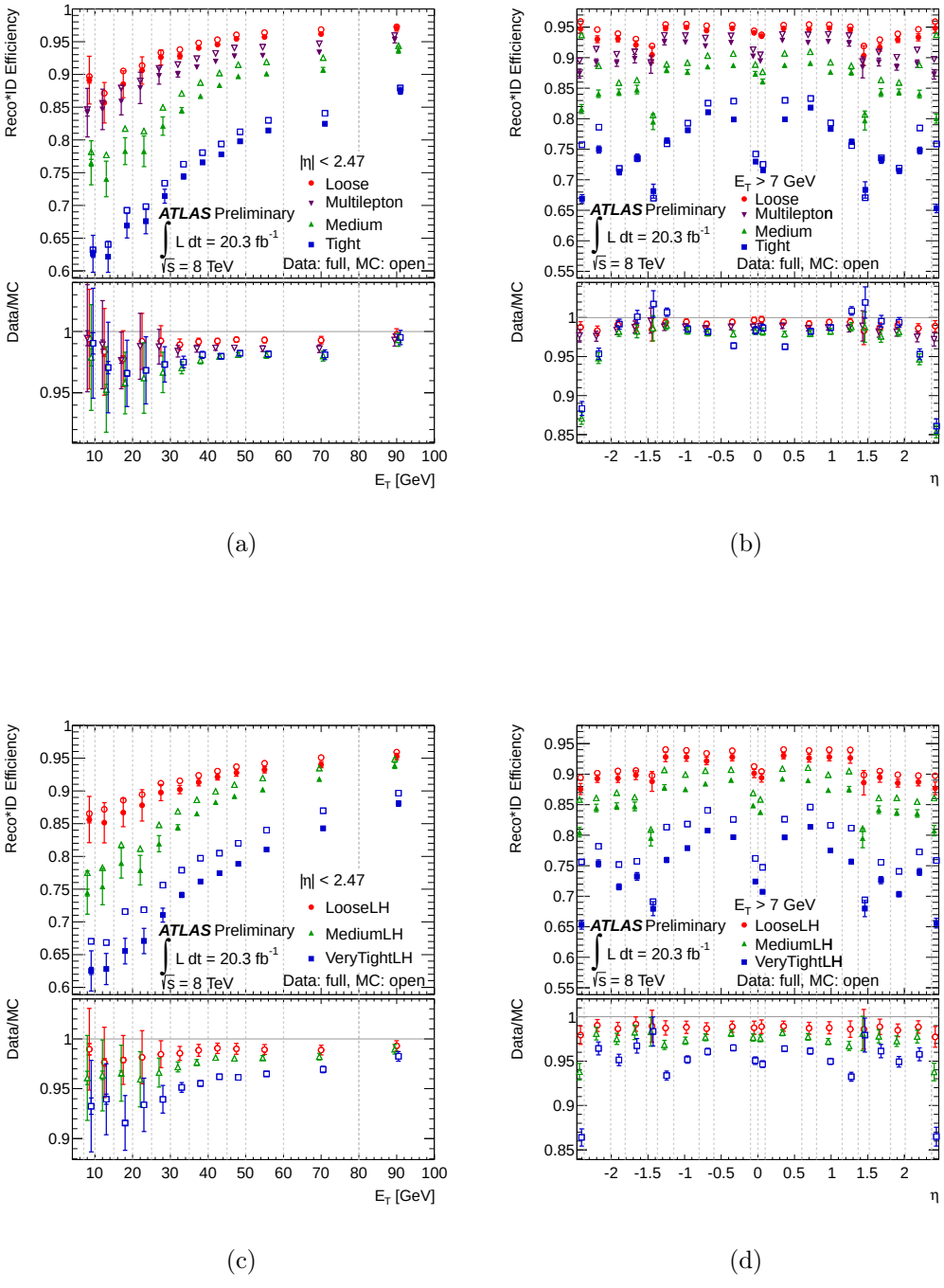

Figure 3.1: Measured combined reconstruction and identification efficiency as a function of E_{T} (left) and η (right) for the cut-based *loose*, *multilepton*, *medium* and *tight* selections (up) and for the LOOSE LH, MEDIUM LH and VERY TIGHT LH selections (bottom), compared to MC expectation for electrons from $Z \to ee$ decay. The lower panel shows the data-to-MC efficiency ratios. The data efficiency is derived from the measured data-to-MC efficiency ratios and the MC prediction for electrons from $Z \to ee$ decays. The uncertainties are statistical (inner error bars) and statistical+systematic (outer error bars).

ciencies to reconstruct and identify electrons with respect to reconstructed energy clusters in the electromagnetic calorimeter for all identification operating points. The efficiencies are shown as a function of E_{T} and η. The measured data-to-MC correction factors are applied to a simulated $Z \to ee$ sample. The resulting efficiencies correspond to the measured data efficiencies and can be compared to the efficiencies of simulated electrons in $Z \to ee$ events. For electrons below $E_{\mathrm{T}} < 15$ GeV, the reconstruction efficiency cannot be measured and is taken instead from MC simulation.

Using the full 2012 dataset of 8 TeV *pp* collision data, corresponding to 20.3 fb^{-1} of integrated luminosity, the electron reconstruction efficiency averaged on η is about 97% for electrons with $E_{\mathrm{T}} = 15$ GeV and reaches about 99% at $E_{\mathrm{T}} = 50$ GeV at $E_{\mathrm{T}} = 50$ GeV. For electrons with $E_{\mathrm{T}} > 15$ GeV the efficiency varies from 99% at low η to 95% at high η. Because of the overwhelming background contamination of the sample, the reconstruction efficiency is not measured below 15 GeV. Finally, the uncertainty on the reconstruction efficiency is below 0.5% for $E_{\mathrm{T}} > 25$ GeV, and between about 0.5 - 1.5 % at lower transverse energies.

The averaged identification efficiency for electrons with $E_{\mathrm{T}} > 15$ GeV lies between 96% for cut-based *loose* selection and 78% for VERY TIGHT LH selection, with strong dependences on E_{T} and, for the tighter operating points, on η. The total uncertainties on the identification efficiency are about 5-6% (1-2%) for electrons below (above) $E_{\mathrm{T}} = 25$ GeV.

The measured data-to-MC efficiency ratios are close to unity, with deviations larger than a couple of percent occurring only for low E_{T} or high η regions, and they are applied as scale factors in analyses.

3.2 Muons

3.2.1 Muon reconstruction and identification

Muons produced in pp collisions are reconstructed in the ATLAS detector using the informations from the muon spectrometer (MS) and from the inner detector (ID) and, to a lesser extent, from the calorimeter. In the MS, tracks are reconstructed in two steps: first local track segments are searched for within each layer of spectrometer and then a full MS track is constructed by combining all track segments from different layers. The ID provides an independent measurement of the muon track close to the interaction point constructed by combining hits within the pixel layer, the SCT and the TRT. Furthermore, the muons pass through the material between the interaction point and the MS, consisting mostly of calorimeters, and the information on energy losses can be added to the muon reconstruction chains. Muon identification is performed by applying several reconstruction criteria, depending on the available informations from the MS, the ID and the calorimeter system. Four muon reconstruction families are defined:

- Combined (CB) muons represents the main reconstruction and the highest muon purity type. Track reconstruction is independently performed in the MS and the ID, then a combined track is built from the matching of a MS track to an ID track;

- Segment-tagged (ST) muons are used to increase the acceptance when the muon crosses only one MS layer either because of its low p_T or because it falls in a region with a reduced MS acceptance. If an ID track extrapolated to the MS matches to at least one local segment in the MDT or CSC chambers of MS, then a muon tracks is built;

- Calorimeter-tagged (CaloTag) muons are used to recover acceptance in the

uninstrumented regions of the MS, representing the muon family with the lowest purity value. If an ID track matches a energy deposit in the calorimeter compatible with a minimum ionizing particle, then the track is classified as a muon track. Anyway, this type identification criteria are optimized for a pseudorapidity region of $|\eta| < 0.1$ and for a transverse momentum range of $25 \lesssim p_{\mathrm{T}} \lesssim 100$ GeV;

- Stand-Alone (SA) muons are used to extend the acceptance to the $2.5 < |\eta| < 2.7$ pseudorapidity range which is not covered by the ID, if they traverse at least two layers of MS chambers. Thus, the muon track is reconstructed only in the MS and the track parameters are determined by extrapolating the trajectory back to the closest point of approach to the beam line.

The reconstruction of CB, ST and SA muons, which uses the MS informations, is performed by following two different strategies [37] for both the muon reconstruction in the MS and the ID-MS matching. The first reconstruction chain, called *Staco*, performs a statistical combination of the track parameters of the MS and ID muon tracks using the corresponding covariance matrices. The second chain, called *MuId*, performs a global fit of the muon track using the hits from both the ID and the MS layers.

In addition to the described reconstruction chains, some quality requirements on the ID tracks are imposed to ensure a good track reconstruction: at least one Pixel hits, at least 5 SCT hits, at most 2 active Pixel or SCT sensors traversed by the track but without hits and at least 9 TRT hits in the region of full TRT acceptance ($0.1 < |\eta| < 1.9$).

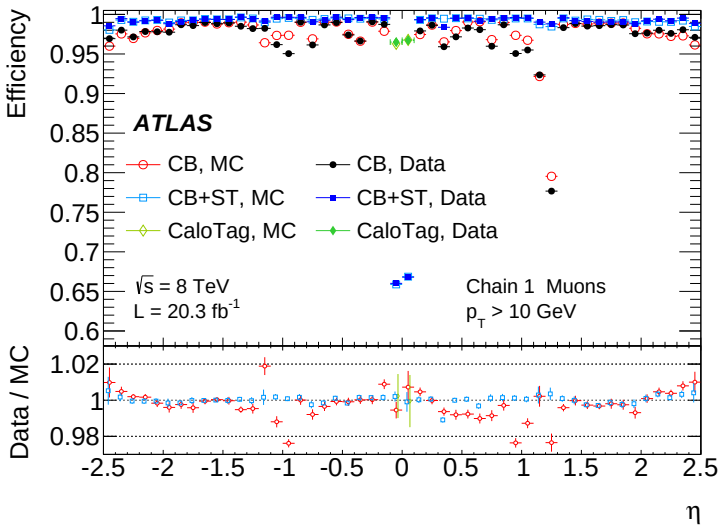

Figure 3.2: Muon reconstruction efficiency as a function of η measured in $Z \to \mu\mu$ events for muons with $p_{\mathrm{T}} > 10$ GeV and different muon reconstruction types. CaloTag muons are only shown in the region $|\eta| < 0.1$, where they are used in physics analyses. The error bars on the efficiencies indicate the statistical uncertainty. The panel at the bottom shows the ratio between the measured and predicted efficiencies. The error bars on the ratios are the combination of statistical and systematic uncertainties.

3.2.2 Reconstruction and identification efficiencies

The muon reconstruction efficiency in the ATLAS detector are determined with a tag-and-probe method applied to $Z \to \mu\mu$ and $J/\psi \to \mu\mu$ samples, using the independent measurements of both the ID and MS in the $|\eta| < 2.5$ region. Data-to-MC ratios from $Z \to \mu\mu$ sample are instead used in the $2.5 < |\eta| < 2.7$ region where SA muons only provide a large efficiency.

Figure 3.2 shows the muon reconstruction efficiency as a function of η as measured from $Z \to \mu\mu$ events. Figure 3.3 shows the reconstruction efficiencies for CB, CB+ST, CaloTag and CB+SA muons as a function of the transverse momentum. Using data from LHC pp collision data at $\sqrt{s} = 7-8$ TeV, the muon reconstruction efficiency is close to 99% over most the pseudorapidity range of $|\eta| < 2.5$ and for $p_{\mathrm{T}} > 10$ GeV with a precision at the 1‰ level. The muon momentum scale has

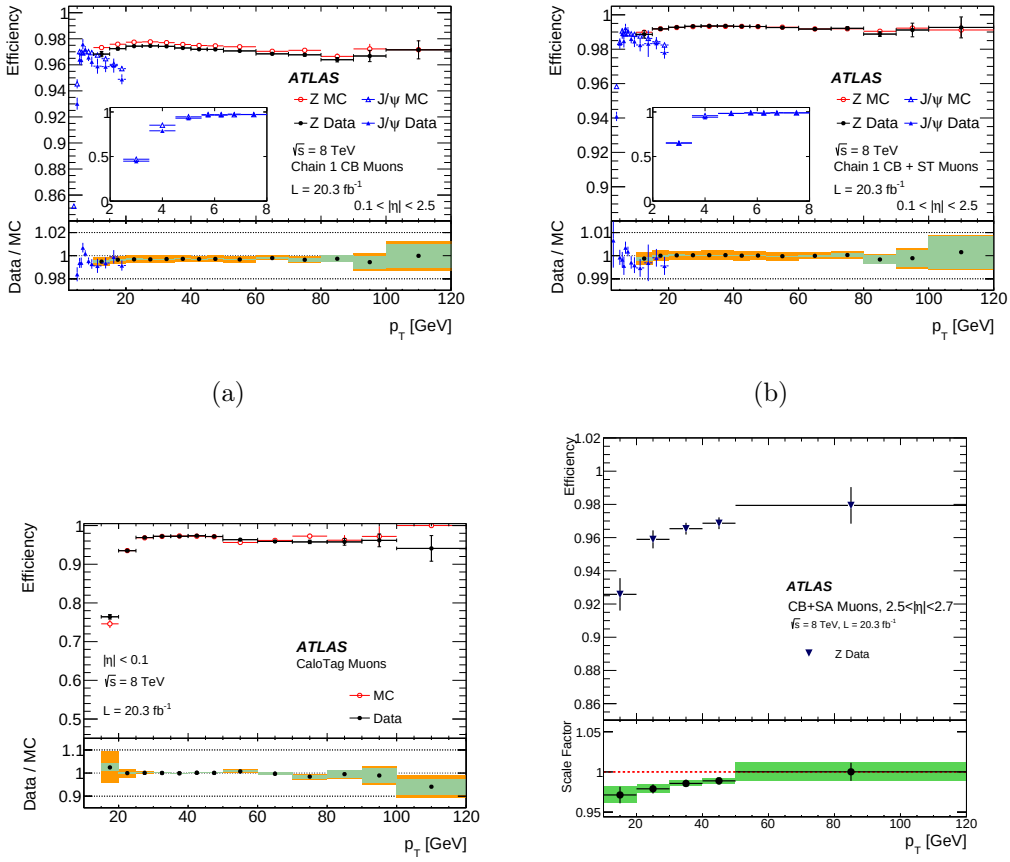

Figure 3.3: Reconstruction efficiency for CB (a), CB+ST (b), CaloTag (c) and CB+SA (d) muons as a function of the p_{T} of the muon, for muons with $0.1 < |\eta| < 2.5$ for CB and CB+ST muons, for $|\eta| < 0.1$ for CaloTag muons and for $2.5 < |\eta| < 2.7$ for CB+SA muons. The upper plots also show the result obtained with $Z \to \mu\mu$ and $J/\psi \to \mu\mu$ events. The inserts on the upper plots show the detail of the efficiencies as a function of p_{T} in the low p_{T} region. The CaloTag (c) and CB+SA (d) muon efficiencies are only measured with $Z \to \mu\mu$ events. The error bars on the efficiencies indicate the statistical uncertainty for $Z \to \mu\mu$ and include also the fit model uncertainty for $J/\psi \to \mu\mu$. The panel at bottom in (a), (b) and (c) plots shows the ratio between the measured and predicted efficiency, the green areas show the pure statistical uncertainty, while orange areas also include systematic uncertainties. In the (d) plot, the efficiencies are obtained as the product of scale factor, shown in the lower panel, and the MC efficiency. The error bars correspond to the statistical uncertainty while the green shaded band corresponds to the statistical and systematic uncertainty added in quadrature.

been studied using large calibration sample of $J/\psi \to \mu\mu$, $\Upsilon \to \mu\mu$ and $Z \to \mu\mu$ to correct the MC simulation improving the data-MC agreement. The uncertainties on the CB muons momentum scale is of 0.05% for $|\eta| < 1$ which increases to $\lesssim 0.2\%$ for $|\eta| > 2.3$. The dimuon mass resolution is $\approx 1.2\%$ (2%) at low-p_{T} increasing to $\approx 2\%$ (3%) at $p_{\mathrm{T}} \approx 100$ GeV for $|\eta| < 1$ ($|\eta| > 1$), with a relative uncertainties of 3% to 10% depending on η and p_{T}.

3.3 Jets

Jets are collimated sprays of energetic hadrons and they are the dominant final state objects of *pp* collisions at LHC. A jet is detected as a group of topologically-related energy deposit in the ATLAS calorimeters. The first step of jet reconstruction is the clustering of energy deposits in *topological clusters* subsequently clustered into a jet using either the anti-k_t [38], the k_t or the Cambridge/Aachen (C/A) [39, 40] jet algorithms. The jet clustering algorithm can be also applied to other inputs such as inner detector tracks associated with charged particles.
The jet energy is calibrated applying a jet energy scale (JES) estimated from truth jets, which are created from stable interacting particles in MC using the same clustering algorithm. Furthermore, the calibration has to account for several effects such as the different scales of the energy measured from hadronic and electromagnetic showers, dead material, calorimeter leakage, out of calorimeter jet, energy deposits below noise thresholds and energy deposits from pile-up events.
The jet calibration is derived using a combination of methods based on both MC simulations and data-driven techniques and the uncertainty on this scaling in data is one of the major systematics in physics analyses of hadronic decay channels.

3.3.1 Jet reconstruction

Jet are reconstructed using a clustering algorithm which is able to group energy deposits produced in the hadronization process of a single parton. Indeed, due to confinement, quarks and gluons can not exist as single particle and a clustering method is necessary to reconstruct their four-momentum.

Clustering algorithms A general description of clustering algorithms starts by introducing distances between two i and j entities d_{ij} (particles, pseudojets) and between entity i and the beam (B) d_{iB}, that are defined as:

$$\begin{aligned} d_{ij} &= min\left(k_{t,i}^{2p}, k_{t,j}^{2p}\right)\frac{\Delta_{ij}^2}{R^2} \\ d_{iB} &= k_{t,i}^{2p} \end{aligned} \tag{3.1}$$

where $\Delta_{ij}^2 = (y_i - y_j)^2 + (\phi_i - \phi_j)^2$ and $k_{t,i}$, y_i, ϕ_i are respectively the transverse momentum, the rapidity and the azimuthal angle of i entity. Furthermore, the R parameter represents the radius of the jet cone whereas the p parameter governs the relative power of the energy with respect to the geometrical scale Δ_{ij}.The inclusive clustering algorithm then proceeds by identifying the smallest of the distances d_{ij} and if it is a d_{ij} recombining i and j entities whereas if it is d_{iB} calling i a jet and removing it from entities list. The distances are then recalculated and the procedure repeated until no entities are left. Depending on the choice of p parameter in Eq.(3.1), different algorithm can be defined: the $p = 1$ choice corresponds to the k_t algorithm which tends to cluster soft entity first; the $p = 0$ choice, instead, corresponds to the Cambridge/Aachen (C/A) algorithm which clusters the nearest particles regardless of the entity transverse momentum; the choice of $p = -1$, finally, corresponds to the anti-k_t algorithm which favors hard entities to construct the clusters.

In ATLAS, jets are reconstructed using the anti-k_t algorithm [38] with a radius parameter R of 0.4, 0.6 or 1.0, or the Cambridge/Aachen (C/A) algorithm [39, 40] with radius parameter $R = 1.2$ using the FastJet software [41]. The inputs to the jet algorithm are either stable simulated "truth" particles, energy deposits in the calorimeter or tracks in the inner detector, and the resulting jets are called respectively *truth jets*, *calorimeter jets* or *track jets*.

Truth jets are reconstructed applying the same algorithm as calorimeter jets to simulated truth particles with a lifetime greater than 30 ps, excluding muons and neutrinos.

Track jets, instead, are built using inner detector tracks which are reconstructed within the full acceptance of the ID ($|\eta| < 2.5$) by applying a sequence of algorithm to build tracks from individual hits [42]. The baseline algorithm uses 3-point seeds in the silicon detectors (Pixel and SCT) to form track candidates, subsequently extrapolated to include TRT measurements. Furthermore, tracks are required to have a transverse momentum of at least 400 MeV besides further requirements on impact parameters and number of hits in the different ID layers.

Finally, the inputs to calorimeter jets are topological clusters of adjacent calorimeter cells, called *topocluster*, that contain a significant energy signal above the noise threshold [34, 43]. *Topoclusters* are treated as massless particles and are assumed to originate from the geometrical center of the detector. Initially, *topoclusters* are reconstructed at the electromagnetic scale (EM scale) [44,45], which correctly measures the calorimeter energy deposits of particles produced in the electromagnetic showers. The EM scale clusters collection are subsequently calibrated to account for the response of calorimeter hadrons by using a local cluster weighting (LCW) method: firstly clusters are classified as electromagnetic or hadronic; then the energy falling outside clustered cells is estimated from how isolated the cluster is; finally, the amount of energy falling in inactive detector regions is estimated from

the position and the energy deposited in each layer of the calorimeter [43]. LCW corrections are determined from MC simulations of charged and neutral pions.
At a first level, the jet flavor is assigned searching for the highest energy parton that points to the jet, *i.e.* with $\Delta R < 0.4$ (0.6) for jets with $R = 0.4$ (0.6). Anyway, jets identified as originating from heavy quarks (c and b quarks) are considered separately from jets originating from light quarks or gluons.

3.3.2 Jet Energy Calibration

The calibration of the jet energy can be divided in several steps: first the jet is corrected to point back to the correct vertex; next the effect of the pile-up is removed using an area based subtraction process; the energy is then calibrated by applying the jet energy scale (JES) derived from MC; finally, a global sequential correction (GSC) is applied to reduce the difference in response between gluon and quark initiated jets and to correct for jets which are not fully contained in the calorimeter.

3.3.2.1 Origin correction

Since the ATLAS calorimeters measure the energy of particles, topoclusters require to be assigned a direction to complete the corresponding four-vector. The jet reconstruction starts assuming that the jet points at the center of the detector, although the assumption that the jet originates from the "first primary vertex" is subsequently considered. Thus, an origin correction is applied to jets by finding the energy center of the jet and then modifying the jet 4-vector such that the energy is unchanged but the direction is actually consistent with the primary vertex.

3.3.2.2 Pile-up correction

The effects of pile-up on jet calibrations are reduced using an area based subtraction method [46]. The pile-up subtraction procedure is based on the pile-up energy density ρ in the $\phi \times \eta$ plane and the area of the jet A in the same plane. The event energy density ρ is estimated from the median energy density, defined for each jet as p_{T}/A, of all jets reconstructed in the central region $|\eta| < 2.0$ using a k_t ($R = 0.4$) reconstruction algorithm. A residual dependence of jet p_{T} on pile-up is then reduced by applying a correction parameterized in terms of the number of primary vertices N_{PV} and the average number of interactions per bunch crossing $\langle\mu\rangle$ to capture both in-time (N_{PV}) and out-of-time ($\langle\mu\rangle$) pile-up dependences. The residual corrections are derived by fitting the dependence on N_{PV} ($\langle\mu\rangle$) at fixed values of $\langle\mu\rangle$ and by averaging the gradients for different fixed $\langle\mu\rangle$ (N_{PV}). The final pile-up subtracted $p_{\mathrm{T}}^{\mathrm{corr}}$ is therefore given by:

$$p_{\mathrm{T}}^{\mathrm{corr}} = p_{\mathrm{T}}^{\mathrm{const}} - \rho \times A - \alpha \times (N_{PV} - 1) - \beta \times \langle\mu\rangle \tag{3.2}$$

where α and β are jet size and algorithm dependent constants derived from MC and $p_{\mathrm{T}}^{\mathrm{const}}$ is the jet p_{T} at the topocluster scale.

3.3.2.3 Jet Energy Scale

The jet energy scale (JES) is derived as a correction which relates the reconstructed jet energy to the truth jet energy [43]. The JES factors are derived from isolated jets, i.e. no other reconstructed (truth) jets with $p_{\mathrm{T}} > 7$ GeV ($p_{\mathrm{T}}^{\mathrm{truth}} > 7$ GeV) at the uncalibrated scale within a cone of $\Delta R = 1.5 \times R$ ($\Delta R = 2.5 \times R$), from an inclusive jet MC sample after the application of pile-up and origin corrections. A ΔR matching method is used to compare reconstructed calorimeter jets to truth particle jets in simulation. Calorimeter jets are required to geometrically match the truth jets within a given angular distance $\Delta R = 0.3$ of the calorimeter jet axis.

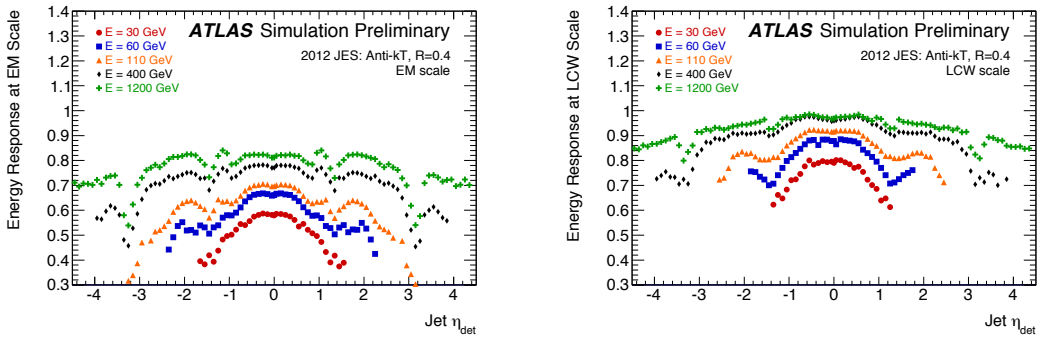

(a) EM scale (b) LCW scale

Figure 3.4: Energy response as a function of η_{det} (the η of the jet relative to the geometric centre of the detector) for EM (a) and LCW (b) scale anti-k_t, $R = 0.4$ jets before calibration

Matching is performed in order of decreasing reconstructed jet p_{T}, discarding jets that have already been matched; ambiguities are resolved by choosing the truth jet with the highest p_{T} as the match. The jet response is then defined using the associated particle jet kinematics and is defined as:

$$\mathcal{R} = \left\langle \frac{p_{\mathrm{T}}^{\mathrm{jet}}}{p_{\mathrm{T}}^{\mathrm{truth}}} \right\rangle \tag{3.3}$$

and the jet calibration is defined as the inverse of the average energy response. An additional correction in purely the angle of the jet is then applied to resolve a residual bias in the η distribution with respect to the truth jets. Figure 3.4 shows the average energy response as a function of the pseudorapidity η_{det} of the jet relative to the geometric centre of the detector.

3.3.2.4 Global Sequential Correction

After the application of the corrections described above, there is still a difference between the closure of quark and gluon initiated jets, as defined by angular match-

ing to patrons in MC, whereby a difference of up to 8% is observed between the corresponding response values [47]. The p_{T} closure is defined by the fit of a Gaussian function to the reconstructed jet p_{T} divided by the truth p_{T} after calibration and the reduction of the difference between the jet responses of quarks and gluons is important to improve both jet resolution and jet energy scale uncertainties. The corrections are sequentially applied depending on the topology of energy deposits in the calorimeter, tracking and muon spectrometer informations but keeping the mean jet energy response unchanged. The five stages correct the jet energy based on, in order:

- the fraction of energy deposited in the first layer of the tile calorimeter;
- the fraction of the energy deposited in the third layer of the electromagnetic calorimeter;
- the number of tracks with $p_{\mathrm{T}} > 1$ GeV associated to the jet;
- the p_{T}-weighted transverse width of the jet measured using tracks with $p_{\mathrm{T}} > 1$ GeV associated to the jet;
- the amount of activity behind the jet as measured in the muon spectrometer.

Only the track-based and muon spectrometer correction steps are applied to LCW calibrated jets, as calorimeter calibrations have already been included in the local calibration weighting.

3.3.2.5 In-situ jet energy calibration

Following the MC-based calibration of jets, in-situ techniques employing the balance of physics objects in the transverse plane are used in the final stage of the JES calibration. The transverse momentum p_{T} of reference objects, *i.e.* photons,

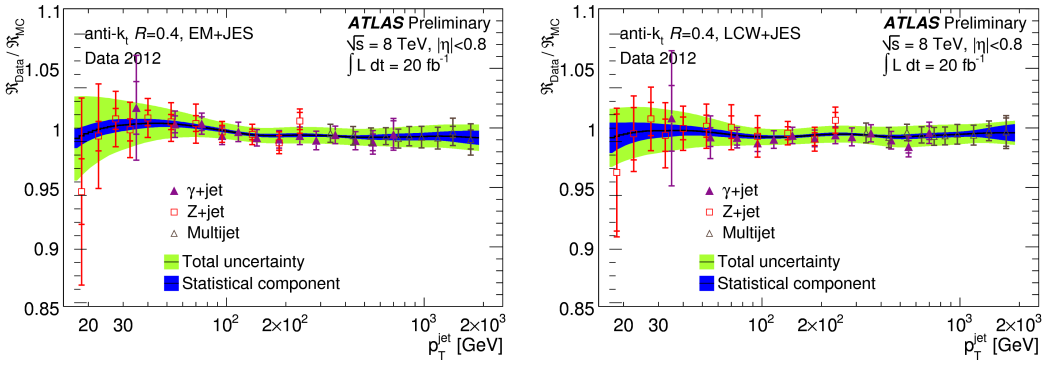

(a) EM+JES (b) LCW+JES

Figure 3.5: Ratio of response measured in data to response measured in data for Z+jet, γ+jet and multijet balance in-situ analyses. Also shown is the combined correction (black line) with its associated uncertainty (green band).

Z bosons or other jets, and the jets being calibrated are compared in both data and MC simulation to measure the ratio:

$$\frac{\mathcal{R}_{\text{data}}}{\mathcal{R}_{\text{MC}}} = \frac{\left\langle \frac{p_{\text{T}}^{\text{jet}}}{p_{\text{T}}^{\text{ref}}} \right\rangle_{\text{data}}}{\left\langle \frac{p_{\text{T}}^{\text{jet}}}{p_{\text{T}}^{\text{ref}}} \right\rangle_{\text{MC}}} \tag{3.4}$$

which defines a residual correction applied to jets reconstructed in data. Firstly, dijet events are employed to apply an η-intercalibration [48] in which the average p_{T} for forward jets ($0.8 \leq |\eta| < 4.5$) is equalized to the p_{T} of balancing jets in the central region ($|\eta| < 0.8$). Generally, the η-intercalibration correction factors are below 2%. The balance of the Z bosons and photons recoiling against jets is then used to derive in-situ JES corrections for jets with $|\eta| < 0.8$ and with $20 \leq p_{\text{T}} \leq 200$ GeV (Z+jet) and $30 \leq p_{\text{T}} \leq 800$ GeV (γ+jet). Finally, high-p_{T} jets are calibrated using a multi-jet events in which a system of low-p_{T} jets recoil against a single high-p_{T} jet (multijet balance) [48], covering a range of $300 \leq p_{\text{T}} \leq 1700$ GeV. The observed response agrees in MC and data at the 1% level across the p_{T} range from 20 GeV up to 2000 GeV and the divergence of the response from unity in the three methods defines the in-situ calibration which is applied to jets in data.

3.3.3 Jet Energy Resolution

The precision of the measurement of the jet energy is as important as the central value of the jet energy scale. The jet energy resolution (JER) is parameterized as a function of three terms [49]:

$$\frac{\sigma\left(p_{\mathrm{T}}\right)}{p_{\mathrm{T}}} = \frac{N}{p_{\mathrm{T}}} \oplus \frac{S}{\sqrt{p_{\mathrm{T}}}} \oplus C \tag{3.5}$$

where N parameterizes the effect of both electronic and pile-up noise, S the stochastic effect related to the sampling nature of calorimeters and C is a p_{T} independent constant term. The JER is measured in MC in the same way as the closure of the jet energy response, by taking the ratio of σ_R width to the R mean value of a gaussian fit to the jet energy response distribution over $\pm 1.5\ \sigma$, where σ is the RMS of the gaussian fit. Figure 3.6 shows the individual measurements of the resolution in the central region. For data, the noise term in Equation (3.5) is estimated using two independent methods, *i.e.* from random cones in data collected exactly one turn after a high-p_{T} level 1 calorimeter trigger and from the distribution of soft jet momenta, subsequently combined to estimate the noise term in the jet energy resolution. The final JER parameters are determined from the measurements of the width of dijet balance and the vector boson plus jet balance combined by fitting the function in Equation 3.5.

3.4 *b*-tagging

The ability to identify the flavor of a jet, separating a b jet from c and light-flavor jets (u, d, s and g originated jets), is a crucial tool in many physics analyses [50]. Various b-tagging algorithms have been developed in ATLAS to achieve high b-tagging efficiencies for real b jets whilst keeping the misidentification efficiency

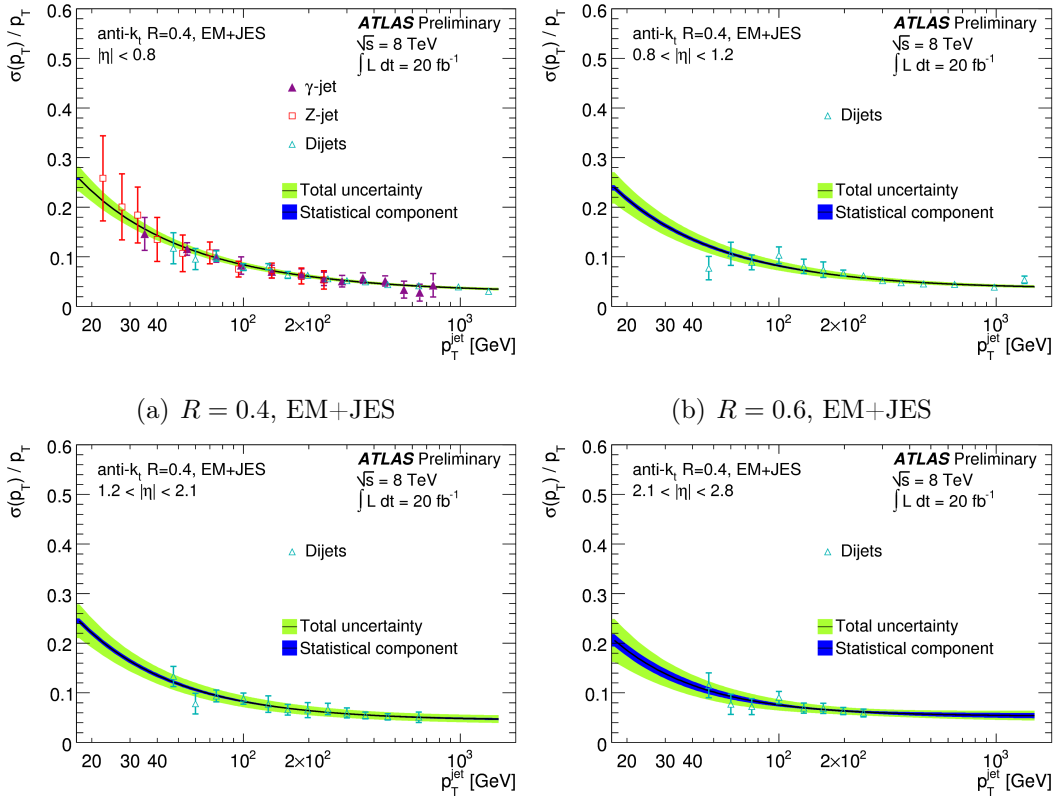

(a) $R = 0.4$, EM+JES

(b) $R = 0.6$, EM+JES

(c) $R = 0.4$, LCW+JES

(d) $R = 0.6$, LCW+JES

Figure 3.6: The jet resolution as a function of p_{T} for the four different jet collections in the central region. The three in-situ inputs to the measurement are shown displaying the compatibility between the measurements. The final fit using the function in Equation 3.5 is included with its associated statistical and total uncertainty.

for c and light-flavour jets at a low level. They range from a relatively simple algorithms based on impact parameters (IP3D) and secondary vertices (SV1) to a more refined algorithm exploiting the topology of weak b and c hadrons decays (JetFitter) [51]. The most discriminating variables resulting from these algorithms are combined in an artificial neural network, and output weight probabilities are evaluated separately for b, c and light-flavor jets. Finally, a multivariate tagging algorithm (MV1) based on these probabilities is used to further enhance the tagging performance.

3.4.1 Lifetime-based tagging algorithms

The lifetime-based tagging algorithms take advantage of the relatively long lifetime of hadrons containing a b quark, which is of the order of 1.5 ps ($c\tau \sim 450$ μm). For example, a b hadron with $p_{\mathrm{T}} = 50$ GeV will have a significant mean flight path length $\langle l \rangle = \beta\gamma c\tau$, traveling on average about 3 mm in the transverse direction before decaying and therefore leading to topologies with at least one vertex displaced from the primary vertex. Two classes of algorithms aim at identifying such topologies. A first class, represented by the IP3D algorithm, is based on an inclusive approach that consists of using the impact parameters of charged-particle tracks from the b-hadron decay products. The transverse impact parameter d_0 is the distance in the $r-\phi$ projection of closest approach of the track to the primary vertex point. The longitudinal impact parameter z_0 is the difference between the z coordinates of the primary vertex position and of the track at the point of closest approach in $r-\phi$. The tracks from b-hadron decay products tend to have large impact parameters which can be distinguished from tracks directly produced in the primary vertex. The second class is based on the explicit reconstruction of the displaced vertices and two algorithms use this approach: the SV1 algorithm attempts to reconstruct an inclusive secondary vertex whereas the JetFitter algorithm aims at reconstruction the complete b-hadron decay chain. Finally the results of these algorithms are combined in the MV1 tagger to improve the light-flavor jets rejection and to increase the range of b-jet tagging efficiency.

3.4.1.1 Impact parameter-based algorithms

For the tagging itself, the impact parameters of tracks are computed with respect to the selected primary vertex. Since the decay point of the b hadron must lie along

its flight path, the transverse impact parameter is signed to further discriminate the tracks from b-hadron decay from tracks originating from the primary vertex: the sign is defined as positive if the track intersects the jet axis in front of the primary vertex, and as negative if the intersection lies behind the primary vertex. The jet axis is defined by the calorimeter-based jet direction, but if an inclusive secondary vertex is found the jet direction is replaced by the direction of the line joining the primary and the secondary vertices.

The IP3D algorithm relies on both the transverse d_0 and longitudinal z_0 impact parameters, as well as their correlation. It is based on a log-likelihood ratio (LLR) method in which for each track the measurement $S \equiv \left(\frac{d_0}{\sigma_{d_0}}, \frac{z_0}{\sigma_{z_0}}\right)$ is compared to pre-determined two-dimensional probability density functions (PDFs) obtained from simulation for both the b and light-flavor jet hypotheses. The ratio of probabilities defines the track weight. The jet weight is the sum of the logarithms of the individual track weights.

3.4.1.2 Vertex-based algorithms

To further increase the discrimination between b jets and light-flavor jets, an inclusive vertex formed by the decay products of the b hadron, including the products of the possible subsequent charm hadron decay, is used. The algorithm starts from all tracks that are significantly displaced from the primary vertex and associated with the jet, and forms vertex candidates for tracks pairs with vertex fit $\chi^2 < 4.5$. Vertices compatible with long-lived particles or material interaction are rejected: the invariant mass of the track four-momenta is used to reject vertices that are likely to originate from K_s, Λ decays and photon conversions, while the position of the vertex in the $r - \phi$ projection is compared to a simplified description of the innermost pixel layers to reject secondary interactions in the detector material.

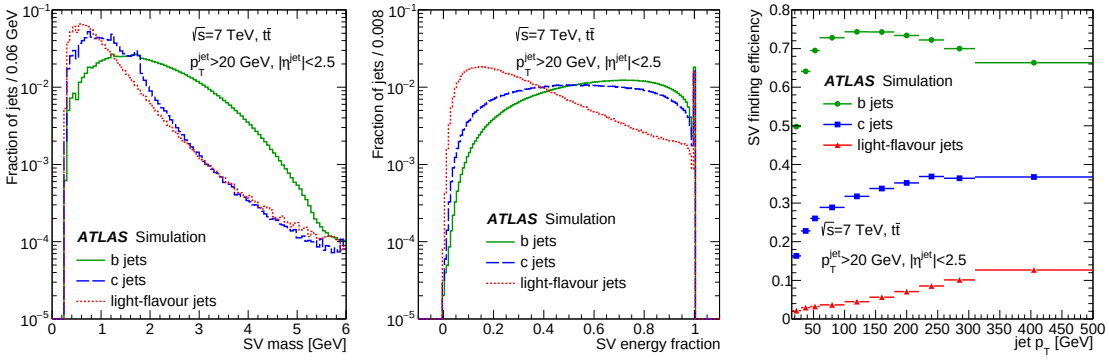

(a) (b) (c)

Figure 3.7: The vertex mass (a), energy fraction (b) and vertex finding efficiency (c) of the inclusive secondary vertices found by the SV1 algorithm, for three different flavours of jets.

All tracks from the remaining two-track vertices are combined into a single inclusive vertex, using an iterative procedure to remove the track yielding the largest contribution to the χ^2 of the vertex fit until this contribution passes a predefined threshold.

The SV1 tagging algorithm is based on the likelihood ratio formalism and exploits three of the vertex properties: the *vertex mass*, *i.e.* the invariant mass of all tracks used to reconstruct the vertex assuming that all tracks are pions, the energy fraction, *i.e.* the ratio of the sum of energies of these tracks to the sum of the energies of all tracks in the jet, and the number of two-track vertices. In addition, the ΔR between the jet direction and the direction of the line joining the primary vertex and the secondary vertex is used in the LLR. Some of these properties are illustrated in Figure 3.7 for b jets, c jets and light-flavour jets.

The JetFitter [37] exploits the topological structure of weak b and c hadron decays inside the jet. A Kalman filter is used to find a common line on which the primary vertex and the bottom and charm vertices lie, as well as their positions on this line approximating the b hadron flight path. With this approach, the b

and c hadron vertices are not merged, even when only a single track is attached to each of them. In the JetFitter algorithm, the decay topology is described by the following discrete variables: the number of vertices with at least two tracks, the total number of tracks at these vertices, and the number of additional single track vertices on the b hadron flight axis. The vertex information, instead, is condensed in the following observables: the vertex mass, the energy fraction and the flight length significance $\frac{L}{\sigma_L}$, *i.e.* the average displaced vertex decay length divided by its uncertainty. The six JetFitter variables defined above are used as input nodes in an artificial neural network and, since the input variable distributions depend on the p_T and $|\eta|$ of the jets, also the p_T and $|\eta|$ kinematic variables are included as two additional input nodes. The JetFitter neural network has three output nodes P_b, P_c and P_l corresponding to b, c and light-flavor jet hypotheses respectively, and the network topology includes two hidden layers with 12 and 7 nodes. A discriminating variable to select b jets and reject light-flavor jets is then defined from the values of the corresponding output nodes: $w_{\text{JetFitter}} = \ln\left(\frac{P_b}{P_l}\right)$.

3.4.1.3 Combined tagging algorithm

The vertex-based algorithms exhibit much lower mistake rates than the impact parameter-based ones, but their efficiency for actual b jets is limited by the secondary vertex finding efficiency. Therefore, both approaches are combined to define a more powerful tagging algorithm.

The MV1 neural network is a perceptron with two hidden layers consisting of three and two nodes, respectively, and an output layer with a single node which holds the final discriminant variable. The input to the MV1 algorithm consists of three variables: the two output weights from IP3D and SV1 algorithms and the discriminant from the IP3D+JetFitter combination. The I3PD+JetFitter algorithm is defined in the same way as the JetFitter algorithm itself but the output

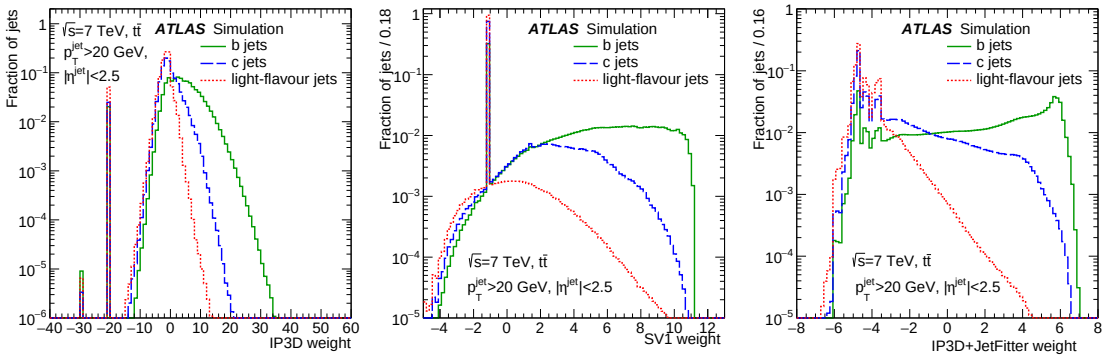

(a) (b) (c)

Figure 3.8: Distribution of the IP3D (a), SV1 (b) and IP3D+JetFitter (c) weights for b, c and light-flavour jets. These three weights are used as inputs for the MV1 algorithm. The spikes at $w_{\mathrm{IP3D}} \approx -20$ and ≈ -30 correspond to pathological cases where the IP3D weight could not be computed, due to the absence of good-quality tracks. The spike at $w_{\mathrm{SV1}} \approx -1$ corresponds to jets in which no secondary vertex could be reconstructed by the SV1 algorithm and where discrete probabilities for a b and light-flavour jet not to have a vertex are assigned. The irregular behavior in $w_{\mathrm{IP3D+JetFitter}}$ arises because both the w_{IP3D} and the $w_{\mathrm{JetFitter}}$ distribution (not shown) exhibit several spikes.

weight of the IP3D algorithm is used as an additional input node and the number of nodes in the two intermediate hidden layers is increased to 14 and 9, respectively. The discriminating variable used in the MV1 algorithm is then defined as $w_{\mathrm{IP3D+JetFitter}} = \ln\left(\frac{P_b}{P_l}\right)$. A specific tuning of the IP3D+JetFitter algorithm to provide a better discrimination between b and c jets uses $w_{\mathrm{IP3D+JetFitter}(c)} = \ln\left(\frac{P_b}{P_c}\right)$ as a discriminant. Distributions of the three MV1 input variables are shown in Figure 3.8 for b jets, c jets and light-flavour jets in simulated $t\bar{t}$ events, while Figure 3.9(a) shows the MV1 output weight distribution. Figure 3.9(b) shows the light-flavour-jet rejection as a function of b-jet tagging efficiency.

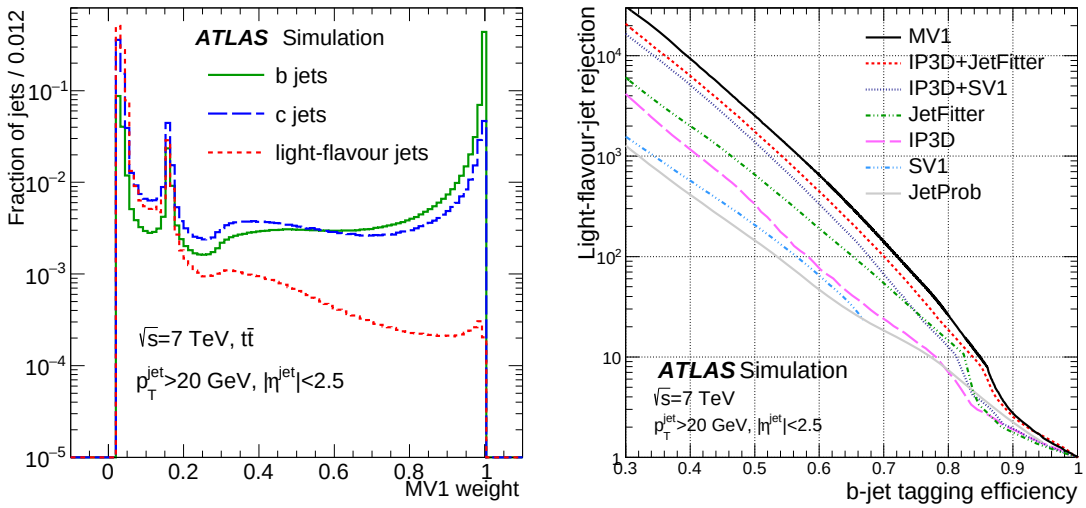

(a) (b)

Figure 3.9: Distribution of the tagging weight obtained with the MV1 algorithm, for three different flavors of jets (a) and light-flavour jet rejection versus b-jet tagging efficiency, for various tagging algorithm (b).

3.5 Missing Transverse Energy

In a hadron collider event the missing transverse energy is defined as the momentum imbalance in plane transverse to the beam axis, where momentum conservation is imposed. The transverse momentum imbalance can account for the presence of undetectable neutrinos as well as new weakly-interacting particles. The missing transverse energy $E_{\mathrm{T}}^{\mathrm{miss}}$ is obtained from the negative vector sum of the momenta of all particles detected in pp collisions.

The $E_{\mathrm{T}}^{\mathrm{miss}}$ reconstruction [52] uses energy deposits in the calorimeters and muons reconstructed in the muon spectrometer. The calculations is based on reconstructed and calibrated physics objects in a specific order: electrons, photons, hadronically decaying τ-leptons, jets and finally muons. Calorimeter deposits not associated with any such objects are also taken into account in the $E_{\mathrm{T}}^{\mathrm{miss}}$ reconstruction in the so called *soft term*. The missing transverse energy is then defined

as:

$$E_{x(y)}^{\text{miss}} = E_{x(y)}^{\text{miss},e} + E_{x(y)}^{\text{miss},\gamma} + E_{x(y)}^{\text{miss},\tau} + E_{x(y)}^{\text{miss,jets}} + E_{x(y)}^{\text{miss,SoftTerm}} + E_{x(y)}^{\text{miss},\mu} \tag{3.6}$$

where each term is calculated as the negative sum of the calibrated reconstructed objects, projected onto the x and y directions. The $E_{\text{T}}^{\text{miss}}$ soft term is calculated using only energy deposits from topological clusters [34] containing a significant signal and, to avoid double counting energy, the parameterized muon energy loss in the calorimeter is subtracted if the combined muon momentum is used [52].
In Eq.(3.6), electrons are calibrated with standard ATLAS electron calibration [45] and photons are calibrated at the EM scale. The τ-jets are calibrated with the local cluster weighting (LCW) [52,53] and corrected for the tau energy scale (TES) [54]. The jets are reconstructed with the anti-k_t algorithm with distance parameter $R = 0.4$ and the LCW+JES calibration is applied. Only jets with calibrated p_{T} greater than 20 GeV are used to calculate the jet term in Equation 3.6.

Chapter 4

The SM Higgs boson at ATLAS

In 2012, the ATLAS and CMS collaborations at the Large Hadron Collider (LHC) [57] reported the observation of a new particle [55,56] at a mass of about 125 GeV. The discovery made in the search for the SM Higgs boson [18–23] is a milestone of the spontaneous electroweak symmetry breaking, achieved through the Brout-Englert-Higgs mechanism which predicts the existence of a neutral scalar particle, commonly known as the Higgs boson. While the SM does not predict the value of its mass m_H, the production cross sections σ and decay branching ratios (BR) of the Higgs boson can be precisely calculated once the mass is known. Therefore, precision measurements of the properties of the new particle are critical in ascertaining whether the newly discovered particle is fully responsible for the electroweak symmetry breaking mechanism and whether there are potential deviations from the SM predictions.

4.1 Higgs boson phenomenology

In the SM, Higgs boson production at the LHC mainly occurs through the following processes, listed in order of decreasing cross section at the center-of-mass energies

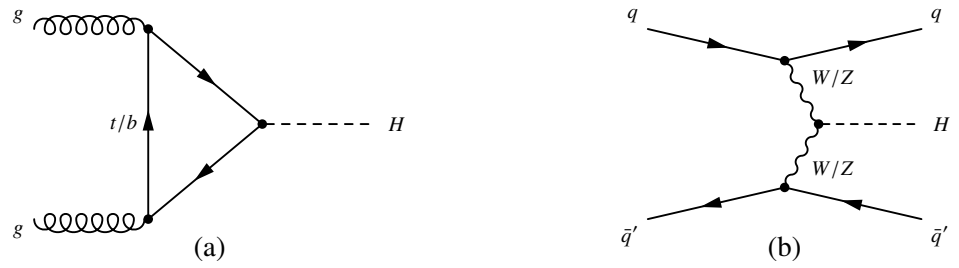

Figure 4.1: Leading-order Feynman diagrams for Higgs boson production via the (a) ggF and (b) VBF production processes.

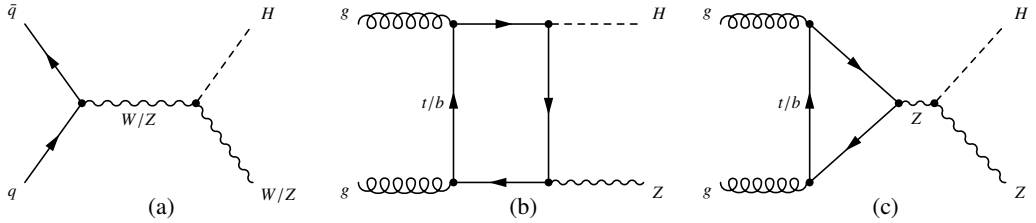

Figure 4.2: Leading-order Feynman diagrams of Higgs boson production via the (a) $q\bar{q} \to VH$ and (b,c) $gg \to ZH$ production processes.

of $\sqrt{s} = 7$ TeV and 8 TeV:

- the gluon fusion process (ggF) $gg \to H$, as in Figure 4.1a;
- the vector boson fusion process (VBF) $q\bar{q} \to q\bar{q}H$, as in Figure 4.1b;
- the associated production with a W boson (WH) qq, $qg \to WH$, as in Figure 4.2a;
- the associated production with a Z boson (ZH) $pp \to ZH$, including the $gg \to ZH$ process ($ggZH$), as in Figures 4.2a, 4.2b and 4.2c;
- the associated production with a pair of top quarks ($t\bar{t}H$) qq, $gg \to t\bar{t}H$, as in Figure 4.3.

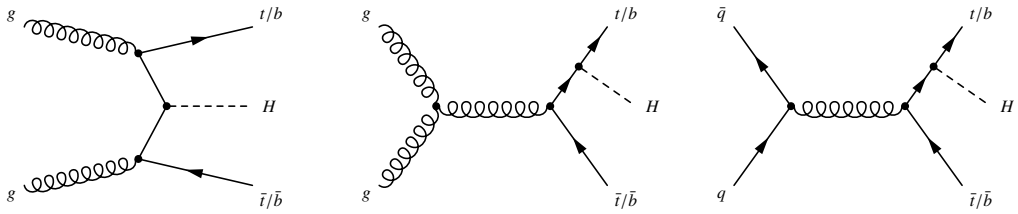

Figure 4.3: Leading-order Feynman diagrams of Higgs boson production via the $q\bar{q}/gg \to t\bar{t}H$ and $q\bar{q}/gg \to bbH$ processes.

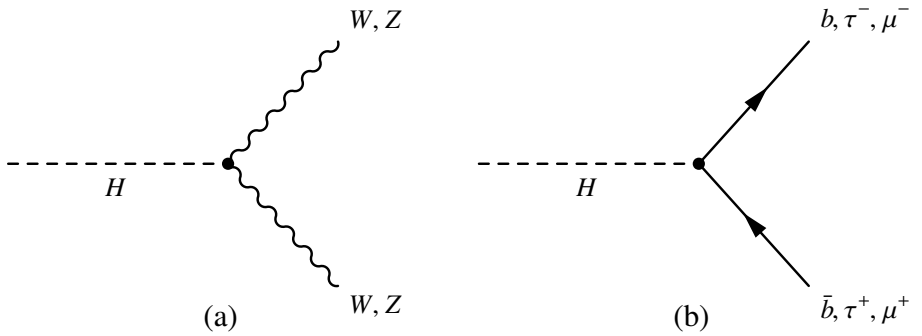

Figure 4.4: Leading-order Feynman diagrams of Higgs boson decays (a) to W and Z bosons and (b) to fermions.

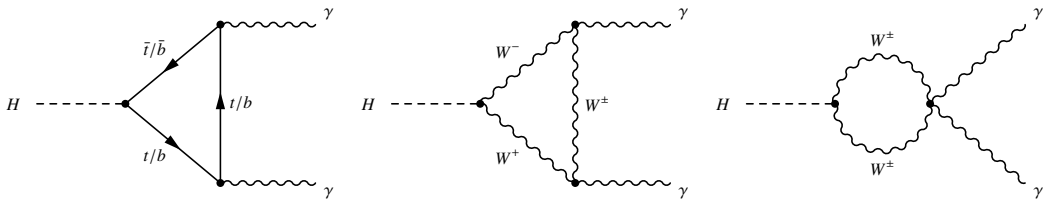

Figure 4.5: Leading-order Feynman diagrams of Higgs boson decays to a pair of photons.

Production process	Cross section [pb]		Order of calculation
	$\sqrt{s} = 7$ TeV	$\sqrt{s} = 8$ TeV	
ggF	15.0 ± 1.6	19.2 ± 2.0	NNLO(QCD)+NLO(EW)
VBF	1.22 ± 0.03	1.58 ± 0.04	NLO(QCD+EW)+ NNLO(QCD)
WH	0.577 ± 0.016	0.703 ± 0.018	NNLO(QCD)+NLO(EW)
ZH	0.334 ± 0.013	0.414 ± 0.016	NNLO(QCD)+NLO(EW)
bbH	0.156 ± 0.021	0.203 ± 0.028	5FS NNLO(QCD)+ 4FS NLO(QCD)
ttH	0.086 ± 0.009	0.129 ± 0.014	NLO(QCD)
tH	0.012 ± 0.001	0.018 ± 0.001	NLO(QCD)
Total	17.4 ± 1.6	22.3 ± 2.0	

Table 4.1: SM predictions of the Higgs boson production cross sections together with their theory uncertainties. The value of the Higgs boson mass is assumed to be $m_H = 125.09$ GeV and the predictions are obtained by linear interpolation from those at 125.0 and 125.1 GeV from Reference [78] except for the tH cross section, which is obtained from Reference [68]. The ZH cross section includes at NNLO(QCD) both the quark-initiated, *i.e.* $qq \to ZH$ or $qg \to ZH$, and the $gg \to ZH$ contributions. The uncertainties on the cross sections are evaluated as the quadratic sum of the uncertainties resulting from variations of QCD scale, parton distribution functions and α_S. The uncertainty on the tH cross section is calculated following the procedure of Reference [79]. The order of the theory calculations for the different production processes is also indicated.

The WH and ZH production process are collectively referred to as the VH process, usually known as *Higgsstrahlung*. Other less important production processes in the SM are the qq, $gg \to bbH$ (bbH), also shown in Figure 4.3, and the production in association with a single top quark (tH). The latter proceeds through either the $qb \to tHq$ (tHq) or $gb \to tHW$ (tHW) process. However, the tH process is expected to have a negligible contribution in the SM.

Leading-order Feynman diagrams of the Higgs boson decays are shown in Figures 4.4 and 4.5. The decays to W and Z bosons (Figure 4.4a) and to fermions (Figure 4.4b) proceed through tree-level processes whereas $H \to \gamma\gamma$ decay is mediated

Decay channel	Branching ratio [%]
$H \to bb$	57.5 ± 1.9
$H \to WW$	21.6 ± 0.9
$H \to gg$	8.56 ± 0.86
$H \to \tau\tau$	6.30 ± 0.36
$H \to cc$	2.90 ± 0.35
$H \to ZZ$	2.67 ± 0.11
$H \to \gamma\gamma$	0.228 ± 0.011
$H \to Z\gamma$	0.155 ± 0.014
$H \to \mu\mu$	0.022 ± 0.001

Table 4.2: SM predictions for the decay branching ratios of a Higgs boson with a mass of 125.09 GeV, together with their uncertainties. The predictions are obtained from Reference [78].

by W-boson or heavy quark loops (Figure 4.5). The theoretical calculation of the SM Higgs boson production cross sections and decay branching ratios are summarized with their overall uncertainties in Tables 4.1 and 4.2 for a Higgs boson mass $m_H = 125.09$ GeV.

To interpret the Higgs boson yields, a signal strength parameter μ is usually used which is defined as the ratio between the measured Higgs boson rate and its SM expectation: for a specific production and decay channel $i \to H \to f$, the signal strength for the i production process μ_i and for the f decay channel μ^f are defined as:

$$\mu_i = \frac{\sigma_i}{(\sigma_i)_{\text{SM}}} \text{ and } \mu^f = \frac{\text{BR}^f}{\left(\text{BR}^f\right)_{\text{SM}}} \tag{4.1}$$

where the "SM" subscript refers to the corresponding SM predictions and so, by definition, $\mu_i = 1$ and $\mu^f = 1$ in the SM. Since σ_i and BR^f cannot be separately measured without additional assumptions, only the product $\mu_i \times \mu^f$ can be ex-

tracted experimentally, leading to a signal strength μ_i^f for the overall $i \to H \to f$ process:

$$\mu_i^f = \frac{\sigma_i \times \mathrm{BR}^f}{(\sigma_i)_{\mathrm{SM}} \times \left(\mathrm{BR}^f\right)_{\mathrm{SM}}} = \mu_i \times \mu^f \tag{4.2}$$

Thus, for a given analysis a, the number of signal events n_s^a can be written as:

$$n_s^a = \sum_i \sum_f \mu_i \left(\sigma_i\right)_{\mathrm{SM}} \times \mu^f \left(\mathrm{BR}^f\right)_{\mathrm{SM}} \times A_{if}^a \times \varepsilon_{if}^a \times \mathcal{L}^a \tag{4.3}$$

where the i and f indices indicate the production processes and decay channels contribution to the considered analysis, A_{if}^a represents the detector acceptance derived from MC simulation of the considered SM processes, ε_{if}^a si the reconstruction efficiency within the acceptance and $\mathcal{L}^a$ the integrated luminosity for the given a analysis.

4.2 Mass measurement

The LHC Collaborations have chosen a model-independent approach to measure the Higgs boson mass based on the mass spectra of the two decay modes $H \to \gamma\gamma$ and $H \to ZZ^* \to 4\ell$. In these two channels the Higgs boson produces a narrow mass peak from which the mass can be extracted without assumptions on the signal production and decay yields. Interference effects are expected between the Higgs boson signal and SM background processes but the contribution is still negligible compared to the present experimental resolution.

4.2.1 $H \to \gamma\gamma$ decay channel

The $H \to \gamma\gamma$ channel provides good sensitivity to Higgs boson mass, due to the excellent mass resolution in the diphoton final state, allowing the observation of a narrow mass peak over a smooth background which can be determined directly

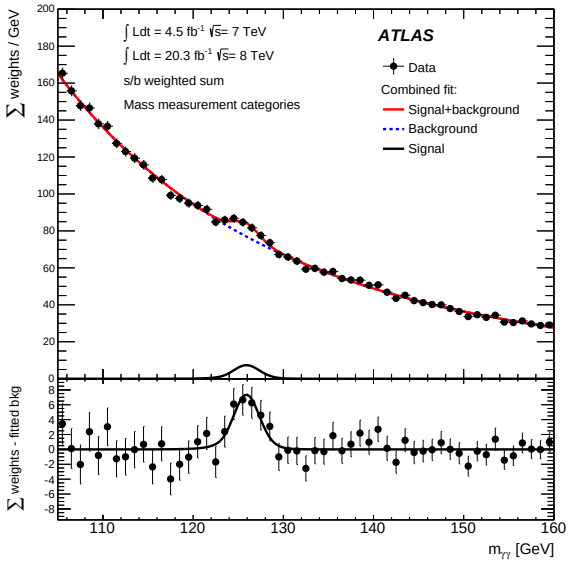

Figure 4.6: Invariant mass distribution in the $H \to \gamma\gamma$ analysis for data (7 TeV and 8 TeV samples combined), showing weighted data points with errors and the result of the simultaneous fit to all categories. The fitted signal plus background is shown, along with the background-only component of this fit. The different categories are summed together with a weight given by the signal-to-background ratio in each category. The bottom panel shows the difference between the summed weights and the background component of the fit.

from data. The EM calorimeter provides a measurement of the photon energy and direction, utilizing its longitudinal segmentation. The typical mass resolution is 1.7 GeV for a 125 GeV Higgs boson mass. The main background is continuum $\gamma\gamma$ production with smaller contribution, of about 20%, from γ+jet and dijet processes. The diphoton invariant mass $m_{\gamma\gamma}$ is computed using the measured photon energies and their opening angle estimated from the selected primary vertex and the photon impact points in the calorimeter. The transverse energy is required to be $E_{\mathrm{T}} > 0.35 \times m_{\gamma\gamma}$ for the photon with the highest E_{T} and $E_{\mathrm{T}} > 0.25 \times m_{\gamma\gamma}$ for the photon with the second highest E_{T}. This selection leads to a smoother background distribution compared to using fixed cuts on E_{T}. The combined signal reconstruction and selection efficiency for the Higgs boson signal at an assumed mass of 125

GeV is around 40%. In total 94627 (17225) events are selected in the 8 TeV (7 TeV) dataset with $105 < m_{\gamma\gamma} < 160$ GeV. The mass spectra is fitted assuming the signal-plus-background hypothesis, using an unbinned maximum likelihood fit with a given background and signal parameterization. Figure 4.6 shows the result of the simultaneous fit to the data over all categories. All categories are summed together with a weight given by the signal-to-background ratio in each category. The fitted parameters of interest for the signal are the Higgs boson mass and the signal strength and the measured Higgs boson mass in the $H \to \gamma\gamma$ decay channel is:

$$m_H = 125.98 \pm 0.42\,(\text{stat}) \pm 0.28\,(\text{syst})\ \text{GeV} = 125.98 \pm 0.50\ \text{GeV} \qquad (4.4)$$

where the first error represents the statistical uncertainty and the second the systematic uncertainty. Finally, the mass measurement is performed leaving the overall signal strength free in the fit and, thus, the measured signal strength μ normalized to the SM expectation is found to be $\mu = 1.29 \pm 0.30$.

4.2.2 $H \to ZZ^* \to 4\ell$ decay channel

The $H \to ZZ^* \to 4\ell$ channel provides good sensitivity to the measurement of the Higgs properties due to its high signal-to-background ratio, which is about two in the signal mass window 120-130 GeV, and its excellent mass resolution.The typical mass resolution varies from 1.6 GeV fro the 4μ final state to 2.2 GeV for the $4e$ final state. For the SM Higgs boson with a mass of about 125 GeV, the dominant background is the $\left(Z^{(*)}/\gamma^*\right)\left(Z^{(*)}/\gamma^*\right) \to 4\ell$ process, with a smaller contribution expected from Z+jets and $t\bar{t}$ processes. Higgs boson candidates are formed by selecting a lepton quadruplet, *i.e.* two same-flavor opposite sign lepton pairs, and, since multiple quadruplets within a single event are possible, the selection is done separately keeping only a single quadruplet per channel with lepton pairs compat-

ible with Z boson mass. For the 8 TeV data, the combined signal reconstruction and selection efficiency for $m_H = 125$ GeV is 39% for the 4μ channel, 27% for the $2e2\mu/2\mu2e$ channel and 20% for the $4e$ channel. To reduce the impact of the ZZ^* background on the cited mass, a multivariate discriminant based on a boosted decision tree (BDT) is used and the Higgs boson mass is extracted applying a two-dimensional (2D) fit to the quadruplet invariant mass $m_{4\ell}$ and BDT output. The measured Higgs boson mass obtained with the 2D method is:

$$m_H = 124.51 \pm 0.52\,(\text{stat}) \pm 0.06\,(\text{syst})\ \text{GeV} = 124.51 \pm 0.52\ \text{GeV} \tag{4.5}$$

where the first error represents the statistical uncertainty and the second the systematic uncertainty. Finally, the measured signal strength for the inclusive selection is $\mu = 1.66^{+0.45}_{-0.38}$ consistent with the SM expectation.

4.2.3 Combined mass measurement

The measured masses from the $H \to \gamma\gamma$ and $H \to ZZ^* \to 4\ell$ channels are combined following a statistical method based on the profile likelihood ratio $\Lambda(\alpha)$, defined as:

$$\Lambda(\alpha) = \frac{L\left(\alpha, \hat{\hat{\theta}}(\alpha)\right)}{L\left(\hat{\alpha}, \hat{\theta}\right)} \tag{4.6}$$

and which depends on one or more parameters of interest α, *e.g.* the Higgs bosons mass m_H or the signal strength μ, as well as on the nuisance parameters θ. The likelihood functions in Equation 4.6 are built using sums of signal and background PDFs in the discriminating variables, *e.g.* the $\gamma\gamma$ mass spectra $m_{\gamma\gamma}$ or the four-lepton invariant mass $m_{4\ell}$ and BDT output distributions. The PDFs are derived from simulation for the signal and from both data and simulation for the background and likelihood fits to the observed data are carried out for parameters of interest. The vector $\hat{\theta}$ denotes the unconditional maximum likelihood estimate of

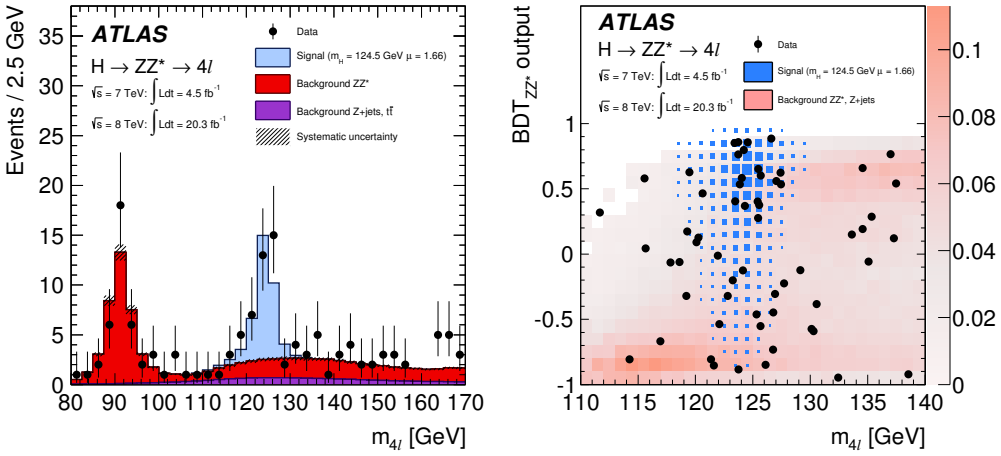

(a) (b)

Figure 4.7: (a) Distribution of the four-lepton invariant mass $m_{4\ell}$ for the selected candidates in the mass range 80 - 170 GeV for the combined 7 TeV and 8 TeV data samples. Superimposed are the expected distributions of a SM Higgs boson signal for $m_H = 124.5$ GeV normalized to the measured signal strength, as well as the expected ZZ^* and reducible backgrounds. (b) Distribution of the BDT_{ZZ^*} output versus $m_{4\ell}$ for the selected candidates in the 110-140 GeV mass range for the combined 7 TeV and 8 TeV data samples. The expected distribution for a SM Higgs with $m_H = 124.5$ GeV is indicated by the size of the blue boxes and the total background is indicated by the intensity of the red shading.

the parameter values and $\hat{\hat{\theta}}$ denotes the conditional maximum likelihood estimate for given fixed values of the parameters of interest α. Systematic uncertainties and their correlations are modeled by introducing nuisance parameters θ described by likelihood functions associated with the estimate of the corresponding effect. the choice of the parameters of interest depends on the test under consideration, with the remaining parameters treated as nuisance parameters, *i.e.* set to the values that maximizes the likelihood function ("profiled") for the given fixed values of the parameters of interest.

For the combined mass measurement, hypothesized values of m_H are tested using the profile likelihood ratio defined in terms of m_H and treating $\mu_{\gamma\gamma}(m_H)$ and

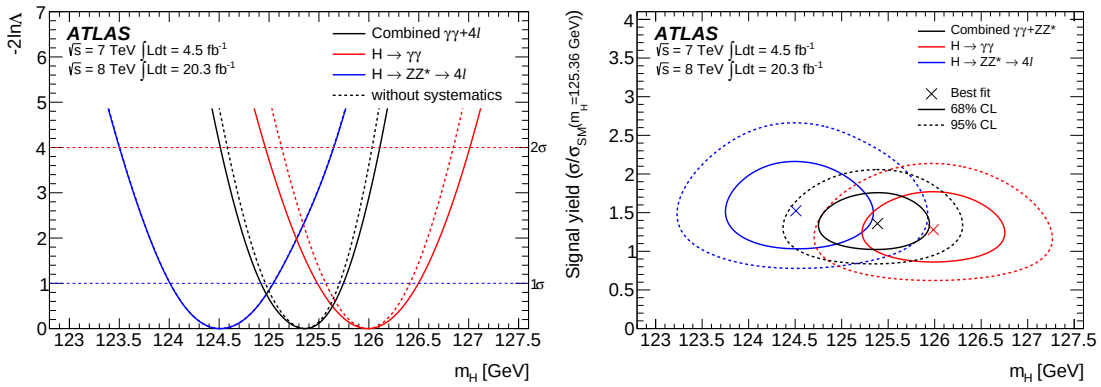

(a) (b)

Figure 4.8: (a) Value of $-2\ln\Lambda$ as a function of m_H for the individual $h \to \gamma\gamma$ and $H \to ZZ^* \to 4\ell$ channels and their combination, where the signal strengths $\mu_{\gamma\gamma}$ and $\mu_{4\ell}$ are allowed to vary independently. The dashed lines show the statistical component of the mass measurements. For the $H \to ZZ^* \to 4\ell$ channel, this is indistinguishable from the solid line that includes that systematic uncertainties. (b) Likelihood contours $-2\ln\Lambda(S, m_H)$ as a function of the normalized signal yield $S = \sigma/\sigma_{\mathrm{SM}}(m_H = 125.36$ GeV) and m_H for the $H \to \gamma\gamma$ and $H \to ZZ^* \to 4\ell$ channels and their combination, including all systematic uncertainties. For the combined contour, a common normalized signal yield S is used. The markers indicate the maximum likelihood estimates in the corresponding channels.

$\mu_{4\ell}(m_H)$ as independent nuisance parameters, so as to make no assumptions about the SM Higgs couplings:

$$\Lambda(m_H) = \frac{L\left(m_H,\, \hat{\hat{\mu}}_{\gamma\gamma}(m_H),\, \hat{\hat{\mu}}_{4l}(m_H),\, \hat{\hat{\theta}}(m_H)\right)}{L\left(\hat{m}_H,\, \hat{\mu}_{\gamma\gamma},\, \hat{\mu}_{4l},\, \hat{\theta}\right)} \tag{4.7}$$

The resulting combined mass measurement is:

$$m_H = 125.36 \pm 0.37\,(\mathrm{stat}) \pm 0.18\,(\mathrm{syst})\ \mathrm{GeV} = 125.36 \pm 0.41\ \mathrm{GeV} \tag{4.8}$$

where the first error represents the statistical uncertainty and the second the systematic uncertainty. The statistical observable $-2\ln\Lambda(m_H)$, which behaves as a χ^2 distribution with one degree of freedom, is shown in Figure 4.8(a). Finally, the profile likelihood ratio $\Lambda(S, m_H)$ as a function of both m_H and the normal-

ized signal yields S is extracted. The normalized signal yield is defined as $S = \sigma/\sigma_{\mathrm{SM}}\,(m_H = 125.36\ \mathrm{GeV})$ which differs from the signal strength $\mu = \sigma/\sigma_{\mathrm{SM}}\,(m_H)$ only for the fixed value of the Higgs boson mass m_H. Asymptotically, the test statistic $-2\ln\Lambda\,(S,\, m_H)$ is distributed as a χ^2 distribution with two degrees of freedom. The resulting 68% and 95% CL contours are shown in Figure 4.8(b) from which no significant correlation between the two fitted variables is observed, confirming the model-independence of the mass measurement.

4.3 Signal strength measurement

In ATLAS, several analyses has been designed for maximum sensitivities to SM Higgs boson production from different processes, exploiting in particular the differences in kinematics through categorization of the selected events. Thus the yields of different Higgs boson production processes and decays can be extracted. The Higgs boson coupling strengths to SM vector bosons and fermions in different benchmark models has been probed for the measured Higgs boson mass of $m_H = 125.36$ GeV. All results have been obtained assuming the Higgs boson has a narrow total decay width such that its production and decay factorize.

4.3.1 $H \to \gamma\gamma$

In the $H \to \gamma\gamma$ analysis [58] the Higgs boson signal is measured in events with at least two isolated and well-identified photon candidates (see Section 4.2.1). The diphoton candidate events are grouped into twelve exclusive categories separately for the $\sqrt{s} = 7$ and 8 TeV datasets; the order of categorization is chosen to give precedence to production modes with the most distinct signatures. Each category is optimized by adjusting the event selection criteria to minimize the expected

uncertainty on the signal yield of the targeted production mode.

The first two categories are designed for ttH production based on the topology of leptonic and hadronic decays of the associated $t\bar{t}$ pair.The next four categories are optimized for VH production, targeting one-lepton, dilepton, $E_{\mathrm{T}}^{\mathrm{miss}}$ and hadronic signatures of W and Z boson decays. Events from VBF production are identified by requiring two well-separated and high-p_{T} jets and little hadronic activity between them.

4.3.2 $H \to ZZ^* \to 4\ell$

The $H \to ZZ^* \to 4\ell$ analysis [59] has a high signal-to-ratio background and the Higgs boson candidates are selected by requiring two pairs of isolated, same-flavor and opposite-charge leptons, as already described in Section 4.2.2.

To measure the rates of different production processes, each $H \to ZZ^* \to 4\ell$ candidate is assigned to one of four categories depending on event characteristics beyond the four selected leptons. The VBF category consists of candidates with two additional jets with dijet mass $m_{jj} > 130$ GeV. The events failing this selection are considered for the VH-hadronic category, where the dijet mass is required to be 40 GeV $< m_{jj} <$ 130 GeV. Events failing the VBF and VH-hadronic categorization criteria are considered for the VH-leptonic category with the requirement of an additional lepton. Finally, the remaining events are assigned to the ggF category.

4.3.3 $H \to WW^*$

Analyses targeting the ggF, VBF and VH production modes [60,61] are performed for the $H \to WW^*$ decay channel. The ggF and VBF production processes are

explored through the $H \to WW^* \to \ell\nu\ell\nu$ decay and the VH process is studied in final states with two or more leptons.

The analysis of the ggF and VBF production processes [60] selects the signal candidate events by requiring two oppositely charged leptons.Candidates are categorized according to the number of jets (N_{jet}) and to the flavors of the leptons. The categorys targeting ggF production include $N_{\text{jet}} = 0$, 1 and ≥ 2 and are further divided into the same- and different-flavor leptons for $N_{\text{jet}} = 0$, 1. Only the different-flavor leptons are considered for $N_{\text{jet}} \geq 2$. The categories targeting VBF production require $N_{\text{jet}} \geq 2$, separately for the same- or different-flavour leptons. The primary background processes are WW, top quark ($t\bar{t}$ and Wt), W+jets, Drell-Yan, and other diboson production. Most of the background contributions are estimated from data. For the ggF categories, the final signal region is selected by requiring the dilepton mass $m_{\ell\ell} < 55$ GeV and their azimuthal angular separation $\Delta\phi_{\ell\ell} < 1.8$ and the signal is extracted through a combined fit to the transverse mass distributions of the dilepton plus $E_{\text{T}}^{\text{miss}}$ system in both the signal and control regions of different categories and lepton flavours.

The VH analysis [61] is optimized for different lepton multiplicities: opposite-charge dileptons, same-charge deletions, three and four leptons. Dilepton final states target VH production with the $H \to WW^*$ decay with two bosons decaying leptonically and the other hadronically. The opposite-charge deletion final state selects events with two or more jets, with the value of m_{jj} required to be close to the W and Z boson masses. The same-charge dilepton category accepts events with either one or two jets. The three-lepton final state targets WH with $H \to WW^*$ and has the highest sensitivity of the four final states. The three leptons are required to have a net charge of ± 1 and the event can have at most one jet. The four-lepton category is designed to accept events from ZH production with the $H \to WW^*$ decay. The net charge of the leptons is required to be

zero and at least one pair of leptons is required to have the same flavour, opposite charge, and an invariant mass close to the Z boson mass.

4.3.4 $H \to \tau\tau$

The $H \to \tau\tau$ analysis [62] considers both the leptonic (τ_{lep}) and hadronic (τ_{had}) decays of the τ lepton. Three sub-channels ($\tau_{\text{lep}}\tau_{\text{lep}}$, $\tau_{\text{lep}}\tau_{\text{had}}$ and $\tau_{\text{had}}\tau_{\text{had}}$) are defined by orthogonal requirements on the number of reconstructed hadronic τ decays and leptons (electrons or muons) in the event.
Candidate events are divided into boosted and VBF categories. the boosted category signal events where the Higgs boson is produced with a large boost, primarily from the ggF process, and requires the transverse momentum of the reconstructed Higgs boson candidate to be greater than 100 GeV. The VBF category contains events with two jets separated in pseudorapidity and targets signal events produced through the vector boson fusion process.
In all three sub-channels, the most important backgrounds are irreducible $Z \to \tau\tau$ events and events with one or two jets misidentified as τ lepton decay products (mostly form multijet and W+jets production).

4.3.5 VH with $H \to b\bar{b}$

The $H \to b\bar{b}$ decay mode is predicted in the SM to have the largest branching ratio (see Table 4.2). In spite of this large branching ratio, an inclusive search for $H \to b\bar{b}$ is not feasible because of the overwhelming background from multijet production. Associated production of a Higgs boson with a vector boson in V, offers a viable alternative because leptonic decays of the vector boson, $W \to \ell\nu$, $Z \to \ell\ell$ and $Z \to \nu\nu$ can be efficiently used for triggering and background reduction.
The search for associated VH production with $H \to b\bar{b}$ [63] is performed for events

containing zero, one or two charged leptons. Contributions from $W \to \tau\nu$ and $Z \to \tau\tau$ decays in which the τ leptons subsequently decay to electrons or muons are also included. A b-tagging algorithm is used to identify jets from $H \to b\bar{b}$ decays. To improve the sensitivity, the three channels are each split into categories according to the vector-boson transverse momentum p_{T}^{V} the number of jets, and the number and quality of the b-tagged jets. Topological and kinematic selection criteria are applied within each of the resulting categories. The categories providing most of the sensitivity are those requiring two b-tagged jets and large p_{T}^{V}. The categories with low sensitivity are used to constrain the contributions of the dominant background processes.

4.3.6 $H \to Z\gamma$

The $H \to Z\gamma$ analysis [64] with $Z \to \ell\ell$ searches for a narrow peak in the reconstructed $\ell\ell\gamma$ invariant-mass distribution around 125 GeV over a smooth background. The $Z+\gamma$ production, $Z \to \ell\ell\gamma$ radiative decays and Z+jets events where a jet is misidentified as a photon dominate the background contributions.

The analysis selects two isolated leptons of same flavor and opposite charge and one isolated photon. The invariant mass of the dilepton system must satisfy $m_{\ell\ell} > m_Z - 10$ GeV and the three-body invariant mass must be consistent with the mass of the Higgs boson. To enhance the sensitivity of the analysis, events are classified into categories with different signal-to-background ratios and invariant-mass resolutions, based on the pseudorapidity difference $\Delta\eta_{Z\gamma}$ between the photon and the Z boson and p_{Tt}, the component of the Higgs boson candidate p_{T} that is orthogonal to the $Z\gamma$ thrust axis in the transverse plane.

4.3.7 $H \to \mu\mu$

The $H \to \mu\mu$ analysis [65] searches for a narrow peak in the dimuon invariant mass $m_{\mu\mu}$ distribution over a smooth background, where the width of the signal is dominated by the experimental resolution. The mass spectrum is dominated by the continuously falling background due to Z/γ^* production, with smaller contributions from top quark and diboson production.

The selected events containing a pair of oppositely charged muons are separated into seven mutually exclusive categories based on the VBF dijet signature, the muon pseudorapidity η_μ and the transverse momentum of the dimuon system $p_{\mathrm{T}}^{\mu\mu}$. The events with two or more jets that match selections designed for the VBF process are accepted in the VBF signal region. This categorisation takes advantage of the higher momentum resolution for muons reconstructed in the central part of the detector, and high $p_{\mathrm{T}}^{\mu\mu}$ for the expected SM signal.

4.3.8 ttH production

Searches for $q\bar{q}/gg \to t\bar{t}H$ production have been performed with three analyses targeting the Higgs boson decays $H \to b\bar{b}$, $H \to (WW^*, \tau\tau, ZZ^*) \to$ leptons and $H \to \gamma\gamma$. The search in the $H \to \gamma\gamma$ decay mode uses both $\sqrt{s} = 7$ and 8 TeV data, while the other two use only the $\sqrt{s} = 8$ TeV data.

The search for ttH production with $H \to b\bar{b}$ [66] considers two separate selections optimised for single-lepton and dilepton final states of $t\bar{t}$ decays. In the single-lepton channel, events are required to have one isolated electron or muon and at least four jets. In the dilepton channel, events are required to have two opposite-charge leptons and at least two jets. In both cases at least two b-tagged jets are required. Candidate events are categorised according to the jet and b-jet multi-

plicities with a total of nine (six) categories for the single-lepton (dilepton) final states.

The ttH search with $H \to WW^*$, $\tau\tau$ and ZZ^* decays [67] exploits several multilepton signatures resulting from leptonic decays of vector bosons and/or the presence of τ leptons. The events are categorised by the number of reconstructed electrons or muons and hadronic τ candidates. The five channels used in this combination are: one lepton with two hadronic τ candidates, two same-charge leptons with zero or one hadronic τ candidate, three leptons, and four leptons.

The ttH search in the $H \to \gamma\gamma$ channel [68] is part of the analysis $H \to \gamma\gamma$ (see Section 4.3.1).

4.3.9 Global signal strength

The signal-strength parameter is a measure of potential deviations from the SM prediction under the assumption that the Higgs boson production and decay kinematics do not change appreciably from the SM expectations. In particular, the transverse momentum and rapidity distributions of the Higgs boson are assumed to be those predicted for the SM Higgs boson by state-of-the-art event generators and calculations of each production process. This assumption is corroborated by studies such as the measurements of differential production cross sections and tests of spin and CP properties of the Higgs boson. Figure 4.9 shows the measurements of the signal-strength parameter μ from a simultaneous fit to all decay channels analysed, assuming SM values for the cross-section ratios of different Higgs boson production processes (or equivalently all μ_i's of Equation 4.2 are set to be equal).

Assuming a multiplier common to all decay modes, signal-strength measurements of individual decay modes can be combined to give a global and more precise measurement, providing the simplest consistency test with the SM expectation.

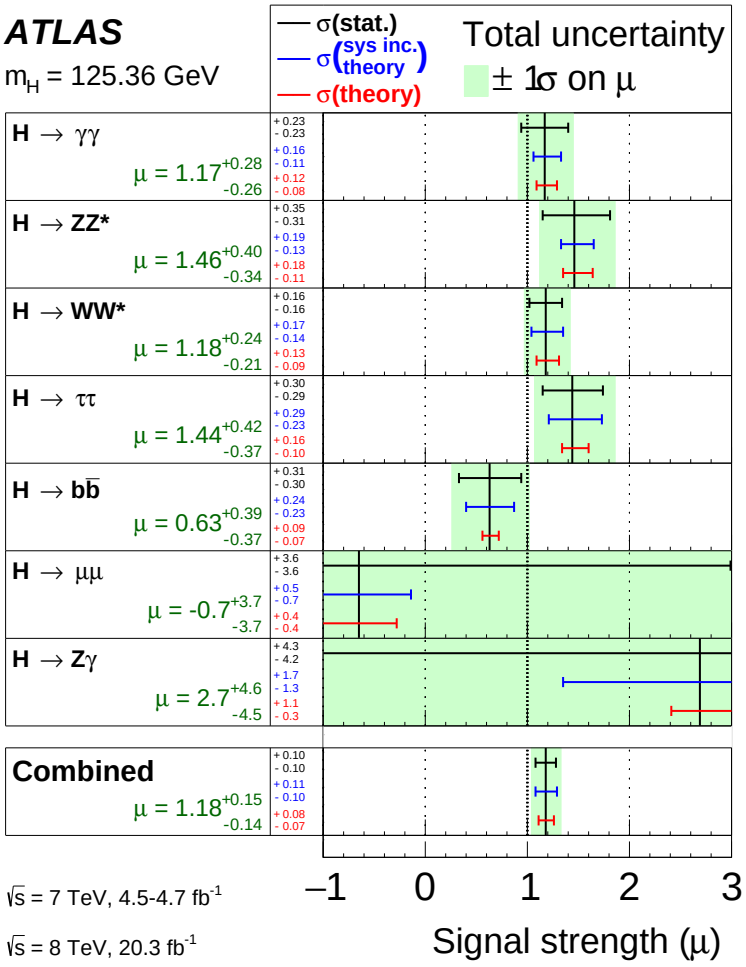

Figure 4.9: The observed signal strengths and uncertainties for different Higgs boson decay channels and their combination for $m_H = 125.36$ GeV. Higgs boson signals corresponding to the same decay channel are combined together for all analyses, assuming SM values for the cross section ratios of different production processes. The best-fit values are shown by the solid vertical lines. The total $\pm 1\sigma$ uncertainties are indicated by green shaded bands, with the individual contributions from the statistical uncertainty (top), the total (experimental and theoretical) systematic uncertainty (middle), and the signal theoretical uncertainty (bottom) on the signal strength shown as horizontal error bars.

Combining all measurements using the profile likelihood ratio $\Lambda(\mu)$ results in a global signal-strength value of:

$$\mu = 1.18^{+0.15}_{-0.14} = 1.18 \pm 0.10(\text{stat.}) \pm 0.07(\text{syst.})^{+0.08}_{-0.07}(\text{theo.}) \tag{4.9}$$

where the labels stat., syst. and theo. refer to statistical, systematic, and signal theoretical uncertainties, respectively. The signal theoretical uncertainty includes contributions from uncertainties in SM cross sections and branching ratios as well as in the modelling of the production and decays of the Higgs boson. The theoretical uncertainties of background processes are included in the uncertainty labelled as systematic uncertainty. This result is consistent with the SM expectation of $\mu = 1$, with a p-value of 18%. All individual measurements of the signal-strength parameters are consistent and compatible with the combined value, with a p-value of 76%.

4.3.10 Individual production processes

The measurements of the signal strengths described above assume the SM predictions of the relative contributions of different Higgs boson production processes and/or decay channels. Thus they may conceal differences between data and theoretical predictions. Therefore, in addition to the signal strengths of different decay channels, the signal strengths of different production modes are also determined, exploiting the sensitivity offered by the use of event categories in the analyses of all channels.

The Higgs boson production modes can be probed with four signal strength parameters: $\mu_{gg\text{F}}$, $\mu_{V\text{BF}}$, μ_{VH} and μ_{ttH}, one for each main production mode, assuming the SM values of the Higgs boson decay branching ratios. This assumption is equivalent to set $\mu_f = 1$ in Equation 4.2. The SM predictions of the signal yields

Production process	Signal strength μ at $m_H = 125.36$ GeV	
	$\sqrt{s} = 8$ TeV	Combined $\sqrt{s} = 7$ and 8 TeV
ggF	$1.23^{+0.25}_{-0.21}$	$1.23^{+0.23}_{-0.20}$
VBF	$1.55^{+0.39}_{-0.35}$	1.23 ± 0.32
VH	0.93 ± 0.39	0.80 ± 0.36
ttH	1.62 ± 0.78	1.81 ± 0.80

Table 4.3: Measured signal strengths μ at $m_H = 125.36$ GeV and their total $\pm 1\sigma$ uncertainties for different production modes for the $\sqrt{s} = 8$ TeV data and the combination with the $\sqrt{s} = 7$ TeV data. The $\sqrt{s} = 7$ TeV data do not have sufficient statistical power to yield meaningful measurements for individual production modes, but are included in the combination. These results are derived using the SM values of the Higgs boson decay branching ratios.

are scaled by these four production-dependent parameters.

The best-fit values of these parameters for the $\sqrt{s} = 8$ TeV data separately and in combination with the $\sqrt{s} = 7$ TeV data are shown in Table 4.3 and in Figure 4.10. The signal strength measurements are in reasonable agreement with the SM predictions of unity. The signal strength measurements are extrapolated to total cross-section measurements for each production process, as shown in Table 4.4. The different cross sections can be summed to obtain an overall extrapolated cross section for Higgs boson production. The resulting total Higgs boson production cross sections at the two energies are

$$\begin{aligned} \sigma_H\,(7\text{ TeV}) &= 22.1^{+7.4}_{-6.0} = 22.1^{+6.7}_{-5.3}(\text{stat.})^{+2.7}_{-2.3}(\text{syst.})^{+1.9}_{-1.4}(\text{theo.})\text{ pb} \\ \sigma_H\,(8\text{ TeV}) &= 27.7 \pm 3.7 = 27.7 \pm 3.0(\text{stat.})^{+2.0}_{-1.7}(\text{syst.})^{+1.2}_{-0.9}(\text{theo.})\text{ pb} \end{aligned} \tag{4.10}$$

to be compared with the theoretical predictions of 17.4 ± 1.6 pb at $\sqrt{s} = 7$ TeV and 22.3 ± 2.0 pb at $\sqrt{s} = 8$ TeV.

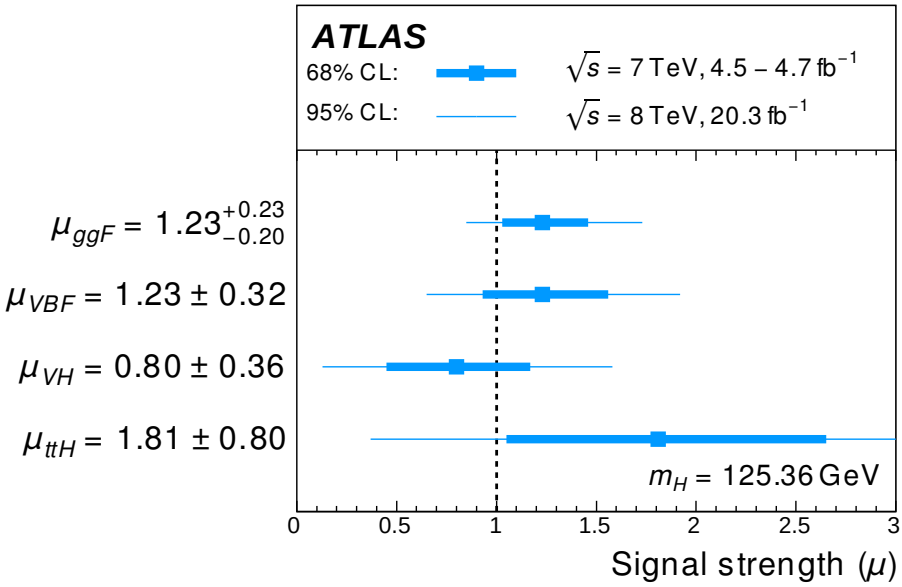

Figure 4.10: The best-fit signal-strength values of different production modes determined from the combined fit to the $\sqrt{s} = 7$ and 8 TeV data. The inner and outer error bars correspond to 68% CL and 95% CL intervals. Total uncertainties combining statistical, experimental and theoretical systematic uncertainties are shown. The fit assumes the SM values of the Higgs boson decay branching ratios for $m_H = 125.36$ GeV.

Production process	Cross section [pb] at $\sqrt{s} = 8$ TeV
ggF	23.9 ± 3.6
VBF	2.43 ± 0.58
VH	1.03 ± 0.53
ttH	0.24 ± 0.11

Table 4.4: Measured cross sections of different Higgs boson production processes at $\sqrt{s} = 8$ TeV for $m_H = 125.36$ GeV obtained from the signal-strength values of Table 4.3. Their SM predictions can be found in Table 4.1. The theoretical uncertainties here arise from the modelling of Higgs boson production and decays. These results are derived using the SM values of the Higgs boson decay branching ratios.

4.4 Indirect limits on BSMs

The searches for deviations from rates of Higgs boson production and decay predicted by the SM are crucial to test theories beyond the Standard Model, as the *2HDM*s discussed in Section 1.4. Simultaneous fits of multiple production and decay channels can be performed to interpret data in various benchmark models, provideing indirect limits on the BSM parameters.

The ATLAS Collaborations performed indirect searches using up to 4.7 fb^{-1} of pp collision data at $\sqrt{s} = 7$ TeV and up to 20.3 fb^{-1} at $\sqrt{s} = 8$ TeV. For the determination of the couplings in the visible Higgs boson decay channels, the experimental inputs include search results and measurements of Higgs boson decays: $h \to \gamma\gamma$ [58], $h \to ZZ^* \to 4\ell$ [59], $h \to WW^* \to 2\ell 2\nu$ [60, 61], $h \to Z\gamma$ [64], $h \to bb$ [63], $h \to \tau\tau$ [62] and $h \to \mu\mu$ [65] ($\ell = e, \mu$).

For each production mode j and visible decay channel k, μ is normalized to the SM expectation for that channel so that $\mu = 1$ corresponds to the SM Higgs boson hypothesis and $\mu = 0$ to the background-only hypothesis:

$$\mu = \frac{\sigma_j \times \text{BR}_k}{\sigma_{j,\text{SM}} \times \text{BR}_{k,\text{SM}}} \tag{4.11}$$

where σ_j is the production cross section, BR_k is the branching ratio and the subscript "SM" denotes their SM expectations.

The likelihood function for the Higgs boson coupling measurements is built as a product of the likelihoods of all measured Higgs boson channels, where for each channel the likelihood is built using sums of signal and background probability density functions in the discriminating variables.

Confidence intervals are extracted by taking $t_\alpha = -2 \ln \Lambda(\alpha)$ to follow an asymptotic χ^2 distribution with the corresponding number of degrees of freedom [67]. For the EW singlet model, a physical boundary imposes a lower bound on the model parameter under study. The confidence intervals reported are based on the

profile likelihood ratio where parameters are restricted to the allowed region of parameter space. This restriction of the likelihood ratio to the allowed region of parameter space is similar to the Feldman-Cousins technique [70] and provides protection against artificial exclusions due to fluctuations into the unphysical regime. However, the confidence interval is defined by the standard χ^2 cutoff, leading to overcoverage near the physical boundaries as demonstrated by toy examples. The Higgs boson couplings also have physical boundaries in the two-dimensional parameter space of the *2HDM*, which are treated in a similar fashion.

4.4.1 *2HDM*s indirect limits

The Higgs boson rate measurements in different production and decay modes are interpreted in each of the four types of *2HDM*s discussed in Section 1.4, taking the observed Higgs boson to be the light CP-even neutral Higgs boson h. This is done by rescaling the production and decay rates as functions of the coupling scale factors [ξ^V, ξ^u, ξ^d, ξ^ℓ]. These coupling scale factors are in turn expressed as a function of the underlying parameters, the two angles β and α, using the relations shown in Table 1.1.

The two parameters of interest correspond to the quantities $\cos(\beta-\alpha)$ and $\tan\beta$. The *2HDM* possesses an "alignment limit" at $\cos(\beta-\alpha)=0$ [71] in which all the Higgs boson couplings approach their respective SM values. The *2HDM* also allows for limits on the magnitudes of the various couplings that are similar to the SM values, but with a negative relative sign of the couplings to particular types of fermions. These limits appear in the regions where $\cos(\beta+\alpha)=0$. For example, in the Type II model the region where $\cos(\beta+\alpha)=0$, corresponding to the sign change $\alpha\to-\alpha$, has a "wrong-sign Yukawa limit" [72, 73] with couplings similar to the SM values except for a negative coupling to down-type quarks. The case for

the Flipped model is similar, but with a negative coupling to both the leptons and down-type quarks. An analogous "symmetric limit" [73] appears in the Lepton-specific model. Figure 4.11 shows the regions of the $[\cos(\beta-\alpha),\ \tan\beta]$ plane that are excluded at a CL of at least 95% for each of the four types of *2HDM*s, overlaid with the exclusion limits expected for the SM Higgs sector. The α and β parameters are taken to satisfy $0 \leq \beta \leq \pi/2$ and $0 \leq \beta - \alpha \leq \pi$ without loss of generality. The observed and expected exclusion regions in $\cos(\beta-\alpha)$ depend on the particular functional dependence of the couplings on β and α, which are different for the down-type quarks and leptons in each of the four types of *2HDM*s. There is a physical boundary $\xi^V \leq 1$ in all four *2HDM* types, to which the profile likelihood ratio is restricted. The data are consistent with the alignment limit at $\cos(\beta-\alpha) = 0$, where the light Higgs boson couplings approach the SM values, within approximately one standard deviation or better in each of the models. In each of the Type II, Lepton-specific, and Flipped models, at the upper right of the $[\cos(\beta-\alpha),\ \tan\beta]$ plane where $\tan\beta$ is moderate, there is a narrow, curved region or "petal" of allowed parameter space with the surrounding region being excluded. These three allowed upper petals correspond respectively to an inverted sign of the coupling to down-type fermions (τ lepton and b quark), leptons (τ and μ), or the b quark. These couplings are measured with insufficient precision to be excluded. There is no upper petal at high $\tan\beta$ in Type I as all the Yukawa couplings are identical.

For this analysis, only the range $0.1 \leq \tan\beta \leq 10$ was considered. The regions of compatibility extend to larger and smaller $\tan\beta$ values, but with a correspondingly narrower range of $\cos(\beta-\alpha)$. The confidence intervals drawn are derived from a χ^2 distribution with two parameters of interest, corresponding to the quantities $\cos(\beta-\alpha)$ and $\tan\beta$. However, at $\cos(\beta-\alpha) = 0$ the likelihood is independent of the model parameter β, effectively reducing the number of parameters of interest

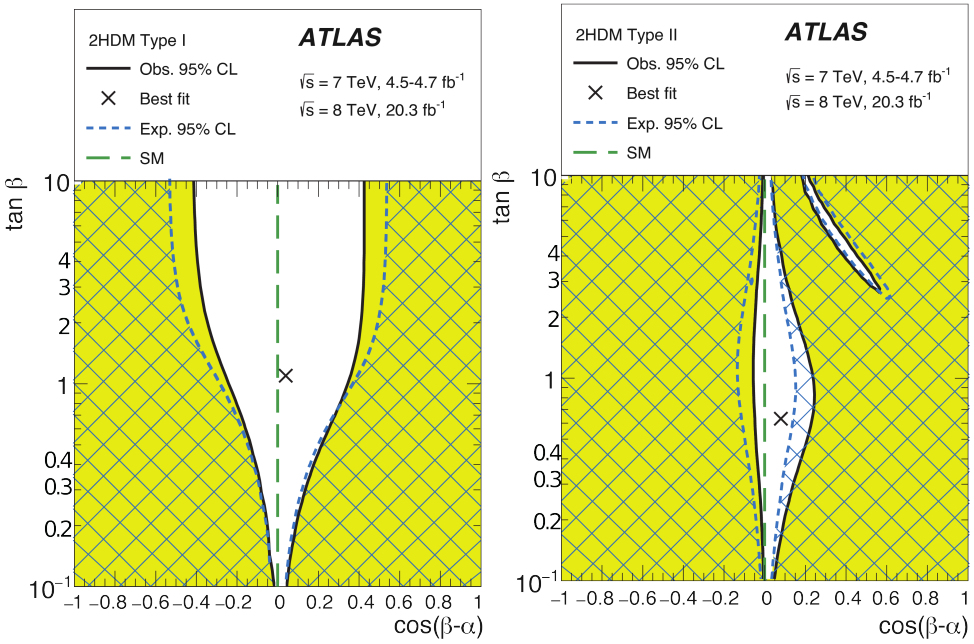

(a) Type I

(b) Type II

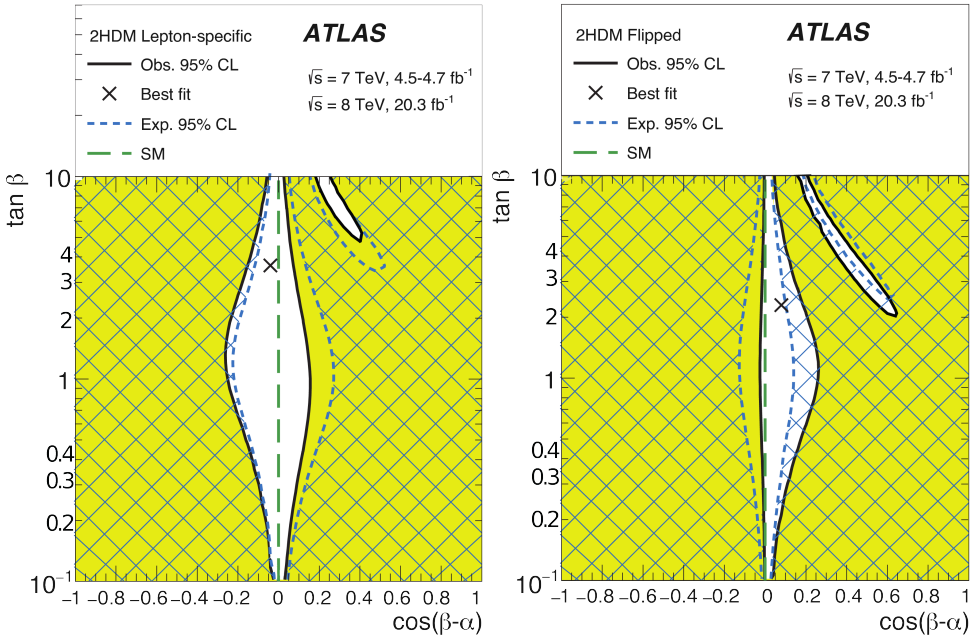

(c) Lepton-specific

(d) Flipped

Figure 4.11: Regions of the $[\cos(\beta-\alpha), \tan\beta]$ plane of four types of *2HDM*s excluded by fits to the measured rates of Higgs boson production and decays. The likelihood contours where $-2\ln\Lambda = 6.0$, corresponding approximately to the 95% CL (2 std. dev.), are indicated for both the data and the expectation for the SM Higgs sector. The cross in each plot marks the observed best-fit value. The light shaded and hashed regions indicate the observed and expected exclusions, respectively. The α and β parameters are taken to satisfy $0 \leq \beta \leq \pi/2$ and $0 \leq \beta - \alpha \leq \pi$ without loss of generality.

locally to one. Hence the test-statistic distribution for two parameters of interest that is used leads to some overcoverage near $\cos(\beta - \alpha) = 0$.

Chapter 5

The $H \to ZZ \to \ell^{\pm}\ell^{\mp}q\bar{q}$ channel

This thesis work presents the search for a heavy Higgs boson in the $H \to ZZ \to \ell\ell q\bar{q}$ channel in the Higgs boson mass range $200 < m_H < 1000$ GeV. The search presented here uses ATLAS data from the Large Hadron Collider (LHC) taken during 2012 at a center-of-mass energy of 8 TeV, corresponding to 20.3 ± 0.6 fb^{-1} of integrated luminosity. The present analysis builds on the previously published analysis of 2011 data for the high-mass (200 - 600 GeV) region [74, 75].

Besides the increased integrated luminosity and collision energy, major changes from the previous analyses include a re-optimized event selection, the inclusion of the vector boson fusion (VBF) production category and separate selections optimized for the case where the Z boson is boosted and the two quarks from the $Z \to qq$ decay are reconstructed as a single jet. The latter selection is important for Higgs boson masses above about 700 GeV.

5.1 Data and Monte Carlo samples

All Monte Carlo samples are generated with a center-of-mass energy of 8 TeV and passed through the simulation of the ATLAS detector [76]. In order to have a sufficient MC statistics, the "ATLFast II" simulation [77] is used for almost all samples with the exception of the signal and the Z/W+jets SHERPA samples with $p_{\mathrm{T}} > 280$ GeV. To account for the differences in the distribution of pile-up events between the MC simulation and data, the MC samples are reweighted according to the standard procedure.

5.1.1 Data sample

The data used in this analysis were recorded by the ATLAS detector during 2012 proton run and comprise 20.3 ± 0.6 fb^{-1} of integrated luminosity. The data are subsequently required to satisfy several conditions ensuring that the ATLAS detector was operational with good efficiency while that data were collected. This is implanted using a Good Run List (GRL) based on the ATLAS Data Quality (DQ) flags. The GRL used is the standard ATLAS "All_Good" one.

5.1.2 Signal samples

In the case of a SM-like heavy Higgs, the signal samples can be divided into two regions in Higgs mass m_H based on the SM Higgs decay width Γ_H: 200 GeV $< m_H <$ 400 GeV and 400 GeV $\leq m_H \leq$ 1000 GeV. The distinction is well-motivated within the SM by theoretical considerations related to the increase of the Higgs width with the Higgs mass (see chapter 12 of Ref. [78]). At next-to-leading-order (NLO) in QCD, the line shape of an unstable particle is typically described in MC generators by a Breit-Wigner (BW) distribution. In the $200 < m_H < 400$ GeV region, ggF and VBF POWHEG BOX [80–82] samples were generated in 20

GeV steps with the line shape described by a running BW distribution. However, for $m_H > 400$ GeV, the Higgs boson line shape is no longer well-described by a BW distribution. The issue has been addressed in detail in Refs. [83–85]. For $m_H \geq 400$ GeV, a more correct description of the Higgs boson line shape, known as the complex pole scheme (CPS), is used. POWHEG BOX samples using CPS were generated in 20 GeV steps in the range $400 \leq m_H \leq 600$ GeV and in 50 GeV steps in the range $600 \leq m_H \leq 1000$ GeV.

Another effect that becomes very large with increasing Higgs boson width, and thus with the Higgs boson mass in the SM, is the interference between the signal and the non-resonant ZZ background. This interference strongly affects the production cross-section as well as kinematic distributions. It has been shown that this effect cannot be neglected for $m_H \gtrsim 400$ GeV [85–87]. The interference effect is known only at leading order (LO) in QCD and is not included either in the ggF or in the VBF signal samples. Consequently, to account for the interference effect, both the ggF and VBF signal samples must be reweighted.

Reference [78] addresses the interference effect including a prescription to compute theoretical uncertainties due to missing higher-order terms in the presently available estimation. In the case of ggF signal, the interference weights have been computed using GG2VV [83,88]. These weights are applied to the CPS POWEHEG samples. For VBF samples, the REPOLO (REweighting POwheg events at Leading Order) tool, provided by the authors of VBFNLO [78,89,90] is used to weight CPS POWHEG samples to account for the interference effect as well as to estimate the sale and modelling uncertainties associated with the procedure.

In addition to the CPS samples, ggF and VBF POWHEG samples with the line shape described by a BW distribution with width fixed to 1 GeV have been generated in the range $400 \leq m_H \leq 1000$ GeV at the masses as the CPS samples. This is referred as the narrow-width approximation (NWA). Because of the narrow

m_H	$\sigma\times$ BR [pb]		m_H	$\sigma\times$ BR [pb]		m_H	$\sigma\times$ BR [pb]	
[GeV]	ggF	VBF	[GeV]	ggF	VBF	[GeV]	ggF	VBF
200	0.1699	0.0208	400	0.073609	0.006408	600	0.0199158	0.0024801
220	0.1597	0.0204	420	0.073609	0.006408	650	0.0089709	0.0020394
240	0.1424	0.0185	440	0.0531432	0.0051313	700	0.0091829	0.00253833
260	0.12535	0.01629	460	0.0446391	0.0051103	750	0.00641312	0.00214112
280	0.11258	0.01438	480	0.0373734	0.004199	800	0.00457449	0.00182021
300	0.103507	0.012695	500	0.0314335	0.0038245	850	0.00331632	0.00156764
320	0.098107	0.011238	520	0.0262974	0.0034784	900	0.00244959	0.00244959
340	0.098083	0.009992	540	0.02210424	0.00318184	950	0.00184016	0.00119133
360	0.094103	0.008418	560	0.01867942	0.00292666	1000	0.0014048	0.00105316
380	0.084652	0.007273	580	0.01575684	0.00268686			

Table 5.1: Cross section times branching ratio ($\sigma \times$BR) of $H \to ZZ$ for $200 \leq m_H \leq 400$ GeV.

width, the interference effect between signal and continuum backgrounds is negligible over the full mass range [86,87]; thus, interference weights are not applied to these samples.

The SM signal cross section has been computed to next-to-next-to-leading order (NNLO) [91–96] in QCD for the ggF process. NLO electroweak (EW) corrections are also applied [97, 98], as well as QCD soft-gluon resummations up to next-to-next-to-leading logarithms (NNLL) [99]. These calculations are detailed in Refs. [100–102], and assume factorization between QCD and EW corrections. Full NLO QCD and EW corrections [103–105] and approximate NNLO QCD corrections [106] are used to calculate the cross sections for VBF signal production. These cross sections are used for the BW and CPS samples. Table 5.1 shows the cross sections for both ggF and VBF production processes for each mass point.

For the interpretation of the results in terms of a heavy SM-like Higgs boson, the CPS samples are used since they reflect the width expected in the SM Higgs boson case, while for the model-independent narrow-width resonance results the NWA samples are of course used. For the *2HDM* interpretation, it is slightly more com-

plicated since the natural width of the heavy Higgs boson varies across parameter space. In this case, the NWA samples are used but a Gaussian smearing is applied to the reconstructed invariant mass distribution to reflect the natural width at the given model point, as described in Section 5.9.2, which is significant given the good invariant mass resolution (see Section 5.6.1). In the EWS interpretation, the width is scanned in the range $\Gamma_{H,\mathrm{NWA}} < \Gamma_H \leq \Gamma_{H,\mathrm{SM}}$ in steps of $0.1 \times \Gamma_{H,\mathrm{SM}}$ by reweighting the SM samples to account for both the width scaling and the relative interference effect (which of course varies with width). The width weights are determined using PowHeg with a BW line shape, while the interference is taken into account using gg2vv (Repolo) in the ggF (VBF) case.

5.1.3 Background samples

Several background processes give rise to final states with signatures similar to the above signal processes. The dominant background process is Z+jets production with the Z boson decaying leptonically, with a significant contribution from top (mainly $t\bar{t}$) when two b-tagged jets are required. These backgrounds are taken from MC but corrected to data as described in Section 5.4.

The subdominant contributions from diboson ($ZZ/WZ/WW$) production and W+jets production are taken directly from MC. The small QCD multi-jet background is derived from data as described in Section 5.4.3. The background processes are modelled with several different event generators, as summarized in Table 5.2. The relevant cross section times branching ratio for each process, taken from the most precise theory calculation available, is also given.

Process	Generator	$\sigma\times$ BR	N_{events}
Vector boson + jets			
$W \to \ell\nu$	SHERPA 1.4.1	12.07 nb	390M
$Z/\gamma^* \to \ell\ell$ ($m_{\ell\ell} > 40$ GeV)	SHERPA 1.4.1	1.24 nb	66M
$Z \to \ell\ell$	ALPGEN	1.16 nb	
Top-quark			
$t\bar{t}$	POWHEG	252.89 pb	100M
t-channel	ACERMC	87.76 pb	9M
s-channel	POWHEG	5.61 pb	6M
Wt-channel	POWHEG	22.37 pb	20M
Diboson			
WW	POWHEG	52.44 pb	10M
WZ ($m_{\ell\ell} > 20$ GeV + 1 boson decaying hadronically)	POWHEG	9.241 pb	10M
ZZ ($m_{\ell\ell} > 20$ GeV + 1 boson decaying hadronically)	POWHEG	3.171 pb	7.5M

Table 5.2: Monte Carlo generators used for modelling background processes and the cross-section times branching ratio ($\sigma \times$ BR) used to normalize the different processes at $\sqrt{s} = 8$ TeV. Branching ratios correspond to the decays shown.

5.1.3.1 Vector boson (V+jets) production

The $W/Z+ \geq 1b$, $W/Z+ \geq 1c$ and $W/Z+ \geq 1$ light jet events are produced with the SHERPA generator [107] with massive b/c quarks and interfaced with CT10 PDFs. Filters are used to select events containing $b-$, $c-$ and light-flavoured hadrons. This allows increasing the statistics of the critical V+heavy-flavor samples within the available resources. Additional samples are generated with the vector boson transverse momentum required to be within one of the ranges $40 < p_{\mathrm{T}}^{V} < 70$, $70 < p_{\mathrm{T}}^{V} < 140$, $140 < p_{\mathrm{T}}^{V} < 280$, $280 < p_{\mathrm{T}}^{V} < 500$ or $p_{\mathrm{T}}^{V} > 500$ GeV. This allows for higher statistics in the high p_{T}^{V} (and hence high invariant mass) regions. For both these reasons, the SHERPA samples are used in preference to the ALPGEN ones, since the latter have insufficient statistics in the high invariant mass region

and tagged ggF category.

The majority of the V+jets samples are simulated using fast simulation; the exceptions are the highly-boosted samples without b-hadrons and those in which the vector boson decays to tau leptons where an accurate description of the detector response is particularly important.

While the SHERPA generator is used to describe the Z+jets process in the resolved and merged categories for the ggF analysis, ALPGEN is used for the VBF analysis since it is found to better model the higher jet multiplicities of the VBF events and related quantities. The ALPGEN event generator is interfaced to PYTHIA for the hadronization. The ALPGEN samples are split depending on both the number of partons (Np) produced in addition to the Z boson (Np = 0,1,2,3,4,5, where Np = 5 also includes events with more than 5 partons) and the flavor of the additional partons (Z+light, $Z + cc$ and $Z + bb$). Any possible overlap of events between these samples is removed using the HFOR tool, which vetoes events depending on the opening angle between the heavy flavour quarks.

5.1.3.2 Top quark pair and single top quark production

Samples of top quark pairs are generated with POWHEG [108–110] interfaced to PYTHIA with a filter which requires that at least one W boson top quark daughter decays into a charged lepton (e, μ, τ). Parton showering and hadronization is generated according to the Perugia2011C tune which uses the CTEQL1 PDF. For the single-top processes, s-channel and Wt-channel samples are generated with POWHEG+PYTHIA and the t-channel sample is generated with ACERMC+PYTHIA. All single-top channels use the CTEQL1 PDF and the Perugia2011C tune.

5.1.3.3 Diboson production

The diboson background includes processes which contain two vector bosons in the final state (WW, WZ, ZZ). The background from ZZ production, where one Z boson decays leptonically and the other hadronically, is largely irreducible since it gives rise to the same final state as the signal process. There is also some contribution from WZ production where the Z boson decays leptonically and the W boson decays hadronically; this is reduced via the dilepton invariant mass requirement. The contribution to the background from WW production is minimal. The PowHeg generator provides a next-to-leading-order (NLO) estimate, relying on the CT10nlo PDF set and interfacing with the Pythia8 parton shower and hadronization model. The estimated NLO cross sections are calculated directly by PowHeg and are used to normalize the different processes. They have been found to be in good agreement with those determined from MCFM using a configuration in which the factorization and renormalization scales of the processes are set to half the diboson invariant mass and the CT10nlo PDF set is used. For the processes with one leptonically decaying Z boson, a cut on $m_{\ell\ell} > 20$ GeV is applied for consistency with the PowHeg samples. For the WW and ZZ processes, the PowHeg cross section does not include the contributions from gluon-gluon initiated processes; these are thus computed and added back to the cross section using the MCFM program. The uncertainties on the cross sections are derived in a jet-multiplicities dependent way and presented in Section 5.5.2.3.

5.1.3.4 SM $Zh, h \to bb$ production

The SM $Zh, h \to bb$ production can potentially contribute to the analysis by entering into the dijet invariant mass sidebands in the tagged channel. These events are modelled using Pythia8 for the $qq \to Zh$ and PowHeg for $gg \to Zh$.

5.2 Physics objects selection

The first step in the selection procedure is to identify the basic physics objects that will form the building blocks of the analysis. The reconstruction of physics objects follows as closely as possible the recommendations of the respective physics performance groups in ATLAS.

5.2.1 Muons

Muons are identified using the MuID (STACO) chain for ggF (VBF) channel. Here, tracks are reconstructed in the muon spectrometer (MS) and are then extrapolated to the beam pipe and an attempt is made to find a matching inner detector track. If such a match is found, a combined muon (CB) is formed incorporating the information from both detectors. To recover muons that did not leave a full track in the inner detector and muon spectrometer, three additional muon categories are defined: segment-tagged muons (ST), calorimeter-tagged muons (CaloTag) and standalone muons (SA) [111]. In the first of these, inner detector tracks that are not used in the combinations are extrapolated to the muon spectrometer and "tagged" as muons if they can be matched to a track segment in the first station. In the second category, an inner detector track is identified as a muon if it can be associated to an energy deposit in the calorimeter which is consistent with being generated by a minimum-ionizing particle. Muons in this category are used to recover acceptance in uninstrumented regions of the muon spectrometer. Finally, standalone muons have tracks only in the muon spectrometer. For these muons, the direction of flight and the impact parameter at the interaction point are determined by extrapolating the MS track back to the point of closest approach to the beam line, taking into account the energy loss of the muon in the calorimeters. Such muons are used to increase the acceptance in $|\eta|$ beyond the inner detector

Quality	Family	Kinematics
Loose	CB+ST	$p_{\mathrm{T}} > 7$ GeV, $\|\eta\| < 2.7$
	CaloTag	$p_{\mathrm{T}} > 20$ GeV, $\|\eta\| < 0.1$ ($\Delta R > 0.1$ from CB/ST/SA muons)
	SA	$p_{\mathrm{T}} > 7$ GeV, $2.5 < \|\eta\| < 2.7$
Medium	CB+ST	$p_{\mathrm{T}} > 25$ GeV, $\|\eta\| < 2.5$

Table 5.3: Definition of "loose" and "medium" muon quality in terms of the muon family and kinematic requirements

acceptance. All four muon categories mentioned above are used in this analysis. Leptons in this analysis are categorized as either "loose" or "medium"; for muons, these definitions are summarized in Table 5.3.

Following the recommendation of the Muon Combined Performance (MCP) group, the inner detector track associated with the muon is required to pass a series of additional requirements based on the number of hits and holes (absence of hits) in the various layers of the inner detector. Muons from cosmic rays are suppressed by requiring that the impact parameter with respect to the primary vertex satisfy $|d_0| < 0.1$ mm and $|z_0| < 0$ mm, where d_0 and z_0 are the transverse and longitudinal impact parameters, respectively. To avoid muons associated with jets, such as those originating from semi-leptonic decays of b-hadrons, muon candidates are required to be isolated by demanding that the sum of the inner detector track momenta in a cone $\Delta R = \sqrt{\Delta\eta^2 + \Delta\phi^2} < 0.2$ around the muon (ignoring the track associated to the muon itself) be less than 10% of that of the muon. The previous two cuts are not applied to standalone muons which are outside the inner detector acceptance and, by definition, do not have an inner detector track. The muon selection is summarized in Table 5.4

The muon momenta in Monte Carlo are smeared to better describe the data and weights are applied to account for the difference in offline and trigger efficiencies.

Identification	Loose or Medium (see Table 5.3)
Inner detector	$N_{\text{hits}}^{\text{pixel}} + N_{\text{dead}}^{\text{pixel}} > 0$ $N_{\text{hits}}^{\text{SCT}} + N_{\text{dead}}^{\text{SCT}} > 4$ $N_{\text{holes}}^{\text{pixel}} + N_{\text{holes}}^{\text{SCT}} < 3$ $\lvert\eta\rvert < 1.9$: $N_{\text{tot}}^{\text{TRT}} > 5$ and $0.1 < N_{\text{outliers}}^{\text{TRT}} < 0.9 \times N_{\text{tot}}^{\text{TRT}}$ where $N_{\text{tot}}^{\text{TRT}} = N_{\text{hits}}^{\text{TRT}} + N_{\text{outliers}}^{\text{TRT}}$
Cosmic rejection	$\lvert d_0\rvert < 1$ mm (not for SA muons) $\lvert z_0\rvert < 10$ mm (not for SA muons)
Track isolation	$\sum_{\text{tracks}} p_{\text{T}} \left(\Delta R < 0.2\right) / p_{\text{T}}^{\mu} < 0.1$ (not for SA muons)

Table 5.4: Summary of muon selection. $N_{\text{hits}}(N_{\text{holes}})$ represents the number of hits (missing hits) in a particular subdetector of the inner tracker, while N_{dead} refers to the number of dead sensors crossed by the muon in a particular subdetector.

In addition, the muon isolation efficiency is also corrected.

The p_{T} and η distributions of the muons forming the leptonic Z boson candidate are shown in Figure 5.1 after the corrections above.

5.2.2 Electrons

Electrons are identified from electromagnetic calorimeter clusters reconstructed with the standard ATLAS sliding window algorithm [37] that are matched to tracks in the inner detector, *i.e.* author "Electron". The electron candidates are required to satisfy the "VeryLoose" quality requirements of the ATLAS electron-likelihood identification. Throughout this analysis, an electron's transverse momentum is reconstructed using the cluster energy measured in the calorimeter and its direction from the associated track. The pseudorapidity η of the electron is taken from the cluster whenever the candidate's position with respect to the calorimeter is

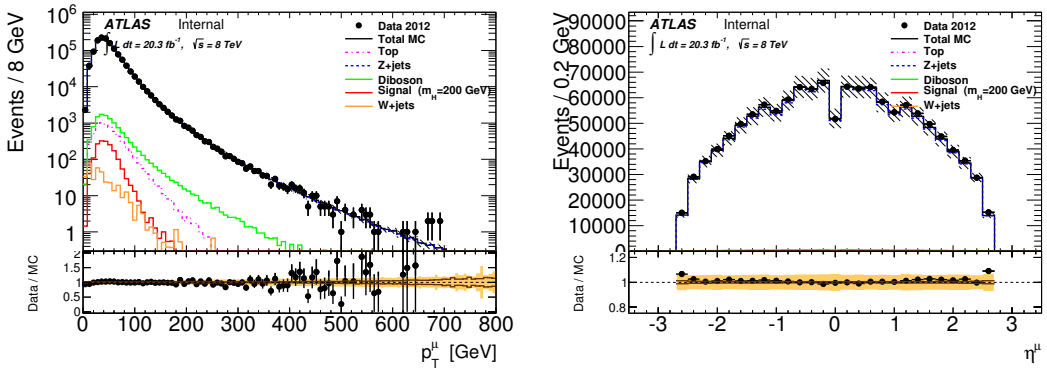

(a) (b)

Figure 5.1: The p_{T} and η distributions of the two muons forming the leptonic Z boson candidate after the Z boson mass selection $83 < m_{\mu\mu} < 99$ GeV. In this and all subsequent plots the MC is normalized to the luminosity of the data and the background are taken from the final fit. The shaded (orange) band in the main (ratio) plot shows the quadratic sum of the MC statistical uncertainty (indicated by the brown histogram on the ratio) and the shape-dependent systematic uncertainty on the total MC background.

required, *e.g.* in the acceptance selection or in the inputs to the smearing and correction tools described below, but from the track in all other cases (such as in calculation invariant masses). To ensure high reconstruction and trigger efficiencies, the candidates are required to lie within the pseudorapidity range $|\eta_{\mathrm{cluster}}| < 2.47$ to keep within the region of precision EM measurement and to have a transverse energy (after energy correction/smearing) $E_{\mathrm{T}} > 25$ GeV (7 GeV) for "medium" ("loose") electrons. The "medium" and "loose" definitions for electrons differ only in the E_{T} requirement; the electron quality requirement for both is "VeryLoose". Electrons in the crack region ($1.37 < |\eta| < 1.52$) are included in the analysis to maximize the electron reconstruction efficiency.

To ensure the electrons are isolated, it required that the sum of the inner detector track transverse momenta in a cone of $\Delta R < 0.2$ around the electron (excluding the track associated to the electron itself) is less than 10% that of the electron itself.

Identification	Author: Electron IsEM: VeryLooseLH
Kinematic cuts	$E_{\mathrm{T}} > 25$ GeV (medium), $E_{\mathrm{T}} > 7$ GeV (loose) $\lvert\eta_{\mathrm{cluster}}\rvert < 2.47$
Cleaning	`BADCLUSELECTRON` quality mask
Track isolation	$\sum_{\mathrm{tracks}} p_{\mathrm{T}} \left(\Delta R < 0.2\right) / p_{\mathrm{T}}^{e} < 0.1$

Table 5.5: Summary of electron selection.

Events with LAr calorimeter data integrity errors are flagged and rejected on an event-by-event basis. Each electron candidate also has a set of object quality flags; candidates that fail any of the selections in the `BADCLUSELECTRON` mask are rejected.

The electron momenta in Monte Carlo are corrected for both energy calibration and resolution in order to better describe the data. In addition, weights are applied to account for the difference in reconstruction and identification efficiencies. These corrections follow the egamma group recommendations. Because we require two leptons and the electron trigger efficiency is very high (relative to offline), a trigger efficiency scale factor is not applied.

The electron selection is summarized in Table 5.5. The p_{T} and $|\eta|$ distributions of electrons forming the leptonic Z boson candidate are shown in Figure 5.2 after the corrections above. It can be seen that the simulation after the corrections provides a reasonable description of data.

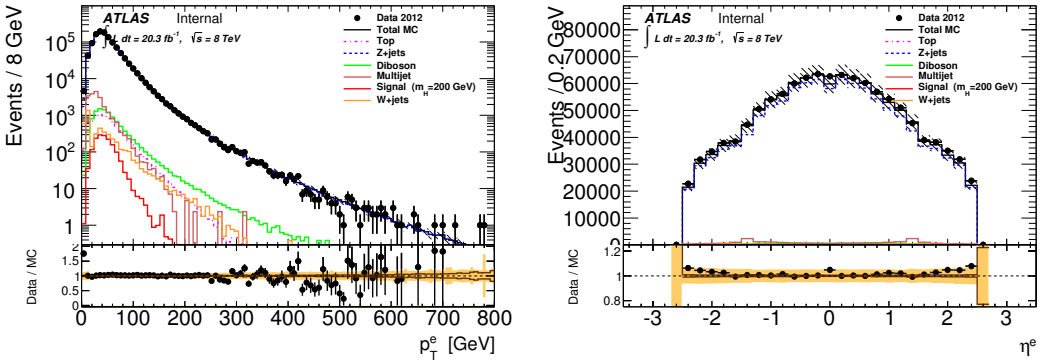

(a) (b)

Figure 5.2: The p_{T} and η distributions of the two electrons forming the leptonic Z boson candidate after the Z boson mass selection $83 < m_{ee} < 99$ GeV.

5.2.3 Jets

Jets are reconstructed from topological clusters [34] using an anti-k_{T} algorithm [38] with a distance parameter $R = 0.4$. The topological clusters are then corrected from electromagnetic scale to the hadronic energy scale using a p_{T}- and η-dependent jet energy scale (JES) determined from Monte Carlo simulations [112, 113]. The corrected jets are available as the `AntiKt4TopoEMJets` jet collection. The jet energy scale is shifted due to effect of pileup interactions, leading to an additional additive offset. This is corrected for by applying an offset correction using a dedicated tool, *i.e.* the `JetCalibrationTool`. A global sequential calibration is also applied, which improves the invariant mass resolution by 8%, even though it also changes the background shape slightly. Typical RMS values for the dijet invariant mass are around 18 GeV, with RMS/mean around 0.17.

Two different jet selections are used to separate $gg\mathrm{F}/V\mathrm{BF}$ production topologies and to reconstruct the Higgs boson candidates. The former, referred to as "veto" jets, are required to have $|\eta| < 4.5$ and $p_{\mathrm{T}} > 20(30)$ GeV for $|\eta| < 2.5$ ($2.5 < |\eta| < 4.5$). The increased threshold in the forward region significantly re-

Identification	Anti-k_{T} $R = 0.4$ topological jets
Kinematic cuts	$p_{\mathrm{T}} > 20$ GeV $\|\eta\| < 2.5$
Quality	Looser quality cuts
Pile-up	$\|\mathrm{JVF}\| > 0.5$
Cleaning	Reject events pointing to LAr hole or hot tile cell

Table 5.6: Summary of "signal" jet selection

duces the contribution from fake jets produced by pile-up. The "signal" jets used to reconstruct the Higgs boson are further required to be within $|\eta| < 2.5$.

The jets are required to pass the standard "looser" quality cuts for ATLAS jets. In addition, events that contain jets within the LAr hole or pointing to the tile cell are rejected.

Jets originating from pile-ip are removed by requiring that at least 50% of the tracks associated with the jet (within $\Delta R = 0.4$ around the jet axis) originate from the primary vertex. This is implemented as a cut on the absolute value of the "jet vertex fraction" $|\mathrm{JVF}| > 0.5$ for jets with $p_{\mathrm{T}} < 50$ GeV and $|\eta| < 2.4$.

The jet selection is summarized in Table 5.6.

The p_{T} and η distributions of "veto" jets are shown in Figure 5.3 for events containing at least 2 signal jets. It can be seen that the simulation after the corrections provides a reasonable description of the data.

5.2.3.1 Jet flavour labelling

The flavor of reconstructed MC jets is determined by hadrons within a cone of $R = 0.4$ around the jet axis. If there is a B-hadron within this cone the jet is

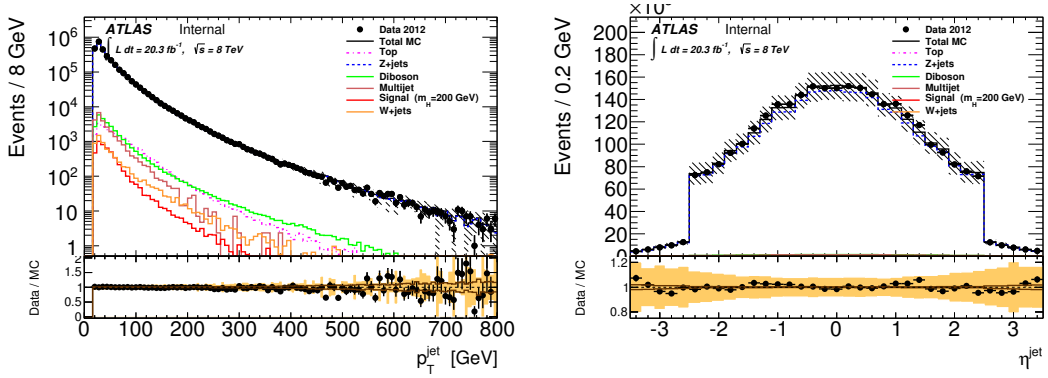

(a) (b)

Figure 5.3: The p_{T} and η distributions of "veto" jets after the $Z \to \ell\ell$ boson mass selection, at least two "signal" jet and $\frac{E_{\mathrm{T}}^{\mathrm{miss}}}{\sqrt{H_{\mathrm{T}}}}$ cut.

labeled as b; else if there is a D-hadron within the cone it is labelled as c. If neither of these is found in the cone, it labelled as a light jet.

5.2.3.2 The identification of b-jets

Jets which originate from b quarks are identified using algorithms which exploit the long lifetime of b hadrons. The b-tagging algorithm MV1c [114–116] is used, which combines information from an impact parameter based algorithm, an inclusive secondary vertex finder and a $b \to c$ hadron decay chain fit into a single neural network based discriminant w, such that jets with a higher w are more likely to be b-jets. Efficiencies and rejection factors determined in semi-leptonic $t\bar{t}$ events with a jet p_{T} threshold of 20 GeV for the calibrated operating point are shown in Table 5.7. This analysis uses the 70% operating point to select b-jets.

The w distribution must be calibrated such that the b-tagging efficiency in MC matches that in data. A combinatorial likelihood method has been used in dilepton $t\bar{t}$ events to calibrate the b-jet efficiency. The c and light jet efficiencies were calibrated via D^* and dijet samples respectively. Previously, the b-tag selection

Operating point	b-jet eff. (%)	c-jet RF	τ-jet RF	l-jet RF
80	79.85	3.04	6.40	29.12
70	70.00	5.34	14.90	135.76
60	59.99	10.45	33.92	453.53
50	49.99	26.22	120.33	1388.28

Table 5.7: The efficiencies for the available calibrated operating points for the MV1c algorithm. These values has been determined in semi-leptonic $t\bar{t}$ events with a jet p_{T} threshold of 20 GeV. RF stands for "rejection factor", which is defined as the reciprocal of the efficiency.

was calibrated only for specific values of the w requirement, but for the current analysis, calibration has been performed for the full w distribution of the MV1c tagger, in the binning given in Table 5.7. This is referred to as *continuous* or *pseudo-continuous*. This allows using the shape of the MV1c distribution to constrain the normalization of the various light and heavy flavour components of the Z+jets background (see Section 5.4.1.1). The MV1c algorithm is used in preference to the previous MV1 algorithm since it has better charm rejection and thus allows to better constrain the $Z + c$-jet background.

The data-to-MC calibration scale factors above were derived with respect to Pythia6 for b-jets and Pythia8+EvtGen for c-jets. However, as may be expected, the b-tagging efficiency has been found to be generator dependent and consequently MC-to-MC scale factors has been derived to take this dependence into account. These correction factors, along with an associated systematic uncertainty (see Section 5.5.1.6), are applied in the current analysis to correct the MC efficiency from that in the MC used to measure the scale factors to the specific MC generators used in the analysis.

5.2.3.3 Truth tagging

Due to the powerful discrimination of the MV1c algorithm against non-b-jets, it is difficult to produce enough simulated MC events to have reasonable statistics after requiring 2 b-tagged jets for events without b-jets. A method known as "truth tagging" is therefore used in 2 b-tag events in which neither of the selected jets is a truth-matched b-jet. Truth tagging is a method by which a random MV1c value above the operating point is generated for a given jet. This is done by creating a "random efficiency" obtained from sampling a cumulative distribution built from the tagging efficiency above the operating point and assigning the MV1c value corresponding to the random efficiency generated to the jet in question. The efficiencies used to build the cumulative distribution are parameterized as a function of the flavour, transverse momentum and pseudorapidity of the given jet as well as the process type. After the generation of a random MV1c value, every jet will, by construction, satisfy the loose b-jet cut, so the event is then weighted by the efficiency of each jet to actually pass the b-jet selection being used. For events in which one of the leading two jets matches (is close in ΔR to) a b-hadron from the Monte Carlo truth information, this procedure is not used; instead, the original MV1c w values of each jet are used directly. Such events are to have been "direct tagged".

The truth tagging method ignores correlations in the tagging efficiencies of jets in the same event. For events with two c-jets, a bias in the tagging efficiency as a function of $\Delta R\,(cc)$ has been observed and a correction has been derived, which is applied along with an associated uncertainty (see Section 5.5.1.6).

Truth tagging is only applied to the dominant Z+jets background.

5.2.3.4 Energy corrections to the selected b-jets

Two corrections are applied to selected signal b-jets. The first, "muon-in-jets", corrections accounts for energy lost due to semi-leptonic decays of b-hadrons to muons. If a muon is identified within $\Delta R < 0.4$ of a b-tagged jet with $p_{\mathrm{T}} > 4$ GeV and passes the inner detector hit requirements for muons, then its four-momentum is added to that of the jet, after subtracting off the energy the muon deposited in the calorimeter. If more than one such muon is found, the one closest to the jet is used. This improves the dijet invariant mass distribution on top of the GSC.
The second, "p_{T}-reco", correction compensates for a bias on reconstructed jet energy. Due to energy mismeasurements, jets can migrate up or down in p_{T}; but where the true jet spectrum is rising, they will more often migrate down, and vice-versa if the spectrum is falling. After this correction is applied, the signal dijet mass resolution improvement from the GSC compared to only using the EM+JES calibration is 3.5%.

5.2.3.5 Jet mass

The "merged", *i.e.* boosted, channel of this analysis is explained in Section 5.3.3.2. In this channel the mass of a single anti-k_{T} $R = 0.4$ jet is used to discriminate between signal and background: the former is expected to give a peak at m_Z over a smooth background in the m_j spectrum, as shown in Figure 5.13. In order to have a reliable jet mass (and hence to have the possibility to use it to discriminate between signal and background), this variable needs to be calibrated. The calibration has been carried out studying the jet mass response, *i.e.* the $\frac{m_{\mathrm{reco}}}{m_{\mathrm{truth}}}$ as a function of several variables and in both QCD and signal samples. Deviations of the jet mass response from unity were found as high as 15% for p_{T} around 200 GeV and even bigger for lower p_{T}. Once the calibration is applied, the jet mass response is very near to 1 in the whole kinematic range. Figure 5.4 shows an example of the impact

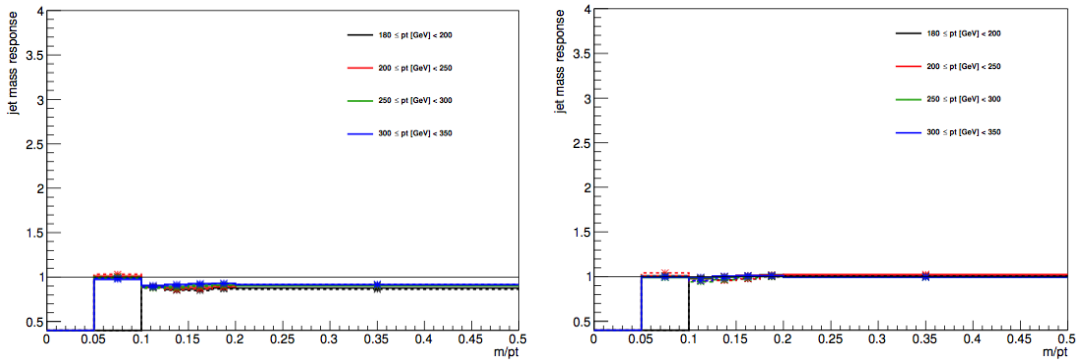

(a) uncalibrated mass (b) calibrated mass

Figure 5.4: An example of the jet mass response before (left) and after (right) the mass calibration. The jet mass response is shown for jets with different p_{T}, $0.6 < |\eta| < 0.8$ and as a function of $\frac{m}{p_{\mathrm{T}}}$

of the jet mass calibration. The mass calibration is applied to all the jets taken into account in the merged channel of the analysis.

5.2.4 Missing transverse energy

Missing transverse energy $E_{\mathrm{T}}^{\mathrm{miss}}$, caused by the presence of neutrinos in an event, is an important characteristic to help separate signal from background. Since the $H \to ZZ \to \ell\ell qq$ signal has little genuine $E_{\mathrm{T}}^{\mathrm{miss}}$, an upper limit on $E_{\mathrm{T}}^{\mathrm{miss}}$ is applied to reduce the background from $t\bar{t}$ events.

The `METRefFinal` variable is used, including all standard terms described in Section 3.5. Each of these terms, with the exception of γ and τ terms, is recalculated from each object synchronizing all corrections and systematic variations for the objects described above. For the γ and τ terms, the precalculated terms in the AOD/D3PD are used. Specific corrections for the jet-egamma overlap have also been used.

5.2.5 Overlap removal

Since it may happen that the same tracks or calorimeter energy deposits are used in multiple reconstructed objects, one must careful to avoid double-counting. This is called "overlap removal".

After all above selections are applied, jets belonging to the "veto" collection within $\Delta R < 0.4$ of an electron are removed. Next, fake jets caused by misreconstructed muon energy deposits in the calorimeter are removed. For jets within $\Delta R < 0.4$ of a muon, the JVF variable is recalculated without the muon track. The jet is removed if this "corrected" JVF is less than 0.5 or if it happens to have just a single associated track with $p_{\mathrm{T}} > 1$ GeV. Next, any muon within $\Delta R < 0.4$ of a jet with $p_{\mathrm{T}} < 20$ GeV is removed. This procedure removes muons from semi-leptonic decays of heavy flavour hadrons, which are likely to have low p_{T}, while keeping events in which a muon deposits significant energy in the calorimeter and fakes a jet or a muon from the Z boson happens to fall on top of the jet. It was seen to yield a significant increase ($\sim 10\%$) in the reconstruction efficiency for $ZH \to \ell\ell bb$ events, which have a similar topology to the signal here at high $p_{\mathrm{T}}^{\ell\ell}$. As the final step of this procedure, any electron within $\Delta R < 0.2$ of a non CaloTag muon is removed; for CaloTag muons, the muon is removed instead.

The overlap removal procedure is summarized in Table 5.8.

5.3 Event selection

The event selection has been optimized in order to maximize the expected significance of the signal over the background. Trigger requirements and a set of preselection cuts are applied first, then a dilepton system compatible with the $Z \to \ell\ell$ process is selected. The analysis is then split into two categories, one

Case	Order	Keep μ	Keep e	Keep jet
$\Delta R(j, e) < 0.4$	1	-	Yes	No
$\Delta R(j, \mu) < 0.4$	2	$N_{\text{trk}} \leq 1$ or JVF(no μ) < 0.5 or $p_{\text{T}}^{\mu} > 20$ GeV	-	$N_{\text{trk}} > 1$ and JVF(no μ) ≥ 0.5
$\Delta R(\mu, e) < 0.2$	3	if not CaloTag μ	if CaloTag μ	-

Table 5.8: Overlap removal hierarchy and the order in which the ambiguity is checked. N_{trk} is the track multiplicity of ghost-matched tracks that have $p_{\text{T}} > 1$ GeV and are compatible with the first primary vertex.

designed to select signal events produced by gluon-gluon fusion and the other selecting events produced by vector boson fusion. In both, the hadronically-decaying Z boson is selected by requiring that the leading two jets have an invariant mass close to that of a Z boson. This is called "resolved" category. In the high-mass region ($m_H \geq 700$ GeV) of the ggF analysis, a separate "merged" category is used in which the $Z \to qq$ decay is reconstructed as a single, high-mass jet. This recovers some of the efficiency loss in the events where the Z boson has a large boost.

5.3.1 Trigger and preselection

Events are selected using the single and deletion triggers with the lowest available p_{T} thresholds that were operated without a preschool throughout 2012. For single electrons, the trigger requirement is a logical OR of `e24vhi_medium1` and `e60_medium1`, while the dielectron trigger is `2e12Tvh_loose1`. For muons `mu24i_tight` and `mu36_tight` are used as single muon triggers and the dimuon trigger is `2mu13`. One or both of the leptons selected in the offline analysis, as described in Section 5.2.1 and in Section 5.2.2, must be matched to trigger leptons for single- and dilepton triggers respectively.

After the trigger selections, a "preselection" is made to ensure good data quality. Data events must pass the standard "`All_Good`" GRL requirement outlined

in Section 5.1.1. Next, any data events that are incomplete, corrupted or have problems in the calorimetric system noted by the flags `larError`, `tileError` and `coreFlags` or `TileTripReader` are removed.

The primary vertex must have at least three associated tracks with $p_{\mathrm{T}} > 150$ MeV. Mismeasured jets, arising from hardware problems, cosmic-ray showers and LHC beam conditions, can give rise to fake E_{T}^{miss} in the event. To avoid this, a MET cleaning procedure is applied: if an isolated low-quality jet, *i.e.* characterized as bad by the "Looser" criteria, with $p_{\mathrm{T}} > 20$ GeV is found, the event is rejected. In addition, events with jets falling in the LAr hole or pointing to hot tile cells are rejected.

5.3.2 $Z \to \ell\ell$ selection

The first step of the selection is to identify a $Z \to \ell\ell$ candidate. There must be two same-flavour, isolated leptons, one of which must pass the "medium" requirements and the other the "loose" requirements, as described in Section 5.2.1 and in Section 5.2.2 for muons and electrons respectively. If there are two muons, they must have opposite sign, but this requirements is not applied for electrons due to their higher rate of charge misidentification. The event is rejected if there are any additional leptons passing the "loose" selection criteria. The invariant mass of the deletion system $m_{\ell\ell}$ must be consistent with the Z boson mass: $83 < m_{\ell\ell} < 99$ GeV. This requirements suppress background without a resonant lepton pair, *i.e.* top quark and multijet production. The dilepton mass spectrum is shown in Figure 5.5 for events with at least two jets after the E_{T}^{miss} significance requirement below.

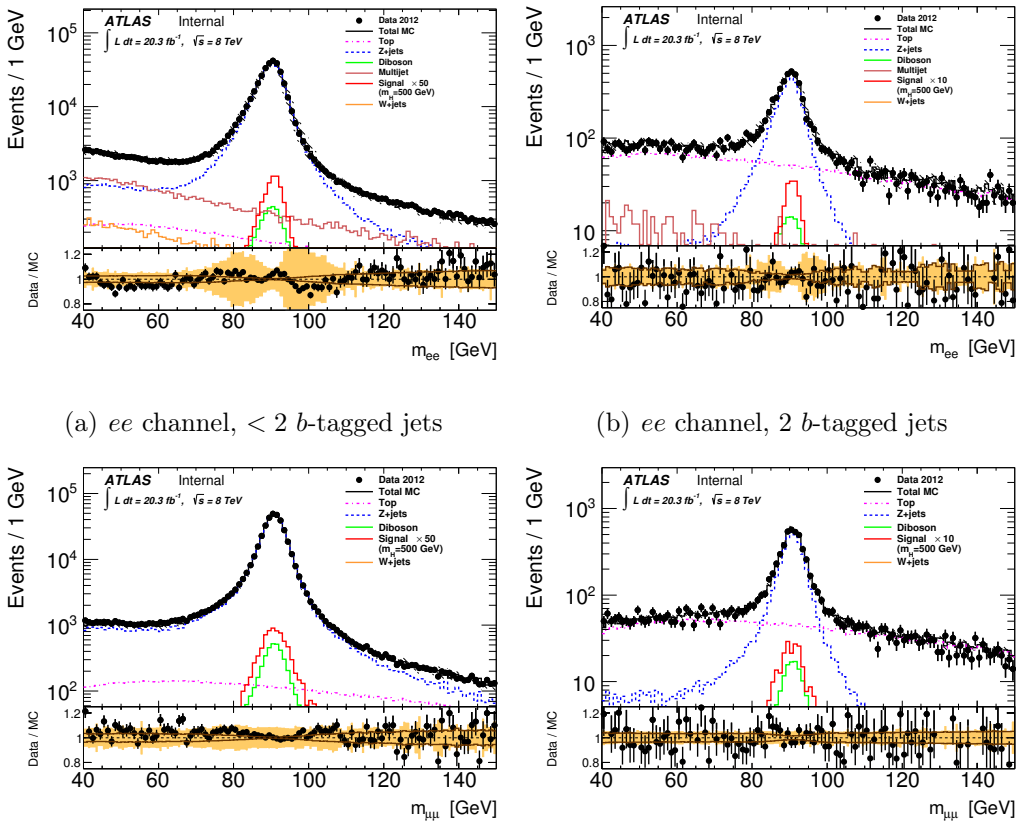

(a) ee channel, < 2 b-tagged jets

(b) ee channel, 2 b-tagged jets

(c) $\mu\mu$ channel, < 2 b-tagged jets

(d) $\mu\mu$ channel, 2 b-tagged jets

Figure 5.5: Dilepton mass spectrum fro events with ≥ 2 jets after the $E_{\mathrm{T}}^{\mathrm{miss}}$ requirement in the (a) untagged electron, (b) tagged electron, (c) untagged muon and (d) tagged muon categories of the resolved ggF channel.

5.3.3 $H \to ZZ \to \ell\ell qq$ selection

Once the $Z \to \ell\ell$ decay is identified, a E_{T}^{miss} significance requirement $\frac{E_{\mathrm{T}}^{miss}/GeV}{\sqrt{H_{\mathrm{T}}/GeV}} <$ 6 (3.5) is applied for the untagged (tagged) channel, where H_{T} is the sum of the selected leptons and "veto" jets, as described in Section 5.2.3. This reduces contamination from top quark events that contain neutrinos in the final state and is tighter in the tagged channel due to the larger top background. E_{T}^{miss} significance is used as opposed to a cut on E_{T}^{miss} itself since it was found to provide a roughly constant efficiency versus m_H, while the efficiency of the latter decreases

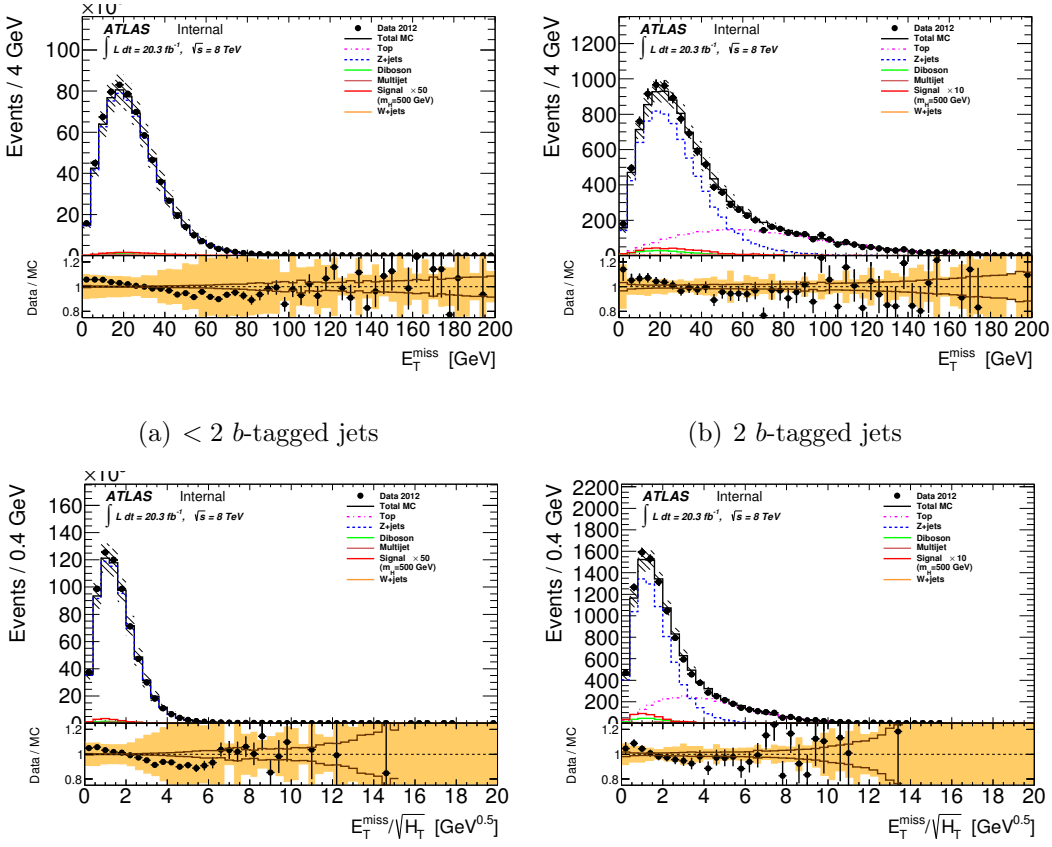

(a) < 2 b-tagged jets

(b) 2 b-tagged jets

(c) < 2 b-tagged jets

(d) 2 b-tagged jets

Figure 5.6: $E_{\mathrm{T}}^{\mathrm{miss}}$ distribution for events with ≥ 2 jets after the $m_{\ell\ell}$ cut in the (a) untagged and (b) tagged resolved ggF category. The same for $E_{\mathrm{T}}^{\mathrm{miss}}$ significance in figures (c) and (d)

significantly as m_H increases. The E_{T}^{miss} significance distribution, as well as the distribution of E_{T}^{miss} itself, is shown in Figure 5.6 for events with at least two jets after the $m_{\ell\ell}$ requirement.

The analysis next requires at least one jet with $p_{\mathrm{T}} > 45$ GeV; this reduces the Z+jets background. The analysis is then split into three categories: the resolved ggF category, the merged ggF and the VBF category.

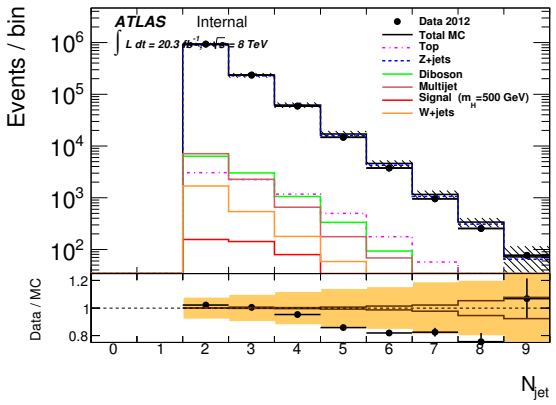

Figure 5.7: Number of "signal" jets after $m_{\ell\ell}$ and $\frac{E_{\mathrm{T}}^{\mathrm{miss}}}{\sqrt{H_{\mathrm{T}}}}$

5.3.3.1 Resolved ggF category

Over most of the mass range considered in this analysis ($m_H \lesssim 700$ GeV), the $Z \to q\bar{q}$ decay results in two well-separated jets that can be individually resolved. For this category, events are selected containing at least two "signal" jets as defined in Section 5.2.3 in addition to the $Z \to \ell\ell$ candidate described above. The distribution of the number of signal jets is shown in Figure 5.7 after the $m_{\ell\ell}$ and E_{T}^{miss} significance cuts. The MC simulation, which is dominated by SHERPA Z+jets, is seen to underestimate the data at high multiplicity. A discrepancy was seen in the ATLAS 7 TeV Z+jets cross section measurement [117] but it is difficult to compare exactly since a different kinematic and a different SHERPA setup is used. However, the present analysis is dominated by events with two or three jets; this population is well-described by the MC simulation and the discrepancy that exists is just within the systematic uncertainty. Furthermore, a test was performed by reweighting the N_{jet} distribution in MC to match data and found to have a negligible impact on the expected limit. A relatively large fraction (21%) of signal events contains b-jets, coming from $Z \to bb$, while those are rare in the $Z(\to \ell\ell)$+jets process that forms the dominant background. This feature is exploited by dividing

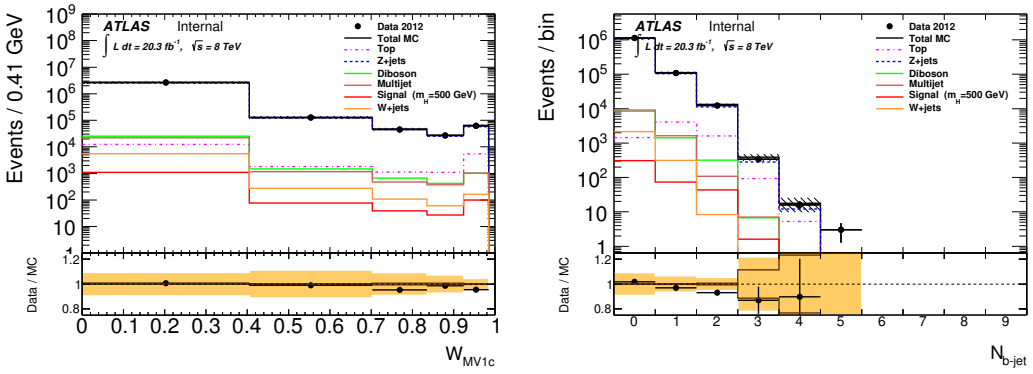

(a) (b)

Figure 5.8: Distribution of (a) MV1c b-tagging discriminant (in the pseudo-continous binning) for all "signal" jets and (b) number of b-tagged jets after the $m_{\ell\ell}$ and $\frac{E_{\mathrm{T}}^{\mathrm{miss}}}{\sqrt{H_{\mathrm{T}}}}$

the two leptons plus two jets sample into a "tagged" subchannel, containing events with two b-tags, and an "untagged" subchannel, containing events with less than two b-tags. Any events with more than two b-tags are rejected. Further splitting the 0 and 1 b-tagged events into separate sub channels did not increase the significance. The distributions of the MV1c b-tagging discriminant in the pseudo-continuous binning and the resulting number of b-jets are shown in Figure 5.8.

The candidate $Z \to jj$ decay is selected as follows. In the tagged subchannel, the two b-tagged jets are selected. For events with no b-tagged jets, the two jets with the largest p_{T} are chosen. If there is a signal event with exactly one b-tagged jet, then this is likely that this was a $Z \to bb$ decay in which one of the b-jets was not identified. So for events with one tagged jet, the tagged jet and the leading untagged jet are chosen for the candidate $Z \to jj$ decay. Dijet mass distributions for the two subchannels are shown in Figure 5.9. In all cases, the dijet mass must satisfy $70 < m_{jj} < 105$ GeV in order to be consistent with Z boson decay. The m_{jj} range is larger than the $m_{\ell\ell}$ range because the jet energy resolution is worse than that of leptons.

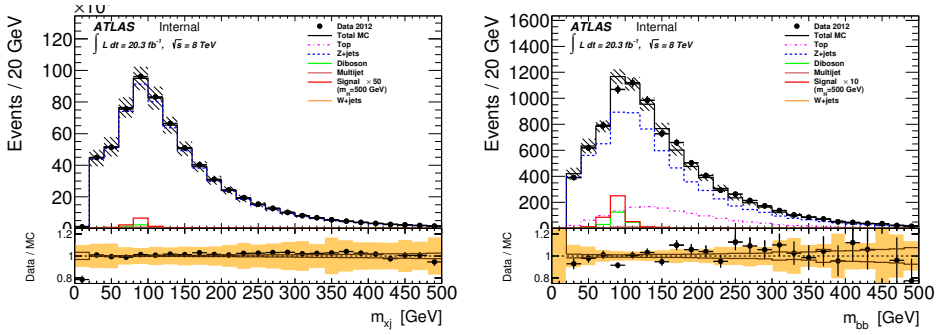

(a) < 2 b-tagged jets, before optimized selection

(b) 2 b-tagged jets, before optimized selection

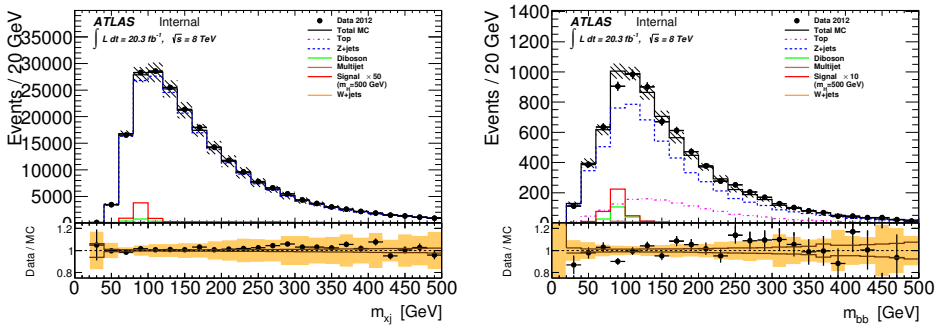

(c) < 2 b-tagged jets, after optimized selection

(d) 2 b-tagged jets, after optimized selection

Figure 5.9: Dijet mass distribution for the (left) untagged and (right) tagged ggF category (top) before and (bottom) after the optimized cuts in Equation 5.1. Here and subsequently x indicates either a tagged or untagged jet and xj represents the two jets in the untagged channel, which combines 0 and 1 b-tag events.

After the m_{jj} cut, the $H \to ZZ$ candidate mass is reconstructed by forming the invariant mass of the $\ell\ell jj$ system $m_{\ell\ell jj}$. The Higgs boson mass resolution is improved by imposing a Z mass constraint on the invariant mass of the two jets, since the reconstructed $Z \to jj$ mass resolution is worse than the intrinsic Z width. A simple approach is chosen such that each jet vector is scaled by $\frac{m_Z}{m_{jj}}$; more complicated kinematic fit approaches did not give a significant improvement in sensitivity.

Once the $\ell\ell jj$ candidate is found, an optimized kinematic selection is applied. Several variables were investigated and the most sensitive ones found to be the transverse momenta of the selected jets, the p_{T} of the deletion system $p_{\mathrm{T}}^{\ell\ell}$ and the azimuthal angle between the two leptons ($\Delta\phi_{\ell\ell}$). The selection was optimized as a function of the Higgs candidate mass and the best significance found for this selection:

$$\begin{aligned} p_{\mathrm{T}}^{j} &> 0.1 \times m_{\ell\ell jj} \text{ for untagged} \\ p_{\mathrm{T}}^{\ell\ell} &> \min[-54.04 + 0.455 \times m_{\ell\ell jj}, 275] \text{ for untagged} \\ p_{\mathrm{T}}^{\ell\ell} &> \min[-79.18 + 0.439 \times m_{\ell\ell jj}, 275] \text{ for tagged} \\ \Delta\phi_{\ell\ell} &< \frac{3.22 \times 10^{8}}{m_{\ell\ell jj}^{3.50}} + 1 \text{ for untagged} \end{aligned} \tag{5.1}$$

where all kinematic quantities involved are expressed in GeV. The p_{T}^{j} and $\Delta\phi_{\ell\ell}$ are not applied in the tagged channel since they were found to give no improvement in significance after the $p_{\mathrm{T}}^{\ell\ell}$ requirement in this case. This selection is applied as a function of reconstructed $m_{\ell\ell jj}$ mass rather than nominal Higgs mass m_H since the latter forces the main Z+jets background to peak under the Higgs signal, which is undesirable since any uncertainties in the size and shape of the background distribution will have a large effect. In addition, using $m_{\ell\ell jj}$ allows using a single background shape for all m_H hypotheses.

The efficiency of the complete selection including the optimized cuts is 9.9% for the 0+1-tag subchannel and 1.3% for the 2-tag subchannel for a plain SM like gluon-gluon fusion signal sample with $m_H = 400$ GeV. Considering a ggF NWA signal sample with $m_H = 900$ GeV, the corresponding efficiencies are 6.3% and 0.8% for the 0+1-tag and 2-tag subchannels respectively. Figure 5.10 shows these efficiencies as a function of m_H. The median significance, defined in [69] as $\sqrt{2[(S+B)\ln(1+\frac{S}{B}) - S]}$ (where S and B are the number of signal and background events respectively), is also shown in Figure 5.11. The fraction of events

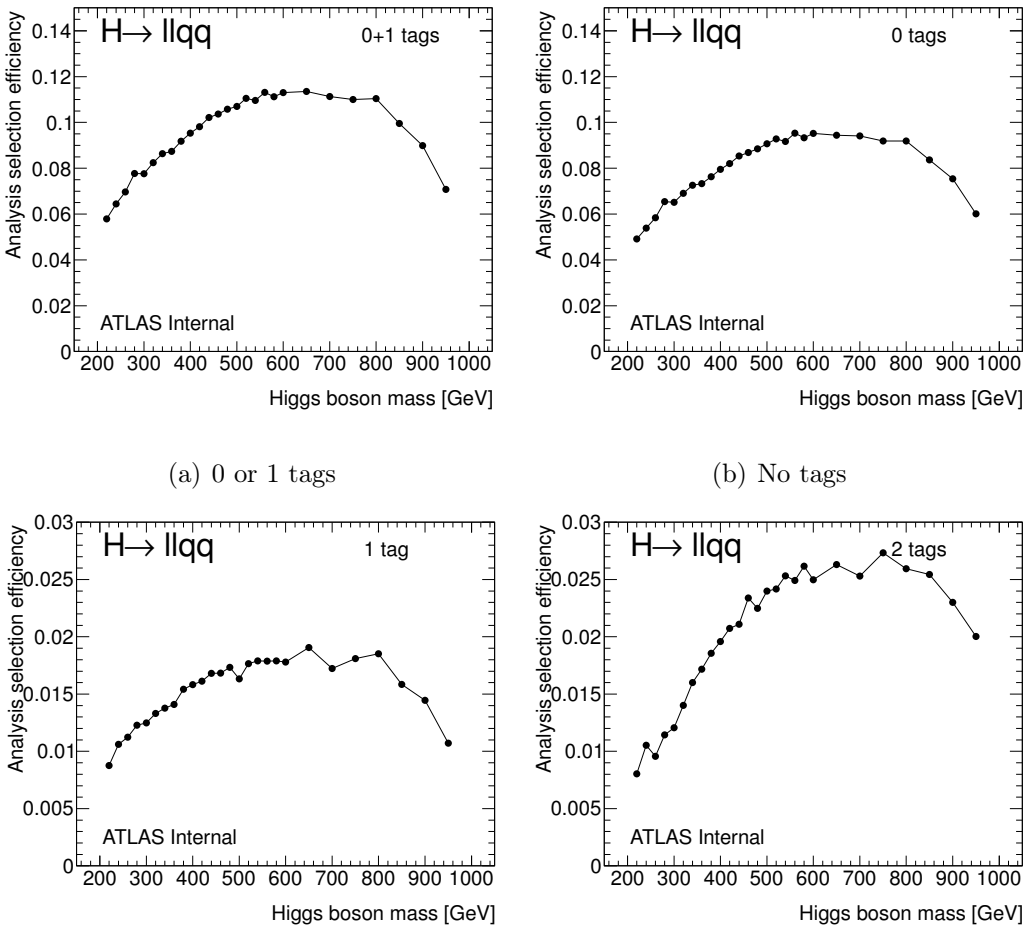

(a) 0 or 1 tags

(b) No tags

(c) 1 tag

(d) 2 tags

Figure 5.10: Total selection efficiency versus m_H for different b-tag selections.

in each jet tag subchannel after the complete selection is shown in Table 5.9.

5.3.3.2 Merged (boosted) ggF category

For large Higgs boson masses, namely $m_H \geq 700$ GeV, the Z bosons coming from the Higgs boson decay are highly boosted, so the opening angle between the Z boson decay products in the laboratory frame is small. Since the jets have finite size ($R = 0.4$ in this analysis), a boosted Z boson decaying to quarks may give rise to jets that overlap each other. Such events will be rejected by the selection

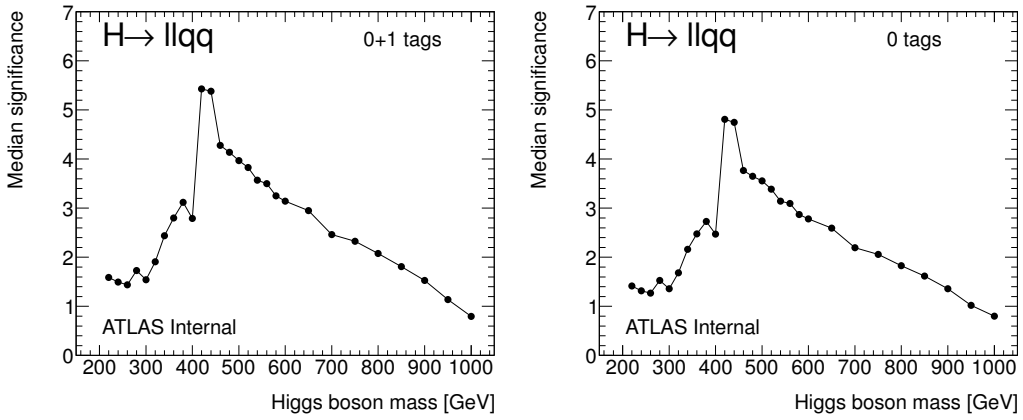

(a) 0 or 1 tags

(b) No tags

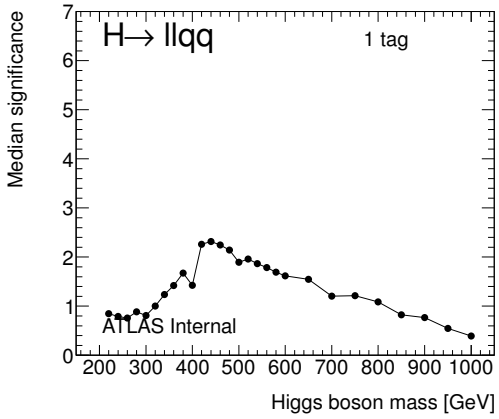

(c) 1 tag

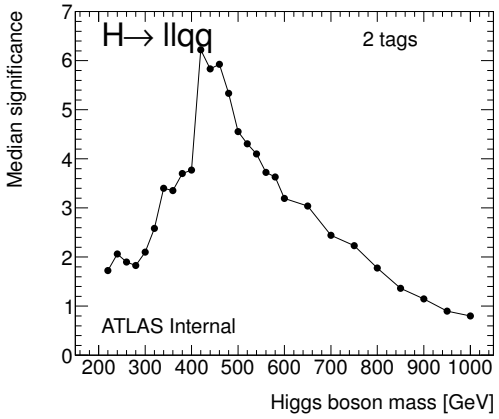

(d) 2 tags

Figure 5.11: Median significance versus m_H for different b-tag selections, calculated from MC simulation for a total integrated luminosity of 20 fb^{-1}. In addition to the standard selection cuts, $m_{\ell\ell jj}$ is required to lie within a symmetric window around the MC input m_H; the width of the window is set to accept 90% of the signal. Cross sections are from Section 5.1; NWA samples are used for $m_H > 400$ GeV

m_H [GeV]	No tags [%]	1 tag [%]	2 tags [%]
220	78.1	13.9	8.0
300	74.9	14.2	10.9
400	74.7	13.1	12.2
500	73.7	13.4	12.8
600	73.8	14.2	11.9
700	73.3	14.5	12.2
800	74.4	13.8	11.8
900	76.1	12.5	11.4
1000	74.4	13.9	11.7

Table 5.9: Fraction of events (in percent) in each jet tag bin for different m_H

described in the previous Section 5.3.3.1, which requires two separated jets with m_{jj} consistent with the Z boson mass. The "merged" category attempts to recover this efficiency loss by looking for a $Z \to q\bar{q}$ decay that is reconstructed as a single jet.

The merged analysis is performed when the standard analysis fails; that is, when the selected dijet system has a mass that is not consistent with the Z boson mass. But since the dijet mass sidebands are used to study the modelling of the Z+jets background (see Section 5.4), the merged analysis is applied when the dijet mass is neither in the dijet mass signal region (70 - 105 GeV) nor in the sidebands region (50 - 70 GeV and 105 - 150 GeV). The merged analysis also accepts events containing only a single high-p_{T} jet in addition to the $Z \to \ell\ell$ candidate. Such events are called "monojet" events. The dilepton mass spectrum for monojet events is shown in Figure 5.12. the merged category also imposes an explicit requirements of a large boost for the leptonically-decaying Z boson: $p_{\mathrm{T}}^{\ell\ell} > 280$ GeV.

For this category, the leading jet is chosen as the candidate $Z \to q\bar{q}$ decay; the

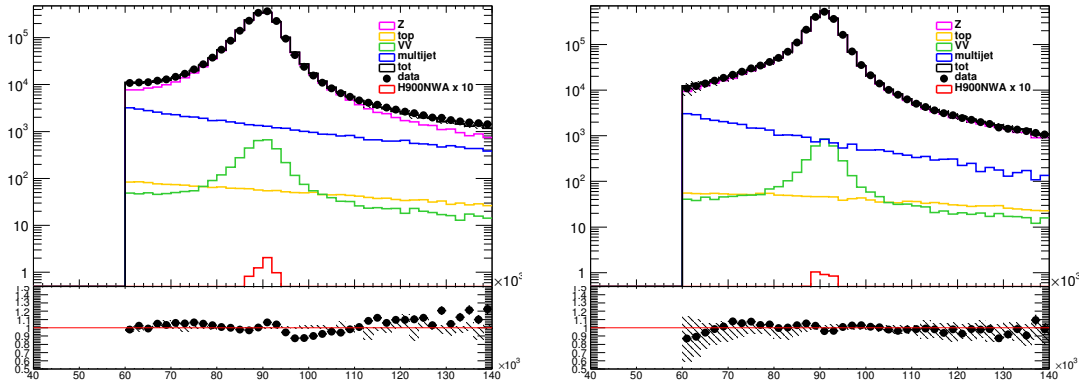

(a) (b)

Figure 5.12: Dilepton mass spectra for monojet events, *i.e.* events containing only a single "good" jet in addition to the leptonic Z decay, for (a) electrons and (b) muons.

invariant mass distribution for such jets is shown in Figure 5.13. The leading jet is required to satisfy the following kinematic requirements: $p_{\mathrm{T}} > 200$ GeV and $\frac{m}{p_{\mathrm{T}}} > 0.05$. These requirements have been studied within the jet mass calibration process and they are needed in order to restrict to a kinematic region in which the jet mass response is properly understood and in which it can be calibrated.

Unlike in the resolved category, the merged analysis does not split events into subchannels based on the number of b-tagged jets. Such a split was studied and found not to be optimal because the b-tagging efficiency for merged jets is poor, yielding extremely poor statistics in the final sample.

Figure 5.13 shows that a peak in the leading jet invariant mass distribution near the Z boson mass is expected for the signal, while the dominant Z+jets background does not give rise to such a peak.

As mentioned above, events in which the leading two jets have an invariant mass within either the signal region or in the control region sidebands are excluded from the merged category. For events with the dijet mass in the sidebands, the leading jet usually has a low mass; thus, this requirement does not result in a significant

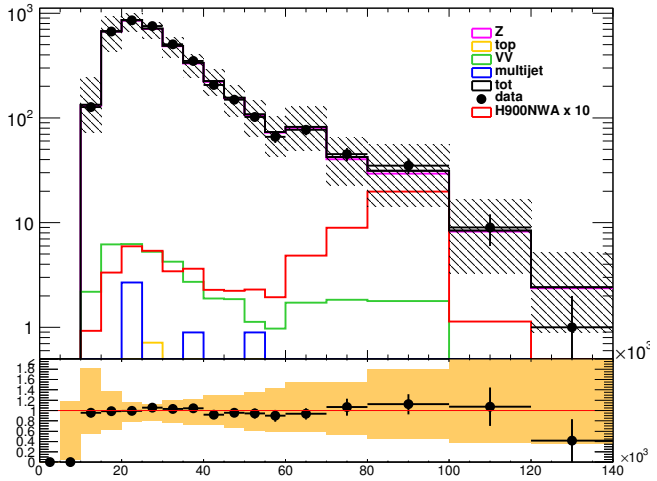

Figure 5.13: Invariant mass of the leading jet in events selected by the merged analysis, after the mass calibration and the kinematic selection.

efficiency loss in the merged category.

Similarly, events that pass the dijet mass requirement in the resolved analysis but which fail the optimized final selection could be considered for the merged category. However, in such events, the leading jet also predominantly has low mass; thus, they would not contribute significantly to the merged category.

A final requirements on the invariant mass of the leading jet $70 < m_j < 105$ GeV is made in order to separate the expected signal peak from non-resonant background. After this selection, the three-body mass $m_{\ell\ell j}$ is used as a discriminating variable. The overall efficiency of the merged selection is 5.3% on a NWA signal sample with $m_H = 900$ GeV, considering only the gluon-gluon fusion process. This selection is exclusive of the resolved category, so this is the net increase in efficiency, *i.e.* the total signal efficiency for the ggF signal sample with $m_H = 900$ GeV is improved by $\simeq 100\%$.

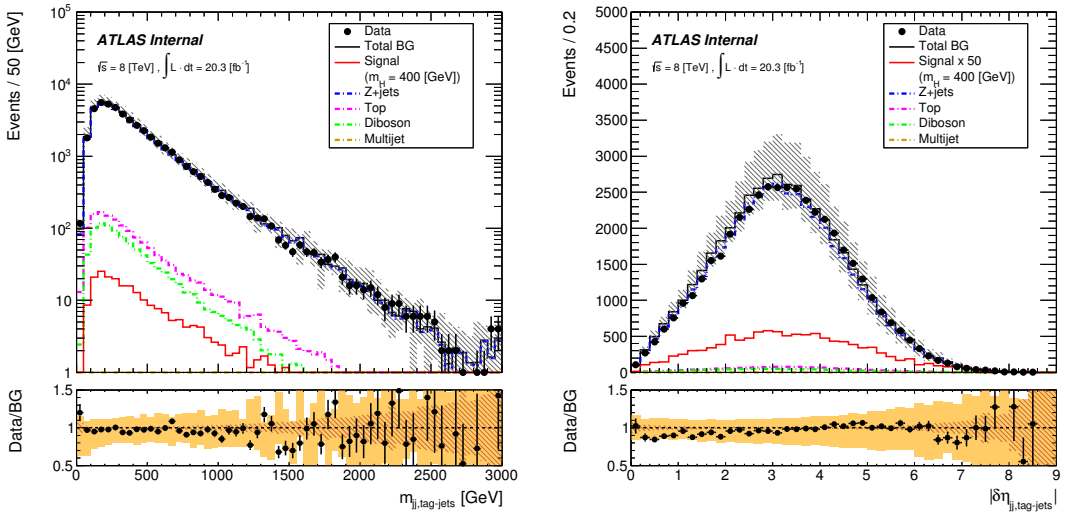

(a) (b)

Figure 5.14: Distribution of the invariant mass (left) and pseudorapidity gap (right)for the VBF "tag jet" pair. In the VBF channel, ALPGEN generator is used for the Z+jets background.

5.3.3.3 VBF category

The VBF process, in addition to the jets from the $Z \to jj$ decay, contains two jets close to the beam pipe, *i.e.* with high $|\eta|$, in opposite directions. These additional jets are called "tag jets". Hence, the selection in this category, after the $m_{\ell\ell}$ and E_{T}^{miss} significance cuts, requires at least four veto jets as described in Section 5.2.3. The selection in the VBF category thus begins by requiring two non-b-tagged jets with $\eta_{\mathrm{jet1}} \times \eta_{\mathrm{jet2}} < 0$. If more than one such pair is found, then the one with the highest invariant mass is selected. Distributions of the invariant mass of the selected of the selected "tag jet" pair $m_{jj,\mathrm{tag}}$ and the pseudorapidity gap between them $\Delta\eta_{jj,\mathrm{tag}}$ are shown in Figure 5.14. In order to reduce the Z+jets background, the "tag jet" pair must have $m_{jj,\mathrm{tag}} > 500$ GeV and $\Delta\eta_{jj,\mathrm{tag}} > 4$. These cuts were optimized for maximum significance.

Once a "tag jet" pair has been identified, the $Z \to q\bar{q}$ decay is reconstructed in

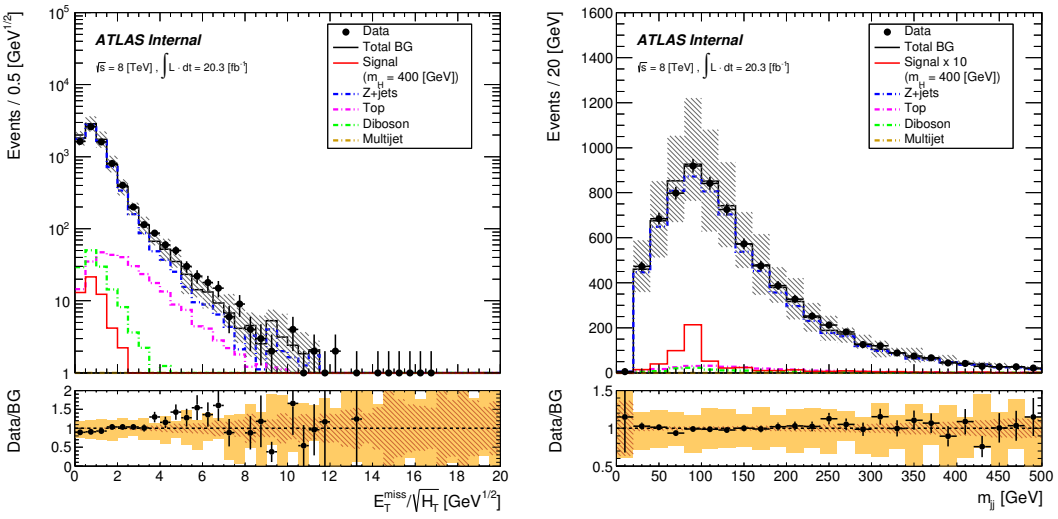

(a) (b)

Figure 5.15: Distribution of $E_{\mathrm{T}}^{\mathrm{miss}}$ significance (left) and the invariant mass of the dijet pair forming the $Z \to q\bar{q}$ candidate in the VBF category (right)

exactly the same manner as for the ggF resolved analysis (see Section 5.3.3.1), except that the jets used for the "tag jet" pair are excluded. Due to the limited statistics in this category, splitting the analysis based on the number of b-tagged jets did not improve the significance of the results; hence an inclusive analysis is performed. The reconstructed dijet invariant mass is shown in Figure 5.15.

The cut optimization outlined in Section 5.3.3.1 for the ggF category was also performed for the VBF category. The same selection was found to be close to optimal for the VBF category too within limited statistics. Hence the $m_{\ell\ell jj}$-dependent cuts of Equation (5.1) are applied for this category. In addition, a cut on the total transverse momentum of the selected leptons and jets $p_{\mathrm{T}}^{\mathrm{tot}}$ was found to give a marginal improvement to the sensitivity with respect to the Z+jets background and also an improved separation between the ggF and VBF signal processes. The $p_{\mathrm{T}}^{\mathrm{tot}}$ distribution is shown in Figure 5.16. A cut of $p_{\mathrm{T}}^{\mathrm{tot}} < 40$ GeV was found to be optimal. However, since the effect of this variable is marginal,

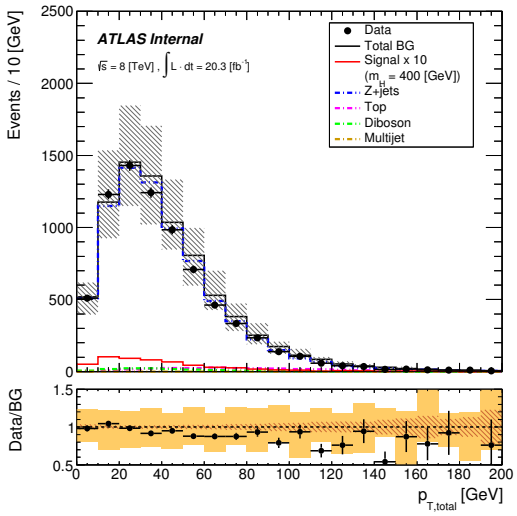

Figure 5.16: Distribution of $p_{\mathrm{T}}^{\mathrm{tot}}$ in the VBF category.

this selection is not applied.

5.4 Backgrounds

The Monte Carlo simulations that model the various backgrounds to this analysis, described in Section 5.1.3, may not describe the data accurately. These backgrounds are studied by defining in data several control regions (CRs) that separate out the main backgrounds and are mostly signal free. The normalization of the backgrounds is performed along with the signal extraction by including these CRs in the final combine profile likelihood fit as described in Section 5.8; this correctly accounts for correlations.

In summary, the shape and the normalization of the Z+jets background is corrected from data while the top background shape is taken from MC but normalized to the data in the CRs; the multijet background is taken from purely data-driven method while all other minor background are taken entirely from MC simulations.

5.4.1 Z+jets background

The dominant background in this analysis is the Z+jets production. It can be studied in data using the sidebands (SBs) of the m_{jj} distribution, which provide an almost pure sample of Z+jets events. The "ZCR" is defined following the nominal, except that the m_{jj} requirement is replaced by either $50 < m_{jj} < 70$ GeV (low-mass SB) or $105 < m_{jj} < 150$ GeV (high-mass SB). These SBs are chosen to keep the kinematics similar to the signal region (SR) but to allow sufficient statistics to study the background. The two SBs are usually combined together, but individual SBs are used to check for systematic effects.
In all channels, the SBs are used to determine scale factors to normalize the MC yields in the SR. In addition, they are used to correct the modelling of the jet angular separation and the p_{T} of the leptonic Z candidate in the resolved ggF channel, while in the VBF channel they are used to correct the $m_{\ell\ell jj}$ discriminant.

5.4.1.1 Z+jets in the resolved ggF channel

To accurately model the Z+jets background, one must determine the relative fractions of Z+light-, c- and b-jets, *i.e.* the "flavour composition", which will not necessarily be predicted correctly by the MC generator. In addition, the ability of the MC simulation to correctly model the Z+jets background distribution is likely to vary for the different flavour components and thus they should be studied separately as far as possible. To facilitate this, separate CRs are defined for events containing untagged and tagged events. Table 5.10 gives a breakdown of the flavour composition of the ZCR in the 0-, 1- and 2-tag case.

Process	0-tag [%]	1-tag [%]	2-tag [%]
$Z + l$	83	22	4.4
$Z + c$	13	16	6.3
$Z + b$	2	46	69
$t\bar{t}$	0.11	3.2	17

Table 5.10: Sample composition for Z+jets modelling studies after background normalization. Here, $Z + b = Zbb + Zbc + Zbl$ refers to Z+jets MC events with at least one jet labelled as b, $Z + c = Zcc + Zcl$ refers to events with no jets labelled as b-jet but at least one labelled as c and $Z + l$ refers to events with no jets labelled as b or c. The small remaining fraction is made up by the other small backgrounds: diboson, multi-jet and W+jets.

Flavour composition As mentioned above, the simulation can not be assumed to correctly predict the relative flavour composition of the Z+jets background; hence, the composition must be denied from data using the SBs for untagged and tagged events. Since the MV1c discriminant is designed to separate between the various flavors, and in particular to distinguish b-jets from both light- and c-jets (unlike MV1), its distribution provides the natural variable to constrain the Z+jets flavour composition. This is now possible due to the pseudo-continuous calibration of MV1c described in Section 5.2.3.2 and provides a significant improvement over the previous 7 TeV analysis, where this was not available. In order to correctly take into account the correlations with the various systematic uncertainties this so called "flavour fit" is performed as part of the final profile likelihood fit described in Section 5.8. The input distribution is the sum of the MV1c weight for the two signal jets in the untagged and tagged SBs; this sum uses the central value of the MV1c bin and as such has a unique value for each combination of the signal jet's MV1c weights. This fit also takes into account the overall normalization of the Z+jets MC simulation to data.

The flavour fit is only applied in the resolved ggF category, which is split into

untagged and tagged categories. Since the VBF and merged ggF categories are inclusive in the number of b-tagged jets due to limited statistics, they are not sensitive to the flavour composition and hence only the overall Z+jets normalization is determined from data.

Signal jets in Z+jets MC are labelled as described in Section 5.2.3.1 to define event categories $Z + bb, bc, bl, cc, cl, ll$. In some cases categories are combined: $Z + b = Zbb + Zbc + Zbl$ refers to events with at least one jet labelled as b, $Z + c = Zcc + Zcl$ refers to events with no jets labelled as b but at least one labelled as c, and $Z + l$ refers to events with no jets labeled as b or c.

$\Delta\phi_{jj}$ and $p_{\mathrm{T}}^{\ell\ell}$ modelling It has been observed in several analyses, in particular $V(H \to bb)$, that SHERPA does not model well the azimuthal separation of the jets from the hadronic Z or W decay $\Delta\phi_{jj}$. This is also seen by the SHERPA authors when comparing to ATLAS 7 TeV W+jets data [118]. In addition, this discrepancy is found to be dependent on $p_{\mathrm{T}}^{\ell\ell}$. No such discrepancy is observed for $\Delta\phi_{\ell\ell}$.

The $\Delta\phi_{jj}$ distributions for the 0, 1 and 2 b-tag SBs are shown in Figure 5.17, split into two $p_{\mathrm{T}}^{\ell\ell}$ regions, $p_{\mathrm{T}}^{\ell\ell} < 120$ GeV (low $p_{\mathrm{T}}^{\ell\ell}$) and $p_{\mathrm{T}}^{\ell\ell} > 120$ GeV (high $p_{\mathrm{T}}^{\ell\ell}$). It can be seen that there is a clear discrepantcy for both the 0 and 1 b-tag categories at low $p_{\mathrm{T}}^{\ell\ell}$, while there no obvious discrepancy at high $p_{\mathrm{T}}^{\ell\ell}$ or in the 2 b-tag category within statistics. This suggests that, at low $p_{\mathrm{T}}^{\ell\ell}$, a correction is needed for the Z+light jet background, which is non negligible in the 1 b-tag sample, but not for the Z+heavy-flavour component.

A correction is derived for this discrepancy by fitting with a linear function $a(1 + b\Delta\phi_{jj})$ the ratio of the data to the Z+jets background for low $p_{\mathrm{T}}^{\ell\ell}$ 0 b-tag events, after subtracting the small non-Z background from MC simulation. This is

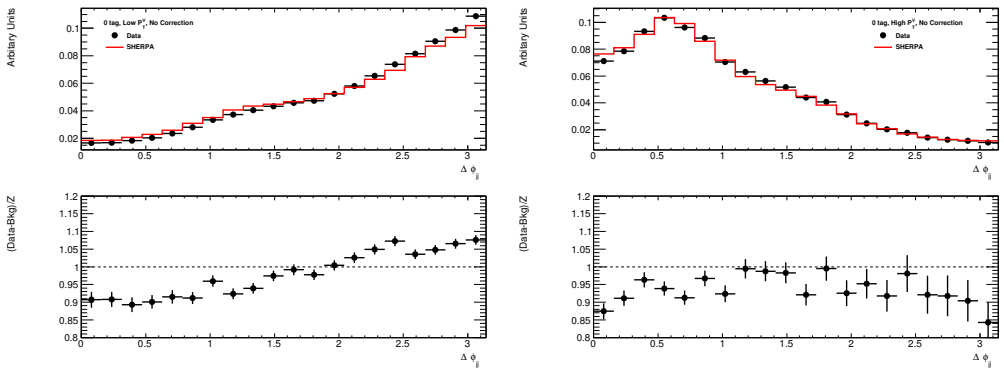

(a) 0-tag, $p_{\mathrm{T}}^{\ell\ell} < 120$ GeV

(b) 0-tag, $p_{\mathrm{T}}^{\ell\ell} > 120$ GeV

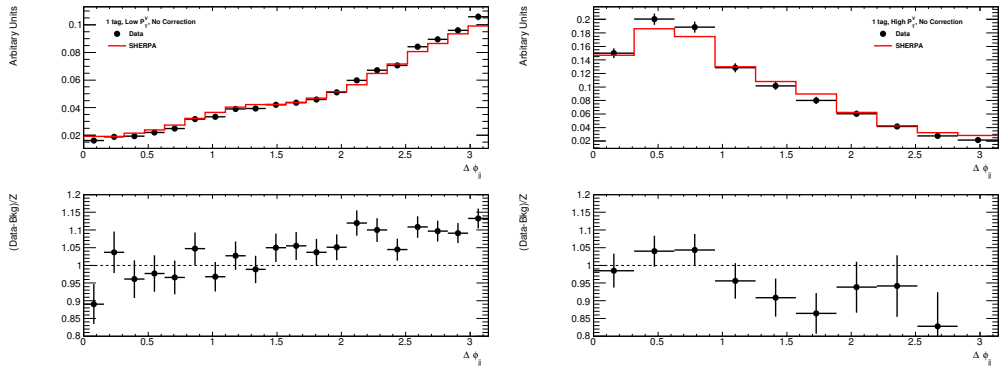

(c) 1-tag, $p_{\mathrm{T}}^{\ell\ell} < 120$ GeV

(d) 1-tag, $p_{\mathrm{T}}^{\ell\ell} > 120$ GeV

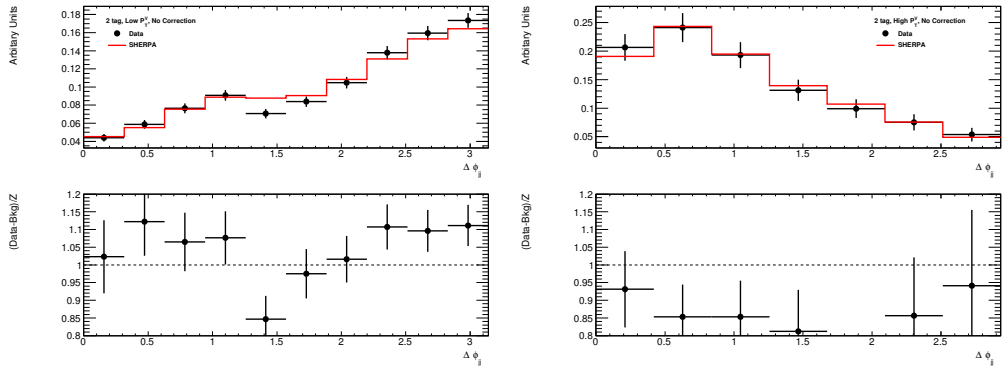

(e) 2-tag, $p_{\mathrm{T}}^{\ell\ell} < 120$ GeV

(f) 2-tag, $p_{\mathrm{T}}^{\ell\ell} > 120$ GeV

Figure 5.17: Normalized $\Delta\phi_{jj}$ distributions and data/MC ratios for 0-, 1- and 2-tag events for low $p_{\mathrm{T}}^{\ell\ell}$ (left) and high $p_{\mathrm{T}}^{\ell\ell}$ (right) before the correction described in the text; the discrepancy in the low $p_{\mathrm{T}}^{\ell\ell}$ 0 and 1 b-tag regions can clearly be seen.

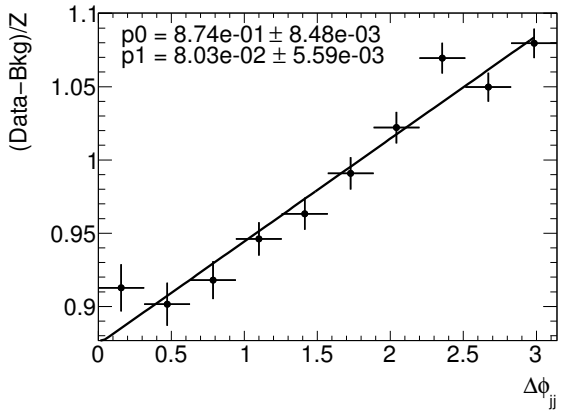

Figure 5.18: Linear fit to the $\frac{\text{Data}-\text{MC}_{\text{bkg}}}{\text{MC}_{Z+\text{jets}}}$ ratio for 0 b-tag events at low $p_{\text{T}}^{\ell\ell}$. Here "bkg" refers to the non-Z background.

shown in Figure 5.18 for the combined SBs, although similar results are obtained for both SBs separately.

Since the 0 b-tag category is almost pure Z+light-jets, this function is used to reweight the Z+light-jets MC sample. After the $\Delta\phi_{jj}$ correction (see Figure 5.19), the 0 b-tag region is found to be reasonably described. The 1 b-tag region is also significantly improved, although there still some slope present at this point.

A systematic uncertainty of half the applied correction is assigned to the Z+light-jet simulation at low $p_{\text{T}}^{\ell\ell}$, while the full correction is taken as a systematic uncertainty in the Z+b/c-jet case where no correction is applied. For the high-$p_{\text{T}}^{\ell\ell}$ region, where no correction is applied, a linear fit is performed to the data/MC ratio in the 0 b-tag subchannel and the statistical uncertainty on the fitted slope applied as a systematic uncertainty for all Z+jets flavours. The systematic uncertainties for the Z+light-jet and $Z + b/c$-jet events are treated us uncorrelated.

After the Z+light-jets $\Delta\phi_{jj}$ correction, the description of the $p_{\text{T}}^{\ell\ell}$ distribution in the SBs, shown in Figure 5.20, is studied. For 0 b-tag events, it is found that after the $\Delta\phi_{jj}$ correction is applied, the $p_{\text{T}}^{\ell\ell}$ distribution is well-described by the simulation. However, there is a clear discrepancy seen in the 1 and 2 b-tag distributions,

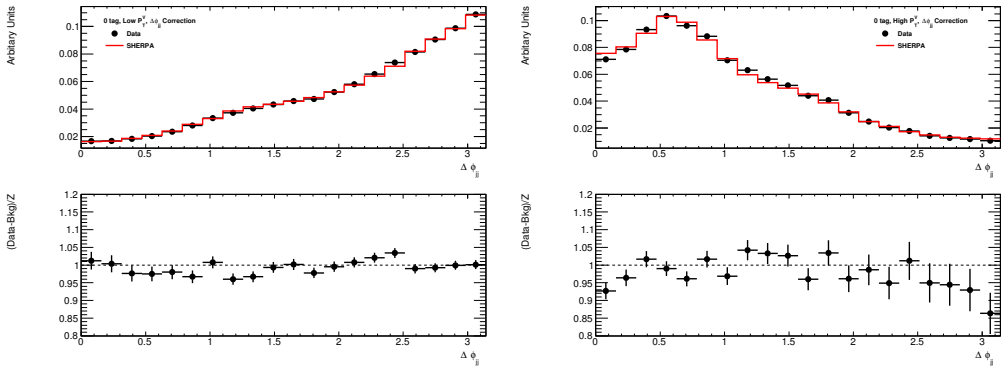

(a) 0-tag, $p_{\mathrm{T}}^{\ell\ell} < 120$ GeV

(b) 0-tag, $p_{\mathrm{T}}^{\ell\ell} > 120$ GeV

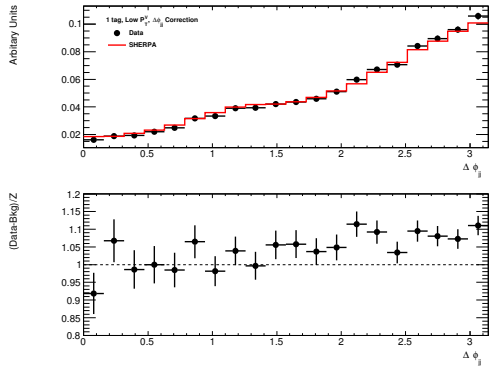

(c) 1-tag, $p_{\mathrm{T}}^{\ell\ell} < 120$ GeV

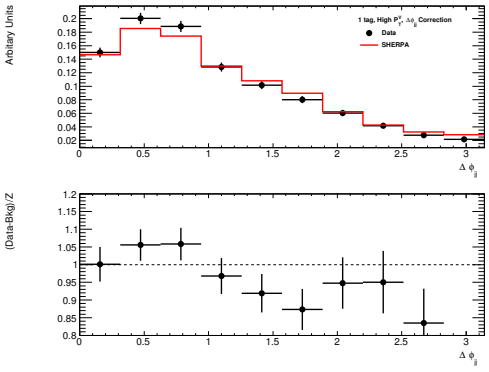

(d) 1-tag, $p_{\mathrm{T}}^{\ell\ell} > 120$ GeV

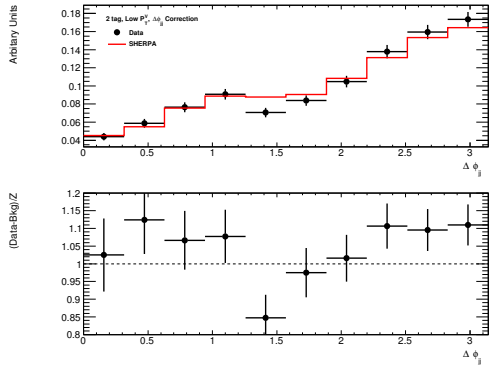

(e) 2-tag, $p_{\mathrm{T}}^{\ell\ell} < 120$ GeV

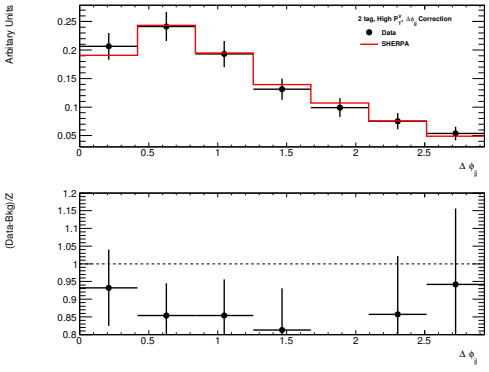

(f) 2-tag, $p_{\mathrm{T}}^{\ell\ell} > 120$ GeV

Figure 5.19: Normalized $\Delta\phi_{jj}$ distributions and data/MC ratios for 0-, 1- and 2-tag events for low $p_{\mathrm{T}}^{\ell\ell}$ (left) and high $p_{\mathrm{T}}^{\ell\ell}$ (right) after the correction described in the text but before the $p_{\mathrm{T}}^{\ell\ell}$ correction. It can be seen at this point that there is still a discrepancy in the low $p_{\mathrm{T}}^{\ell\ell}$ 1 b-tag region.

indicating that a $p_{\mathrm{T}}^{\ell\ell}$ correction is needed for the Z+heavy-flavour simulation. Due to the limited statistics in the 2 b-tag subchannel, a correction is derived from the 1 and 2 b-tag distributions combined by fitting the ratio of the data to the Z+heavy-flavour background with $a + b \log p_{\mathrm{T}}^{\ell\ell}$; both the Z+light-jet and small non-Z background from MC simulation are subtracted from data. This resulting parameterization is shown in Figure 5.21 for the combined SBs. This is used to correct the $Z + c/b$ simulation. A systematic uncertainty of half the correction is assigned to the entire Z+jet simulation but decorated between Z+light-jet and $Z + c/b$-jet.

The $\Delta\phi_{jj}$ and $p_{\mathrm{T}}^{\ell\ell}$ distributions in the combined SB for all b-tag categories after both corrections are shown in Figure 5.22; Figures 5.23 and 5.24 show the corresponding plots for the low- and high-m_{jj} SBs, respectively. A good description of the data is observed for all distributions, including $\Delta\phi_{jj}$ in the 1 b-tag region.

m_{jj} modelling A mismodelling of the m_{jj} distribution does not directly affect the $m_{\ell\ell jj}$ discriminant, since the dijet invariant mass is constrained to the Z boson mass when reconstructing $m_{\ell\ell jj}$. However, the modelling of this variable is still important since it affects the extrapolation of the Z+jets background normalization and flavour composition fits, described previously, from the ZCR to the SR. The full m_{jj} spectrum is shown in Figure 5.25 and is seen to be reasonably described. Consequently, no correction is applied, but a systematic uncertainty on the shape is derived by reweighting the Z+jets MC such that it covers by eye any residual data/MC disagreement in the m_{jj} SB. The reweight used is a linear parameterization of the form $a(m_{jj} \times 10^{-3} - b)$ and is also shown in Figure 5.25. This uncertainty is somewhat conservative in the 0 b-tag case (see Figure 5.25(a)), but was chosen to allow the same uncertainty to be applied across all b-tag categories.

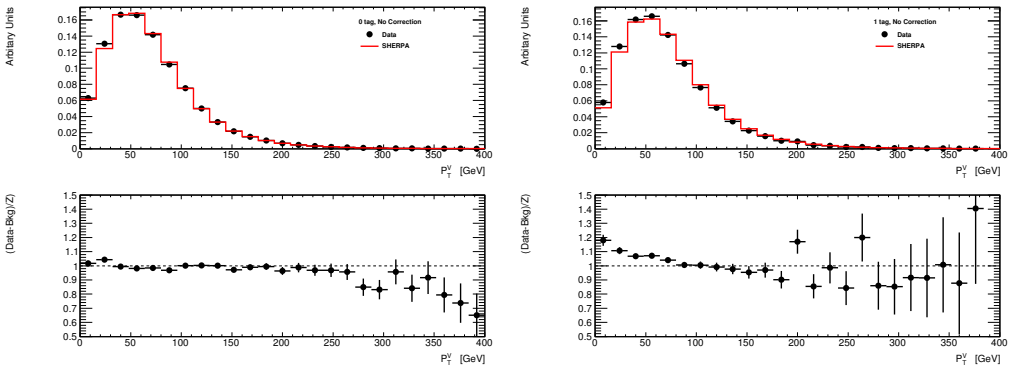

(a) 0-tag

(b) 1-tag

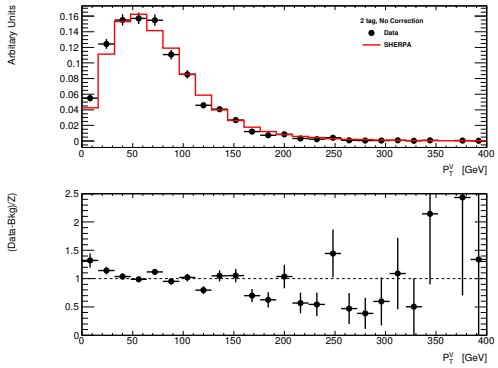

(c) 2-tag

Figure 5.20: The normalized $p_{\mathrm{T}}^{\ell\ell}$ distributions and data/MC ratios for (a) 0, (b) 1 and (c) 2 b-tag events before the correction described in the text; the discrepancy in the 1 and 2 b-tag regions can clearly be seen.

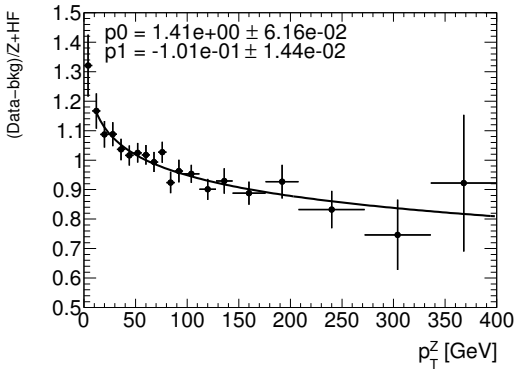

Figure 5.21: Fit to the $\frac{\mathrm{Data}-\mathrm{MC_{bkg}}}{\mathrm{MC}_{Z+\mathrm{heavy-flavour}}}$ ratio for 1 and 2 b-tag events combined. Here "bkg" refers to the Z+light-jet and non-Z background.

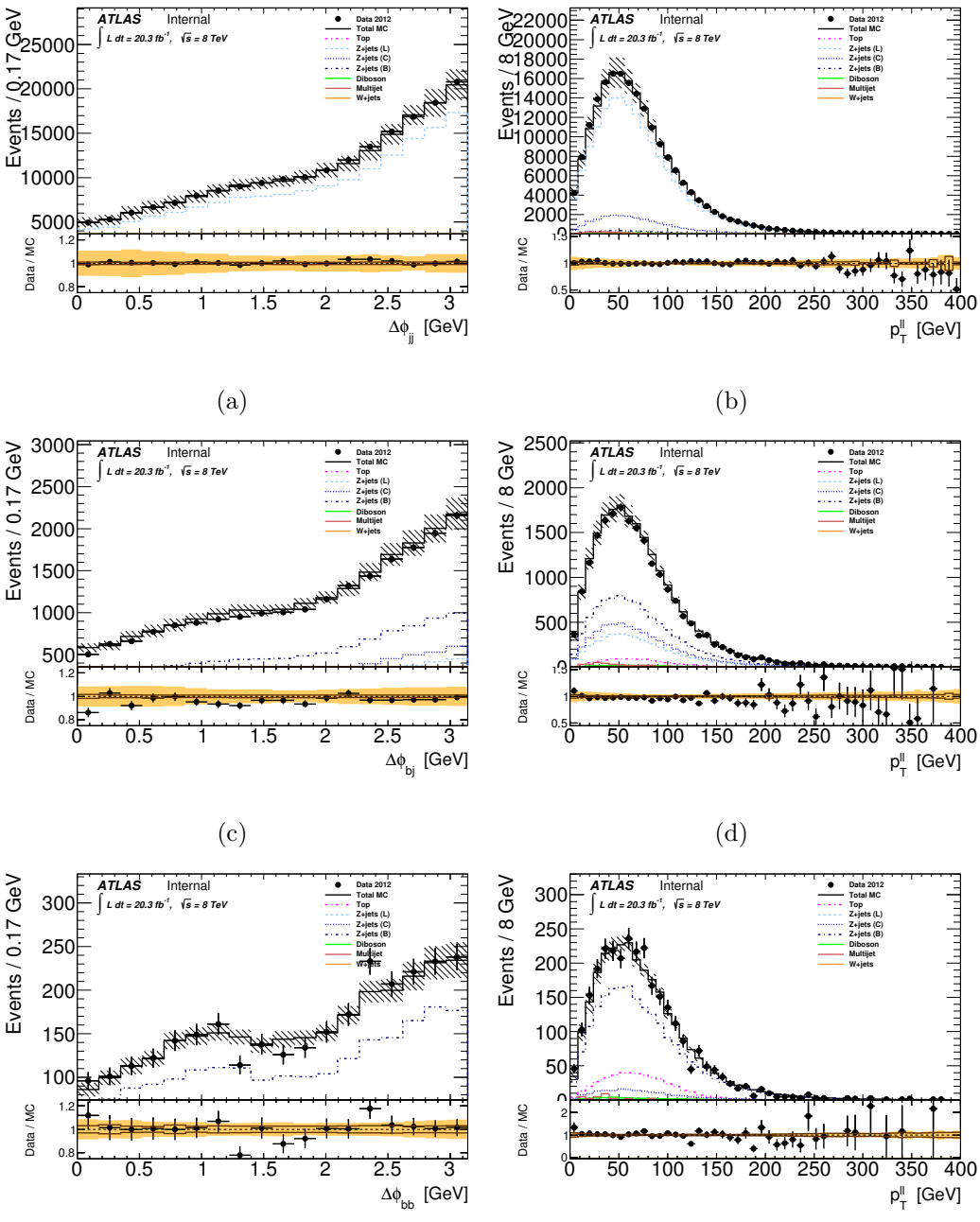

Figure 5.22: $\Delta\phi_{jj}$ (left) and $p_{\mathrm{T}}^{\ell\ell}$ (right) distributions for (a, c) 0, (b, d) 1 and (e, f) 2 b-tag events in the combined SB after the corrections in the text. The bands show the systemic uncertainties including those associated with these corrections.

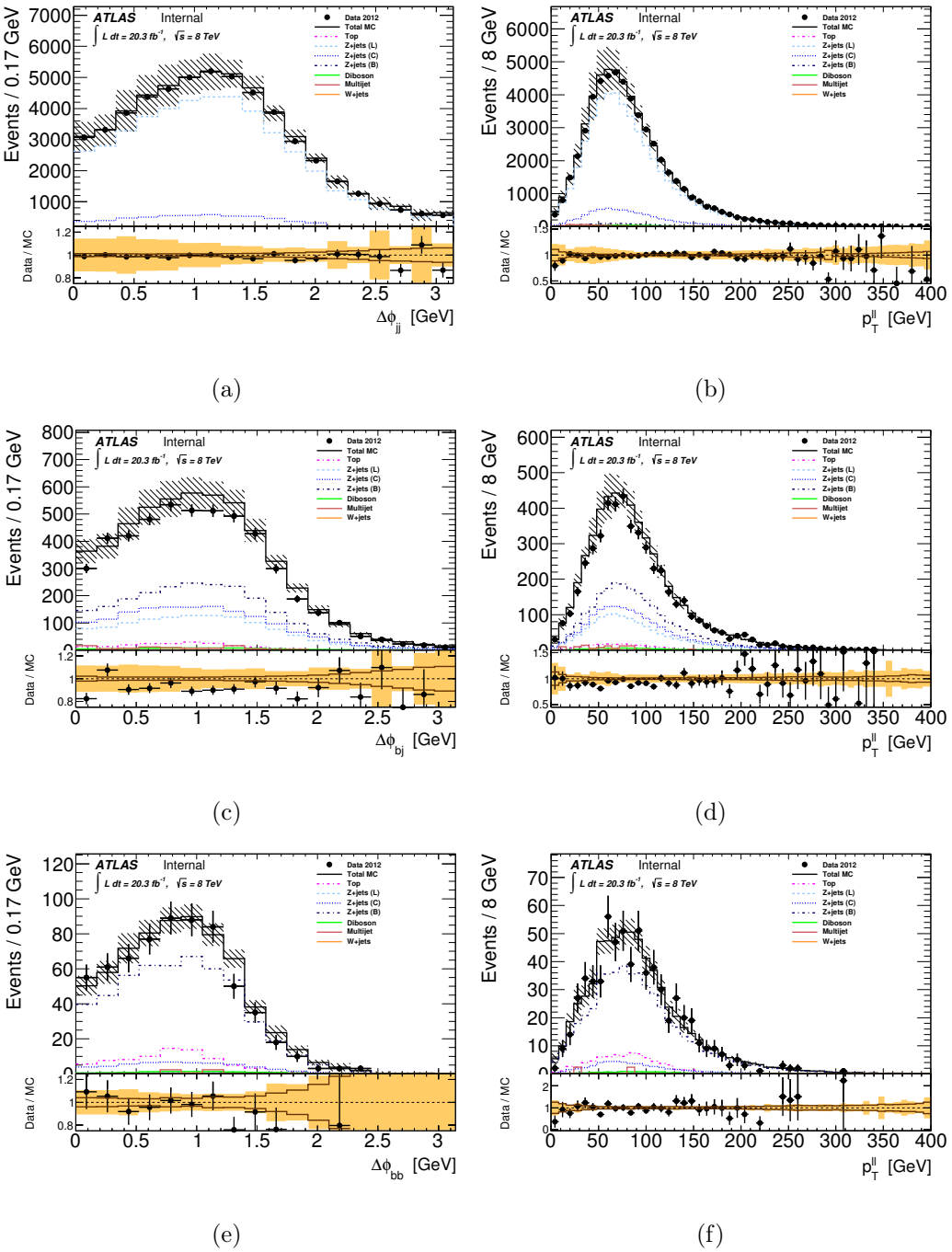

Figure 5.23: $\Delta\phi_{jj}$ (left) and $p_{\mathrm{T}}^{\ell\ell}$ (right) distributions for (a, c) 0, (b, d) 1 and (e, f) 2 b-tag events in the low-m_{jj} SB after the corrections in the text. The bands show the systemic uncertainties including those associated with these corrections.

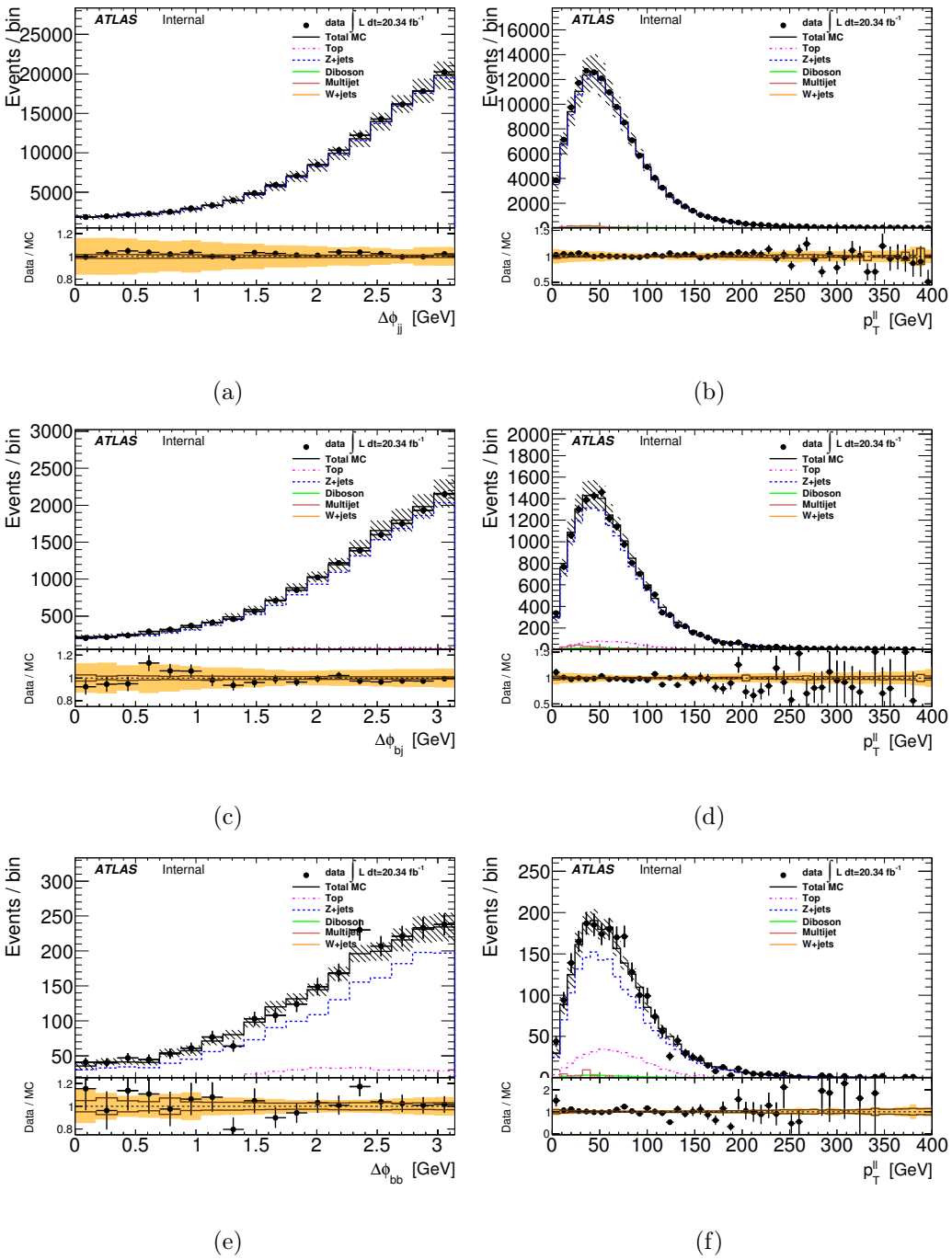

(a) (b) (c) (d) (e) (f)

Figure 5.24: $\Delta\phi_{jj}$ (left) and $p_{\mathrm{T}}^{\ell\ell}$ (right) distributions for (a, c) 0, (b, d) 1 and (e, f) 2 b-tag events in the high-m_{jj} SB after the corrections in the text. The bands show the systemic uncertainties including those associated with these corrections.

$m_{\ell\ell jj}$ modelling Figure 5.26 shows the final $m_{\ell\ell jj}$ discriminants in the ZCR after the application of all corrections described in this section and after applying the Z+jets normalization, including the relative flavour composition, from the final combined fit. The distributions are shown both before and after the optimized selection of Eq. 5.1. The data are well described by the MC simulation within the assigned uncertainties, including those on the modelling described above. Consequently, no further correction or uncertainty is applied.

5.4.1.2 Z+jets in the merged category

As in the resolved category, the Z+jets process is the dominant background in the merged category, as can be seen from Figure 5.13. Similarly to the resolved category, this background is studied in a control region obtained in the sidebands of the m_j distribution, away from the signal region defined in Section 5.3.3.2. The sideband is defined in the $30 < m_j < 70$ GeV range. Distributions of the three-body mass spectra for this sideband are shown in Figure 5.27. These plots show that the MC simulation correctly reproduces the shape of the data distribution and therefore no additional shape correction is needed. However, there is a disagreement in the normalization between data and MC simulation and therefore a scale factor (SF) is determined from the ratio of the data to MC simulation, after subtracting the residual contribution from other backgrounds (top quark, multijet and diboson). The result is SF $= 0.899 \pm 0.020$ for $30 < m_j < 70$ GeV. These uncertainties are statistical only. The effect of applying the scale factors can be seen in Figure 5.27. The final normalization of the Z+jets background is actually taken from the final fit explained in Section 5.8.

Figure 5.28 shows the p_{T} spectrum of the leading jet in the merged regime. In this

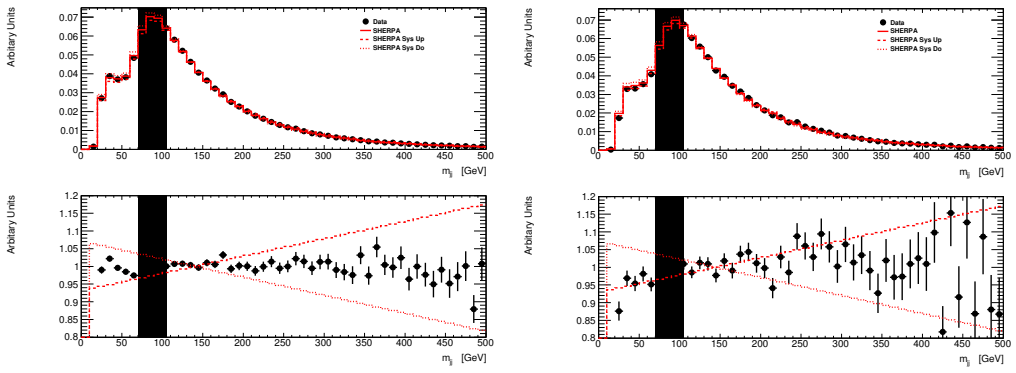

(a) 0-tag

(b) 1-tag

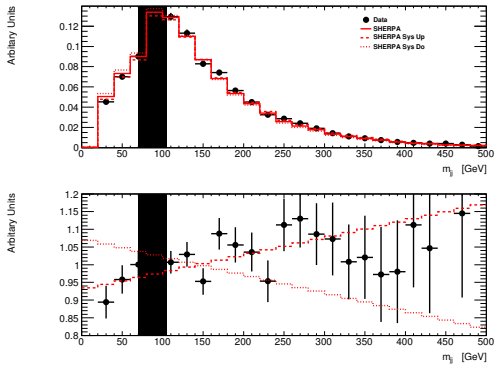

(c) 2-tag

Figure 5.25: The full m_{jj} distribution in data, after subtracting the non-Z background determined from MC simulation, compared to the nominal (solid line) Z+jets MC expectation (after $\Delta\phi_{jj}$ and $p_{\mathrm{T}}^{\ell\ell}$ corrections), along with their ratio. The signal region is blinded (as indicated by the black bandstring). the dashed lines show the Z+jets MC distribution after the downward and upward shape variation described in the text. Note, since these lines indicate the MC simulation after the reweight in the two directions, they just represent the shape variation and not an uncertainty band. As such it should be made clear that the region where the two lines cross does not correspond to a vanishing uncertainty but rather just to the pivot point.

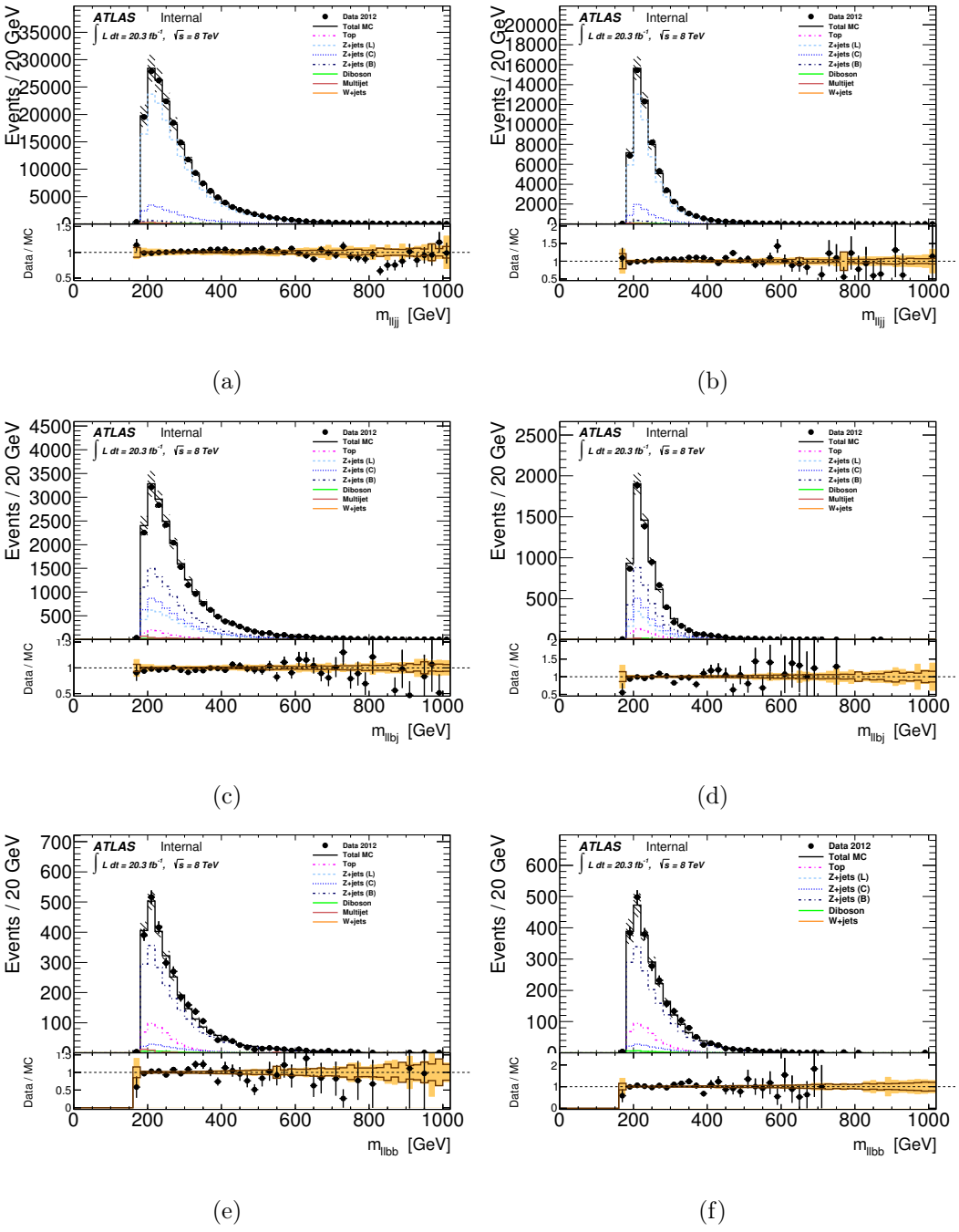

Figure 5.26: $m_{\ell\ell jj}$ distribution for (a, c) 0, (b, d) 1 and (e, f) 2 b-tag events, after the corrections in the text, before (left) and after (right) the optimized selection. The systematic uncertainty bands include the uncertainties associated with these corrections.

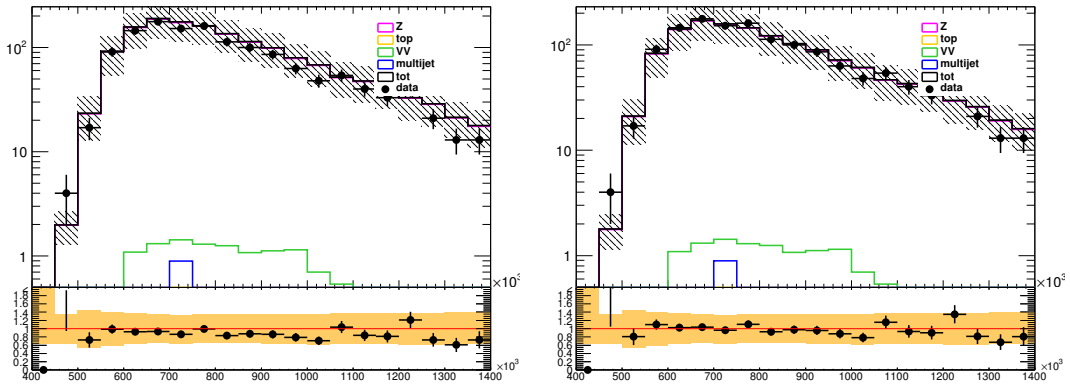

(a) $30 < m_j < 70$ GeV, before scale factor (b) $30 < m_j < 70$ GeV, after scale factor

Figure 5.27: Three-body mass distributions ($m_{\ell\ell j}$) obtained in the m_j sideband before (left) and after (right) the application of the scale factor described in the text.

channel p_{T}^{j} and p_{T}^{Z} are equivalent to each other (a part from the resolution). The good data-MC agreement in this plot shows that no other corrections are needed for the Z+jets background.

5.4.1.3 Z+jets in the VBF category

The Z+jets process is also the dominant background in the VBF category, as can be seen from Figure 5.15. Its normalization is estimated from the data using the same m_{jj} sideband Z+jets control regions as for the resolved ggF category. Due to limit statistics, the control regions are defined at an earlier stage of the VBF event selection, specifically right after the identification of the two candidate jets associated from the decay of the Z boson.

The normalization of the final distribution is derived as part of the final profile likelihood fit as described in Section 5.8. The systematic uncertainty associated to the extrapolation of the normalization between the control region and the signal region, is estimated following the procedure described previously. As in the

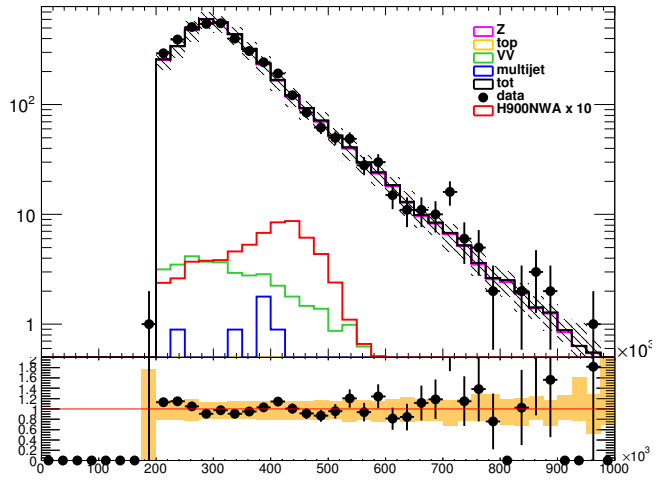

Figure 5.28: p_{T} spectrum of the leading jet in the merged regime.

resolved ggF channel, the reweight used in the VBF case is also a linear parameterization of the form $a(m_{jj} \times 10^{-3} - b)$ and is shown in Figure 5.29.

The Z+jets control region is used to derive a correction to the MC simulation in order to improve the modelling of the $m_{\ell\ell jj}$ distribution. The correction is derived directly from the binned ratio of the data, after subtracting the small contributions from the other background processes, to the MC Z+jets distribution. In order to reduce the effect of statistical fluctuations, the binning is set such that all bins have a statistical uncertainty of less than 10%. The derived shape correction is then propagated to the signal region and to the later stages of the selection. Figure 5.30 shows the agreement of the MC simulation to data after this correction has been applied. The entirety of the shape variation obtained by applying this correction is taken as a systematic uncertainty for this category.

The variables that were used for the shape reweighting of the ggF category were also tested as reweighting variables for the Z+jets background in the VBF category. However, this category uses the ALPGEN MC generator, as it better describes the multijet final state; as a consequence, the variables used to reweight

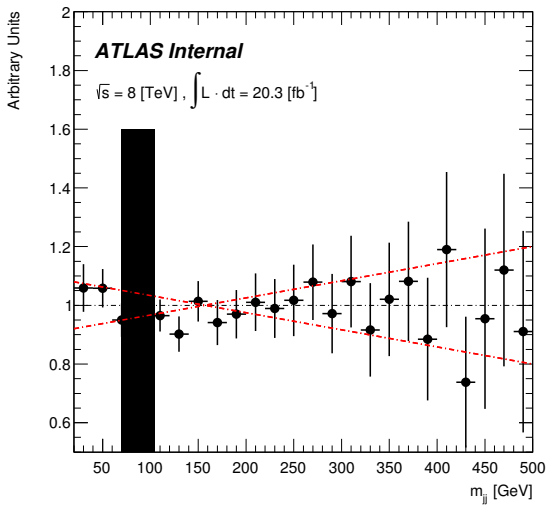

Figure 5.29: The ratio of the full m_{jj} distribution in data, after subtracting the non-Z background determined from MC simulation, over the nominal Z+jets MC expectation. The signal region is blinded. The dashed line show the reweight factors applied to the Z+jets MC distribution in order to acquire the upward/downward variations associated to the normalization from the Z+jets control region.

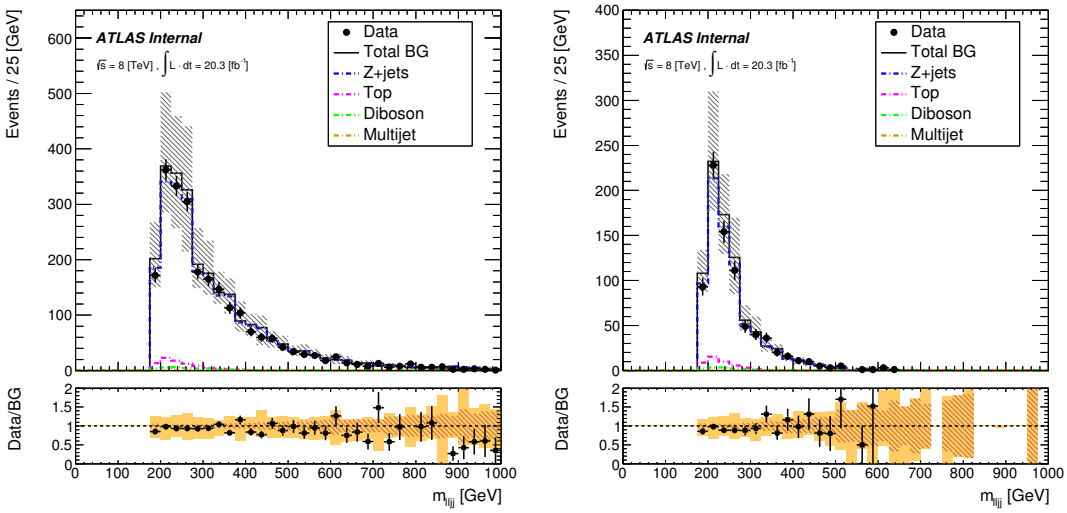

(a) (b)

Figure 5.30: $m_{\ell\ell jj}$ distribution for the control region of the Z+jets background, in the VBF channel, before (a) and after (b) the optimized selection.

the Z+jets background in the ggF category did not provide a better description of the background than the above approach.

5.4.2 Top quark background

Top quark production is a significant background in the 2 b-tag ggF subchannel. This background is dominated by $t\bar{t}$ decays in which both W bosons decay into leptons, and the two leptons and two b-jets from top quark decay have invariant masses that happen to be close to the Z boson mass. The contribution from single top production, primarily Wt, is very small: in the 2 b-tag subchannel only 3.3% of the top quark background is from a single top process and 85% of that comes from Wt production. Another sort of top quark background has leptons that originate from the decay of the b-jet daughters of top quarks. This background is reduced by the isolation requirements described in Sections 5.2.1 and 5.2.2. The presence of neutrinos in the leptonic $t\bar{t}$ decays leads to large values of $E_{\mathrm{T}}^{\mathrm{miss}}$; hence, requiring low values of missing energy (see Section 5.3.3) also reduces this background considerably.

A sample dominated by top quark events is obtained by selecting events with opposite-flavour, *i.e.* $e\mu$, same-sign leptons. The remaining parts of the nominal selection are then applied, including the $m_{\ell\ell}$ requirement. Since top quark production is a small background in all except the tagged subchannel, the "Top2CR" is defined primarily for 2 b-tagged events. However, in order to cross-check the results with higher statistics, the 1 b-tag sample, "Top1CR", is also studied. Here a $\frac{E_{\mathrm{T}}^{\mathrm{miss}}}{\sqrt{H_{\mathrm{T}}}} > 3.5$ requirement is applied to obtain a sample dominated by $t\bar{t}$ decay.

Figure 5.31 shows the m_{jj} and $m_{\ell\ell jj}$ distributions in the top quark control sample for 1 and 2 b-tag events. The data are reasonably described by MC simulation and hence no corrections are applied.

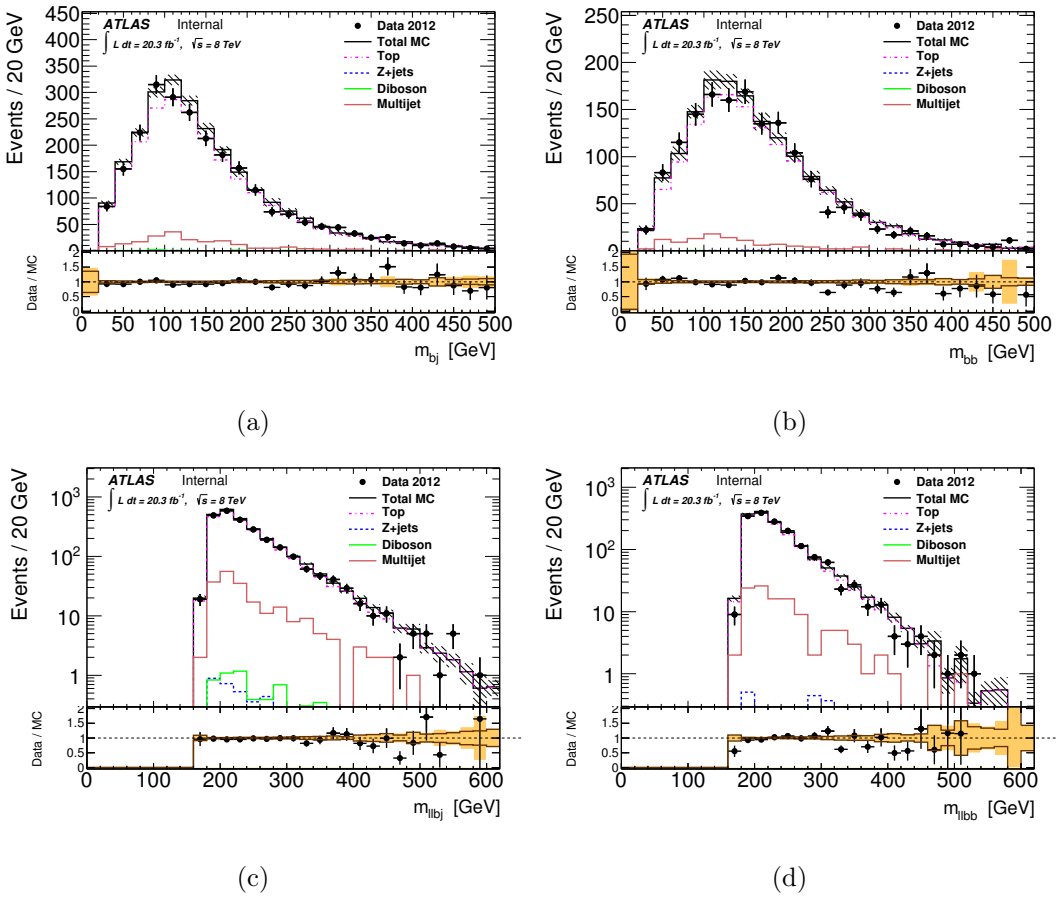

Figure 5.31: The (a, b) m_{jj} and (c, d) $m_{\ell\ell jj}$ distributions for the top control region (CR) in the subchannels with 1 (left) and 2 (right) b-tagged jets.

The unfolded 7 TeV ATLAS $t\bar{t}$ measurement shows that the top quark p_{T} distribution in MC simulation is hard than that observed in data. This difference between data and MC is used to correct the $t\bar{t}$ MC and half or double the correction applied as a systematic uncertainty (see Section 5.5.2.2)

The normalization of the top quark background is determined in the final profile likelihood fit described in Section 5.8 using the $m_{\ell\ell jj}$ distribution in the 2 b-tag $e\mu$ CR as input.

5.4.3 Multi-jet background

Multi-jet events in which two jets are mistakenly identified as leptons form a background if the two misidentified leptons have an invariant mass compatible with the Z boson mass. Photon conversions contribute in the case of electrons, while in-flight pion decays add to muon channel. In addition to "fake" leptons, true leptons from semi-leptonic decay of heavy flavour hadrons may contribute in both electron and muon channels.

The multi-jet background in the electron channel is estimated from data. The shape of the background is obtained from a sample dominated by multi-jet events and then subsequently normalized to the signal selection. A data sample dominated by multi-jet events is obtained by reversing the track isolation cut of the two electrons. The remaining analysis selections are applied and the resulting data histograms are used as templates to describe the shape of the multi-jet background in the various distributions.

Although the templates describe the shape of the multi-jet background, they must be normalized to take into account the difference in efficiency between the two electron selections. The normalization is estimated by fitting the di-electron invariant mass distribution after applying the nominal section up to the requirement of ≥ 2 jets. the is performed over the range $40 < m_{ee} < 150$ GeV using three components:

- the multi-jet template derived from data using the loosened electron selection;
- the $Z \to ee$ background distribution from the MC simulation using the nominal electron selection;
- the sum of all other background distributions from the MC simulation using the nominal electron selection.

Only the normalization of the multi-jet template and $Z \to ee$ background are allowed to vary (the other background are fixed). The fit is performed separately for events with 0, 1 and 2 b-tagged jets and the scale factors obtained are 2.36 ± 0.02(stat.), 1.89 ± 0.04(stat.) and 2.22 ± 0.20(stat.), respectively. Due to the low statistics and the large contribution from top quark background in the 2 b-tag subchannel, this scale factors has a large uncertainty. Due to the smaller background in the 0 b-tag subchannel, this scale factor is used for all b-tag subchannels and a 50% uncertainty assigned to account for the difference. The results of the fit can be seen in Figure 5.5, where the QCD is seen to reasonably model the data in the m_{ee} sidebands.

The residual small multi-jet background in the $e\mu$ TopCR is taken from the opposite-sign $e\mu$ data, which also accounts for the small W+jets background in that region.

The multi-jet background in the muon channel was investigated by comparing the data and MC simulation in the $m_{\mu\mu}$ sidebands (see Figure 5.5) and found to be negligible.

5.4.3.1 Multi-jet background in the merged category

The multi-jet background in the merged category is estimated in the same way as for the resolved category; the estimate is carried out separately for the monojet and the multiple jet subsamples. Since this category is not subdivided based on the number of b-tagged jets, the events containing two or more jets are fit inclusively. The result of the fit in the monojet subchannel is shown in Figure 5.12, which shows overall good data-MC agreement.

5.4.4 Diboson background

Since no suitable data control region can be defined for the diboson background, this background is estimated directly from MC simulation as described in Section 5.1.3.3 with the uncertainties described in Section 5.5.

5.4.5 W+jets background

The W+jets background is found to be negligible except in the top control region, for which the small contribution is taken from same-sign $e\mu$ data events.

5.4.6 SM $Zh, h \to bb$ production

The SM $Zh, h \to bb$ production, taken from MC simulation as described in Section 5.1.3.4, is found to be negligible, contributing to the m_{jj} SB in the tagged channel at the level of 0.5%. Of course, in the BSM Higgs scenarios probed here the coupling may not be the SM values. However, it has been measured to be $\mu_{bb} = 0.52 \pm 0.32$ (stat.) $\pm$ 0.24 (syst.), compatible with the SM prediction. Hence this background is included in the limit fit with the SM strength and a symmetric 50% uncertainty to cover the measured value.

5.5 Systematic uncertainties

Systematic uncertainties can be divided into two categories: the uncertainties on the measurement itself, described in Section 5.5.1, and those associated with the modelling of the signal and background processes, described in Section 5.5.2.

Except where explicitly specified, the systematic uncertainties are treated as fully correlated across all categories and subchannels.

5.5.1 Experimental systematic uncertainties

The experimental uncertainties originate from efficiency corrections and/or the calibrations of simulated objects. The majority of these uncertainties have been provided by the combined performance groups for the relevant objects. To evaluate some of these uncertainties, the smoothing procedure described in Section 5.5.1.7 has been used to minimize the effects of limited MC statistics.
The largest uncertainties of this type in this analysis are those on the jets, as can be seen in Section 5.8.7.

5.5.1.1 Luminosity and pile up

The uncertainty on the integrated luminosity is $\pm 2.8\%$ and is applied to the signal and to the backgrounds estimated from MC simulation (only the diboson background).
An uncertainty due to the modelling of the additional pile-up interactions is applied following the official guidelines.

5.5.1.2 Electrons

The electron reconstruction and identification efficiencies are corrected and have relatively small associated uncertainties $\mathcal{O}(1\%)$. Since the trigger efficiency is very high, no uncertainty is applied for it. Each efficiency correction weight is shifted

coherently to evaluate one systematic variation for the combined effect. The associated nuisance parameter is `ElecEffic`. Uncertainties on the electron energy and resolution corrections, `ElecE` and `ElecEResol` respectively, are evaluated separately by shifting the electron energies up and down and rerunning the event selection.

5.5.1.3 Muons

The muon trigger, reconstruction and identification [111] efficiencies are corrected and have relatively small associated uncertainties $\mathcal{O}(1\%)$. each efficiency correction weight is shifted coherently to evaluate one systematic variation for the combined effect. The associated nuisance parameter is `MuonEffic`. Uncertainties on the resolution smearing from the inner detector and muon system component of the muon reconstruction [111], `MuonEResolID` and `MuonEResolMS` respectively, are evaluated separately by shifting the smearing up and down and rerunning the event selection.

5.5.1.4 Jets

The experimental uncertainties relating to jets are uncertainties on the energy scale, resolution and JVF cut efficiency.

The jet energy scale uncertainty A detailed discussion of the JES and its associated uncertainty is found in [119]. As discussed in Section 5.2.3, the so-called GSC calibration is used. the jet energy scale has been broken down into 54 nuisance parameters:

- 47 for the various in-situ JES calibration analyses. These are combined by an eigenvector decomposition into 6 parameters, `JetNP1-JetNP1`. This does

not allow for correlations between 7 TeV and 8 TeV analyses but here only 8 TeV dataset is analyzed;

- two for η inter-calibration, specifically comparisons of PYTHIA and HERWIG and the statistical component of this comparison, `JetEtaModel` and `JetEtaStat`. It arises from potential mismodelling of the additional radiation that may affect the p_{T} and η of the dijet system;

- one for the MC non-closure, `JetNonClos`, relative MC12a/PYTHIA8 with full simulation, since other MC generators do not fully satisfy closure. The calibration was derived on MC12a and any given MC sample can be classified as MC12a, PYTHIA8 or AFII;

- four for pile-up, three of which are μ/N_{PV} dependent and the last of which is dependent on the event energy density ρ, `JetMu`, `JetNPV`, `JetPilePt` and `JetPileRho`.

Four additional components are included for flavour and kinematic uncertainties:

- one for differences in (truth) b-jet response that are seen across different MC simulations, `JetFlavB`;

- one for μ and ν energies from b-hadron decay (truth b-jets only), `JetBE`;

- one for the unknown mixture of light-quarks and gluons (non-truth b-jets only), `JetFlavComp_X`;

- one for the difference in response between light-quarks and gluons assessed from MC comparisons (non-truth b-jets only), `JetFlavResp_X`.

The b-jet energy scale uncertainty is $\sim 1 - 2\%$. The flavour composition and response above are separated for different processes as the quark/gluon mixture can

be different in each (`X = Wjets, Zjets, Top` or `signal/VV`). The quark/gluon mixture of non-b-jets is assumed to be 50% with 100% uncertainty; thus the effect of this uncertainty is maximal. After including all sources of uncertainty, the total fractional systematic uncertainty on the JES ranges from $\sim 3\%$ at 20 GeV to $\sim 1\%$ for a 1 TeV jet.

The jet energy resolution uncertainty Two systematic uncertainties are applied:

- one for jet resolution, `JetEResol`;
- one for b-jet resolution (truth b-jets only), `BJetReso`.

Good jet energy resolution (JER) is important for this analysis since it allows a narrow m_{jj} window, thus reducing Z+jets background. The range for the relative JER is from $\sim 25\%$ at 20 GeV to $\sim 5\%$ near 1 TeV. The resolution is found to be well-described by MC simulation when validated by in-situ analyses using the dijet balance and bisector methods. The relative uncertainty was determined from the observed differences between data and MC simulation in the resolution as determined by those in-situ studies as well as from uncertainties on the methods themselves. This is known to be an overestimate; therefore, constraints in the profile likelihood can be expected. The effect of both JER uncertainties is obtained in this analysis by smearing the jet p_{T} according to a Gaussian distribution centered at 1, with a width equal to the true resolution plus the value of the relative uncertainty given by the jet's p_{T} and, for the general JER uncertainty, the η as well. The effect on the final variable is then symmetrized to obtain a two-sided uncertainty.

Jet vertex fraction uncertainty The JVF efficiency uncertainty, `JetJVF`, is obtained from differences between data and MC simulation in Z+jets events. The cut value is nominally 0.5 and varied between 0.47 and 0.53 to evaluate the uncertainty.

Jet mass scale uncertainty The jet mass scale uncertainty is of crucial importance when the single jet mass is used as a discriminant variable as in the merged regime of this search. This uncertainty is usually evaluated studying the so called "double ratio", *i.e.* $R^{m_{\text{trackcalo}}} = \frac{r^{m,\text{data}}_{\text{trackcalo}}}{r^{m,\text{MC}}_{\text{trackcalo}}}$ where $r^{m,X}_{\text{trackcalo}} = \frac{m^X_{\text{calo}}}{m^X_{\text{track}}}$ (X = data or MC). The value of this uncertainty of course is a function of p_{T}, m and η of the jet. In order to account for this uncertainties in this analysis a flat 10% value is assumed, as it contains the variations of the double-ratio in the considered phase space. An example of this can be seen in Figure 5.32 where $R^{m_{\text{trackcalo}}}$, $r^{m,\text{data}}_{\text{trackcalo}}$ and $r^{m,\text{MC}}_{\text{trackcalo}}$ are shown.

Another source of uncertainty on the jet mass scale comes from the different topology that characterizes the jets coming from the decay of a boosted boson with respect to those coming from hadronization of a single parton. It has been shown that this effect can be accounted fro with an additional 10%.
The final value for the JMS uncertainty is hence derived by summing in quadrature the two values obtained, thus leading to a JMS uncertainty of 14%.

5.5.1.5 Missing transverse energy

All systematic variations of object energies are propagated to the $E^{\text{miss}}_{\text{T}}$ calculation. Uncertainties on $E^{\text{miss}}_{\text{T}}$ itself come from variations of he energy scale, `METScaleSoftTerms`, and resolution, `METResoSoftTerms`, of calorimeter clusters

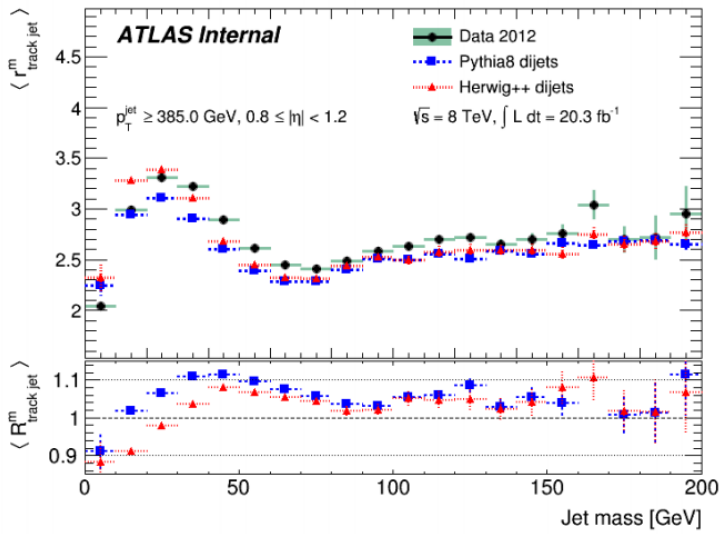

Figure 5.32: $R^{m_{\text{trackcalo}}}$, $r^{m,\text{data}}_{\text{trackcalo}}$ and $r^{m,\text{MC}}_{\text{trackcalo}}$ used to parameterized the uncertainty on the jet mass scale.

which have not been associated with a reconstructed object, the so-called "soft terms".

5.5.1.6 Flavour tagging

As discussed in Section 5.2.3.2, the MV1c discriminant is used to separate light- and heavy-flavour jets. In MC simulation, jets are matched to truth jets and on that basis labelled as "b", "c" and "light". Scale factors have been derived for each flavour as a function of jet p_{T} and MV1c output to correct the MC efficiency to that of data. Representative scale factors with associated uncertainties are shown in Figure 5.33. These uncertainties include experimental components (*i.e.* JES), theoretical components (*i.e.* the top quark p_{T} spectrum in $t\bar{t}$ events), and a statistical component from the data in each $p_{\text{T}} \times$ MV1c ($\times\eta$ for light jets) bin. As for the JES uncertainty, this collection of uncertainties is made more manageable by performing an eigenvector decomposition. Only the leading ten (15 for c-jets)

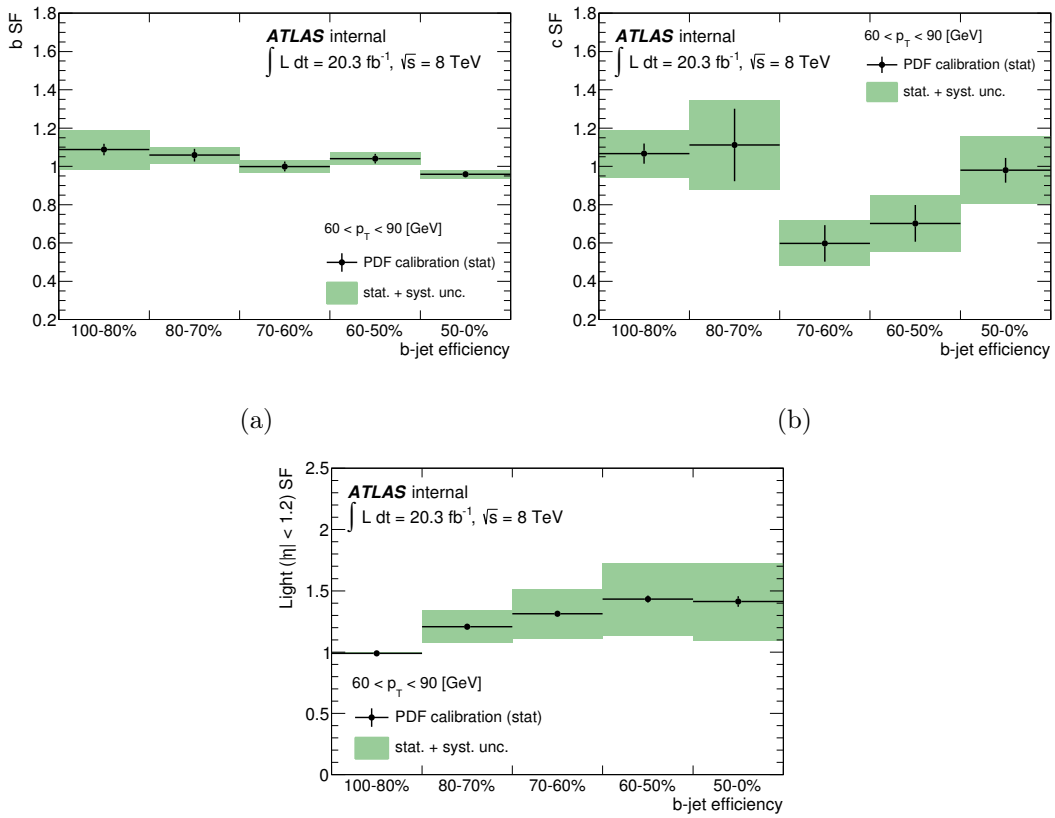

Figure 5.33: The final MC-to-data calibration scale factors for the MV1c b-, c-jet and $|\eta| < 1.2$ light-jet calibration for a representative jet p_{T} bin. The data results are compared to MC expectations. Error bars show statistical uncertainties, while the bands include systematic uncertainties as well.

components are kept. The remaining nuisance parameters are neglected; they were found to have an effect of less than 1% on the analysis.

On top of the flavour tagging eigenvector uncertainties described above, an additional systematic uncertainty is applied on the MC-to-MC dependent corrections used to take into account the generator dependence of the scale factors described in Section 5.2.3.2, `SysBTagCSherpa` (`SysBTagCPythia8`) and `SysBTagBSherpa` (`SysBTagCPythia8`) for SHERPA (PYTHIA8). This uncertainty is taken to be half the applied correction for each MC generator.

As discussed in Section 5.2.3.3, truth tagging is used for events that do not contain a jet which matches b-hadrons from the MC truth information. However, a bias has been measured as a function of $\Delta R(j, j)$ for events with two c-jets only. The effect was not seen in light-light events, not in c-light events and truth tagging is not used in events with a truth-matched b-jet. A correction has been derived for cc events as outlined in Section 5.2.3.3 and an associated systematic uncertainty applied, `TruthTagDR`.

5.5.1.7 Smoothing

The uncertainties on reconstructed objects are evaluated in two different ways: by shifting weights or by re-selecting events. For flavor tagging, where a scale factor is used to correct the simulation efficiency to data, this weight is shifted up (down) and the change in the final distribution is noted as the $+1(-1)\sigma$ shift. For jet energy scale (JES) uncertainties, the jet energies are shifted and therefore events can migrate in and out of the acceptance. Again the difference in the final variable is noted as the 1σ error but if the variations are small and/or the sample statistics are small, the MC statistical uncertainty can make up a substantial part of this supposed systematic difference. If there are multiple JES uncertainties as in this analysis, then this MC uncertainty should not be included in each one.

To mitigate these effects, two so-called "smoothing" algorithms are used to merge consecutive bins in the MC templates. First, bins from one extremum to the next are merged until at most one local extremum remains in the $m_{\ell\ell jj}$ distribution. If there are more than two extrema, merging is performed at each step of this iterative process where the difference between merged and unmerged template is smallest. Second, the bins resulting from this first algorithm are sequentially merged, starting rom the upper end of the distribution, until the statistical uncertainty in each

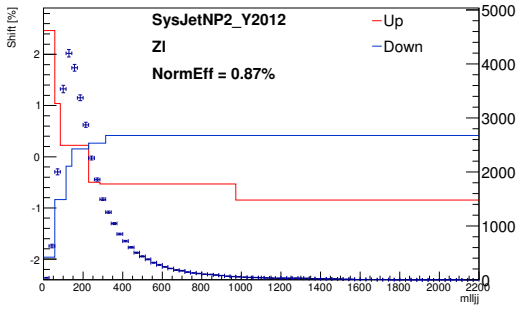

Figure 5.34: An example of the smoothing procedure used for systematic uncertainties. The nominal distribution without rebinning is shown as points and the relative systematic variation using the binning determined by the smoothing procedure is shown as the histogram. Up and down refer to the nominal name of the systematic not necessary change on the current distribution.

of the merged bins, calculated in the nominal template, is smaller than 5%. In each of these sets bins, the integrals of the nominal and systematically shifted distributions are compared to give the $\pm 1\sigma$ variation. This value is then used as the associated uncertainty for all the nominal bins in the set. Figure 5.34 shows such rebinned distribution.

In the MV1c distribution, it does not make sense to merge neighbouring bins since the MV1c distribution is discrete and hence the smoothing procedure described above is not applied.

5.5.2 Signal and background modelling systematics

The systematics uncertainties on the signal arise from the signal acceptance and the interference effect whereas the background systematics are related to the modelling of the Z+jets, top quark and multi-jet backgrounds.

5.5.2.1 Z+jets backgrounds

As described in Section 5.4.1.1, corrections are applied to the $\Delta\phi_{jj}$ and $p_{\mathrm{T}}^{\ell\ell}$ distributions of the Z+jets background MC simulation in the ggF channel to improve the description of the data in the sideband regions. For the $\Delta\phi_{jj}$ correction to the Z+light-jet simulation in the low $p_{\mathrm{T}}^{\ell\ell}$ case, an uncertainty of half the applied correction is assigned, while the full correction is taken as the uncertainty in the $Z + b/c$-jet case, where no correction is applied, `ZDPhi`. In the high-$p_{\mathrm{T}}^{\ell\ell}$ case, where no correction is applied to any flavour, the statistical uncertainty on the fitted slope is applied as a systematic uncertainty to the entire Z+jets simulation. These uncertainties are treated as uncorrelated between Z+light-jets and $Z + b/c$-jets. A correction is also applied to the $p_{\mathrm{T}}^{\ell\ell}$ distribution of the $Z + b/c$-jets simulation. An uncertainty of half the correction is used for the entire Z+jet simulation; this is treated as uncorrelated between Z+light-jets and $Z + b/c$-jets, `ZPtV`.

In the VBF channel, a correction is instead applied to the $m_{\ell\ell jj}$ distribution to reproduce the data in the sideband and, as described in Section 5.4.1.3, a conservative systematic uncertainty applied on this by removing or doubling this correction, `ZMlljj`.

The uncertainty on the modelling of the m_{jj} distribution by the Z+jets simulation, in both the ggF and VBF channels, is described in Section 5.4.1.1. This systematic uncertainty used for all Z+jets events, but is uncorrelated between Z+light-jets and $Z + b/c$-jets, `ZMjj`.

As described in Section 5.4.1.1, the flavour composition of the Z+jets sample in the ggF channel is determined from the sum of the MV1c weight for the two signal jets in the 0, 1 and 2 b-tag sidebands and is performed as part of the final profile likelihood fit describe in 5.8. The heavy flavour scale factors obtained in the fit have some dependence on the MC model used to unfold them. A truth-level comparison of Sherpa with Alpgen+Pythia is used to determine an uncertainty o

the ratio of $Z + bc$ to $Z + bb$ of 12%, `ZbcZbbRatio`, and on the ratio of $Z + cc$ to $Z + bb$ of 12%, `ZccZbbRatio`.

5.5.2.2 Top quark background

As described in Section 5.4.2, the top quark p_{T} distribution is corrected using the ATLAS $t\bar{t}$ measurement [120]. A systematic uncertainty on this correction is applied by halving or doubling the correction applied, `TopPt`. An uncertainty on the shape of the m_{jj} distribution is derived by comparing the default $t\bar{t}$ NLO MC simulation (PowHeg+Pythia) with an array of different models which probe different sources of modelling uncertainty, `TtbarMBBCont`. to investigate the uncertainty on the modelling of the parton showering, samples of AcerMC with either more or less parton showering are used. PowHeg+Herwig is used to investigate the effects of a different parton shower and hadronization model. The effects of the modelling of higher orders in perturbation theory are estimated by comparing with the LO MC generator Alpgen and another NLO MC generator, aMC@NLO, is used to estimate effects due to different matrix element calculations. The dependence of the cross sections on the PDF set are investigated with PowHeg+Pythia using the HERA PDF.

a similar procedure is used to derive uncertainties on the single-top background. As described in Section 5.4.2, the single-top background is only a small part of the total top quark background and is dominated by the Wt channel. Normalization uncertainties are derived by varying in cross section calculations the renormalization and factorization scales, the values of α_{S} and the PDF eigenvectors; the results are 7% for single-top Wt channel, 4% for the t-channel and 4% for the s-channel. Since the Wt channel is by far the dominant component, the 7% uncertainty is applied to the full single top background, `stopNorm`. In addition, for the dominant Wt channel, shape uncertainties on the m_{jj} and leading jet distributions are de-

rived from comparisons with HERWIG, `WtChanPythiaHerwig`, and with ACERMC, `WtChanAcerMC`.

5.5.2.3 Diboson background

The uncertainty on the diboson background is determined by evaluating the perturbative QCD uncertainties of the fixed-order NLO calculating using MCFM. The uncertainties on the cross section are derived by varying the renormalization and factorization scales used in the calculation. In order to be more robust against underestimating cross section uncertainties due to cancellations, the "Stewart-Tackmann" method [121, 122] is used. Normalization and shape uncertainties as a function of $p_{\mathrm{T}}^{\ell\ell}$ are derived for the exclusive two-jet, `VVjetScalePtST2`, and three-jet cross sections, `VVJetPDFAlphaPt`. These are 3% for ZZ/WW production and 4% for WZ. Additional shape uncertainties on the m_{jj} distribution are obtained by comparing LO MC simulation (HERWIG) with a NLO one (POWHEG+PYTHIA), `VVMbb`.

5.5.2.4 Multi-jet background

As described in Section 5.4.3, the multi-jet background templates and normalization are determined from data. The normalization factor derived from the 0 b-tag selection is used for all b-tag subchannels and 50% systematic uncertainty is assigned, `MJ`. A separate uncorrelated multijet normalization parameter is applied in the top $e\mu$ CR, `MJ_regiontopemu` since the multijet background is determined by a different method (see Section 5.4.3).

5.5.2.5 SM $Zh, h \to bb$ background

A 50% uncertainty is assigned to the $Zh, h \to bb$ background as described in Section 5.4.6.

5.5.2.6 Signal

An uncertainty in the experimental acceptance for the Higgs boson signal due to the modelling of Higgs production is evaluated by varying the parameters of the PowHeg+Pythia samples and comparing the results by applying that analysis selection at generator level. The following variations are considered:

- renormalization μ_{R} and factorization μ_{F} scales are varied up and down both separately and coherently by a factor of two;
- the amount of initial and final state are increased and decreased separately following a procedure suggested by the Monte Carlo Generators group;
- the nominal CT10 PDF is replaced by either the MSTW2008nlo68cl or NNPDF23_nnlo_noLHC_as_0120 PDFs.

The resulting change in signal acceptance for the resolved ggF channel are shown in Figs. 5.35 and 5.36 for the NWA signal in the ggF and VBF channels, respectively. Figure 5.37 shows the same systematics in the merged channel. For the μ_{F} and μ_{R} variations it can be seen that there is no resulting change in the signal acceptance within statistical uncertainties so this variation is neglected. The PDF variations give rise to a small change in acceptance which is independent of Higgs mass and amounts to 2% for resolved ggF and VBF, while it is 3% for the merged. In the case of the ISR/FSR variations it can be seen that the dominant effect comes from FSR and is dependent on the Higgs mass. The acceptance change

due to FSR increases at low m_H and also at high m_H for the untagged and VBF categories; the latter is due to the optimised p_{T}^{j} cut, which is not applied in the tagged case. The ISR and FSR variations are added in quadrature and the overall change in acceptance approximated by a quadratic function in m_H that is symmetric about the nominal, as shown in Figures 5.35(e), 5.35(f) and 5.36(c). In the ggF channel, this variation amounts to around 5% at low m_H, decreasing to about 1% at intermediate mass and then increasing to about 10% (5%) for untagged (tagged) at high m_H; in the VBF channel it is around 10% at low and high m_H, decreasing to 5% at intermediate m_H. This is added in quadrature with 2% from the PDF variation to give the overall signal acceptance uncertainty as a function of m_H. The same studies have been carried out for the merged channel, where the uncertainty obtained varying the ISR and the FSR is bigger than in the resolved category, as can be seen in Figure 5.37. Here, this uncertainty is parameterized as a linear function and it amounts to around 30% at $m_H = 800$ GeV and goes down to around 10% at $m_H = 1$ TeV. As in the resolved channel, this uncertainty is added in quadrature to the 3% coming from the PDF variation.

It has been checked that the acceptance variations do not change the shape of the $m_{\ell\ell jj}$ ($m_{\ell\ell j}$ for the merged channel) distribution, only the acceptance. The NWA variations was also found to adequately cover the uncertainties for the complex pole scheme sample.

In addition to the signal acceptance uncertainties, a shape uncertainty is applied on the $m_{\ell\ell jj}$ distribution due to the interference reweighting.

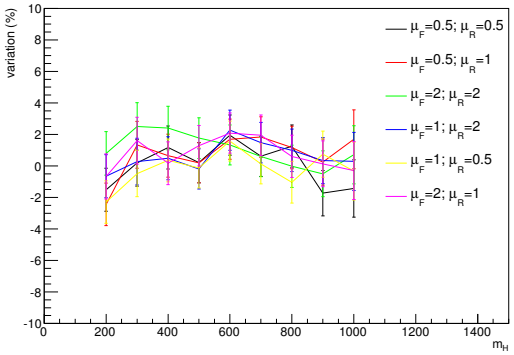

(a) Renormalization/Factorization, untagged

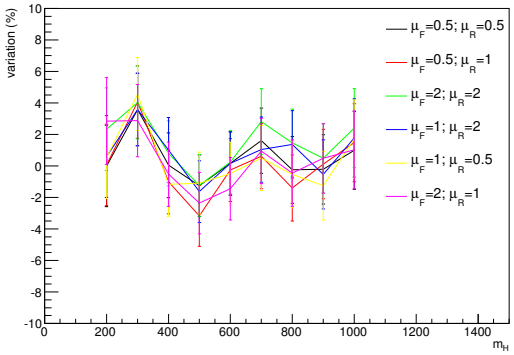

(b) Renormalization/Factorization, tagged

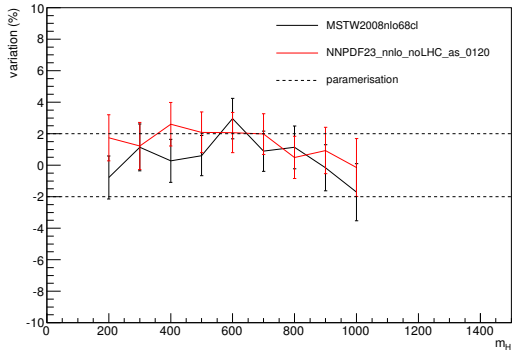

(c) PDF, untagged

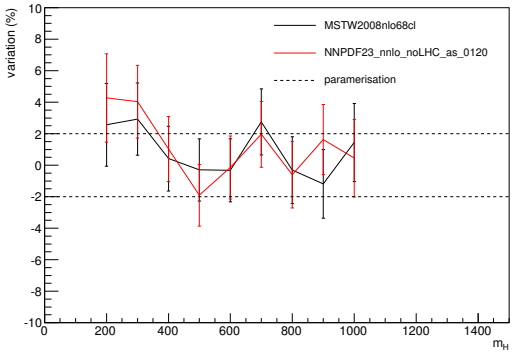

(d) PDF, tagged

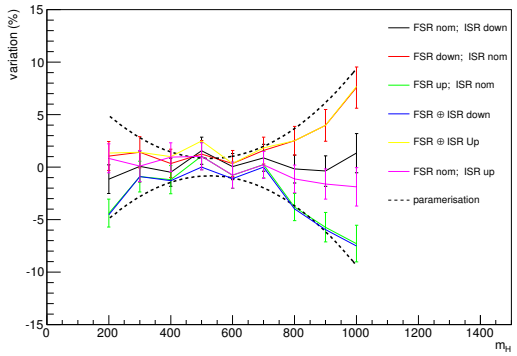

(e) ISR/FSR, untagged

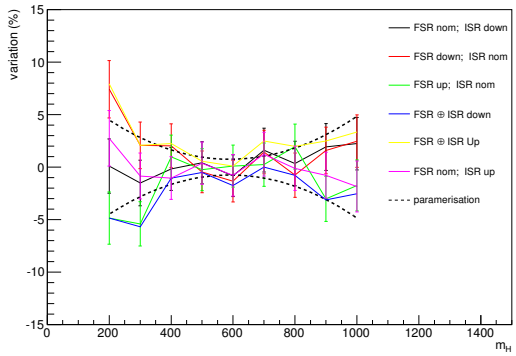

(f) ISR/FSR, tagged

Figure 5.35: The signal acceptance variations for the NWA signal in the ggF channel due to changes in (a, b) renormalization/factorization scale, (c, d) PDF and (e, f) ISR/FSR. The left (right) column is for the untagged (tagged) category.

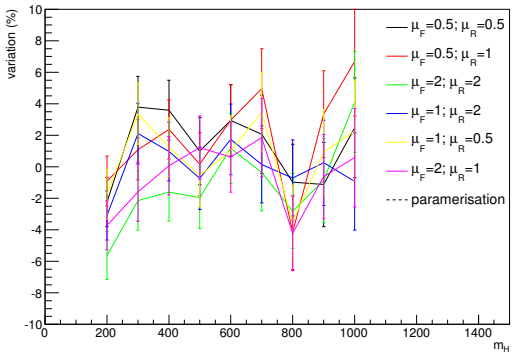

(a) Renormalization/Factorization

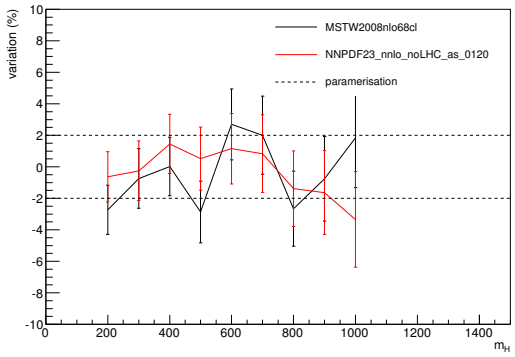

(b) PDF

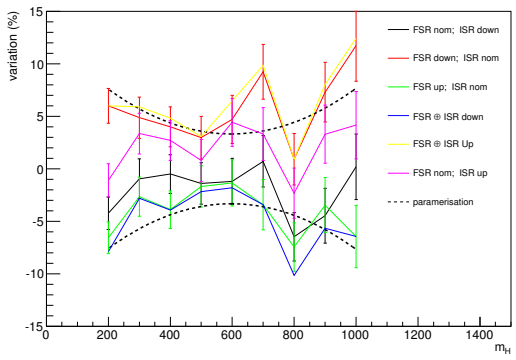

(c) ISR/FSR

Figure 5.36: The signal acceptance variations for the NWA signal in the VBF channel due to changes in (a) renormalization/factorization scale, (b) PDF and (c) ISR/FSR.

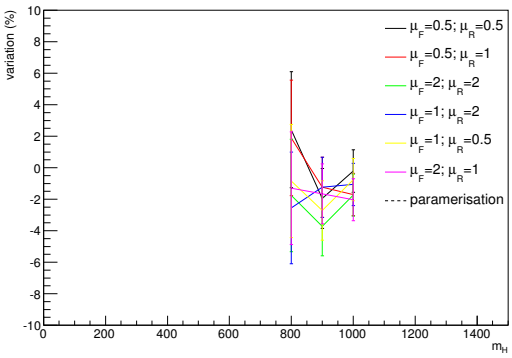

(a) Renormalization/Factorization

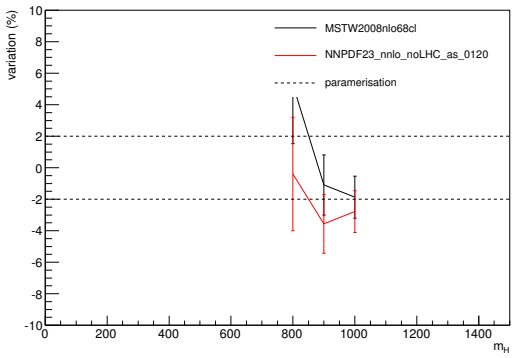

(b) PDF

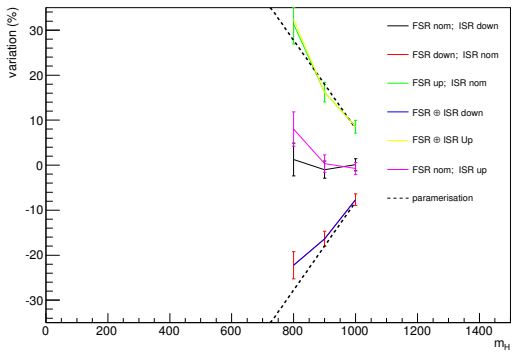

(c) ISR/FSR

Figure 5.37: The signal acceptance variations for the NWA signal in the ggF channel for the merged category alone, due to changes in (a) renormalization/factorization scale, (b) PDF and (c) ISR/FSR.

5.6 Resolution and binning of the $m_{\ell\ell jj}$ distributions

5.6.1 Resolution

The resolution of the signal $m_{\ell\ell jj}$ distribution has important consequences for the applicability of the NWA signal samples in the *2HDM*s; if the experimental resolution is less than the signal width predicted at a given point in the *2HDM* plane the NWA is non longer valid. To investigate this, the experimental resolution is extracted by iteratively fitting a Gaussian to the reconstructed $m_{\ell\ell jj}$ distribution of the NWA signal over a $\pm 2\sigma$ window until no change above 1% is observed. The results of the resolution versus m_H are shown in Figure 5.38, where it can be seen that the width increases from around 5 - 25 GeV as m_H increases. Figure 5.39 shows the fractional resolution relative to m_H, which is relatively flat in the range 2 - 3 %. This is significantly narrower than the natural width in some of the *2HDM* plane, which therefore must be taken into account (see Section 5.9.2).

5.6.2 Binning

Variable sized binning was chosen since the background distribution falls sharply with increasing $m_{\ell\ell jj}$ and the $m_{\ell\ell jj}$ resolution increases with increasing $m_{\ell\ell jj}$, as seen in Figures 5.38. The binning scheme is chosen to ensure a reasonable number of background events and that the bin size is not smaller than the signal resolution. The binning is defined as follows:

- a minimum bin width of 8 GeV;
- bin width either remains the same or increases with increasing $m_{\ell\ell jj}$;

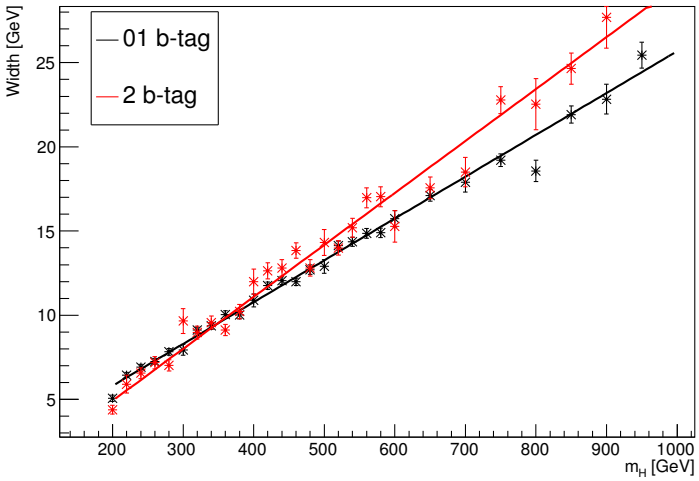

Figure 5.38: The resolution of the $m_{\ell\ell jj}$ distribution as a function of m_H for both untagged and tagged ggF channels. The errors are statistical only.

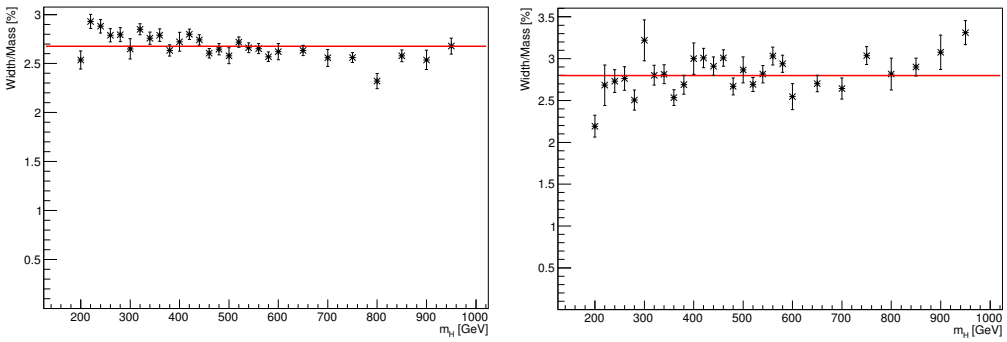

(a) untagged (b) tagged

Figure 5.39: The fractional resolution of the $m_{\ell\ell jj}$ distribution as a function of m_H for both untagged (left) and tagged (right) ggF channels. The errors are statistical only.

- for the ggF channel (both 2 and $< 2b$ tagged events) with $300 < m_{\ell\ell jj} < 900$ GeV ($m_{\ell\ell jj} > 900$ GeV) a maximum of 5% (15%) total MC statistical error;
- for VBF events and $300 < m_{\ell\ell jj} < 600$ GeV ($m_{\ell\ell jj} > 600$ GeV) a maximum of 15% (25%) total MC statistical error.

The maximum MC statistical error is increased at higher masses in order to prevent a very large bin much greater than the mass resolution. The larger maximum MC statistical error in the VBF channel is due to the smaller background efficiency and worse MC statistics in the ALPGEN Z+jets sample compared to the SHERPA used in the ggF channels.

5.7 Results

Results consist of the final discriminant plots for the signal region in the different analysis categories for several Higgs boson masses using the NWA signal with the SM cross section as a benchmark.
The MC simulation has all the modelling corrections described in Section 5.4 applied. It is normalized (including Z+jets flavour composition) using the final combined limit fit described in Section 5.8.

5.7.1 Resolved ggF category

Figures 5.40 and 5.41 show the final $m_{\ell\ell jj}$ discriminant (as described in Section 5.3.3.1) for the untagged and tagged subchannels after the optimized selection of Eq. 5.1. The signal combines both ggF and VBF production modes and is shown for $200 \leq m_H \leq 1$ TeV in 200 GeV steps.

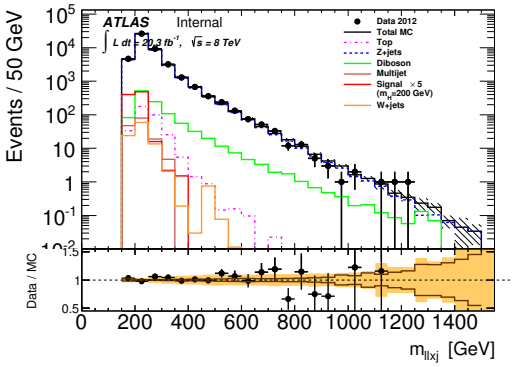

(a) $m_H = 200$ GeV

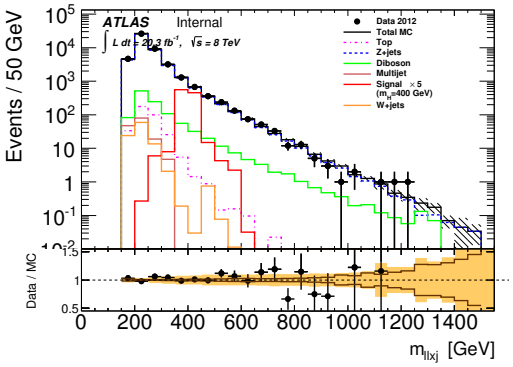

(b) $m_H = 400$ GeV

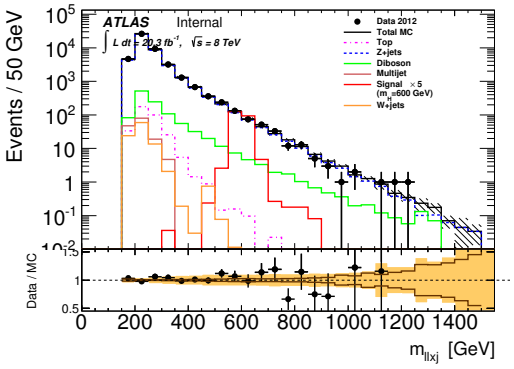

(c) $m_H = 600$ GeV

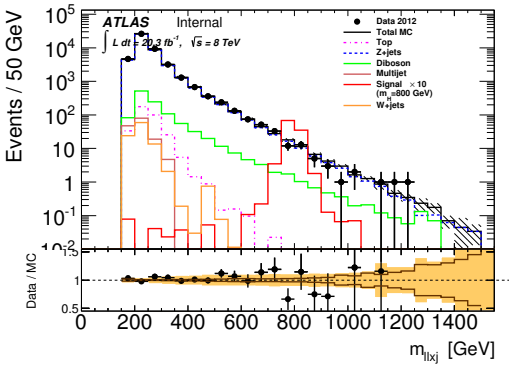

(d) $m_H = 800$ GeV

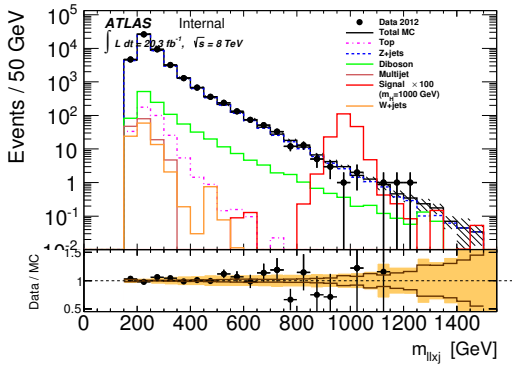

(e) $m_H = 1$ TeV

Figure 5.40: $m_{\ell\ell jj}$ distribution for various Higgs boson signal masses in the untagged subchannel of the (resolved) ggF category. The hashed band indicates the systematic uncertainty. Note that the signal is multiplied by various scale factors for clarity.

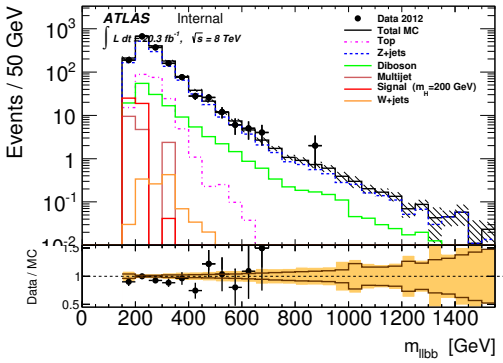

(a) $m_H = 200$ GeV

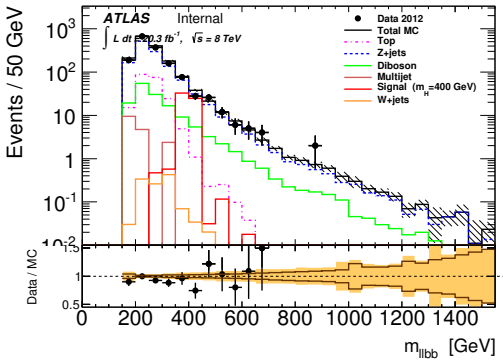

(b) $m_H = 400$ GeV

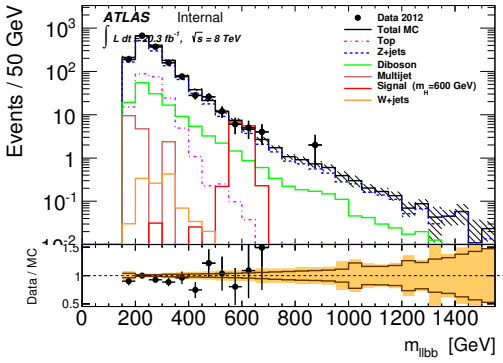

(c) $m_H = 600$ GeV

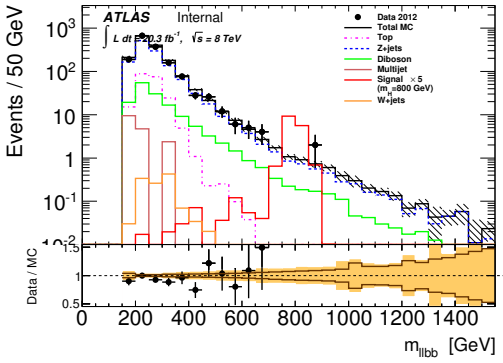

(d) $m_H = 800$ GeV

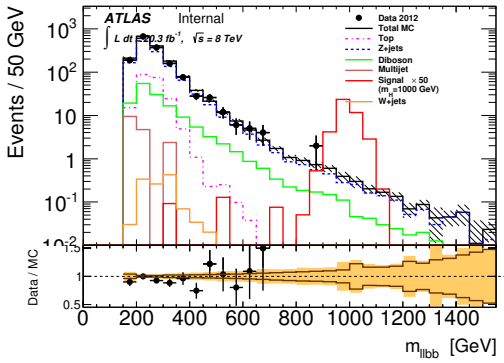

(e) $m_H = 1$ TeV

Figure 5.41: $m_{\ell\ell jj}$ distribution for various Higgs boson signal masses in the tagged subchannel of the (resolved) ggF category. The hashed band indicates the systematic uncertainty. Note that the signal is multiplied by various scale factors for clarity.

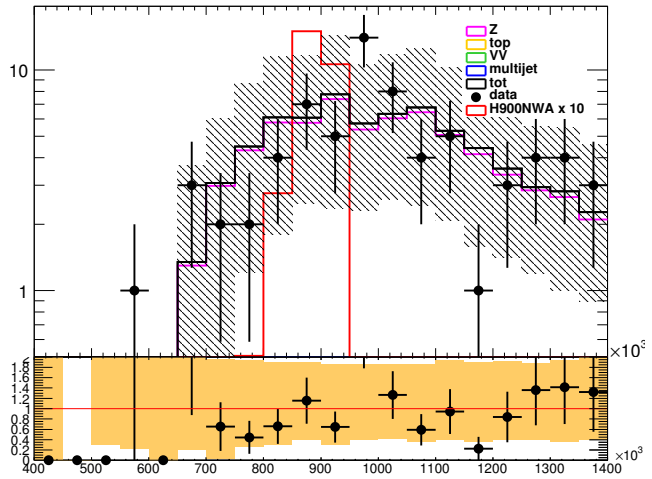

Figure 5.42: $m_{\ell\ell}$ distribution for the merged category using $m_H = 900$ GeV. The dashed band shows the systematic uncertainty.

5.7.2 Merged ggF category

Figure 5.42 shows the final $m_{\ell\ell j}$ discriminant (as described in Section 5.3.3.2) for the merged category. The signal is ggF only and it is shown for $m_H = 900$ GeV.

5.7.3 VBF category

Figure 5.43 shows the final $m_{\ell\ell jj}$ discriminant (as described in Section 5.3.3.3) for the VBF category. The signal combined both ggF and VBF production modes and is shown for $200 \leq m_H \leq 1$ TeV in 200 GeV steps.

5.8 Statistical interpretation

The culmination of this analysis is a combined profile likelihood in which our knowledge, and lack thereof, is parameterized and tested against data.

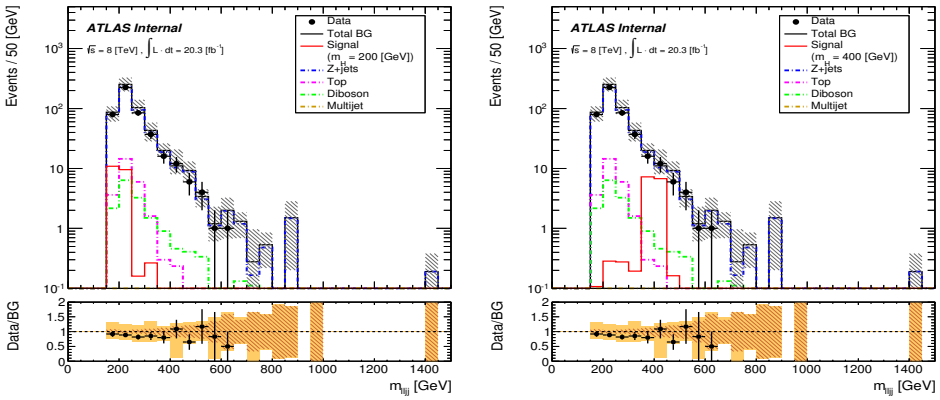

(a) $m_H = 200$ GeV (b) $m_H = 400$ GeV

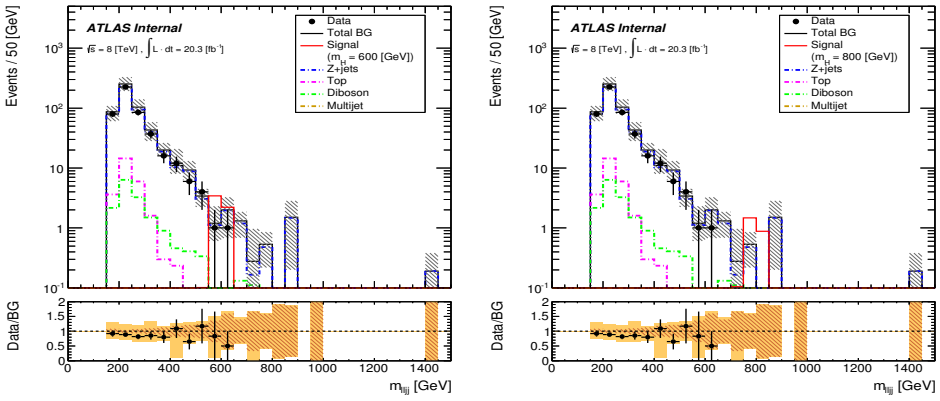

(c) $m_H = 600$ GeV (d) $m_H = 800$ GeV

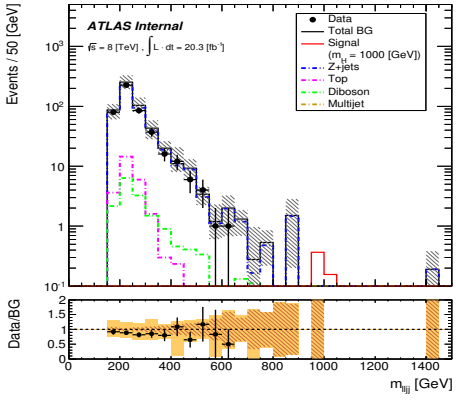

(e) $m_H = 1$ TeV

Figure 5.43: $m_{\ell\ell jj}$ distribution for different Higgs boson signal masses in the VBF category. The hashed band indicates the systematic uncertainty. Note that the signal at $m_H = 1$ TeV is multiplied by 10.

5.8.1 Likelihood definition

The statistical analysis of the data uses a binned likelihood function constructed as the product of Poisson probability terms:

$$\text{Pois}\left(n|\mu S + B\right) = \prod_{b\in\text{bins}}^{n} \left(\frac{\mu\nu_b^{\text{sig}} + \nu_b^{\text{bkg}}}{\mu S + B} \right) \tag{5.2}$$

where a signal strength parameter μ multiplies the expected signal yield ν_b^{sig} in each histogram bin b and ν_b^{bkg} represents the background content for bin b. The dependence of the signal and background predictions on the systematic uncertainties is described by a set of nuisance parameters (NP) θ, which are parameterized by Gaussian or log-normal priors; the latter are used for normalization uncertainties in order to maintain a positive likelihood. The expected numbers of signal and background events in each bin are functions of θ and parameterized such that the rates in each categories are log-normally distributed for a normally distributed θ. The priors act to constrain the NPs to their nominal values within their assigned uncertainties. They are implemented via the so-called penalty or auxiliary measurements added to the likelihood which will always increase when any nuisance parameter is shifted from the nominal value. The likelihood function $\mathcal{L}(\mu, \theta)$ is therefore a function of μ and θ.

The nominal fit result in terms of μ and σ_μ is obtained by maximizing the likelihood function with respect to all parameters. This is referred to as the maximized log-likelihood value MLL. The test statistics q_μ is then constructed according to the profile likelihood as:

$$q_\mu = 2\ln\left[\frac{\mathcal{L}\left(\mu, \hat{\hat{\theta}}_\mu\right)}{\mathcal{L}\left(\hat{\mu}, \hat{\theta}\right)}\right] \tag{5.3}$$

where $\hat{\mu}$ and $\hat{\theta}$ are the parameters that maximize the likelihood (with the constraint $0 \leq \hat{\mu} \leq \mu$) and $\hat{\hat{\theta}}_\mu$ are the nuisance parameter values that maximize the

likelihood for a given μ. This test statistic is used to measure the compatibility of the background-only model with the observed data and for exclusion intervals derived with the CL_S method [69, 123].

5.8.2 Fit inputs and variables

A combined profile likelihood fit is performed across the three analysis categories: ggF, merged and VBF. As already mentioned, the ggF category is further divided into untagged and tagged subchannels, while the other two categories are treated inclusively in b-tag multiplicity (mostly due to low statistics). For each of these categories, the input to the likelihood is the final ZZ invariant mass distribution: $m_{\ell\ell jj}$ in the $gg\mathrm{F}/VBF$ categories and $m_{\ell\ell j}$ in the merged category.
In addition to the signal distributions for the various categories, control region distributions are also included to constrain the normalization of the Z+jets and top quark backgrounds as described in Section 5.4. The other minor backgrounds are taken from MC simulation (or data-driven techniques in the case of the multi-jet background) normalized to the cross-section defined in Section 5.1.3. The control region distributions used are

- for Z+jets background in the ggF category: the MV1c distribution in the combined m_{jj} sidebands for untagged and tagged events separately, as outlined in Section 5.4.1.1; this allows constraining the flavour composition of the Z+jets background;
- for Z+jets background in the VBF category: the $m_{\ell\ell jj}$ distribution in the combined m_{jj} sidebands (inclusive in b-tag multiplicity);
- for Z+jets background in the merged category: the $m_{\ell\ell j}$ distribution in the combined m_j sidebands (inclusive in b-tag multiplicity);

$N_{b-\text{tag}}$	Categories						
	ggF			Merged		VBF	
	m_{jj} SR	m_{jj} CR	$e\mu$ CR	m_j SR	m_j CR	m_{jj} SR	m_{jj} CR
0 b-tag	$m_{\ell\ell jj}$	MV1c	-	$m_{\ell\ell j}$	$m_{\ell\ell j}$	$m_{\ell\ell jj}$	$m_{\ell\ell jj}$
1 b-tag			-				
2 b-tag	$m_{\ell\ell jj}$	MV1c	$m_{\ell\ell jj}$				

Table 5.11: Summary of the regions entering the likelihood fit and the distribution used in each. Vertically merged rows should be interpreted as regions treated with one distribution, *e.g.* there is no b-tag separation in merged/VBF categories and 0/1 b-tag regions are combined in ggF category. Rows with "-" mean that this region is not included in the fit. "SR" stands for the signal regions and "CR" for the control regions.

- for top quark background: the $m_{\ell\ell jj}$ distribution in the 2 b-tag $e\mu$ control region for the ggF category.

In total this amounts to 4 signal regions and 6 control regions, which are summarized in Table 5.11.

5.8.3 Nuisance parameters: normalization and systematic uncertanties

As stated above, systematic uncertainties in the analysis are modelled with nuisance parameters. Two different types of nuisance parameters are used: floating parameters and parameters with a prior.

A floating normalization is generally associated with the cross-section and acceptance, where absolute ignorance of the rate is assumed and completely determined from data. The fit contains nine freely-floating normalization parameters that are constrained by the signal and control regions described above:

- for signal: signal strengths for ggF ($\mu_{gg\text{F}}$) and VBF ($\mu_{V\text{BF}}$) production. When setting a limit on ggF production, $\mu_{gg\text{F}}$ is the parameter of interest and $\mu_{V\text{BF}}$ is profiled; the converse is true for the limit in the VBF channel;

- for Z+jets background in the ggF category: Z+light-jets (`ZlNorm`), Z + c/light-jets (`ZclNorm`), Z+b/light-jets (`ZblNorm`) and Z+heavy-flavour (`ZhfNorm`). The latter applies to $Z + bb/cc/bc$ with the relative ratios of $Z + cc/Z + bb$ and $Z + bc/Z + bb$ constrained by priors as defined in Section 5.5.2.1;

- for Z+jets background in the merged category: overall Z boson production normalization (`ZMergedNorm`). Since the merged category selects a very different phase space, the normalization is separate from the ggF case;

- for Z+jets background in the VBF category: overall Z boson production normalization (`ZVBFNorm`). This is separate from the ggF/merged categories since the VBF category uses ALPGEN rather than SHERPA to model the Z+jets process;

- for top quark background: overall top quark production normalization (`TopNorm`). This is correlated across all categories since the top quark background is small in the merged and VBF categories, as they are inclusive in b-tag multiplicity.

A nuisance parameter with a prior corresponds to a systematic uncertainty, where there is a prior constraint on the value of the parameter. The fit contains 72 nuisance parameters from experimental-related uncertainties (see Section 5.5.1) and 21 nuisance parameters from modelling uncertainties (see Section 5.5.2), in addition to 7 floating normalization parameters.

5.8.4 Nuisance parameters: statistical uncertainties

In addition to the systematic uncertainties described above, one must take into account that the background MC samples do not have infinite systematics. In this case the histograms are not good descriptions of the underlying distribution, but are estimates of that distribution with some statistical uncertainty. In particular, the $Z + l$ SHERPA samples for $p_{\mathrm{T}}^{Z} < 70$ GeV are known to have lower statistics than the data, which particularly affects the low-m_H limit results.
These statistical uncertainties are taken into account in the profile likelihood using a light weight version of the "Barlow-Beeston" method. This essentially adds an extra nuisance parameter representing the statistical uncertainty on the total MC background in each bin, which is completely uncorrelated across bins. These nuisance parameters are not added to all bins but only those bins where the relative statistical uncertainty in the bin is above a certain threshold. By comparing the limit results for various thresholds (see Table 5.12), a threshold of 1% is chosen.

5.8.5 Pruning of the systematic uncertainties

Several of uncertainties described in Section 5.5 have a negligible effect on the distributions entering the fit. In addition, limited statistics in the MC nominal distributions can produce systematic templates with large fluctuations, introducing noise in the fit. Therefore, uncertainties are removed according to the following "pruning" procedure which is carried out for each category/subchannel in each region:

- reduce statistical fluctuations by the smoothing procedure described in Section 5.5.1.7 only for those systematic which require a re-sampling of the events, *e.g.* JES and not b-tagging;

m_H [GeV]	No stat.	Stat. 5%	Stat. 1%	Stat. 0%
200	245.79	253.93	272.81	272.83
300	59.33	59.43	62.78	62.78
400	22.31	22.44	23.03	23.03
500	12.07	12.17	12.35	12.35
600	8.11	8.25	8.26	8.26
700	5.62	5.65	5.65	5.65
800	4.29	4.29	4.30	4.30
900	4.08	4.09	4.09	4.09
1000	4.05	4.07	4.07	4.07

Table 5.12: The limit on $\sigma_{gg\mathrm{F}} \times \mathrm{BR}$ with no statistical error and including the statistical error on bins with a relative error above 5%, 1% and 0% (*i.e.* all bins) respectively. It can be seen that the limit decreases as more statistical errors are included (as expected) but becomes constant once reaching a threshold of 1%. Note that these tests are not necessarily done with the very final limit results.

- neglect the normalization uncertainty for a given sample in a region if either of the following is true:
  - the variation is less than 0.5%;
  - both up and down variations have the same sign;
- neglect the shape uncertainty for a given sample in a given region if either of the following is true:
  - not one single bin has a deviation over 0.5% after overall normalization is removed;
  - if only up or down variation is non-zero and passed the previous pruning steps;

- neglect the shape and normalization uncertainty for a given sample in a given region if the sample is less than 2% of the total background:
  - if the signal $< 2\%$ of the total background in all bins and the shape and normalization error are each $< 0.5\%$ of the total background;
  - if at least one bin has a signal contribution $> 2\%$ of the total background, only in those bins where that shape and normalization error are each $< 2\%$ of the signal yield.

In the ggF control region, where the MV1c distribution (which can not be smoothed as mentioned in Section 5.5.1.7) is fitted, the only pruning performed is to remove one-sided systematics in a given MV1c bin.

5.8.6 Understanding the fit configuration

Various tests have been performed on the limit fitting procedure.

5.8.6.1 Nuisance parameter pulls and constraints

The nuisance parameter pulls and constraints for the Asimov and data fit has been studied. In general the NP are well behaved. There are some pulls on the b-tagging nuisance parameters, particularly c-tagging, and the jet nuisance parameters. This is expected since the MV1c distribution is fitted in the SBs and have large statistics and hence have power to constrain these NP.

Regarding the background normalization scale factors, the results are close to 1 with the exception of the Zbb SF of 1.18 ± 0.06. This is consistent both with the value measured in the SM $ZH, H \to bb$ analysis and with the 7 TeV ATLAS SM σ_{Z+bb} measurement (1.23 ± 0.18) [124]. In the ggF fit, where the unknown potential VBF is profiled, the fit does not have much power to constrain the VBF

normalization; however, this is improved when doing a combined fit to all high-mass $H \to ZZ$ channels. The NP has been studied in all categories (resolved ggF, merged ggF and VBF) and they are in good agreement.

5.8.7 Nuisance parameter ranking

After the MLL value is found, each NP is pulled $\pm\sigma$ and the likelihood is maximized again. The change in the best fit μ value gives the inclusive sensitivity of the measured value to the given NP. The impact is judged using fits to data. Figures 5.44 and 5.45 show the nuisance parameter ranking in the ggF and VBF categories at various m_H values for the top 15 ranked nuisance parameters in the ggF and VBF channels, respectively. The rankings come from the fit to data with the best-fit μ value. The plots show both pre-fit and post-fit impacts, together with displaying the pulls on the data. It can be seen that the `JetEtaModelling` and `JVF` systematics are asymmetric. This comes from the fact that the inputs uncertainty is asymmetric.
Figure 5.44(d) shows the NP ranking in the ggF channel when both the merged and the resolved categories are considered.

5.8.8 Post-fit plots

Figures 5.46 and 5.47 show the post-fit plots of the discriminant entering the fit in the various signal and control regions for the ggF and VBF channels, respectively. Figures 5.48 - 5.51 show post-fit plots of other variables cut on in the ggF channel, while Figures 5.53 - 5.55 show similar plots in the VBF channel. Since no signal is observed, all post-fit plots are extracted via a background-only fit. The signal is currently shown for a SM-like Higgs at $m_H = 400$ GeV.

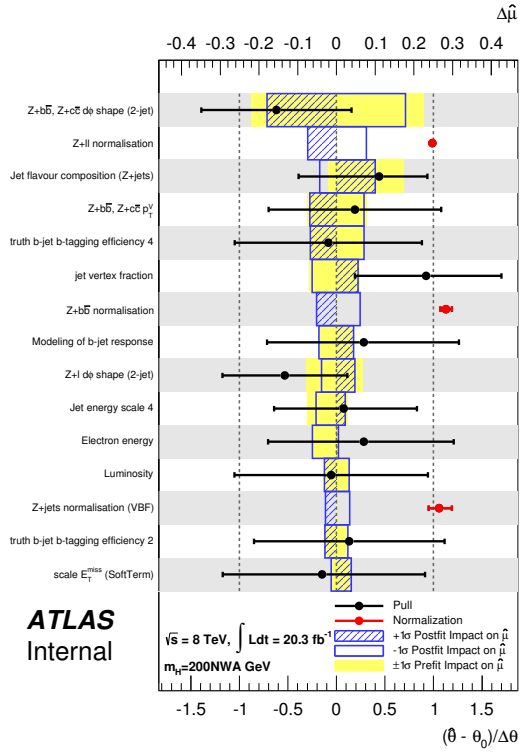

(a) $m_H = 200$ GeV, resolved category

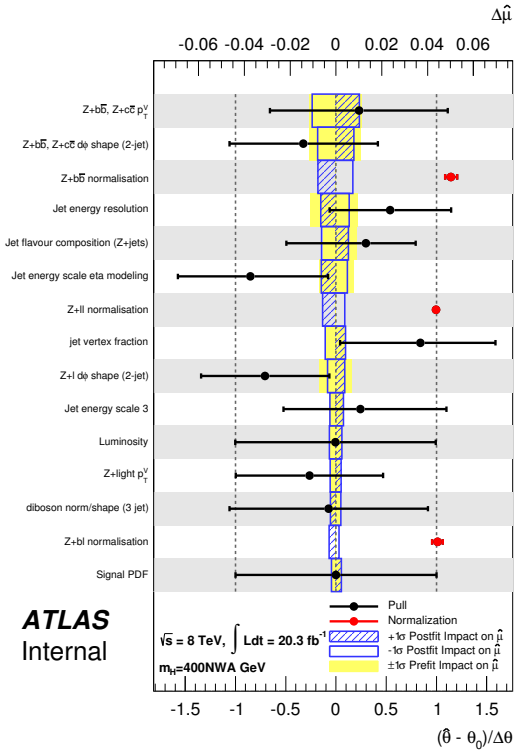

(b) $m_H = 400$ GeV, resolved category

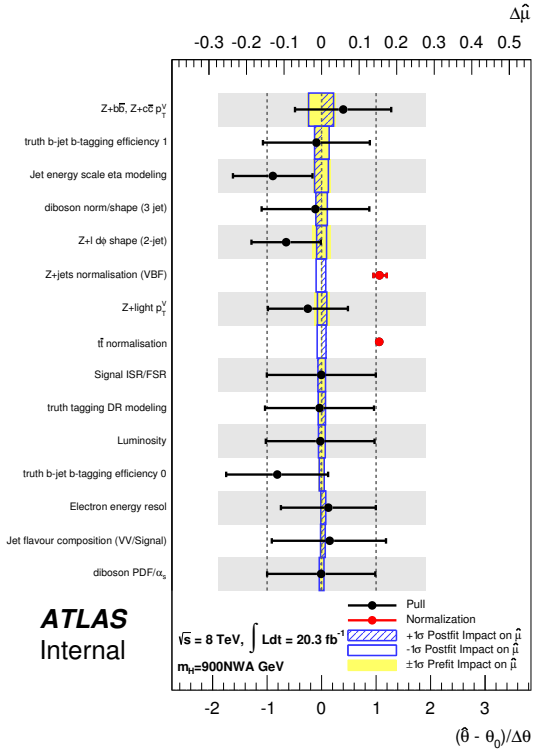

(c) $m_H = 900$ GeV, resolved category

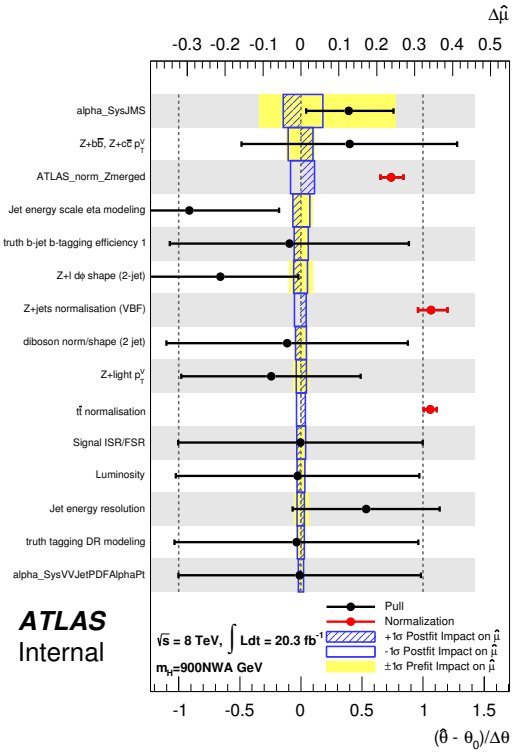

(d) $m_H = 900$ GeV, both resolved and merged category

Figure 5.44: Ranking of the top 15 nuisance parameters in the ggF fit for different Higgs boson mass values considering the resolved-only (a,b,c) and both resolved and merged (d) category.

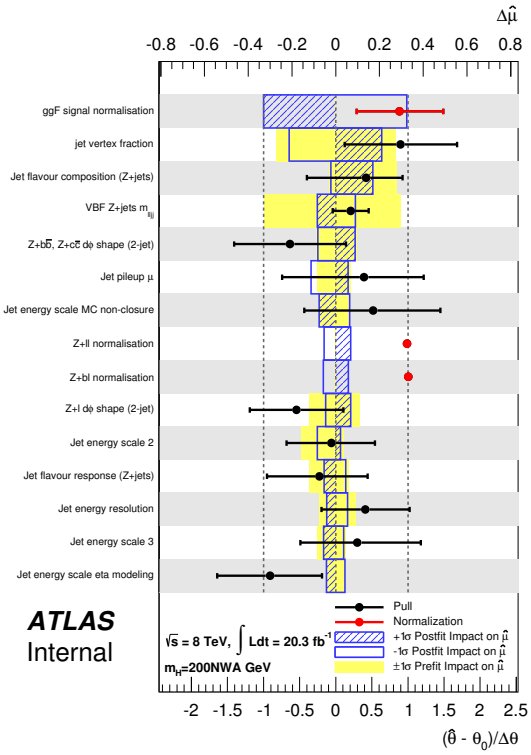

(a) $m_H = 200$ GeV

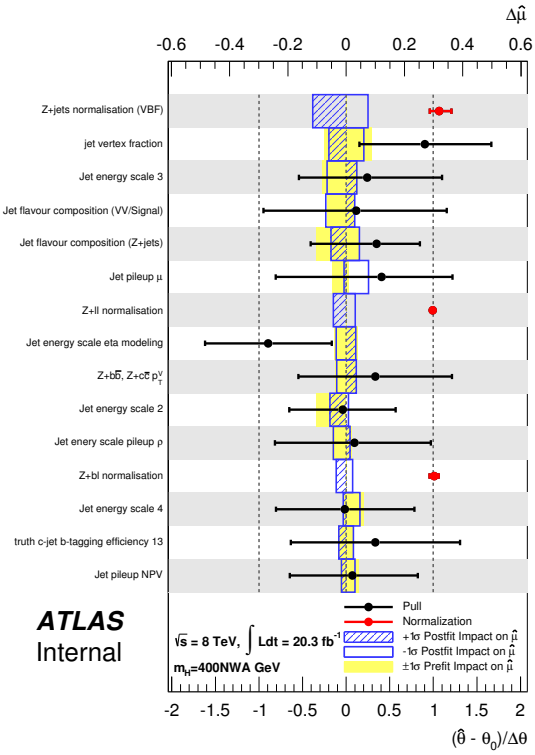

(b) $m_H = 400$ GeV

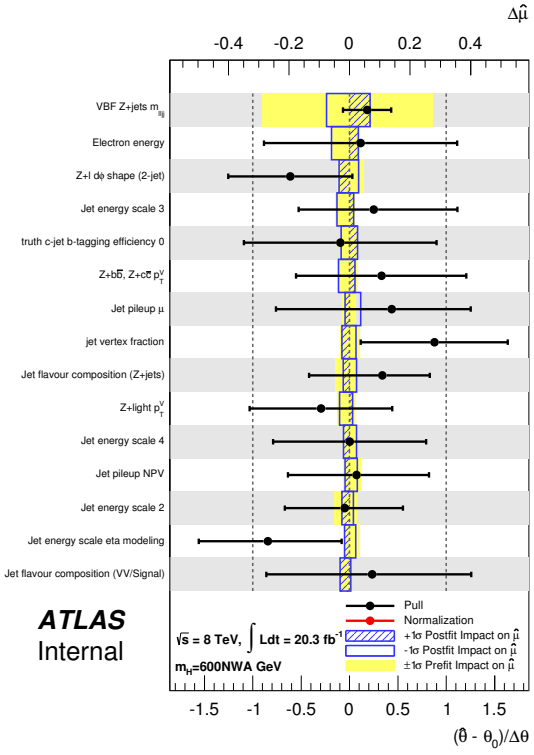

(c) $m_H = 600$ GeV

Figure 5.45: Ranking of the top 15 nuisance parameters in the VBF fit for different Higgs boson mass values.

Figure 5.52 shows the post-fit plots of the three-bodies mass $m_{\ell\ell j}$ in the m_j sidebands and in the signal region when considering the merged and the resolved categories together.

5.9 Exclusion limits

5.9.1 Exclusion limits on narrow-width Higgs

Figures 5.56 and 5.57 present the final exclusion limits on $\sigma \times$ BR at 95% CL for the ggF and VBF channel, respectively, in the NWA. The corresponding limits are also given in Tables 5.13 and 5.14. Table 5.15 shows the expected limit for the ggF channel when both the resolved and the merged categories are considered. It can be seen that the expected limit is improved with respect to the case in which only the resolved channel is considered. The corresponding expected limit is shown in Figure 5.58

5.9.2 Exclusion limits on *2HDM*

For the *2HDM* limits it is necessary to take into account that the natural width of the heavy Higgs boson H and the ratio of ggF to VBF production cross section vary across the parameter space. The small bbH production mechanism is neglected. The non-zero width is taken into account by smearing each signal histogram to include a natural width up to 5% of m_H. The smearing was performed by looping over each bin of the input histogram and redistributing the events according to a relativistic BW, centered on the bin center with width $m_H \times s$, where s is the smearing factor and m_H the generated H mass. For such widths the interference

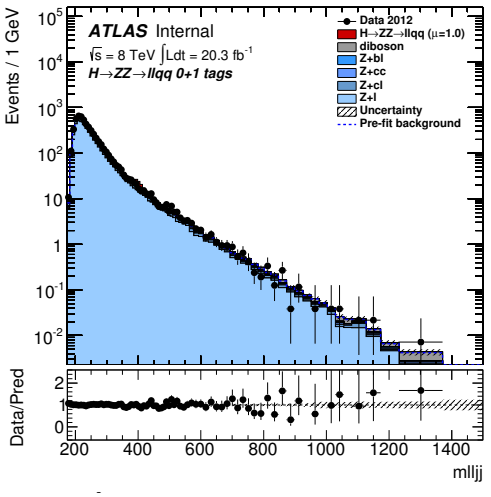

(a)

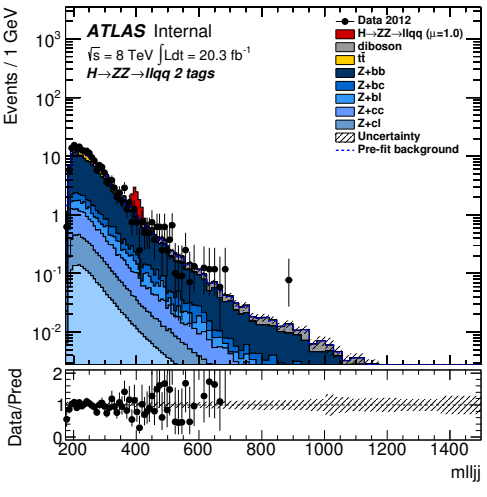

(b)

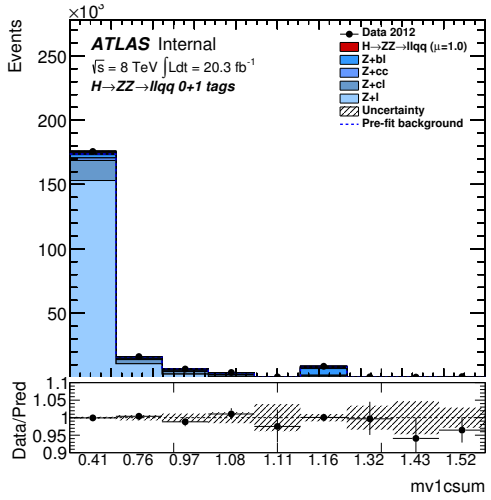

(c)

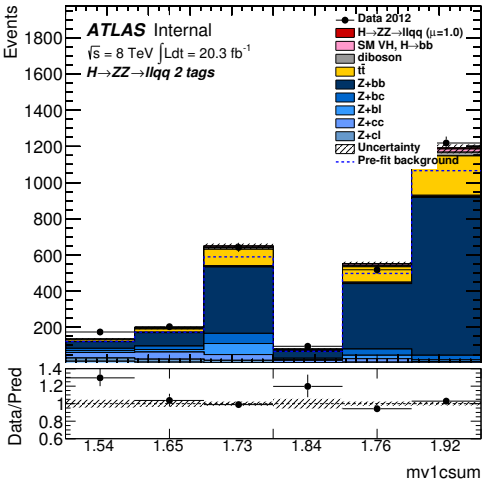

(d)

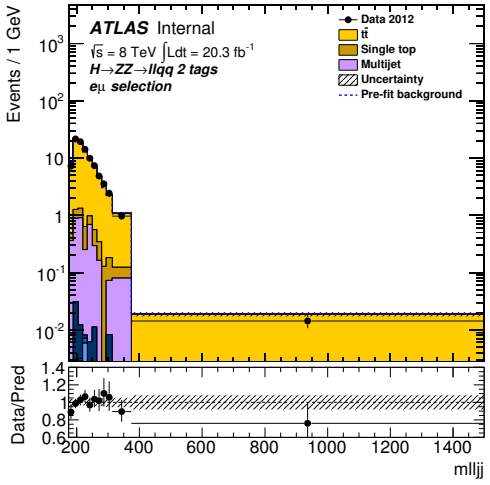

(e)

Figure 5.46: Post-fit plots of discriminant entering the *gg*F limits in the SRs (top), Z CRs (middle) and top CR (bottom), showing a 400 GeV NWA signal with $\mu = 1$. The binning is the same as that used in the fit.

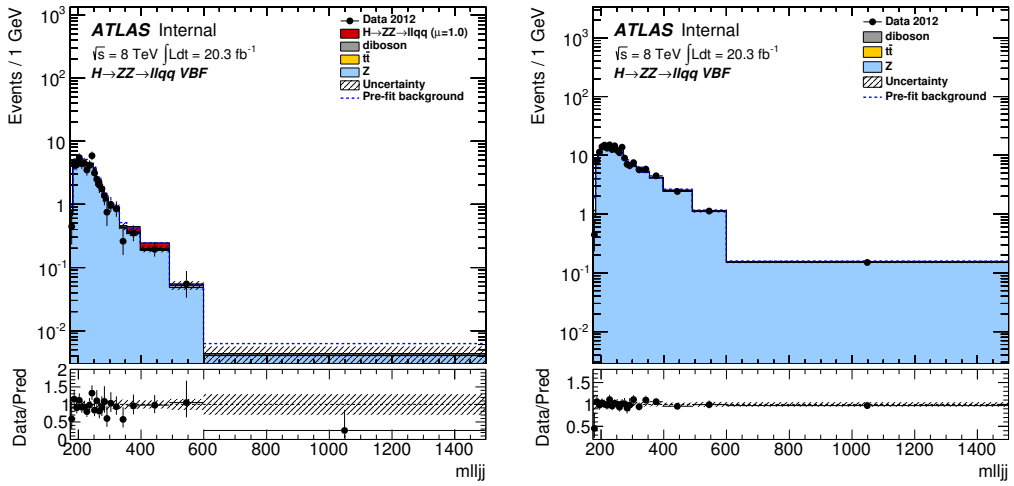

(a) (b)

Figure 5.47: Post-fit plots of discriminant entering the VBF limits in the SR (left) and Z CR (right), showing a 400 GeV NWA signal with $\mu = 1$. The binning is the same as that used in the fit.

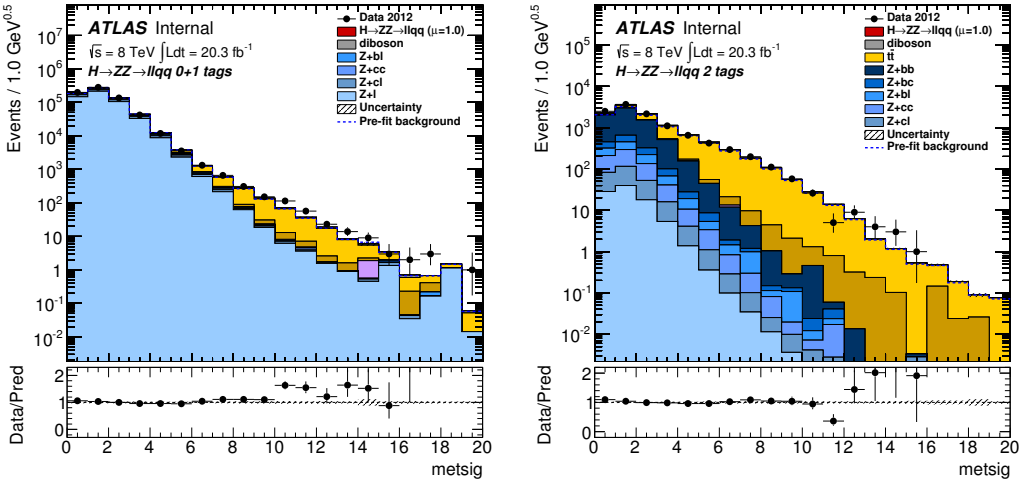

(a) untagged (b) tagged

Figure 5.48: Post-fit plots of $\frac{E_{\mathrm{T}}^{\mathrm{miss}}}{\sqrt{H_{\mathrm{T}}}}$ in the ggF untagged (left) and tagged (right) channels.

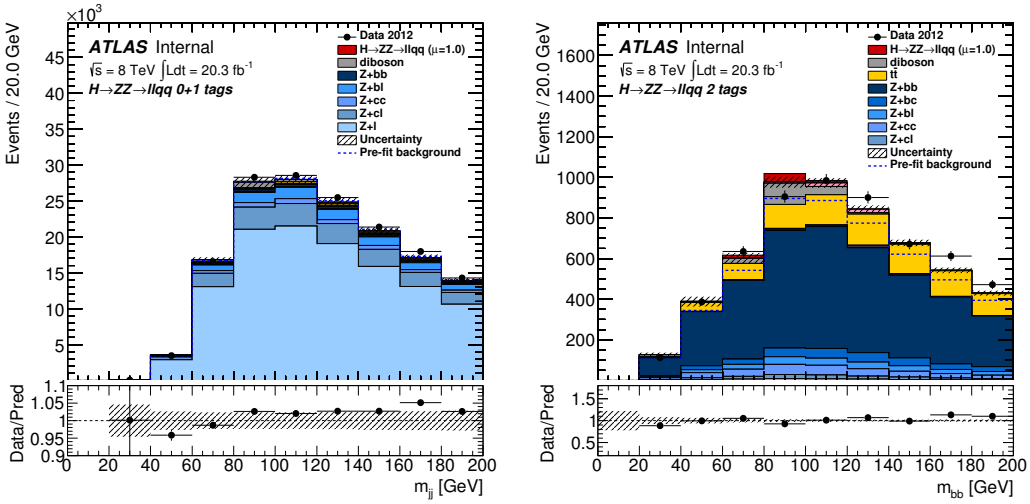

(a) untagged (b) tagged

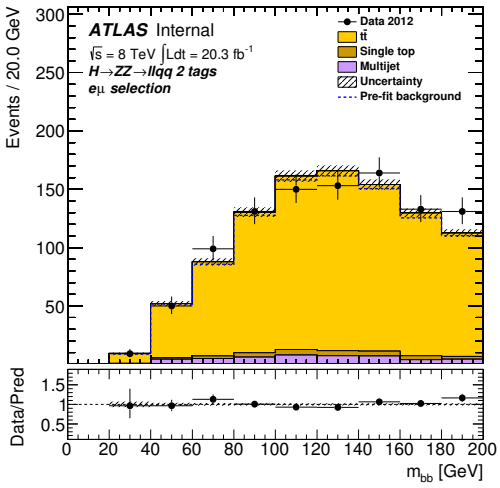

(c) TopCR

Figure 5.49: Post-fit plots of m_{jj} in the ggF untagged (a) and tagged (b) channels, along with the top $e\mu$ CR.

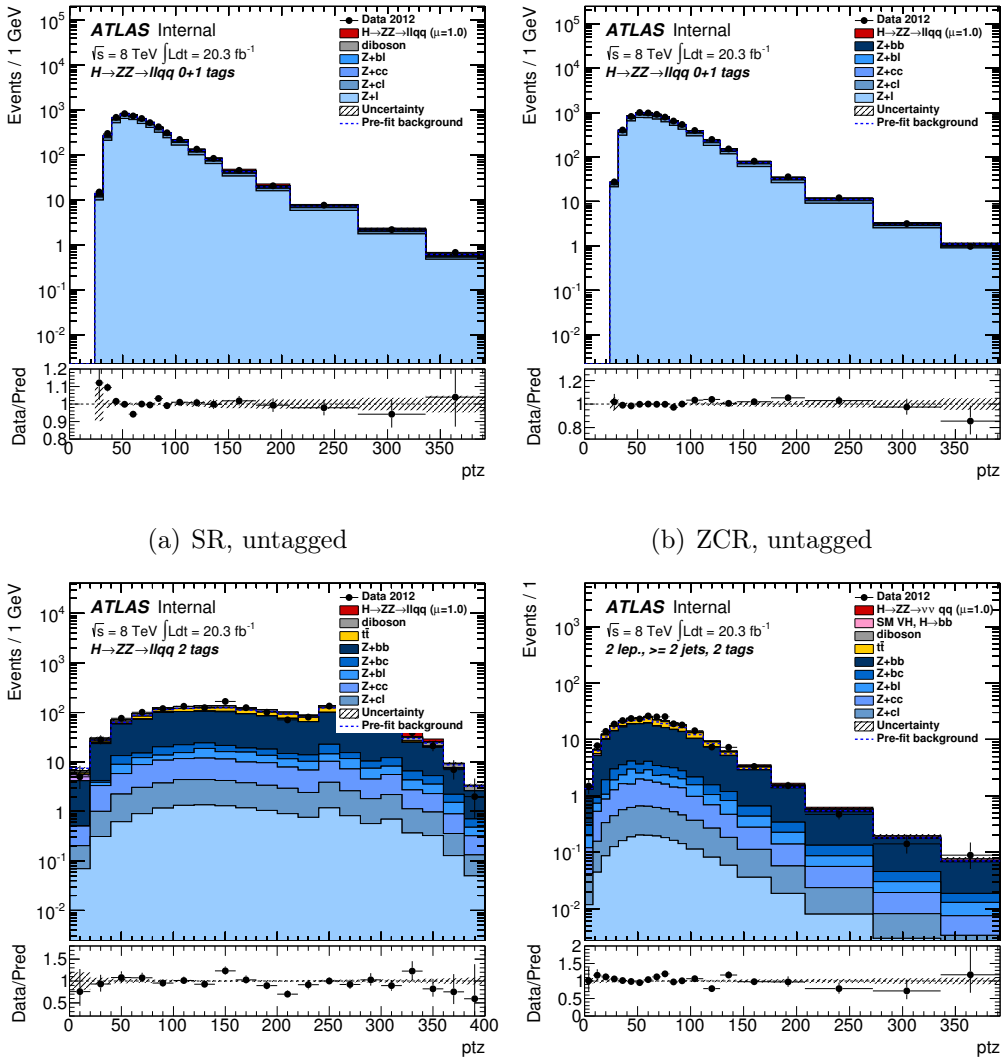

(a) SR, untagged

(b) ZCR, untagged

(c) SR, tagged

(d) ZCR, tagged

Figure 5.50: Post-fit plots of $p_{\mathrm{T}}^{\ell\ell}$ in the SR (left) and Z CR (right) in the untagged (top) and tagged (bottom) channel.

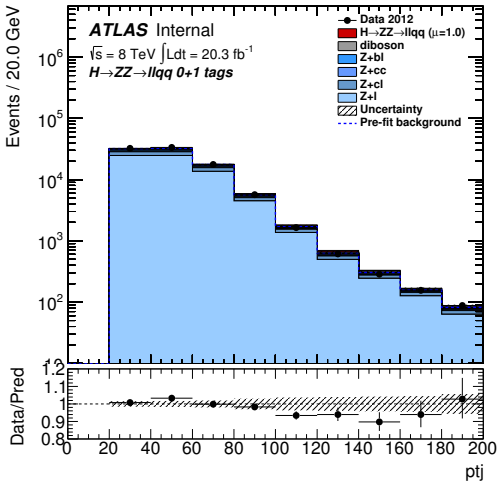

(a) SR

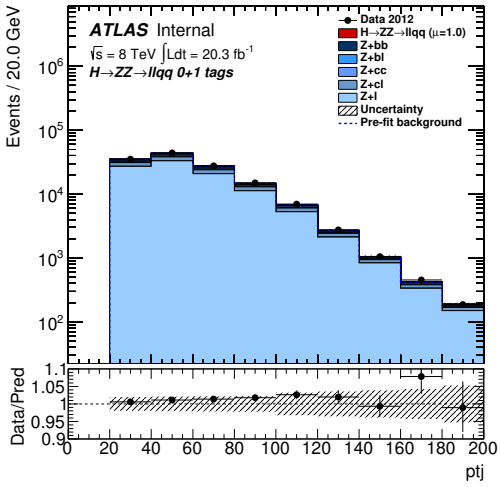

(b) ZCR

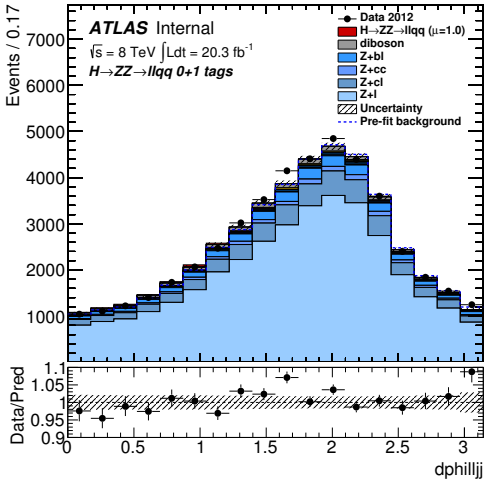

(c) SR

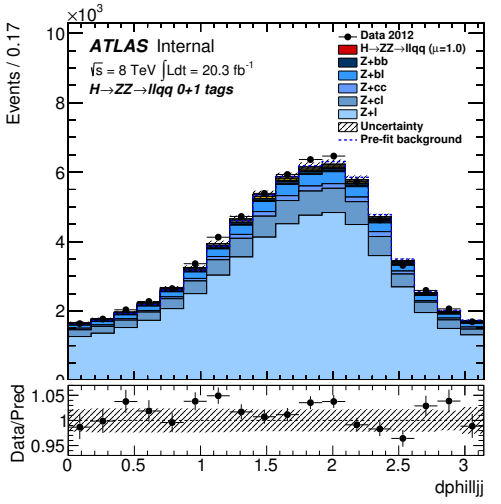

(d) ZCR

Figure 5.51: Post-fit plots of p_{T}^{j} (top) and $\Delta\phi_{\ell\ell}$ (bottom) in the SR (left) and Z CR (right) for the ggF channel.

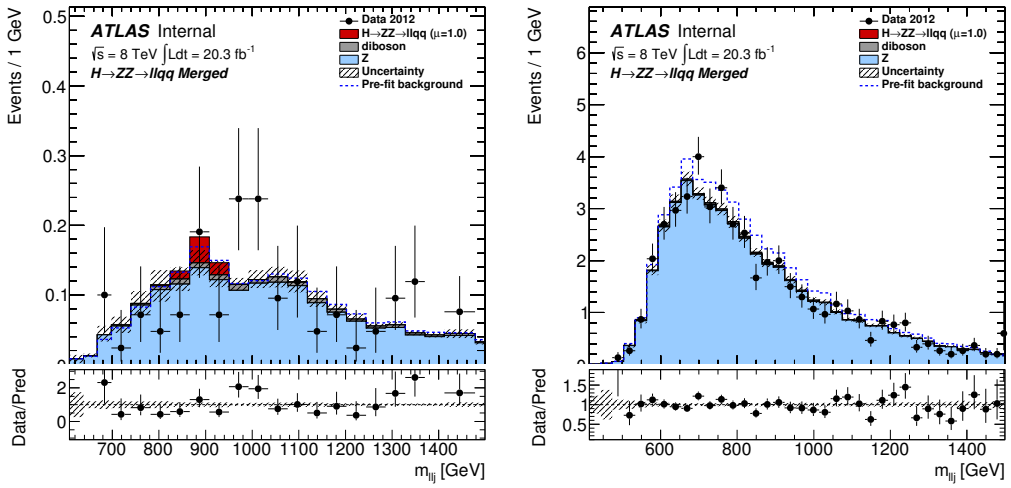

(a) (b)

Figure 5.52: Post-fit plots of discriminant entering the ggF limits obtained considering both the resolved and the merged category in the SR (left) and ZCR (right) with a 900 GeV NWA signal with $\mu = 1$. The binning is the same as that used in the fit.

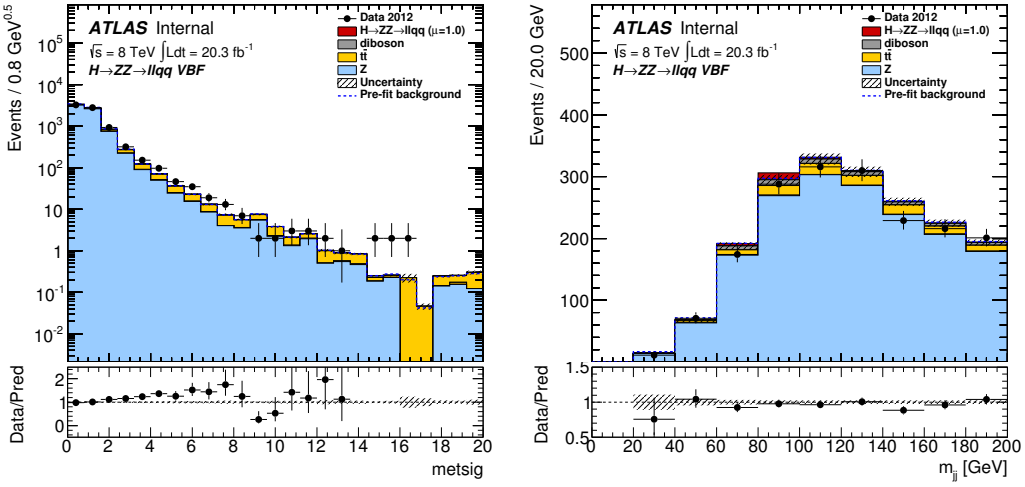

(a) (b)

Figure 5.53: Post-fit plots of $\frac{E_{\mathrm{T}}^{\mathrm{miss}}}{\sqrt{H_{\mathrm{T}}}}$ (a) and m_{jj} (b) in the VBF channel.

m_H [GeV]	Obs. [fb]	-2σ [fb]	-1σ [fb]	Exp. [fb]	$+1\sigma$ [fb]	$+2\sigma$ [fb]
200	3329.10	1133.12	1521.21	2111.16	2938.13	3938.77
220	1291.63	775.59	1041.23	1445.04	2011.08	2695.99
240	1200.54	667.78	896.50	1244.18	1731.54	2321.25
260	1371.30	455.57	611.61	848.80	1181.29	1583.60
280	797.99	327.07	439.09	609.38	848.08	1136.91
300	514.11	256.12	343.85	477.20	664.12	890.30
320	335.58	206.01	276.57	383.83	534.19	716.11
340	226.87	159.11	213.61	296.45	412.57	553.07
360	172.57	136.99	183.91	255.23	355.21	476.18
380	146.81	111.49	149.68	207.73	289.09	387.55
400	99.18	91.30	122.56	170.10	236.73	317.35
420	79.95	77.81	104.46	144.97	201.75	270.46
440	138.69	70.16	94.19	130.72	181.93	243.89
460	108.31	59.49	79.87	110.85	154.27	206.80
480	117.91	58.11	78.01	108.26	150.67	201.98
500	155.38	54.27	72.86	101.11	140.72	188.64
520	135.38	48.70	65.37	90.73	126.27	169.27
540	66.65	40.77	54.73	75.95	105.71	141.71
560	65.72	38.07	51.11	70.93	98.72	132.34
580	60.79	34.71	46.60	64.67	90.01	120.66
600	52.38	33.13	44.48	61.73	85.91	115.17
650	57.97	26.56	35.66	49.49	68.88	92.34
700	44.92	22.67	30.44	42.24	58.78	78.80
750	21.54	19.36	25.99	36.07	50.19	67.29
800	17.81	17.33	23.26	32.29	44.93	60.24
850	25.46	16.56	22.19	30.79	42.85	57.45
900	30.38	16.28	21.86	30.33	42.22	56.60
950	19.69	18.19	24.42	33.89	47.17	63.23
1000	19.87	19.59	26.30	36.50	50.80	68.11

Table 5.13: Observed and expected limits, along with $\pm 1\sigma$ and $\pm 2\sigma$ variations, at 95% CL for the ggF channel considering the resolved category alone.

m_H [GeV]	Obs. [fb]	-2σ [fb]	-1σ [fb]	Exp. [fb]	$+1\sigma$ [fb]	$+2\sigma$ [fb]
200	446.04	260.30	349.46	484.99	674.96	904.83
220	264.24	212.99	285.24	396.83	552.28	740.30
240	521.00	198.18	266.05	369.23	513.87	688.88
260	241.07	159.51	214.15	297.20	413.61	554.48
280	169.05	125.52	168.51	233.85	325.46	436.30
300	150.91	103.26	138.62	192.38	267.74	358.93
320	124.51	85.12	114.27	158.59	220.71	295.88
340	63.36	58.61	78.68	109.20	151.97	203.73
360	76.14	59.47	79.85	110.81	154.22	206.74
380	80.06	50.26	67.48	93.65	130.33	174.72
400	81.98	60.73	81.53	113.15	157.48	211.11
420	62.78	45.04	60.47	83.93	116.80	156.58
440	80.24	44.99	60.40	83.82	116.65	156.38
460	71.66	39.15	52.55	72.94	101.51	136.08
480	81.27	44.69	60.00	83.27	115.89	155.35
500	62.59	34.23	45.95	63.77	88.76	118.98
520	46.49	25.55	34.31	47.61	66.26	88.83
540	40.13	21.99	29.52	40.96	57.01	76.42
560	38.27	20.91	28.07	38.96	54.22	72.69
580	37.25	22.04	29.60	41.07	57.16	76.63
600	30.25	23.73	31.85	44.21	61.52	82.47
650	21.14	19.65	26.38	36.61	50.95	60.30
700	20.48	17.65	23.69	32.88	45.75	61.34
750	13.90	15.37	20.63	28.63	39.85	53.42
800	12.63	14.60	19.60	27.21	37.86	50.76
850	16.60	15.02	20.16	27.98	38.94	52.20
900	20.33	17.51	23.50	32.62	45.40	60.86
950	16.37	18.35	24.64	34.19	47.58	63.79
1000	18.08	21.23	28.50	39.56	55.05	76.80

Table 5.14: Observed and expected limits, along with $\pm 1\sigma$ and $\pm 2\sigma$ variations, at 95% CL for the VBF channel.

m_H [GeV]	Obs. [fb]	-2σ [fb]	-1σ [fb]	Exp. [fb]	$+1\sigma$ [fb]	$+2\sigma$ [fb]
200	3329.10	1133.12	1521.21	2111.16	2938.13	3938.77
220	1291.63	775.59	1041.23	1445.04	2011.08	2695.99
240	1200.54	667.78	896.50	1244.18	1731.54	2321.25
260	1371.30	455.57	611.61	848.80	1181.29	1583.60
280	797.99	327.07	439.09	609.38	848.08	1136.91
300	514.11	256.12	343.85	477.20	664.12	890.30
320	335.58	206.01	276.57	383.83	534.19	716.11
340	226.87	159.11	213.61	296.45	412.57	553.07
360	172.57	136.99	183.91	255.23	355.21	476.18
380	146.81	111.49	149.68	207.73	289.09	387.55
400	99.18	91.30	122.56	170.10	236.73	317.35
420	79.95	77.81	104.46	144.97	201.75	270.46
440	138.69	70.16	94.19	130.72	181.93	243.89
460	108.31	59.49	79.87	110.85	154.27	206.80
480	117.91	58.11	78.01	108.26	150.67	201.98
500	155.38	54.27	72.86	101.11	140.72	188.64
520	135.38	48.70	65.37	90.73	126.27	169.27
540	66.65	40.77	54.73	75.95	105.71	141.71
560	65.72	38.07	51.11	70.93	98.72	132.34
580	60.79	34.71	46.60	64.67	90.01	120.66
600	52.38	33.13	44.48	61.73	85.91	115.17
650	57.97	26.56	35.66	49.49	68.88	92.34
700	46.79	22.65	30.41	42.20	60.60	85.84
750	21.18	19.28	25.88	35.92	51.78	74.01
800	16.27	16.84	22.61	31.38	45.30	64.95
850	21.13	15.42	20.70	28.73	41.59	59.76
900	26.66	14.04	18.85	26.16	37.92	54.67
950	20.09	13.17	17.68	24.53	35.53	51.12
1000	33.68	11.32	15.20	21.09	30.53	43.87

Table 5.15: Observed and expected limits, along with $\pm 1\sigma$ and $\pm 2\sigma$ variations, at 95% CL for the ggF channel when both the resolved and the merged categories are considered.

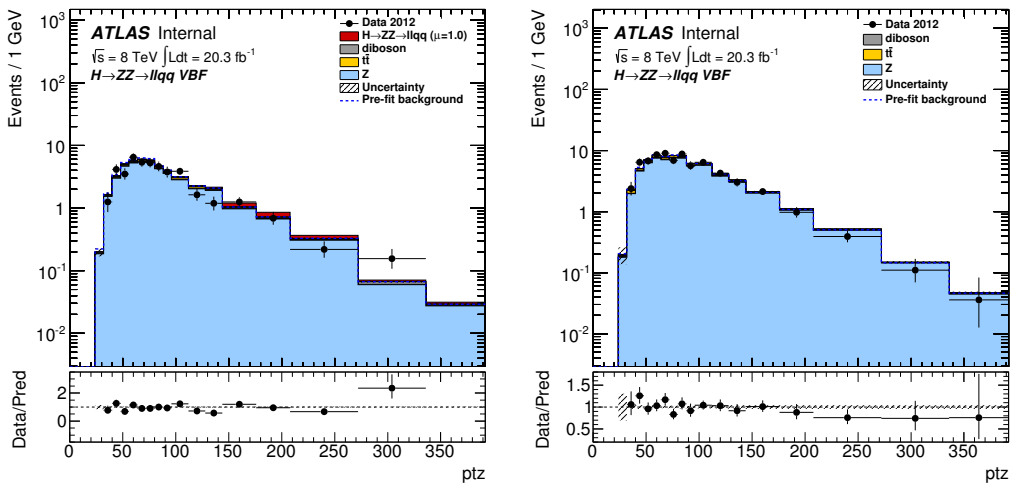

Figure 5.54: Post-fit plots of $p_{\mathrm{T}}^{\ell\ell}$ in the SR (left) and ZCR (right) in the VBF channel.

with the ZZ continuum background is negligible.

In order to avoid performing the limit fit at each point in the *2HDM* parameter space, which is computationally intensive, the following approach is taken. The limits are first extracted as a function of both the width/m_H and the $\frac{\sigma_{VBF}}{\sigma_{ggF}+\sigma_{VBF}}$ production ratio in a 2D scan. The width is varied from 0% to 6% in 1% steps and, for each width, the $\frac{\sigma_{VBF}}{\sigma_{ggF}+\sigma_{VBF}}$ is varied from 0 to 1 in 0.1 steps. Once the limits as a function of the production ratio and the width are extracted they are used to linearly interpolate between points. For each point in the *2HDM* plane the predicted $\frac{\sigma_{VBF}}{\sigma_{ggF}+\sigma_{VBF}}$ and width/m_H are used to look up the limit.

Figures 5.59 and 5.60 present the final exclusion limit on $\tan\beta$ vs $\cos(\beta-\alpha)$ and m_H, respectively, at 95% CL in the type II 2HDM. The results for type I are very similar.

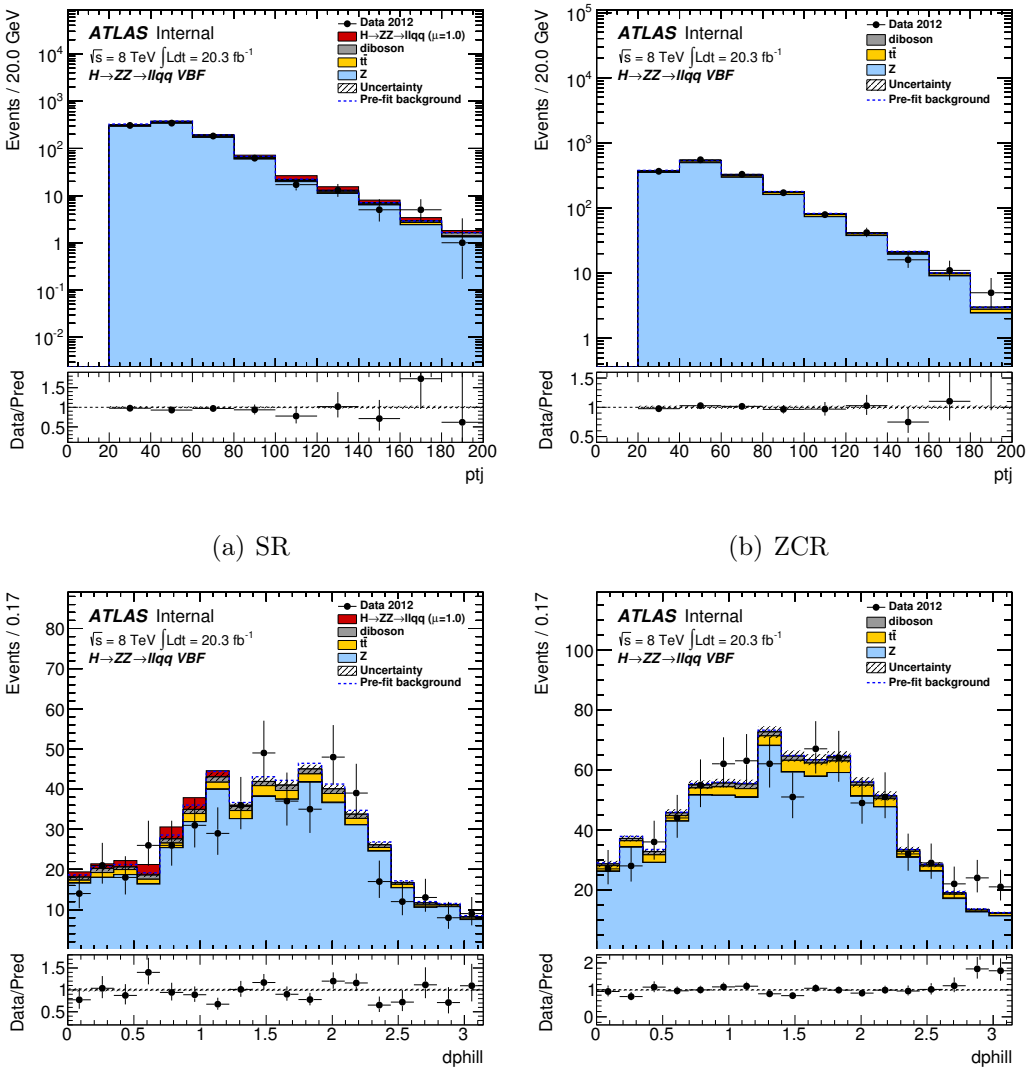

(a) SR (b) ZCR

(c) SR (d) ZCR

Figure 5.55: Post-fit plots of p_{T}^{j} (top) and $\Delta\phi_{\ell\ell}$ (bottom) in the SR (left) and ZCR (right) for the VBF channel.

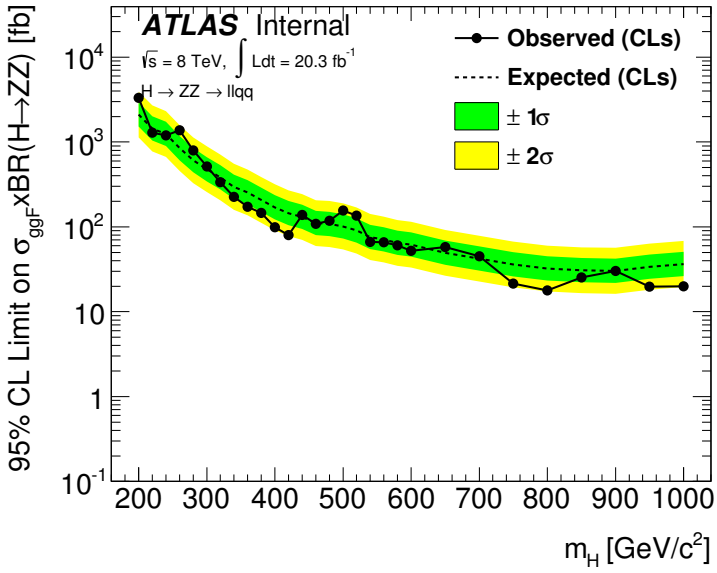

Figure 5.56: Exclusion limit on $\sigma \times$ BR at 95% CL for a narrow resonance in the ggF channel. The SM σ is shown for comparison.

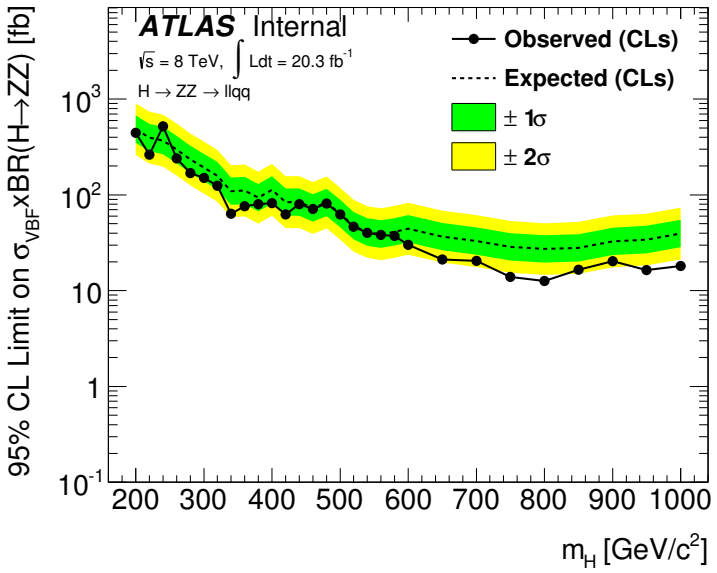

Figure 5.57: Exclusion limit on $\sigma \times$ BR at 95% CL for a narrow resonance in the VBF channel. The SM σ is shown for comparison.

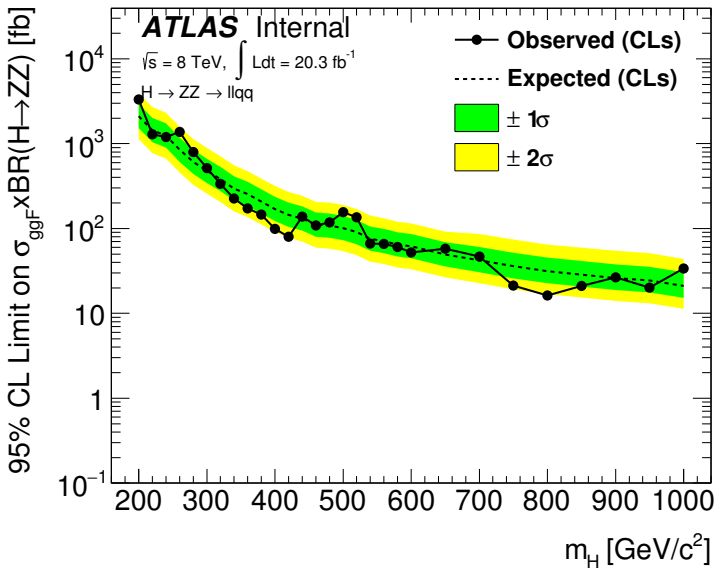

Figure 5.58: Exclusion limit on $\sigma \times$ BR at 95% CL for a narrow resonance in the ggF channel obtained considering both the merged and the resolved categories. The SM σ is shown for comparison.

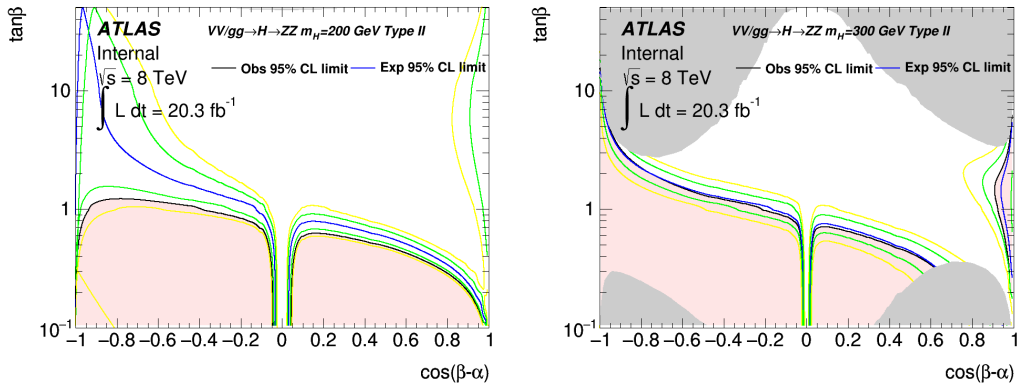

(a) (b)

Figure 5.59: Exclusion limit on $\tan\beta$ vs $\cos(\beta-\alpha)$ at 95% CL in the Type II *2HDM* for ggF production at Higgs mass of (left) 200 and (right) 300 GeV. The green and yellow line represent, respectively, the $\pm 1\sigma$ and $\pm 2\sigma$ variations of the expected limit. The grey band represents the region where the limits are not valid since $\frac{\Gamma_H}{m_H} > 5\%$. Type I results are almost identical.

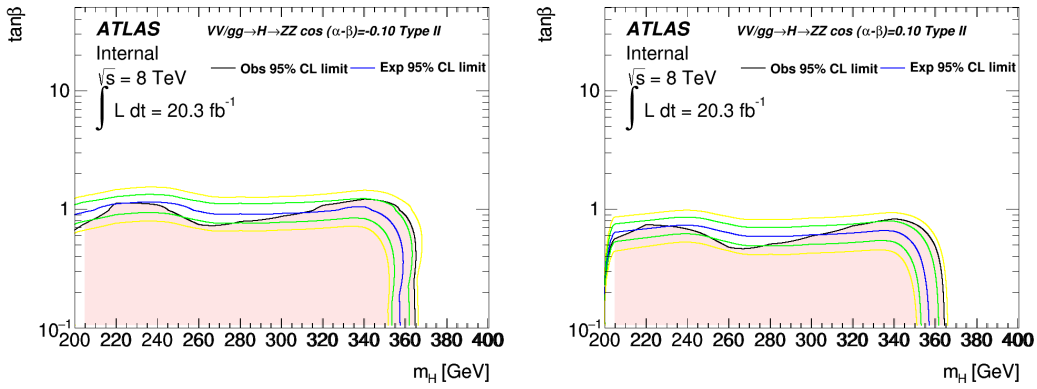

(a) (b)

Figure 5.60: Exclusion limits on $\tan\beta$ vs m_H at 95% CL in the Type II *2HDM* for ggF production at $\cos(\beta - \alpha) = \pm 0.1$. Type I are very similar. The green and yellow lines represent, respectively, the $\pm 1\sigma$ and $\pm 2\sigma$ variations of the expected limit.

5.10 Combination of $H \to ZZ$ searches

The results presented in this chapter has been combined into the search for a heavy Higgs boson decaying into two Z bosons [125], encompassing the present $\ell\ell qq$ decay channel $H \to ZZ \to \ell^{\pm}\ell^{\mp}q\bar{q}$, the 4ℓ channel $H \to ZZ \to \ell^{\pm}\ell^{\mp}\ell^{\pm}\ell^{\mp}$, the $\ell\ell\nu\nu$ channel $H \to ZZ \to \ell^{\pm}\ell^{\mp}\nu\bar{\nu}$ and the $\nu\nu qq$ channel $H \to ZZ \to \nu\bar{\nu}q\bar{q}$.

Since the 4ℓ decay mode has an excellent mass resolution and high signal-to-background ratio, this channel is well-suited for a search for a narrow resonance in the range $140 < m_H < 500$ GeV; thus, the $H \to ZZ$ search covers the m_H range down to 140 GeV. Furthermore, the 4ℓ search includes channels sensitive to VH production as well as to the VBF and ggF production modes. The $\ell\ell\nu\nu$ search, instead, considers ggF and VBF channels only (as the $\ell\ell qq$ search) and covers the m_H range down to 240 GeV. Finally, the $\nu\nu qq$ search covers the m_H range down to 400 GeV and does not distinguish between ggF and VBF production. For all four searches considered in the combination the m_H range extends up to 1 TeV. Due to their higher branching ratios, the $\ell\ell qq$, $\ell\ell\nu\nu$ and $\nu\nu qq$ decay modes dominate

at higher masses and contribute to the overall sensitivity of the combined results. The ggF production mode for 4ℓ search is further divided into four channels based on lepton flavour, while the $\ell\ell\nu\nu$ search includes four channels, corresponding to two lepton flavours for each of the ggF and VBF production modes. For the $\nu\nu qq$ search, as for the $\ell\ell qq$ channel, the ggF production mode is divided into two sub-channels each based on the number of b-tagged jets in the event.

For each channel, a discriminating variable sensitive to m_H is identified and used in a likelihood fit. As for the $\ell\ell qq$ decay, the 4ℓ search use the invariant mass of the four-fermion system as the final discriminant, while the $\ell\ell\nu\nu$ and $\nu\nu qq$ searches use a transverse mass distribution. Distributions of these discriminants for each channel are combined in a simultaneous likelihood fit which estimates the rate of heavy Higgs boson production and simultaneously the nuisance parameters corresponding to systematic uncertainties. As already described for the $\ell\ell qq$ search, additional distributions from background-dominated control regions also enter the fit in order to constrain nuisance parameters. All results are finally interpreted in the scenario of a new Higgs boson with a narrow width, as well as in Type I and Type II *2HDM*s.

Limits on the cross section times branching ratio from the combination of all of the searches are shown in Figure 5.61. Also shown are expected limits from the $\ell\ell\ell\ell$, $\ell\ell\nu\nu$ and the combined $\ell\ell qq + \nu\nu qq$ searches (the latter two searches are only shown in combination as they share control regions). At low mass the $\ell\ell\ell\ell$ search has the best sensitivity while at high mass the sensitivity of the combined $\ell\ell qq + \nu\nu qq$ search is greatest, with the sensitivity of the $\ell\ell\nu\nu$ channel only slightly inferior. In the mass range considered for this search the 95% confidence level (CL) upper limits on the cross section times branching ratio for heavy Higgs boson production vary between 0.53 (0.31) pb at $m_H = 195$ GeV and 0.008 (0.009) pb at $m_H = 950$ GeV in the ggF (VBF) channel. The excursions into the 2σ band around the

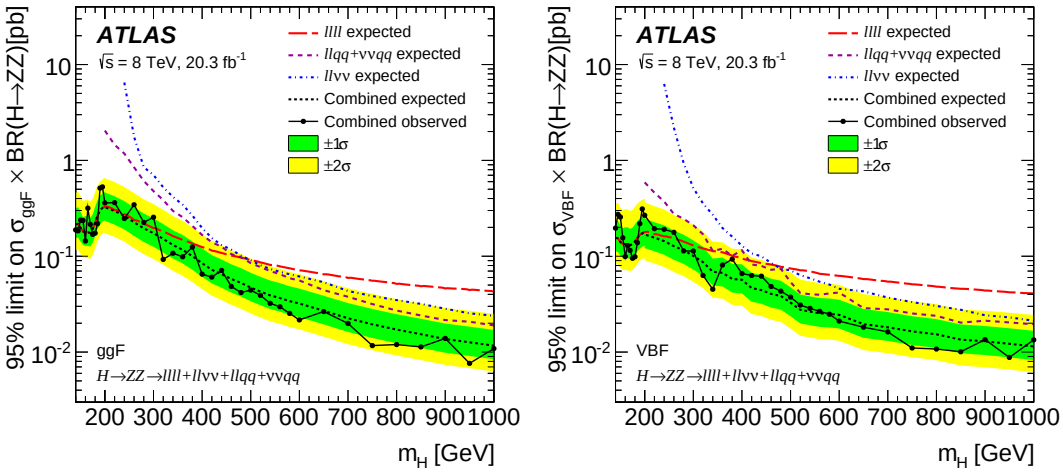

(a) ggF production (b) VBF production

Figure 5.61: 95% CL upper limits on $\sigma \times \mathrm{BR}(H \to ZZ)$ as function of m_H, resulting from the combination of all of the searches in the (a) ggF and (b) VBF channels. The solid black line and points indicate the observed limit. The dashed black line indicates the expected limit and the bands the 1σ and 2σ uncertainty ranges about the expected limit. The dashed colored lines indicate the expected limits obtained from the individual searches; for the $\ell\ell qq$ and $\nu\nu qq$ searches, only the combination of the two is shown since they share control regions.

expected limit originate from local deviations in the input distributions, *e.g.* the excess occurring around 200 GeV and the deficit occurring around 300 GeV arise from $\ell\ell\ell\ell$ search whereas deficits at higher mass are driven by fluctuations in the $\ell\ell qq$ search.

Figure 5.62 shows exclusion limits in the $\tan\beta$ versus $\cos(\beta-\alpha)$ plane for Type I and Type II *2HDM*s, for a heavy Higgs boson with mass $m_H = 200$ GeV. This m_H values is chosen so the assumption of a narrow width Higgs boson is valid over most of the parameter space, and the experimental sensitivity is at a maximum. The range of $\cos(\beta-\alpha)$ and $\tan\beta$ explored is limited to the region where the assumption of a heavy narrow-width Higgs boson with negligible interference is valid. When calculating the limits at a given choice of $\cos(\beta-\alpha)$ and $\tan\beta$,

the relative rate of ggF and VBF production in the fit is set according to the prediction of the *2HDM* for the parameter choice. Figure 5.63 shows exclusion limits as a function of the heavy Higgs boson mass m_H and the parameter $\tan\beta$ for $\cos(\beta - \alpha) = -0.1$. The white regions in the exclusion plots indicate regions of parameter space not excluded by the present analysis; in these regions the cross section predicted by the *2HDM* is below the experimental sensitivity. Compared with recent studies of indirect limits (see Section 4.4.1), these exclusion limits are more stringent for Type I with $\cos(\beta - \alpha) < 0$ and $1 < \tan\beta < 2$, and for Type II with $0.5 < \tan\beta < 2$.

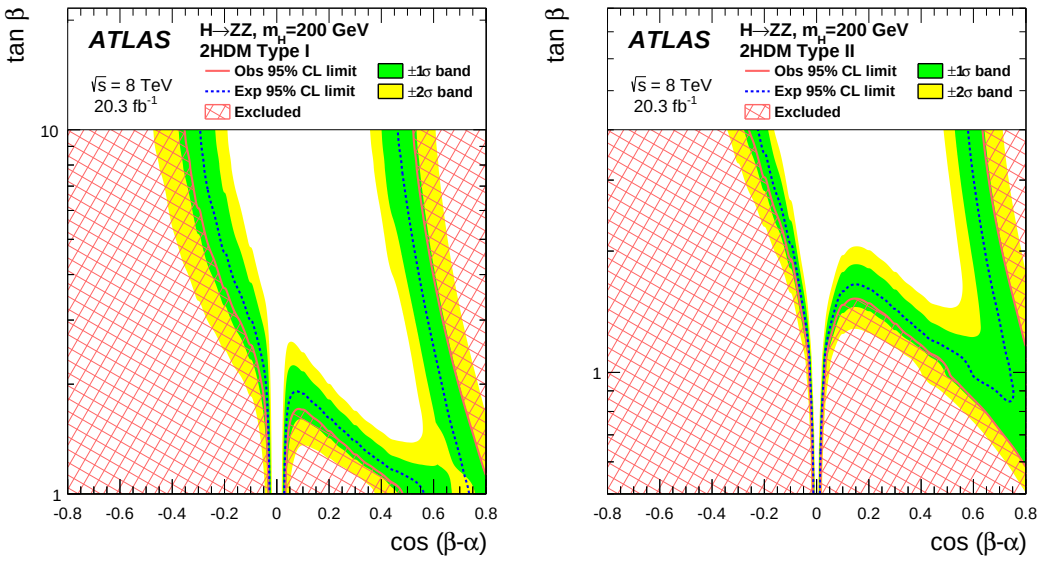

(a) Type I *2HDM* (b) Type II *2HDM*

Figure 5.62: 95% CL exclusion contours in the *2HDM* (a) Type I and (b) Type II for $m_H = 200$ GeV, shown as a function of the parameters $\cos(\beta - \alpha)$ and $\tan\beta$. The red hashed area shows the observed exclusion, with the solid line denoting the edge of the excluded region. The dashed blue line represents the expected exclusion contour and the shaded bands the 1σ and 2σ uncertainties on the expectation. The vertical axis range is set such that regions where the light Higgs couplings are enhanced by more than a factor of three from their SM values are avoided.

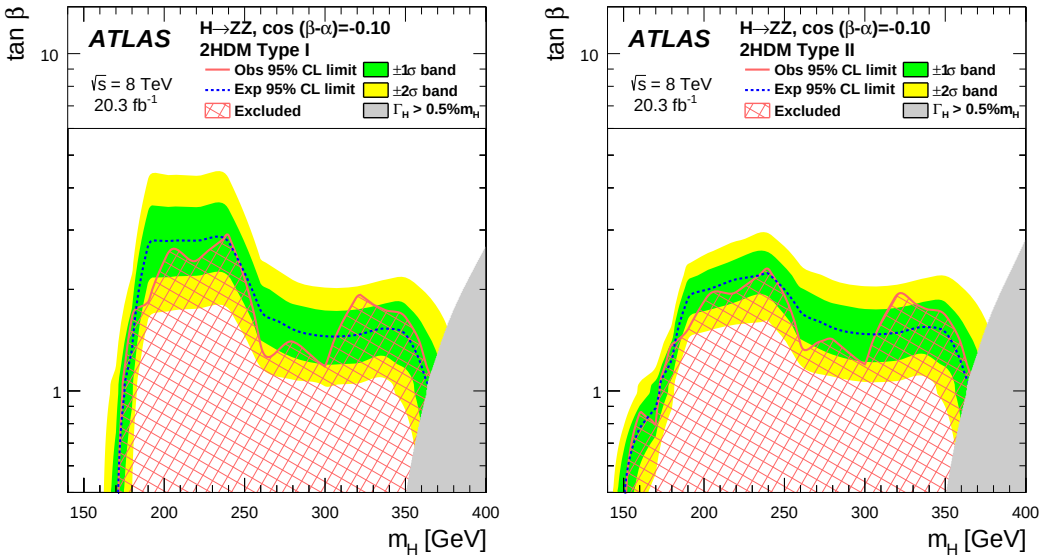

(a) Type I *2HDM* (b) Type II *2HDM*

Figure 5.63: 95% CL exclusion contours in the *2HDM* (a) Type I and (b) Type II for $\cos(\beta-\alpha) = -0.1$, shown as a function of the heavy Higgs boson mass m_H and the $\tan\beta$ parameter. The shaded area shows the observed exclusion, with the black line denoting the edge of the excluded region. The blue line represents the expected exclusion contour and the shaded bands the 1σ and 2σ uncertainties on the expectation. The grey area masks regions where the width of the boson is greater than 0.5% of m_H. For the choice of $\cos(\beta-\alpha) = -0.1$ the light Higgs couplings are not altered from their SM values by more than a factor two.

Chapter 6

Conclusions

The discovery of the Higgs boson announced by the ATLAS and CMS Collaborations at CERN on 4^{th} July 2012 has been a milestone for the particle and high energy physics. The Standard Model succeeded so far to describe the electroweak and strong interactions between elementary particles and its powerful predictions has been confirmed through decades thanks to the efforts of many particle physicists involved in several worldwide experiments. Nevertheless, the existence of physics Beyond the Standard Model (BSM) can not be excluded and it constitutes a very important and rich research field. In fact the Higgs sector, for instance, can further be explored by searching for additional heavy Higgs bosons which are predicted by many BSM models as the two-Higgs-doublet models.

In this thesis work, the search for a high-mass Higgs boson in the $H \to ZZ \to \ell^{\pm}\ell^{\mp}q\bar{q}$ channel in the $200 - 1000$ GeV mass range has been presented. The results has been obtained by using the 2012 pp collisions data collected by the ATLAS detector at the CERN Large Hadron Collider at a center-of-mass energy of 8 TeV and corresponding to an integrated luminosity of 20.3 fb^{-1}. The major challenge of this analysis is represented by the presence of two jets in the final state. Be-

sides the intrinsic difficulty of jets analyses, in the mass range above 700 GeV, the complexity of jet reconstruction reflects on the ability to singularly resolve the two final state jets. In fact, at very high mass values, the jets coming from the hadronically decaying Z boson are boosted along the flight direction and eventually reconstructed as a single jet. To recover the loss in the selection efficiency due to this effect, a dedicated selection has been developed which permitted to include into the ggF production analysis a new subchannel, the merged channel. Finally, the inclusion of a dedicated VBF production mode selection and the re-optimization of the overall event selection complete the major improvements with respect to 2011 $\ell\ell qq$ analysis previously published [75].

The search results has been interpreted in the scenario of a heavy Higgs boson with a width that is small compared with the experimental mass resolution. No significant excess of events over the Standard Model prediction has been found. Limits on production and decay in the $\ell\ell qq$ channel of a heavy Higgs boson has been set separately for ggF and VBF production modes. The 95% CL upper limits range from 3.33 pb at $m_H = 200$ GeV to 0.03 pb at $m_H = 1$ TeV for the ggF production mode (including the merged channel) and from 0.45 pb at $m_H = 200$ GeV to 0.02 pb at $m_H = 1$ TeV for the VBF production mode. The results has been also interpreted in the context of Type I and Type II two-Higgs-doublet models, with exclusion contours given in the $\tan\beta$ versus $\cos(\beta - \alpha)$ plane for $m_H = 200$ GeV. Compared to recent studies of indirect limits, the two-Higgs-doblet model exclusion presented is considerably more stringent for Type I with $\cos(\beta - \alpha) < 0$ and $0.5 < \tan\beta < 1$ and for Type II with $0.5 < \tan\beta < 1$.

The results presented in this work has been published [125] in combination with the $H \to \ell\ell\ell\ell$, $H \to \ell\ell\nu\nu$ and $H \to \nu\nu qq$ decay modes analyses.

List of Figures

1.1 List of elementary particles in the Standard Model 2

1.2 Feynman diagrams for two QED processes 6

1.3 Feynman diagram for a simple $q\bar{q} \to q'\bar{q}'$ QCD process. 9

1.4 Representation of the potential term $V(\phi)$ for the $\mu^2 > 0$ (left) and $\mu^2 < 0$ (right) cases as a function of the two field components ϕ_1 and ϕ_2. 13

1.5 Some Feynman diagrams for the scattering of W bosons at high energy. 18

1.6 Typical Feynman diagrams for the tree-level and one-loop Higgs self-coupling. 20

1.7 The triviality (upper) bound and the vacuum stability (lower) bound on the Higgs boson mass as a function of the new physics or cut-off scale Λ for a top quark mass $m_t = 175 \pm 6$ GeV and $\alpha_s(M_Z) = 0.118 \pm 0.002$; the allowed region lies between the bands and the colored/shaded bands illustrate the impact of various uncertainties. 21

1.8 (a) Summary of electroweak precision measurements at LEP1, LEP2, SLC and Tevatron. The SM fits results, which have been derived including all radiative corrections, and the standard deviations are also shown. (b) Electroweak precision measurements as a function of the Higgs boson mass; the vertical green band denotes the overall constraint on the Higgs mass derived from the fit to all data, while the vertical black line denotes the limit on the Higgs mass obtained from the direct search at LEP2. 23

1.9 (a) The $\Delta\chi^2$ of the fit to the electroweak precision data as a function of Higgs boson mass m_H. The solid line results when all data are included and the blue shaded band is the estimated theoretical error from unknown higher-order corrections. The effect of including the low Q^2 data and the use of a different value for $\Delta\alpha_{(\mathrm{had})}$ are also shown. The excluded (yellow) region corresponds to the July 2011 Tevatron combination (156-177 GeV) and the December 2011 LHC exclusion (127-600 GeV, CMS). (b) Confidence level CL_S for the signal plus background hypothesis in Higgs production at LEP2. The solid/red line is for the observation, the dashed line is the median background expectation, the green and yellow shaded bands around the median expected line correspond to the 68% and 95% simulated probability bands. The intersection of the horizontal line at $\mathrm{CL}_S = 0.05$ with the observed curve defines the 95% CL lower bound for m_H. 24

1.10 Observed and expected (median, for the background-only hypothesis) 95% CL upper limits on the ratios to the SM cross section, as functions of the Higgs boson mass for the combined CDF and D0 analyses. The limits are expressed as a multiple of the SM prediction for test masses (every 5 GeV/c^2) for which both experiments have performed dedicatedsearches in different channels. The points are joined by stra ight lines for better readability. The bands indicate the 68% and 95% probability regions where the limits can fluctuate, in the absence of signal. The limits displayed in this figure are obtained with the Bayesian calculation. 26

1.11 (a) Evolution through years of the ATLAS observed (solid) local p_0 as a function of m_H in the low mass range. The dashed curve shows the expected local p_0 under the hypothesis of a SM Higgs boson signal at that mass. The horizontal dashed lines indicate the p-values corresponding to significances of 1 to 6 σ. (b) The observed CMS local p-value for 7 TeV and 8 TeV data, and their combination as a function of the SM Higgs boson mass. The dashed line shows the expected local p-values for a SM Higgs boson with a mass m_H. . 27

1.12 Invariant mass distribution of ATLAS (a) and CMS (b) diphoton candidates for the combined $\sqrt{s} = 7$ TeV and 8 TeV data samples. The result of a fit to the data of the sum of a signal and background component is superimposed. The bottom inset in (a) displays the residuals of the data with respect to the fitted background component. 28

1.13 The distribution of the four-lepton invariant mass $m_{4\ell}$ for the selected candidates compared to the background expectation for the low mass range for the $\sqrt{s} = 7$ TeV and 8 TeV combined datasets. Both ATLAS (a) and CMS (b) plots are shown. 28

2.1 Schematic view of the underground area where LHC is located. . . . 37
2.2 Diagram of the pre-acceleration and acceleration devices at the LHC. 39
2.3 LHC grid structure 41
2.4 The peak instantaneous luminosity $\mathcal{L}$ delivered to ATLAS per day versus time during the *pp* runs of 2010, 2011 and 2012. 42
2.5 The number of colliding bunches in ATLAS versus time during the *pp* runs of 2010, 2011 and 2012. 43
2.6 Cumulative luminosity versus time delivered to (green) and recorded by ATLAS (yellow) during stable beams and for *pp* collisions at 7 and 8 TeV centre-of-mass energy in 2011 and 2012. 43
2.7 Luminosity-weighted distribution of the mean number of interactions per crossing for the 2011 and 2012 data. This shows the full 2011 and 2012 *pp* runs. 44
2.8 Diagram of the ATLAS experimental apparatus. 45
2.9 Global coordinate reference system used in ATLAS. 47
2.10 Pseudorapidity η for some given polar angle values θ. 47
2.11 Geometry of the coils and magnetic structures. Eight coils which generate the toroidal magnetic field are visible in the *barrel* and *end-cap* regions. The structure that generates the solenoid magnetic field is located within the calorimetric system schematically depicted by four layers with different magnetic properties. The last layer is the return yoke. 48

2.12 (a) Magnetic field lines in the x-y plane. (b) Bending power as a function of η. 50
2.13 ATLAS Inner Detector structure. 51
2.14 3D view of the pixel detector. 52
2.15 3D view of the TRT detector. The *barrel* TRT is located in the center with the *endcap* discs placed at each end. 54
2.16 Calorimetric system. 56
2.17 Structure of the electromagnetic calorimeter. 57
2.18 Muon spectrometer section in the x-y plane. 62
2.19 Layout of the muon spectrometer and the arrangement of the different chambers within the spectrometer. 62
2.20 MDT chambers 64
2.21 Diagram of a CSC detector. 65
2.22 (a) Diagram of a RPC with single gap. (b) Position of the RPCs along z the direction. 66
2.23 (a) Trigger chamber composed by assembling two RPC unit. (b) Detail of the overlapping region of two RPC unit 67
2.24 The event rate at which interesting physics occur (referred to LHC design parameters) and the processing time of each trigger level . . 68
2.25 Main structure of the ATLAS trigger system: it is made of three levels, each improving the measurement of the previous levels also combining informations from different subdetectors 69
2.26 Total trigger rates at each level of the ATLAS trigger 71
2.27 The L1 trigger for calorimetric objects in the Electromagnetic calorimeter: the green area represents the RoI cluster, the yellow area is the region used for the isolation requirements, and the pink area is the region used for the hadronic isolation. 71

2.28 E/p distribution found by the HLT and the offline for the electron trigger. The distributions are shown for L2 and EF separately . . . 73

2.29 L1 muon trigger algorithm: a muon coming from the interaction point leaves hits on the three layers of RPC detectors installed in the muon spectrometer. The position of the different hits is correlated as a function of the muon p_{T} 74

2.30 Correlation between the muon p_{T} reconstructed at several trigger levels (level 2 in (a) and event filter in (b)) and the offline reconstruction. 75

3.1 Measured combined reconstruction and identification efficiency as a function of E_{T} (left) and η (right) for the cut-based *loose*, *multilepton*, *medium* and *tight* selections (up) and for the LOOSE LH, MEDIUM LH and VERY TIGHT LH selections (bottom), compared to MC expectation for electrons from $Z \to ee$ decay. The lower panel shows the data-to-MC efficiency ratios. The data efficiency is derived from the measured data-to-MC efficiency ratios and the MC prediction for electrons from $Z \to ee$ decays. The uncertainties are statistical (inner error bars) and statistical+systematic (outer error bars). 83

3.2 Muon reconstruction efficiency as a function of η measured in $Z \to \mu\mu$ events for muons with $p_{\mathrm{T}} > 10$ GeV and different muon reconstruction types. CaloTag muons are only shown in the region $|\eta| < 0.1$, where they are used in physics analyses. The error bars on the efficiencies indicate the statistical uncertainty. The panel at the bottom shows the ratio between the measured and predicted efficiencies. The error bars on the ratios are the combination of statistical and systematic uncertainties. 87

3.3 Reconstruction efficiency for CB (a), CB+ST (b), CaloTag (c) and CB+SA (d) muons as a function of the p_{T} of the muon, for muons with $0.1 < |\eta| < 2.5$ for CB and CB+ST muons, for $|\eta| < 0.1$ for CaloTag muons and for $2.5 < |\eta| < 2.7$ for CB+SA muons. The upper plots also show the result obtained with $Z \to \mu\mu$ and $J/\psi \to \mu\mu$ events. The inserts on the upper plots show the detail of the efficiencies as a function of p_{T} in the low p_{T} region. The CaloTag (c) and CB+SA (d) muon efficiencies are only measured with $Z \to \mu\mu$ events. The error bars on the efficiencies indicate the statistical uncertainty for $Z \to \mu\mu$ and include also the fit model uncertainty for $J/\psi \to \mu\mu$. The panel at bottom in (a), (b) and (c) plots shows the ratio between the measured and predicted efficiency, the green areas show the pure statistical uncertainty, while orange areas also include systematic uncertainties. In the (d) plot, the efficiencies are obtained as the product of scale factor, shown in the lower panel, and the MC efficiency. The error bars correspond to the statistical uncertainty while the green shaded band corresponds to the statistical and systematic uncertainty added in quadrature. . 88

3.4 Energy response as a function of η_{det} (the η of the jet relative to the geometric centre of the detector) for EM (a) and LCW (b) scale anti-k_t, $R = 0.4$ jets before calibration 94

3.5 Ratio of response measured in data to response measured in data for Z+jet, γ+jet and multijet balance in-situ analyses. Also shown is the combined correction (black line) with its associated uncertainty (green band). 96

3.6 The jet resolution as a function of p_{T} for the four different jet collections in the central region. The three in-situ inputs to the measurement are shown displaying the compatibility between the measurements. The final fit using the function in Equation 3.5 is included with its associated statistical and total uncertainty. 98

3.7 The vertex mass (a), energy fraction (b) and vertex finding efficiency (c) of the inclusive secondary vertices found by the SV1 algorithm, for three different flavours of jets. 101

3.8 Distribution of the IP3D (a), SV1 (b) and IP3D+JetFitter (c) weights for b, c and light-flavour jets. These three weights are used as inputs for the MV1 algorithm. The spikes at $w_{\mathrm{IP3D}} \approx -20$ and ≈ -30 correspond to pathological cases where the IP3D weight could not be computed, due to the absence of good-quality tracks. The spike at $w_{\mathrm{SV1}} \approx -1$ corresponds to jets in which no secondary vertex could be reconstructed by the SV1 algorithm and where discrete probabilities for a b and light-flavour jet not to have a vertex are assigned. The irregular behavior in $w_{\mathrm{IP3D+JetFitter}}$ arises because both the w_{IP3D} and the $w_{\mathrm{JetFitter}}$ distribution (not shown) exhibit several spikes. 103

3.9 Distribution of the tagging weight obtained with the MV1 algorithm, for three different flavors of jets (a) and light-flavour jet rejection versus b-jet tagging efficiency, for various tagging algorithm (b). 104

4.1 Leading-order Feynman diagrams for Higgs boson production via the (a) ggF and (b) VBF production processes. 107

4.2 Leading-order Feynman diagrams of Higgs boson production via the (a) $q\bar{q} \to VH$ and (b,c) $gg \to ZH$ production processes. 107

4.3 Leading-order Feynman diagrams of Higgs boson production via the $q\bar{q}/gg \to t\bar{t}H$ and $q\bar{q}/gg \to bbH$ processes. 108

4.4 Leading-order Feynman diagrams of Higgs boson decays (a) to W and Z bosons and (b) to fermions. 108

4.5 Leading-order Feynman diagrams of Higgs boson decays to a pair of photons. 108

4.6 Invariant mass distribution in the $H \to \gamma\gamma$ analysis for data (7 TeV and 8 TeV samples combined), showing weighted data points with errors and the result of the simultaneous fit to all categories. The fitted signal plus background is shown, along with the background-only component of this fit. The different categories are summed together with a weight given by the signal-to-background ratio in each category. The bottom panel shows the difference between the summed weights and the background component of the fit. 112

4.7 (a) Distribution of the four-lepton invariant mass $m_{4\ell}$ for the selected candidates in the mass range 80 - 170 GeV for the combined 7 TeV and 8 TeV data samples. Superimposed are the expected distributions of a SM Higgs boson signal for $m_H = 124.5$ GeV normalized to the measured signal strength, as well as the expected ZZ^* and reducible backgrounds. (b) Distribution of the BDT_{ZZ^*} output versus $m_{4\ell}$ for the selected candidates in the 110-140 GeV mass range for the combined 7 TeV and 8 TeV data samples. The expected distribution for a SM Higgs with $m_H = 124.5$ GeV is indicated by the size of the blue boxes and the total background is indicated by the intensity of the red shading. 115

4.8 (a) Value of $-2\ln\Lambda$ as a function of m_H for the individual $h \to \gamma\gamma$ and $H \to ZZ^* \to 4\ell$ channels and their combination, where the signal strengths $\mu_{\gamma\gamma}$ and $\mu_{4\ell}$ are allowed to vary independently. The dashed lines show the statistical component of the mass measurements. For the $H \to ZZ^* \to 4\ell$ channel, this is indistinguishable from the solid line that includes that systematic uncertainties. (b) Likelihood contours $-2\ln\Lambda(S, m_H)$ as a function of the normalized signal yield $S = \sigma/\sigma_{\mathrm{SM}}(m_H = 125.36\ \mathrm{GeV})$ and m_H for the $H \to \gamma\gamma$ and $H \to ZZ^* \to 4\ell$ channels and their combination, including all systematic uncertainties. For the combined contour, a common normalized signal yield S is used. The markers indicate the maximum likelihood estimates in the corresponding channels. 116

4.9 The observed signal strengths and uncertainties for different Higgs boson decay channels and their combination for $m_H = 125.36$ GeV. Higgs boson signals corresponding to the same decay channel are combined together for all analyses, assuming SM values for the cross section ratios of different production processes. The best-fit values are shown by the solid vertical lines. The total $\pm 1\sigma$ uncertainties are indicated by green shaded bands, with the individual contributions from the statistical uncertainty (top), the total (experimental and theoretical) systematic uncertainty (middle), and the signal theoretical uncertainty (bottom) on the signal strength shown as horizontal error bars. 124

4.10 The best-fit signal-strength values of different production modes determined from the combined fit to the $\sqrt{s} = 7$ and 8 TeV data. The inner and outer error bars correspond to 68% CL and 95% CL intervals. Total uncertainties combining statistical, experimental and theoretical systematic uncertainties are shown. The fit assumes the SM values of the Higgs boson decay branching ratios for $m_H =$ 125.36 GeV. 127

4.11 Regions of the $[\cos(\beta-\alpha), \tan\beta]$ plane of four types of *2HDM*s excluded by fits to the measured rates of Higgs boson production and decays. The likelihood contours where $-2\ln\Lambda = 6.0$, corresponding approximately to the 95% CL (2 std. dev.), are indicated for both the data and the expectation for the SM Higgs sector. The cross in each plot marks the observed best-fit value. The light shaded and hashed regions indicate the observed and expected exclusions, respectively. The α and β parameters are taken to satisfy $0 \leq \beta \leq \pi/2$ and $0 \leq \beta - \alpha \leq \pi$ without loss of generality. 131

5.1 The p_{T} and η distributions of the two muons forming the leptonic Z boson candidate after the Z boson mass selection $83 < m_{\mu\mu} < 99$ GeV. In this and all subsequent plots the MC is normalized to the luminosity of the data and the background are taken from the final fit. The shaded (orange) band in the main (ratio) plot shows the quadratic sum of the MC statistical uncertainty (indicated by the brown histogram on the ratio) and the shape-dependent systematic uncertainty on the total MC background. 144

5.2 The p_{T} and η distributions of the two electrons forming the leptonic Z boson candidate after the Z boson mass selection $83 < m_{ee} < 99$ GeV. 146

5.3 The p_{T} and η distributions of "veto" jets after the $Z \to \ell\ell$ boson mass selection, at least two "signal" jet and $\frac{E_{\mathrm{T}}^{\mathrm{miss}}}{\sqrt{H_{\mathrm{T}}}}$ cut. 148
5.4 An example of the jet mass response before (left) and after (right) the mass calibration. The jet mass response is shown for jets with different p_{T}, $0.6 < |\eta| < 0.8$ and as a function of $\frac{m}{p_{\mathrm{T}}}$ 152
5.5 Dilepton mass spectrum fro events with ≥ 2 jets after the $E_{\mathrm{T}}^{\mathrm{miss}}$ requirement in the (a) untagged electron, (b) tagged electron, (c) untagged muon and (d) tagged muon categories of the resolved ggF channel. 156
5.6 $E_{\mathrm{T}}^{\mathrm{miss}}$ distribution for events with ≥ 2 jets after the $m_{\ell\ell}$ cut in the (a) untagged and (b) tagged resolved ggF category. The same for $E_{\mathrm{T}}^{\mathrm{miss}}$ significance in figures (c) and (d) 157
5.7 Number of "signal" jets after $m_{\ell\ell}$ and $\frac{E_{\mathrm{T}}^{\mathrm{miss}}}{\sqrt{H_{\mathrm{T}}}}$ 158
5.8 Distribution of (a) MV1c b-tagging discriminant (in the pseudo-continous binning) for all "signal" jets and (b) number of b-tagged jets after the $m_{\ell\ell}$ and $\frac{E_{\mathrm{T}}^{\mathrm{miss}}}{\sqrt{H_{\mathrm{T}}}}$ 159
5.9 Dijet mass distribution for the (left) untagged and (right) tagged ggF category (top) before and (bottom) after the optimized cuts in Equation 5.1. Here and subsequently x indicates either a tagged or untagged jet and xj represents the two jets in the untagged channel, which combines 0 and 1 b-tag events. 160
5.10 Total selection efficiency versus m_H for different b-tag selections. . . 162

5.11 Median significance versus m_H for different b-tag selections, calculated from MC simulation for a total integrated luminosity of 20 fb^{-1}. In addition to the standard selection cuts, $m_{\ell\ell jj}$ is required to lie within a symmetric window around the MC input m_H; the width of the window is set to accept 90% of the signal. Cross sections are from Section 5.1; NWA samples are used for $m_H > 400$ GeV 163

5.12 Dilepton mass spectra for monojet events, *i.e.* events containing only a single "good" jet in addition to the leptonic Z decay, for (a) electrons and (b) muons. 165

5.13 Invariant mass of the leading jet in events selected by the merged analysis, after the mass calibration and the kinematic selection. . . 166

5.14 Distribution of the invariant mass (left) and pseudorapidity gap (right)for the VBF "tag jet" pair. In the VBF channel, ALPGEN generator is used for the Z+jets background. 167

5.15 Distribution of $E_{\mathrm{T}}^{\mathrm{miss}}$ significance (left) and the invariant mass of the dijet pair forming the $Z \to q\bar{q}$ candidate in the VBF category (right) 168

5.16 Distribution of $p_{\mathrm{T}}^{\mathrm{tot}}$ in the VBF category. 169

5.17 Normalized $\Delta\phi_{jj}$ distributions and data/MC ratios for 0-, 1- and 2-tag events for low $p_{\mathrm{T}}^{\ell\ell}$ (left) and high $p_{\mathrm{T}}^{\ell\ell}$ (right) before the correction described in the text; the discrepancy in the low $p_{\mathrm{T}}^{\ell\ell}$ 0 and 1 b-tag regions can clearly be seen. 173

5.18 Linear fit to the $\frac{\mathrm{Data}-\mathrm{MC}_{\mathrm{bkg}}}{\mathrm{MC}_{Z+\mathrm{jets}}}$ ratio for 0 b-tag events at low $p_{\mathrm{T}}^{\ell\ell}$. Here "bkg" refers to the non-Z background. 174

5.19 Normalized $\Delta\phi_{jj}$ distributions and data/MC ratios for 0-, 1- and 2-tag events for low $p_{\mathrm{T}}^{\ell\ell}$ (left) and high $p_{\mathrm{T}}^{\ell\ell}$ (right) after the correction described in the text but before the $p_{\mathrm{T}}^{\ell\ell}$ correction. It can be seen at this point that there is still a discrepancy in the low $p_{\mathrm{T}}^{\ell\ell}$ 1 b-tag region. 175

5.20 The normalized $p_{\mathrm{T}}^{\ell\ell}$ distributions and data/MC ratios for (a) 0, (b) 1 and (c) 2 b-tag events before the correction described in the text; the discrepancy in the 1 and 2 b-tag regions can clearly be seen. . . 177

5.21 Fit to the $\frac{\mathrm{Data-MC_{bkg}}}{\mathrm{MC}_{Z+\mathrm{heavy-flavour}}}$ ratio for 1 and 2 b-tag events combined. Here "bkg" refers to the Z+light-jet and non-Z background. 177

5.22 $\Delta\phi_{jj}$ (left) and $p_{\mathrm{T}}^{\ell\ell}$ (right) distributions for (a, c) 0, (b, d) 1 and (e, f) 2 b-tag events in the combined SB after the corrections in the text. The bands show the systemic uncertainties including those associated with these corrections. 178

5.23 $\Delta\phi_{jj}$ (left) and $p_{\mathrm{T}}^{\ell\ell}$ (right) distributions for (a, c) 0, (b, d) 1 and (e, f) 2 b-tag events in the low-m_{jj} SB after the corrections in the text. The bands show the systemic uncertainties including those associated with these corrections. 179

5.24 $\Delta\phi_{jj}$ (left) and $p_{\mathrm{T}}^{\ell\ell}$ (right) distributions for (a, c) 0, (b, d) 1 and (e, f) 2 b-tag events in the high-m_{jj} SB after the corrections in the text. The bands show the systemic uncertainties including those associated with these corrections. 180

5.25 The full m_{jj} distribution in data, after subtracting the non-Z background determined from MC simulation, compared to the nominal (solid line) Z+jets MC expectation (after $\Delta\phi_{jj}$ and $p_{\mathrm{T}}^{\ell\ell}$ corrections), along with their ratio. The signal region is blinded (as indicated by the black bandstring). the dashed lines show the Z+jets MC distribution after the downward and upward shape variation described in the text. Note, since these lines indicate the MC simulation after the reweight in the two directions, they just represent the shape variation and not an uncertainty band. As such it should be made clear that the region where the two lines cross does not correspond to a vanishing uncertainty but rather just to the pivot point. 182

5.26 $m_{\ell\ell jj}$ distribution for (a, c) 0, (b, d) 1 and (e, f) 2 b-tag events, after the corrections in the text, before (left) and after (right) the optimized selection. The systematic uncertainty bands include the uncertainties associated with these corrections. 183

5.27 Three-body mass distributions ($m_{\ell\ell j}$) obtained in the m_j sideband before (left) and after (right) the application of the scale factor described in the text. 184

5.28 p_{T} spectrum of the leading jet in the merged regime. 185

5.29 The ratio of the full m_{jj} distribution in data, after subtracting the non-Z background determined from MC simulation, over the nominal Z+jets MC expectation. The signal region is blinded. The dashed line show the reweight factors applied to the Z+jets MC distribution in order to acquire the upward/downward variations associated to the normalization from the Z+jets control region. . . 186

5.30 $m_{\ell\ell jj}$ distribution for the control region of the Z+jets background, in the VBF channel, before (a) and after (b) the optimized selection. 186

5.31 The (a, b) m_{jj} and (c, d) $m_{\ell\ell jj}$ distributions for the top control region (CR) in the subchannels with 1 (left) and 2 (right) b-tagged jets. 188

5.32 $R^{m_{\text{trackcalo}}}$, $r^{m,\text{data}}_{\text{trackcalo}}$ and $r^{m,\text{MC}}_{\text{trackcalo}}$ used to parameterized the uncertainty on the jet mass scale. 197

5.33 The final MC-to-data calibration scale factors for the MV1c b-, c-jet and $|\eta| < 1.2$ light-jet calibration for a representative jet p_{T} bin. The data results are compared to MC expectations. Error bars show statistical uncertainties, while the bands include systematic uncertainties as well. 198

5.34 An example of the smoothing procedure used for systematic uncertainties. The nominal distribution without rebinning is shown as points and the relative systematic variation using the binning determined by the smoothing procedure is shown as the histogram. Up and down refer to the nominal name of the systematic not necessary change on the current distribution. 200

5.35 The signal acceptance variations for the NWA signal in the ggF channel due to changes in (a, b) renormalization/factorization scale, (c, d) PDF and (e, f) ISR/FSR. The left (right) column is for the untagged (tagged) category. 206

5.36 The signal acceptance variations for the NWA signal in the VBF channel due to changes in (a) renormalization/factorization scale, (b) PDF and (c) ISR/FSR. 207

5.37 The signal acceptance variations for the NWA signal in the ggF channel for the merged category alone, due to changes in (a) renormalization/factorization scale, (b) PDF and (c) ISR/FSR. 208

5.38 The resolution of the $m_{\ell\ell jj}$ distribution as a function of m_H for both untagged and tagged ggF channels. The errors are statistical only. . 210
5.39 The fractional resolution of the $m_{\ell\ell jj}$ distribution as a function of m_H for both untagged (left) and tagged (right) ggF channels. The errors are statistical only. 210
5.40 $m_{\ell\ell jj}$ distribution for various Higgs boson signal masses in the untagged subchannel of the (resolved) ggF category. The hashed band indicates the systematic uncertainty. Note that the signal is multiplied by various scale factors for clarity. 212
5.41 $m_{\ell\ell jj}$ distribution for various Higgs boson signal masses in the tagged subchannel of the (resolved) ggF category. The hashed band indicates the systematic uncertainty. Note that the signal is multiplied by various scale factors for clarity. 213
5.42 $m_{\ell\ell}$ distribution for the merged category using $m_H = 900$ GeV. The dashed band shows the systematic uncertainty. 214
5.43 $m_{\ell\ell jj}$ distribution for different Higgs boson signal masses in the VBF category. The hashed band indicates the systematic uncertainty. Note that the signal at $m_H = 1$ TeV is multiplied by 10. 215
5.44 Ranking of the top 15 nuisance parameters in the ggF fit for different Higgs boson mass values considering the resolved-only (a,b,c) and both resolved and merged (d) category. 224
5.45 Ranking of the top 15 nuisance parameters in the VBF fit for different Higgs boson mass values. 225
5.46 Post-fit plots of discriminant entering the ggF limits in the SRs (top), Z CRs (middle) and top CR (bottom), showing a 400 GeV NWA signal with $\mu = 1$. The binning is the same as that used in the fit. 227

5.47 Post-fit plots of discriminant entering the VBF limits in the SR (left) and Z CR (right), showing a 400 GeV NWA signal with $\mu = 1$. The binning is the same as that used in the fit. 228
5.48 Post-fit plots of $\frac{E_{\mathrm{T}}^{\mathrm{miss}}}{\sqrt{H_{\mathrm{T}}}}$ in the ggF untagged (left) and tagged (right) channels. 228
5.49 Post-fit plots of m_{jj} in the ggF untagged (a) and tagged (b) channels, along with the top $e\mu$ CR. 229
5.50 Post-fit plots of $p_{\mathrm{T}}^{\ell\ell}$ in the SR (left) and Z CR (right) in the untagged (top) and tagged (bottom) channel. 230
5.51 Post-fit plots of p_{T}^{j} (top) and $\Delta\phi_{\ell\ell}$ (bottom) in the SR (left) and Z CR (right) for the ggF channel. 231
5.52 Post-fit plots of discriminant entering the ggF limits obtained considering both the resolved and the merged category in the SR (left) and ZCR (right) with a 900 GeV NWA signal with $\mu = 1$. The binning is the same as that used in the fit. 232
5.53 Post-fit plots of $\frac{E_{\mathrm{T}}^{\mathrm{miss}}}{\sqrt{H_{\mathrm{T}}}}$ (a) and m_{jj} (b) in the VBF channel. 232
5.54 Post-fit plots of $p_{\mathrm{T}}^{\ell\ell}$ in the SR (left) and ZCR (right) in the VBF channel. 236
5.55 Post-fit plots of p_{T}^{j} (top) and $\Delta\phi_{\ell\ell}$ (bottom) in the SR (left) and ZCR (right) for the VBF channel. 237
5.56 Exclusion limit on $\sigma \times \mathrm{BR}$ at 95% CL for a narrow resonance in the ggF channel. The SM σ is shown for comparison. 238
5.57 Exclusion limit on $\sigma \times \mathrm{BR}$ at 95% CL for a narrow resonance in the VBF channel. The SM σ is shown for comparison. 238
5.58 Exclusion limit on $\sigma \times \mathrm{BR}$ at 95% CL for a narrow resonance in the ggF channel obtained considering both the merged and the resolved categories. The SM σ is shown for comparison. 239

5.59 Exclusion limit on $\tan\beta$ vs $\cos(\beta-\alpha)$ at 95% CL in the Type II *2HDM* for ggF production at Higgs mass of (left) 200 and (right) 300 GeV. The green and yellow line represent, respectively, the $\pm1\sigma$ and $\pm2\sigma$ variations of the expected limit. The grey band represents the region where the limits are not valid since $\frac{\Gamma_H}{m_H} > 5\%$. Type I results are almost identical. 239

5.60 Exclusion limits on $\tan\beta$ vs m_H at 95% CL in the Type II *2HDM* for ggF production at $\cos(\beta-\alpha) = \pm0.1$. Type I are very similar. The green and yellow lines represent, respectively, the $\pm1\sigma$ and $\pm2\sigma$ variations of the expected limit. 240

5.61 95% CL upper limits on $\sigma \times \mathrm{BR}(H \to ZZ)$ as function of m_H, resulting from the combination of all of the searches in the (a) ggF and (b) VBF channels. The solid black line and points indicate the observed limit. The dashed black line indicates the expected limit and the bands the 1σ and 2σ uncertainty ranges about the expected limit. The dashed colored lines indicate the expected limits obtained from the individual searches; for the $\ell\ell qq$ and $\nu\nu qq$ searches, only the combination of the two is shown since they share control regions. 242

5.62 95% CL exclusion contours in the *2HDM* (a) Type I and (b) Type II for $m_H = 200$ GeV, shown as a function of the parameters $\cos(\beta-\alpha)$ and $\tan\beta$. The red hashed area shows the observed exclusion, with the solid line denoting the edge of the excluded region. The dashed blue line represents the expected exclusion contour and the shaded bands the 1σ and 2σ uncertainties on the expectation. The vertical axis range is set such that regions where the light Higgs couplings are enhanced by more than a factor of three from their SM values are avoided. 244

5.63 95% CL exclusion contours in the *2HDM* (a) Type I and (b) Type II for $\cos(\beta - \alpha) = -0.1$, shown as a function of the heavy Higgs boson mass m_H and the $\tan\beta$ parameter. The shaded area shows the observed exclusion, with the black line denoting the edge of the excluded region. The blue line represents the expected exclusion contour and the shaded bands the 1σ and 2σ uncertainties on the expectation. The grey area masks regions where the width of the boson is greater than 0.5% of m_H. For the choice of $\cos(\beta - \alpha) = -0.1$ the light Higgs couplings are not altered from their SM values by more than a factor two. 245

List of Tables

1.1 Yukawa couplings of u-type quarks, d-type quarks and leptons ℓ to the neutral Higgs bosons h, H, A in the four different models. . . . 34

4.1 SM predictions of the Higgs boson production cross sections together with their theory uncertainties. The value of the Higgs boson mass is assumed to be $m_H = 125.09$ GeV and the predictions are obtained by linear interpolation from those at 125.0 and 125.1 GeV from Reference [78] except for the tH cross section, which is obtained from Reference [68]. The ZH cross section includes at NNLO(QCD) both the quark-initiated, *i.e.* $qq \to ZH$ or $qg \to ZH$, and the $gg \to ZH$ contributions. The uncertainties on the cross sections are evaluated as the quadratic sum of the uncertainties resulting from variations of QCD scale, parton distribution functions and α_S. The uncertainty on the tH cross section is calculated following the procedure of Reference [79]. The order of the theory calculations for the different production processes is also indicated. 109

4.2 SM predictions for the decay branching ratios of a Higgs boson with a mass of 125.09 GeV, together with their uncertainties. The predictions are obtained from Reference [78]. 110

4.3 Measured signal strengths μ at $m_H = 125.36$ GeV and their total $\pm 1\sigma$ uncertainties for different production modes for the $\sqrt{s} = 8$ TeV data and the combination with the $\sqrt{s} = 7$ TeV data. The $\sqrt{s} = 7$ TeV data do not have sufficient statistical power to yield meaningful measurements for individual production modes, but are included in the combination. These results are derived using the SM values of the Higgs boson decay branching ratios. 126

4.4 Measured cross sections of different Higgs boson production processes at $\sqrt{s} = 8$ TeV for $m_H = 125.36$ GeV obtained from the signal-strength values of Table 4.3. Their SM predictions can be found in Table 4.1. The theoretical uncertainties here arise from the modelling of Higgs boson production and decays. These results are derived using the SM values of the Higgs boson decay branching ratios. 127

5.1 Cross section times branching ratio ($\sigma \times \mathrm{BR}$) of $H \to ZZ$ for $200 \leq m_H \leq 400$ GeV. 136

5.2 Monte Carlo generators used for modelling background processes and the cross-section times branching ratio ($\sigma \times \mathrm{BR}$) used to normalize the different processes at $\sqrt{s} = 8$ TeV. Branching ratios correspond to the decays shown. 138

5.3 Definition of "loose" and "medium" muon quality in terms of the muon family and kinematic requirements 142

5.4 Summary of muon selection. $N_{\mathrm{hits}}(N_{\mathrm{holes}})$ represents the number of hits (missing hits) in a particular subdetector of the inner tracker, while N_{dead} refers to the number of dead sensors crossed by the muon in a particular subdetector. 143

5.5 Summary of electron selection. 145

5.6 Summary of "signal" jet selection 147
5.7 The efficiencies for the available calibrated operating points for the MV1c algorithm. These values has been determined in semi-leptonic $t\bar{t}$ events with a jet p_{T} threshold of 20 GeV. RF stands for "rejection factor", which is defined as the reciprocal of the efficiency. 149
5.8 Overlap removal hierarchy and the order in which the ambiguity is checked. N_{trk} is the track multiplicity of ghost-matched tracks that have $p_{\mathrm{T}} > 1$ GeV and are compatible with the first primary vertex. 154
5.9 Fraction of events (in percent) in each jet tag bin for different m_H . 164
5.10 Sample composition for Z+jets modelling studies after background normalization. Here, $Z + b = Zbb + Zbc + Zbl$ refers to Z+jets MC events with at least one jet labelled as b, $Z + c = Zcc + Zcl$ refers to events with no jets labelled as b-jet but at least one labelled as c and $Z + l$ refers to events with no jets labelled as b or c. The small remaining fraction is made up by the other small backgrounds: diboson, multi-jet and W+jets. 171
5.11 Summary of the regions entering the likelihood fit and the distribution used in each. Vertically merged rows should be interpreted as regions treated with one distribution, *e.g.* there is no b-tag separation in merged/VBF categories and 0/1 b-tag regions are combined in ggF category. Rows with "-" mean that this region is not included in the fit. "SR" stands for the signal regions and "CR" for the control regions. 218

5.12 The limit on $\sigma_{ggF} \times$ BR with no statistical error and including the statistical error on bins with a relative error above 5%, 1% and 0% (*i.e.* all bins) respectively. It can be seen that the limit decreases as more statistical errors are included (as expected) but becomes constant once reaching a threshold of 1%. Note that these tests are not necessarily done with the very final limit results. 221

5.13 Observed and expected limits, along with $\pm 1\sigma$ and $\pm 2\sigma$ variations, at 95% CL for the ggF channel considering the resolved category alone. 233

5.14 Observed and expected limits, along with $\pm 1\sigma$ and $\pm 2\sigma$ variations, at 95% CL for the VBF channel. 234

5.15 Observed and expected limits, along with $\pm 1\sigma$ and $\pm 2\sigma$ variations, at 95% CL for the ggF channel when both the resolved and the merged categories are considered. 235

Bibliography

[1] P. A. M. Dirac, "*The quantum theory of the electron*", Proc. Roy. Soc. Lond. A **117** (1928) 610. doi:10.1098/rspa.1928.0023

[2] W. Heisenberg and W. Pauli, "*Zur Quantendynamik der Wellenfelder*", Z. Phys. **56** (1929) 1. doi:10.1007/BF01340129

[3] W. Heisenberg and W. Pauli, "*Zur Quantentheorie der Wellenfelder. II*", Z. Phys. **59** (1930) 168. doi:10.1007/BF01341423

[4] R. P. Feynman, "*Space - time approach to quantum electrodynamics*", Phys. Rev. **76** (1949) 769. doi:10.1103/PhysRev.76.769

[5] R. P. Feynman, "*The Theory of positrons*", Phys. Rev. **76** (1949) 749. doi:10.1103/PhysRev.76.749

[6] R. P. Feynman, "*Mathematical formulation of the quantum theory of electromagnetic interaction*", Phys. Rev. **80** (1950) 440. doi:10.1103/PhysRev.80.440

[7] J. S. Schwinger, "*On Quantum electrodynamics and the magnetic moment of the electron*", Phys. Rev. **73** (1948) 416. doi:10.1103/PhysRev.73.416

[8] J. S. Schwinger, "*Quantum electrodynamics. I A covariant formulation*", Phys. Rev. **74** (1948) 1439. doi:10.1103/PhysRev.74.1439

[9] F. J. Dyson, "*The Radiation theories of Tomonaga, Schwinger, and Feynman*", Phys. Rev. **75** (1949) 486. doi:10.1103/PhysRev.75.486

[10] F. J. Dyson, "*The S matrix in quantum electrodynamics*", Phys. Rev. **75** (1949) 1736. doi:10.1103/PhysRev.75.1736

[11] S. Tomonaga, "*On a relativistically invariant formulation of the quantum theory of wave fields*", Prog. Theor. Phys. **1** (1946) 27. doi:10.1143/PTP.1.27

[12] E. Fermi, "*Tentativo di una Teoria dei Raggi β*", Nuovo Cim. **11** (1934) 1. doi:10.1007/BF02959820

[13] E. Fermi, "*Versuch einer Theorie der β-Strahlen. I*", Z. Phys. **88** (1934) 161. doi:10.1007/BF01351864

[14] S. L. Glashow, "*Partial Symmetries of Weak Interactions*", Nucl. Phys. **22** (1961) 579. doi:10.1016/0029-5582(61)90469-2

[15] S. Weinberg, "*A Model of Leptons*", Phys. Rev. Lett. **19** (1967) 1264. doi:10.1103/PhysRevLett.19.1264

[16] A. Salam, "*Weak and Electromagnetic Interactions*", Conf. Proc. C **680519** (1968) 367.

[17] C. N. Yang and R. L. Mills, "*Conservation of Isotopic Spin and Isotopic Gauge Invariance*", Phys. Rev. **96** (1954) 191. doi:10.1103/PhysRev.96.191

[18] P. W. Higgs, "*Broken symmetries, massless particles and gauge fields*", Phys. Lett. **12** (1964) 132. doi:10.1016/0031-9163(64)91136-9

[19] P. W. Higgs, "*Broken Symmetries and the Masses of Gauge Bosons*", Phys. Rev. Lett. **13** (1964) 508. doi:10.1103/PhysRevLett.13.508

[20] P. W. Higgs, "*Spontaneous Symmetry Breakdown without Massless Bosons*", Phys. Rev. **145** (1966) 1156. doi:10.1103/PhysRev.145.1156

[21] F. Englert and R. Brout, "*Broken Symmetry and the Mass of Gauge Vector Mesons*", Phys. Rev. Lett. **13** (1964) 321. doi:10.1103/PhysRevLett.13.321

[22] G. S. Guralnik, C. R. Hagen and T. W. B. Kibble, "*Global Conservation Laws and Massless Particles*", Phys. Rev. Lett. **13** (1964) 585. doi:10.1103/PhysRevLett.13.585

[23] T. W. B. Kibble, "*Symmetry breaking in nonAbelian gauge theories*", Phys. Rev. **155** (1967) 1554. doi:10.1103/PhysRev.155.1554

[24] J. Goldstone, "*Field Theories with Superconductor Solutions*", Nuovo Cim. **19** (1961) 154. doi:10.1007/BF02812722

[25] J. Goldstone, A. Salam and S. Weinberg, "*Broken Symmetries*", Phys. Rev. **127** (1962) 965. doi:10.1103/PhysRev.127.965

[26] T. Hambye and K. Riesselmann, "*Matching conditions and Higgs mass upper bounds revisited*", Phys. Rev. D **55** (1997) 7255 doi:10.1103/PhysRevD.55.7255 [hep-ph/9610272].

[27] [ATLAS Collaboration], "*ATLAS inner detector: Technical design report. Vol. 1*", CERN-LHCC-97-16, ATLAS-TDR-4.

[28] [ATLAS Collaboration], "*ATLAS inner detector: Technical design report. Vol. 2*", CERN-LHCC-97-17.

[29] M. S. Alam *et al.* [ATLAS Collaboration], "*ATLAS pixel detector: Technical design report*", CERN-LHCC-98-13.

[30] A. Airapetian *et al.* [ATLAS Collaboration], "*ATLAS calorimeter performance Technical Design Report*", CERN-LHCC-96-40.

[31] [ATLAS Collaboration], "*ATLAS tile calorimeter: Technical design report*", CERN-LHCC-96-42.

[32] [ATLAS Collaboration], "*ATLAS muon spectrometer: Technical design report*", CERN-LHCC-97-22, ATLAS-TDR-10.

[33] [ATLAS Collaboration], "*ATLAS Trigger Performances*", ATL-COM-PHYS-2008-067, CERN (2008)

[34] W. Lampl *et al.*, "*Calorimeter clustering algorithms: Description and performance*", ATL-LARG-PUB-2008-002, ATL-COM-LARG-2008-003.

[35] T. Cornelissen, M. Elsing, S. Fleischmann, W. Liebig, E. Moyse and A. Salzburger, "*Concepts, Design and Implementation of the ATLAS New Tracking (NEWT)*", ATL-SOFT-PUB-2007-007, ATL-COM-SOFT-2007-002.

[36] [ATLAS Collaboration], "*Improved electron reconstruction in ATLAS using the Gaussian Sum Filter-based model for bremsstrahlung*", ATLAS-CONF-2012-047.

[37] G. Aad *et al.* [ATLAS Collaboration], "*Expected Performance of the ATLAS Experiment - Detector, Trigger and Physics*", arXiv:0901.0512 [hep-ex].

[38] M. Cacciari, G. P. Salam and G. Soyez, "*The Anti-k(t) jet clustering algorithm*", JHEP **0804** (2008) 063 doi:10.1088/1126-6708/2008/04/063 [arXiv:0802.1189 [hep-ph]].

[39] Y. L. Dokshitzer, G. D. Leder, S. Moretti and B. R. Webber, "*Better jet clustering algorithms*", JHEP **9708** (1997) 001 doi:10.1088/1126-6708/1997/08/001 [hep-ph/9707323].

[40] M. Wobisch and T. Wengler, "*Hadronization corrections to jet cross-sections in deep inelastic scattering*", In *Hamburg 1998/1999, Monte Carlo generators for HERA physics* 270-279 [hep-ph/9907280].

[41] M. Cacciari, G. P. Salam and G. Soyez, "*FastJet User Manual*", Eur. Phys. J. C **72** (2012) 1896 doi:10.1140/epjc/s10052-012-1896-2 [arXiv:1111.6097 [hep-ph]].

[42] [ATLAS Collaboration], "*Performance of the ATLAS Inner Detector Track and Vertex Reconstruction in the High Pile-Up LHC Environment*", ATLAS-CONF-2012-042.

[43] G. Aad *et al.* [ATLAS Collaboration], "*Jet energy measurement with the ATLAS detector in proton-proton collisions at* $\sqrt{s} = 7$ *TeV*", Eur.

Phys. J. C **73** (2013) no.3, 2304 doi:10.1140/epjc/s10052-013-2304-2 [arXiv:1112.6426 [hep-ex]].

[44] J. Colas *et al.*, "*Response Uniformity of the ATLAS Liquid Argon Electromagnetic Calorimeter*", Nucl. Instrum. Meth. A **582** (2007) 429 doi:10.1016/j.nima.2007.08.157 [arXiv:0709.1094 [physics.ins-det]].

[45] G. Aad *et al.* [ATLAS Collaboration], "*Electron performance measurements with the ATLAS detector using the 2010 LHC proton-proton collision data*", Eur. Phys. J. C **72** (2012) 1909 doi:10.1140/epjc/s10052-012-1909-1 [arXiv:1110.3174 [hep-ex]].

[46] The ATLAS collaboration [ATLAS Collaboration], "*Pile-up subtraction and suppression for jets in ATLAS*", ATLAS-CONF-2013-083.

[47] G. Aad *et al.* [ATLAS Collaboration], "*Jet energy measurement and its systematic uncertainty in proton-proton collisions at* $\sqrt{s} = 7$ *TeV with the ATLAS detector*", Eur. Phys. J. C **75** (2015) 17 doi:10.1140/epjc/s10052-014-3190-y [arXiv:1406.0076 [hep-ex]].

[48] The ATLAS collaboration [ATLAS Collaboration], "*Data-driven determination of the energy scale and resolution of jets reconstructed in the ATLAS calorimeters using dijet and multijet events at* $\sqrt{s} = 8$ *TeV*", ATLAS-CONF-2015-017.

[49] G. Aad *et al.* [ATLAS Collaboration], "*Jet energy resolution in proton-proton collisions at* $\sqrt{s} = 7$ *TeV recorded in 2010 with the ATLAS detector*", Eur. Phys. J. C **73** (2013) no.3, 2306 doi:10.1140/epjc/s10052-013-2306-0 [arXiv:1210.6210 [hep-ex]].

[50] G. Aad *et al.* [ATLAS Collaboration], "*The ATLAS Experiment at the CERN Large Hadron Collider*", JINST **3** (2008) S08003. doi:10.1088/1748-0221/3/08/S08003

[51] [ATLAS Collaboration], "*Commissioning of the ATLAS high-performance b-tagging algorithms in the 7 TeV collision data*", ATLAS-CONF-2011-102.

[52] G. Aad *et al.* [ATLAS Collaboration], "*Performance of Missing Transverse Momentum Reconstruction in Proton-Proton Collisions at 7 TeV with ATLAS*", Eur. Phys. J. C **72** (2012) 1844 doi:10.1140/epjc/s10052-011-1844-6 [arXiv:1108.5602 [hep-ex]].

[53] T. Barillari *et al.* [ATLAS Collaboration], "*Local hadronic calibration*", ATL-LARG-PUB-2009-001-2, ATL-COM-LARG-2008-006.

[54] [ATLAS Collaboration], "*Determination of the tau energy scale and the associated systematic uncertainty in proton-proton collisions at sqrts= =*

7 TeV with the ATLAS detector at the LHC in 2011", ATLAS-CONF-2012-054.

[55] G. Aad *et al.* [ATLAS Collaboration], "*Observation of a new particle in the search for the Standard Model Higgs boson with the ATLAS detector at the LHC*", Phys. Lett. B **716** (2012) 1 doi:10.1016/j.physletb.2012.08.020 [arXiv:1207.7214 [hep-ex]].

[56] S. Chatrchyan *et al.* [CMS Collaboration], "*Observation of a new boson at a mass of 125 GeV with the CMS experiment at the LHC*", Phys. Lett. B **716** (2012) 30 doi:10.1016/j.physletb.2012.08.021 [arXiv:1207.7235 [hep-ex]].

[57] L. Evans and P. Bryant, "*LHC Machine*", JINST **3** (2008) S08001. doi:10.1088/1748-0221/3/08/S08001

[58] G. Aad *et al.* [ATLAS Collaboration], "*Measurement of Higgs boson production in the diphoton decay channel in pp collisions at center-of-mass energies of 7 and 8 TeV with the ATLAS detector*", Phys. Rev. D **90** (2014) no.11, 112015 doi:10.1103/PhysRevD.90.112015 [arXiv:1408.7084 [hep-ex]].

[59] G. Aad *et al.* [ATLAS Collaboration], "*Measurements of Higgs boson production and couplings in the four-lepton channel in pp collisions at center-of-mass energies of 7 and 8 TeV with the ATLAS detector*", Phys. Rev. D **91** (2015) no.1, 012006 doi:10.1103/PhysRevD.91.012006 [arXiv:1408.5191 [hep-ex]].

[60] G. Aad *et al.* [ATLAS Collaboration], "*Observation and measurement of Higgs boson decays to WW* with the ATLAS detector*", Phys. Rev. D **92** (2015) no.1, 012006 doi:10.1103/PhysRevD.92.012006 [arXiv:1412.2641 [hep-ex]].

[61] G. Aad *et al.* [ATLAS Collaboration], "*Study of (W/Z)H production and Higgs boson couplings using $H \to WW^*$ decays with the ATLAS detector*", JHEP **1508** (2015) 137 doi:10.1007/JHEP08(2015)137 [arXiv:1506.06641 [hep-ex]].

[62] G. Aad *et al.* [ATLAS Collaboration], "*Evidence for the Higgs-boson Yukawa coupling to tau leptons with the ATLAS detector*", JHEP **1504** (2015) 117 doi:10.1007/JHEP04(2015)117 [arXiv:1501.04943 [hep-ex]].

[63] G. Aad *et al.* [ATLAS Collaboration], "*Search for the $b\bar{b}$ decay of the Standard Model Higgs boson in associated $(W/Z)H$ production with the ATLAS detector*", JHEP **1501** (2015) 069 doi:10.1007/JHEP01(2015)069 [arXiv:1409.6212 [hep-ex]].

[64] G. Aad *et al.* [ATLAS Collaboration], "*Search for Higgs boson decays to a photon and a Z boson in pp collisions at $\sqrt{s}$=7 and 8 TeV with the ATLAS detector*", Phys. Lett. B **732** (2014) 8 doi:10.1016/j.physletb.2014.03.015 [arXiv:1402.3051 [hep-ex]].

[65] G. Aad *et al.* [ATLAS Collaboration], "*Search for the Standard Model Higgs boson decay to $\mu^+\mu^-$ with the ATLAS detector*" Phys. Lett. B **738** (2014) 68 doi:10.1016/j.physletb.2014.09.008 [arXiv:1406.7663 [hep-ex]].

[66] G. Aad *et al.* [ATLAS Collaboration], "*Search for the Standard Model Higgs boson produced in association with top quarks and decaying into $b\bar{b}$ in pp collisions at $\sqrt{s}$ = 8 TeV with the ATLAS detector*", Eur. Phys. J. C **75** (2015) no.7, 349 doi:10.1140/epjc/s10052-015-3543-1 [arXiv:1503.05066 [hep-ex]].

[67] G. Aad *et al.* [ATLAS Collaboration], "*Search for the associated production of the Higgs boson with a top quark pair in multilepton final states with the ATLAS detector*", Phys. Lett. B **749** (2015) 519 doi:10.1016/j.physletb.2015.07.079 [arXiv:1506.05988 [hep-ex]].

[68] G. Aad *et al.* [ATLAS Collaboration], "*Search for $H \to \gamma\gamma$ produced in association with top quarks and constraints on the Yukawa coupling between the top quark and the Higgs boson using data taken at 7 TeV and 8 TeV with the ATLAS detector*", Phys. Lett. B **740** (2015) 222 doi:10.1016/j.physletb.2014.11.049 [arXiv:1409.3122 [hep-ex]].

[69] G. Cowan, K. Cranmer, E. Gross and O. Vitells, "*Asymptotic formulae for likelihood-based tests of new physics*", Eur. Phys. J. C **71** (2011) 1554 [Eur. Phys. J. C **73** (2013) 2501] doi:10.1140/epjc/s10052-011-1554-0, 10.1140/epjc/s10052-013-2501-z [arXiv:1007.1727 [physics.data-an]].

[70] G. J. Feldman and R. D. Cousins, "*A Unified approach to the classical statistical analysis of small signals*", Phys. Rev. D **57** (1998) 3873 doi:10.1103/PhysRevD.57.3873 [physics/9711021 [physics.data-an]].

[71] G. C. Branco, P. M. Ferreira, L. Lavoura, M. N. Rebelo, M. Sher and J. P. Silva, "*Theory and phenomenology of two-Higgs-doublet models*", Phys. Rept. **516** (2012) 1 doi:10.1016/j.physrep.2012.02.002 [arXiv:1106.0034 [hep-ph]].

[72] P. M. Ferreira, J. F. Gunion, H. E. Haber and R. Santos, "*Probing wrong-sign Yukawa couplings at the LHC and a future linear collider*", Phys. Rev. D **89** (2014) no.11, 115003 doi:10.1103/PhysRevD.89.115003 [arXiv:1403.4736 [hep-ph]].

[73] P. M. Ferreira, R. Guedes, M. O. P. Sampaio and R. Santos, "*Wrong sign*

and symmetric limits and non-decoupling in 2HDMs", JHEP **1412** (2014) 067 doi:10.1007/JHEP12(2014)067 [arXiv:1409.6723 [hep-ph]].

[74] G. Aad *et al.* [ATLAS Collaboration], "*Search for a heavy Standard Model Higgs boson in the channel $H \to ZZ \to \ell^+\ell^- q\bar{q}$ using the ATLAS detector*", Phys. Lett. B **707** (2012) 27 doi:10.1016/j.physletb.2011.11.056 [arXiv:1108.5064 [hep-ex]].

[75] G. Aad *et al.* [ATLAS Collaboration], "*Search for a standard model Higgs boson in the mass range 200-600 GeV in the $H \to ZZ \to \ell^+\ell^- q\bar{q}$ decay channel with the ATLAS detector*", Phys. Lett. B **717** (2012) 70 doi:10.1016/j.physletb.2012.09.020 [arXiv:1206.2443 [hep-ex]].

[76] G. Aad *et al.* [ATLAS Collaboration], "*The ATLAS Simulation Infrastructure*", Eur. Phys. J. C **70** (2010) 823 doi:10.1140/epjc/s10052-010-1429-9 [arXiv:1005.4568 [physics.ins-det]].

[77] W. Lukas, "*Fast Simulation for ATLAS: Atlfast-II and ISF*", ATL-SOFT-PROC-2012-065, ATL-COM-SOFT-2012-137.

[78] S. Heinemeyer *et al.* [LHC Higgs Cross Section Working Group Collaboration], "*Handbook of LHC Higgs Cross Sections: 3. Higgs Properties*", doi:10.5170/CERN-2013-004 arXiv:1307.1347 [hep-ph].

[79] J. Alwall *et al.*, "*The automated computation of tree-level and next-to-leading order differential cross sections, and their matching to parton shower simulations*", JHEP **1407** (2014) 079 doi:10.1007/JHEP07(2014)079 [arXiv:1405.0301 [hep-ph]].

[80] P. Nason, "*A New method for combining NLO QCD with shower Monte Carlo algorithms*", JHEP **0411** (2004) 040 doi:10.1088/1126-6708/2004/11/040 [hep-ph/0409146].

[81] S. Frixione, P. Nason and C. Oleari, "*Matching NLO QCD computations with Parton Shower simulations: the POWHEG method*", JHEP **0711** (2007) 070 doi:10.1088/1126-6708/2007/11/070 [arXiv:0709.2092 [hep-ph]].

[82] S. Alioli, P. Nason, C. Oleari and E. Re, "*A general framework for implementing NLO calculations in shower Monte Carlo programs: the POWHEG BOX*", JHEP **1006** (2010) 043 doi:10.1007/JHEP06(2010)043 [arXiv:1002.2581 [hep-ph]].

[83] N. Kauer and G. Passarino, "*Inadequacy of zero-width approximation for a light Higgs boson signal*", JHEP **1208** (2012) 116 doi:10.1007/JHEP08(2012)116 [arXiv:1206.4803 [hep-ph]].

[84] S. Goria, G. Passarino and D. Rosco, "*The Higgs Boson Lineshape*",

Nucl. Phys. B **864** (2012) 530 doi:10.1016/j.nuclphysb.2012.07.006 [arXiv:1112.5517 [hep-ph]].

[85] G. Passarino, "*Higgs Interference Effects in gg → ZZ and their Uncertainty*", JHEP **1208** (2012) 146 doi:10.1007/JHEP08(2012)146 [arXiv:1206.3824 [hep-ph]].

[86] J. M. Campbell, R. K. Ellis and C. Williams, "*Vector boson pair production at the LHC*", JHEP **1107** (2011) 018 doi:10.1007/JHEP07(2011)018 [arXiv:1105.0020 [hep-ph]].

[87] J. M. Campbell, R. K. Ellis and C. Williams, "*Gluon-Gluon Contributions to W+ W- Production and Higgs Interference Effects*", JHEP **1110** (2011) 005 doi:10.1007/JHEP10(2011)005 [arXiv:1107.5569 [hep-ph]].

[88] T. Binoth, N. Kauer and P. Mertsch, "*Gluon-induced QCD corrections to pp —> ZZ —> l anti-l l-prime anti-l-prime*", doi:10.3360/dis.2008.142 arXiv:0807.0024 [hep-ph].

[89] K. Arnold *et al.*, "*Release Note – Vbfnlo-2.6.0*", arXiv:1207.4975 [hep-ph].

[90] K. Arnold *et al.*, "*VBFNLO: A Parton Level Monte Carlo for Processes with Electroweak Bosons – Manual for Version 2.5.0*", arXiv:1107.4038 [hep-ph].

[91] A. Djouadi, M. Spira and P. M. Zerwas, "*Production of Higgs bosons in proton colliders: QCD corrections*", Phys. Lett. B **264** (1991) 440. doi:10.1016/0370-2693(91)90375-Z

[92] S. Dawson, "*Radiative corrections to Higgs boson production*", Nucl. Phys. B **359** (1991) 283. doi:10.1016/0550-3213(91)90061-2

[93] M. Spira, A. Djouadi, D. Graudenz and P. M. Zerwas, "*Higgs boson production at the LHC*", Nucl. Phys. B **453** (1995) 17 doi:10.1016/0550-3213(95)00379-7 [hep-ph/9504378].

[94] R. V. Harlander and W. B. Kilgore, "*Next-to-next-to-leading order Higgs production at hadron colliders*", Phys. Rev. Lett. **88** (2002) 201801 doi:10.1103/PhysRevLett.88.201801 [hep-ph/0201206].

[95] C. Anastasiou and K. Melnikov, "*Higgs boson production at hadron colliders in NNLO QCD*", Nucl. Phys. B **646** (2002) 220 doi:10.1016/S0550-3213(02)00837-4 [hep-ph/0207004].

[96] V. Ravindran, J. Smith and W. L. van Neerven, "*NNLO corrections to the total cross-section for Higgs boson production in hadron hadron collisions*", Nucl. Phys. B **665** (2003) 325 doi:10.1016/S0550-3213(03)00457-7 [hep-ph/0302135].

[97] U. Aglietti, R. Bonciani, G. Degrassi and A. Vicini, "*Two loop light fermion contribution to Higgs production and decays*", Phys. Lett. B **595** (2004) 432 doi:10.1016/j.physletb.2004.06.063 [hep-ph/0404071].

[98] S. Actis, G. Passarino, C. Sturm and S. Uccirati, "*NLO Electroweak Corrections to Higgs Boson Production at Hadron Colliders*", Phys. Lett. B **670** (2008) 12 doi:10.1016/j.physletb.2008.10.018 [arXiv:0809.1301 [hep-ph]].

[99] S. Catani, D. de Florian, M. Grazzini and P. Nason, "*Soft gluon resummation for Higgs boson production at hadron colliders*", JHEP **0307** (2003) 028 doi:10.1088/1126-6708/2003/07/028 [hep-ph/0306211].

[100] C. Anastasiou, R. Boughezal and F. Petriello, "*Mixed QCD-electroweak corrections to Higgs boson production in gluon fusion*", JHEP **0904** (2009) 003 doi:10.1088/1126-6708/2009/04/003 [arXiv:0811.3458 [hep-ph]].

[101] D. de Florian and M. Grazzini, "*Higgs production through gluon fusion: Updated cross sections at the Tevatron and the LHC*", Phys. Lett. B **674** (2009) 291 doi:10.1016/j.physletb.2009.03.033 [arXiv:0901.2427 [hep-ph]].

[102] J. Baglio and A. Djouadi, "*Higgs production at the LHC*", JHEP **1103** (2011) 055 doi:10.1007/JHEP03(2011)055 [arXiv:1012.0530 [hep-ph]].

[103] M. Ciccolini, A. Denner and S. Dittmaier, "*Strong and electroweak corrections to the production of Higgs + 2jets via weak interactions at the LHC*", Phys. Rev. Lett. **99** (2007) 161803 doi:10.1103/PhysRevLett.99.161803 [arXiv:0707.0381 [hep-ph]].

[104] M. Ciccolini, A. Denner and S. Dittmaier, "*Electroweak and QCD corrections to Higgs production via vector-boson fusion at the LHC*", Phys. Rev. D **77** (2008) 013002 doi:10.1103/PhysRevD.77.013002 [arXiv:0710.4749 [hep-ph]].

[105] K. Arnold *et al.*, "*VBFNLO: A Parton level Monte Carlo for processes with electroweak bosons*", Comput. Phys. Commun. **180** (2009) 1661 doi:10.1016/j.cpc.2009.03.006 [arXiv:0811.4559 [hep-ph]].

[106] P. Bolzoni, F. Maltoni, S. O. Moch and M. Zaro, "*Higgs production via vector-boson fusion at NNLO in QCD*", Phys. Rev. Lett. **105** (2010) 011801 doi:10.1103/PhysRevLett.105.011801 [arXiv:1003.4451 [hep-ph]].

[107] T. Gleisberg, S. Hoeche, F. Krauss, M. Schonherr, S. Schumann, F. Siegert and J. Winter, "*Event generation with SHERPA 1.1*", JHEP **0902** (2009) 007 doi:10.1088/1126-6708/2009/02/007 [arXiv:0811.4622 [hep-ph]].

[108] S. Alioli, P. Nason, C. Oleari and E. Re, "*NLO Higgs boson production via gluon fusion matched with shower in POWHEG*", JHEP **0904** (2009) 002 doi:10.1088/1126-6708/2009/04/002 [arXiv:0812.0578 [hep-ph]].

[109] P. Nason and C. Oleari, "*NLO Higgs boson production via vector-boson fusion matched with shower in POWHEG*", JHEP **1002** (2010) 037 doi:10.1007/JHEP02(2010)037 [arXiv:0911.5299 [hep-ph]].

[110] C. Oleari and L. Reina, "*W +- b $\bar{b}$ production in POWHEG*", JHEP **1108** (2011) 061 [JHEP **1111** (2011) 040] doi:10.1007/JHEP11(2011)040, 10.1007/JHEP08(2011)061 [arXiv:1105.4488 [hep-ph]].

[111] G. Aad *et al.* [ATLAS Collaboration], "*Measurement of the muon reconstruction performance of the ATLAS detector using 2011 and 2012 LHC protonÐproton collision data*", Eur. Phys. J. C **74** (2014) 11, 3130 doi:10.1140/epjc/s10052-014-3130-x [arXiv:1407.3935 [hep-ex]].

[112] [ATLAS Collaboration], "*Properties of Jets and Inputs to Jet Reconstruction and Calibration with the ATLAS Detector Using Proton-Proton Collisions at $\sqrt{s} = 7$ TeV*", ATLAS-CONF-2010-053.

[113] [ATLAS Collaboration], "*ATLAS jet energy scale uncertainties using tracks in proton proton collisions at $\sqrt{s} = 7$ TeV*", ATLAS-CONF-2011-067.

[114] [ATLAS Collaboration], "*b-jet tagging calibration on c-jets containing D^{*+} mesons*", ATLAS-CONF-2012-039.

[115] [ATLAS Collaboration], "*Measurement of the Mistag Rate with 5 fb^{-1} of Data Collected by the ATLAS Detector*", ATLAS-CONF-2012-040.

[116] [ATLAS Collaboration], "*Measurement of the b-tag Efficiency in a Sample of Jets Containing Muons with 5 fb^{-1} of Data from the ATLAS Detector*" ATLAS-CONF-2012-043.

[117] G. Aad *et al.* [ATLAS Collaboration], "*Measurement of the production cross section of jets in association with a Z boson in pp collisions at $\sqrt{s}$ = 7 TeV with the ATLAS detector*", JHEP **1307** (2013) 032 doi:10.1007/JHEP07(2013)032 [arXiv:1304.7098 [hep-ex]].

[118] S. Hoeche, F. Krauss, M. Schonherr and F. Siegert, "*QCD matrix elements + parton showers: The NLO case*", JHEP **1304** (2013) 027 doi:10.1007/JHEP04(2013)027 [arXiv:1207.5030 [hep-ph]].

[119] The ATLAS collaboration [ATLAS Collaboration], "*Calibration of b-tagging using dileptonic top pair events in a combinatorial likelihood approach with the ATLAS experiment*", ATLAS-CONF-2014-004.

[120] G. Aad *et al.* [ATLAS Collaboration], "*Measurements of top quark pair relative differential cross-sections with ATLAS in pp collisions at $\sqrt{s} = 7$ TeV*", Eur. Phys. J. C **73** (2013) 1, 2261 doi:10.1140/epjc/s10052-012-2261-1 [arXiv:1207.5644 [hep-ex]].

[121] I. W. Stewart and F. J. Tackmann, "*Theory Uncertainties for Higgs and Other Searches Using Jet Bins*", Phys. Rev. D **85** (2012) 034011 doi:10.1103/PhysRevD.85.034011 [arXiv:1107.2117 [hep-ph]].

[122] S. Gangal and F. J. Tackmann, "*Next-to-leading-order uncertainties in Higgs+2 jets from gluon fusion*", Phys. Rev. D **87** (2013) 9, 093008 doi:10.1103/PhysRevD.87.093008 [arXiv:1302.5437 [hep-ph]].

[123] A. L. Read, "*Presentation of search results: The CL(s) technique*", J. Phys. G **28** (2002) 2693. doi:10.1088/0954-3899/28/10/313

[124] G. Aad *et al.* [ATLAS Collaboration], "*Measurement of differential production cross-sections for a Z boson in association with b-jets in 7 TeV proton-proton collisions with the ATLAS detector*", JHEP **1410** (2014) 141 doi:10.1007/JHEP10(2014)141 [arXiv:1407.3643 [hep-ex]].

[125] G. Aad *et al.* [ATLAS Collaboration], "*Search for an additional, heavy Higgs boson in the $H \to ZZ$ decay channel at $\sqrt{s} = 8$ TeV in pp collision data with the ATLAS detector*", Eur. Phys. J. C **76** (2016) no.1, 45 doi:10.1140/epjc/s10052-015-3820-z [arXiv:1507.05930 [hep-ex]].